Technical Report Documentation Page

1. Report No.	2. Government Accession No.	3. Recipient's Catalog No.

4. Title and Subtitle
Fracture Analysis and Corrosion Fatigue in Pipelines

5. Report Date
September 1983

6. Performing Organization Code

8. Performing Organization Report No.

7. Author(s) F. Erdogan and R.P. Wei

9. Performing Organization Name and Address
Department of Mechanical Engineering and Mechanics
Lehigh University
Bethlehem, PA 18015

10. Work Unit No. (TRAIS)

11. Contract or Grant No.
DTRS 56 82-C-00014

12. Sponsoring Agency Name and Address
U.S. Department of Transportation
Research and Special Programs Administration
Office of University Research
Washington, D.C.

13. Type of Report and Period Covered
Annual Report
October 1982-September 198

14. Sponsoring Agency Code

15. Supplementary Notes

16. Abstract

In this report the completed part of the research project on the fracture analysis and corrosion fatigue in pipelines is presented. The report consists of two parts. The first part describes the theoretical work on the flaw evaluation as it relates to weld defects in pipelines. The experimental work on the corrosion fatigue in pipeline steels is discussed in the second part. The fracture mechanics methodology is used throughout the investigation. First, the possible weld defects have been reviewed and classified from a viewpoint of their importance in a fracture initiation and propagation process. Then a group of flaw-flaw and flaw-free surface interaction problems have been identified and investigated. Three groups of defects which are identified are pores and solid inclusions with smooth boundaries, pores, notches, and solid inclusions with sharp corners, and cracks and planar inclusions. The results for the following interaction problems have been presented: the interaction between a crack and a solid inclusion or a pore, between cracks and boundaries, between multiple cracks, between flat inclusions and cracks, and planar cracks of finite size. In the second part of the report after briefly discussing the mechanisms of corrosion fatigue, the electrochemical measurement techniques for determining the kinetics of passivation or surface reaction of clean surfaces are described. The completed part of the studies on the kinetics of corrosion fatigue crack propagation in X70 linepipe steel is then presented. The experiments were carried out with distilled water and 1N Na_2CO_3-1N $NaHCO_3$ solution under constant stress intensity conditions at four different temperatures rangine from 20°C to 90°C and at frequencies ranging from 10^{-2} to 10 Hz.

17. Key Words	18. Distribution Statement
Fracture Mechanics, Pipelines, Flaw Interaction, Weld Defects, Cracks, Inclusions, Fatigue Crack Propagation, Corrosion Fatigue, Chemical Reactions, Environmental Effects	This document is available to the U.S. public through the National Technical Information Service, Springfield, Virginia 22161

19. Security Classif. (of this report)	20. Security Classif. (of this page)	21. No. of Pages	22. Price
Unclassified	Unclassified		

Form DOT F 1700.7 (8-72) Reproduction of completed page authorized

FRACTURE ANALYSIS AND CORROSION FATIGUE IN PIPELINES

Scope of the Project

The primary objectives of this research program are

(a) Classification and assessment of the relative importance of various types of weld defects
(b) An in-depth study of the problem of interaction between two flaws and between flaws and pipe surfaces
(c) Fracture analysis of pipes with crack arrestors
(d) The effect of crack orientation on the strength of pipes
(e) The development of quantitative understanding of the early stage of chemical reactions in relation to the corrosion fatigue crack initiation and propagation
(f) Elucidating the mechanisms for corrosion fatigue crack initiation and propagation, including the influences of chemical, mechanical and metallurgical variables in pipeline steels
(g) The formulation and evaluation of models for predicting cracking response and service performance by using a combined fracture mechanics, surface chemistry and materials science approach.

In this first annual report the completed part of the research program is described and the results are presented.

General Information

The research presented in this report is supported by the U.S. Department of Transportation, Office of University Research, and by the U.S. Department of Interior, Minerals Management Service. Mr. Duglas B. Chisholm of DOT Research and Special Programs Administration, Office of Pipeline Safety Regulation is the Project Monitor. Dr. Charles

E. Smith, Research Program Manager, Technology Assessment and Research Branch, Minerals Management Service is the Department of Interior technical representative.

Part I of the report describes the theoretical research carried out by Professor F. Erdogan, the Principal Investigator, Mr. B. Aksel and Dr. X-H Liu. Part II presents the experimental work which was carried out by Professor R.P. Wei, the Co-Principal Investigator and Mr. S. Chiou.

FRACTURE ANALYSIS AND CORROSION FATIGUE IN PIPELINES

PART I

THE FLAW INTERACTION STUDIES

In this part of the report various kinds of flaws which may be found in pipelines, particularly in girth welds are classified and the problem of interaction between the stress fields of typical flaws are considered. The emphasis in the study is on the application of fracture mechanics techniques to the problem of flaw evaluation.

1. INTRODUCTION

The standards of acceptability of welds in pipelines are generally based on certain empirical criteria in which primary importance is placed on flaw length. Specifically for girth welds such standards are described in API STANDARD 1104 prepared by the "American Petroleum Institute - American Gas Association Joint Committee on Oil and Gas Pipeline Field Welding Practices". However, the API Standard also recognizes fitness for purpose criteria based on fracture mechanics methodology as an alternative technique for flaw evaluation. The advantage of the fracture mechanics approach is that since it takes into account all factors which may be relevant to the failure of the pipe such as the type and the relative size, shape, orientation and location of the flaw, the effect of multiple flaws, the nature of the applied stresses, and the environmental conditions, it could be somewhat more precise than the empirical rules which are largely based on the flaw length.

In fracture mechanics approach to flaw evaluation it is implicitly assumed that the material contains some macroscopic flaws which may form the nucleus of fracture initiation. Generally, these flaws may be mapped by using an appropriate nondestructive flaw detection technique. Aside from the weld defects the pipe may also have flaws which may be external

in origin. Generally the initial phase of the failure in a pipe is the rupture of the net ligament adjacent to the critical flaw in the pipe wall. In most cases the resulting through crack is arrested and the pipe is repaired before further damage. However, in some cases the resulting through crack, after some stable growth, may become unstable leading to circumferential pipe break or dynamic propagation of an axial crack. The initial rupture of the net ligament in the pipe wall is usually preceded by some subcritical crack growth due to fatigue, corrosion fatigue, or stress corrosion cracking and the actual net ligament rupture is generally a ductile fracture process.

Therefore, it is seen that in order to apply fracture mechanics analysis to welded pipes, first one needs to characterize the material itself (the base metal, the weld material and the material in the heat affected zone) with regard to fatigue and corrosion fatigue crack propagation, stress corrosion cracking, fracture toughness and ductile fracture. Next, for a given flaw geometry and loading conditions one has to solve the related mechanics problem to calculate the appropriate fracture mechanics parameter such as the stress intensity factor, the crack tip opening displacement, or the J-integral. The third step in the process would be the selection or development of a proper failure theory and the application of the related quantitative failure criterion. The type of analysis and the experimental work to be performed and the particular criterion to be used are clearly dependent on the expected or the most likely mode of failure.

Even though the primary applied load in the pipelines is the internal pressure which is largely time-independent, there may be some small variations in pressure and some vibrations particularly near the pumping stations which may add a fluctuating component to the static stresses just high enough to cause concern. There are also secondary stresses which are mainly time-varying in nature and therefore would enhance the subcritical crack propagation. Some of the sources of these secondary stresses are misalignment and fit-up, daily, seasonal and other thermal fluctuations, ground settlement and possible earthquakes, axial constraint,

and gross bending in offshore piping due to buoyancy and other hydroelastic effects. It should be added that the "stress transients" may also play a major role in the subcritical crack propagation and particularly in the final phase of the fracture process, if one takes place. These stresses are generally caused by the pressure waves resulting from changes in flow rate due to partially or fully closing of the valves. In the case of pipes carrying liquids such as petroleum pipelines this is known as the "water hammer" effect due to which the peak pressure may be as high as multiples of the then operating pressure in the pipe. In the natural gas pipelines, this increase in the peak pressure may be somewhat more moderate. Nevertheless, in either case, such sudden surges of pressure are probably responsible in most cases for the final stage of the net ligament failure in the pipe wall resulting in leaks or in a catastrophic failure.

A detailed description and classification of weld discontinuities (including "flaws" which are considered to be undesirable) and a critical review of the literature as well as very extensive references on the subject up to 1976 may be found in [1]. The problem of interaction between two (planar) cracks and some empirical rules to define a single equivalent crack are discussed in [2]. The procedures dealing with the subcritical crack propagation by using the tools of linear elastic fracture mechanics (LEFM) is highly standardized and may be found, for example, in [3] or [4]. Similarly, the process of brittle or quasi-brittle fracture is relatively well-understood and is easily dealt with techniques based on LEFM and the concept of fracture toughness. The process which is not well-understood and not standardized, however, is the ductile fracture. The Appendix in the API Standard 1104 concerning the fracture mechanics applications is based on the critical crack tip opening displacement concept, whereas the J-integral seems to be more widely used in pressure vessel technology. The description, some applications of and extensive references on the crack opening displacement approach to fracture may be found in [5]-[7]. Application of a general fracture instability concept based on the crack opening displacement to shells and plates with a part-through crack is described in [8].

In this report the emphasis is on the flaw evaluation based on fracture mechanics techniques. In particular this part of the study is concerned with the effect flaw-flaw and flaw-boundary interaction on the fracture mechanics parameters. After classifying possible flaws which may be found in welds from a viewpoint of their importance in fracture mechanics applications, some of the more important flaw interaction problems have been identified, their method of solution is briefly discussed and some typical and useful results are given.

2. TYPES OF FLAWS

In this report our primary interest in flaws is from a viewpoint of their influence on enhancing or inhibiting fracture initiation and propagation in the pipe. Generally a flaw may be defined as a discontinuity in material constants or geometry. Variety of inclusions come under first and notches, pores and cracks come under the second group of flaws. A common feature of all flaws is that they disturb or perturb the stress field around them. Generally this perturbation gives rise to a stress concentration around the flaw. However, for certain types of flaws there may also be a reduction in key components of the stresses. With their importance in the application of fracture mechanics analysis in mind, in this study we will, therefore, introduce a somewhat unconventional classification of flaws.

2.1 Pores and Solid Inclusions

Pores are the holes or voids in the material having entirely smooth surfaces (Fig. 1.a1). If σ_o refers to the magnitude of the uniform stress field outside the perturbation region of the pore, then the pore leads to a stress concentration which is of the form

$$\sigma_{max} = K\sigma_o \quad , \quad K = \frac{A}{\sqrt{\rho}} \quad , \tag{1}$$

where K is the "stress concentration factor", A is a (finite) constant which depends on the geometry of the medium and ρ is radius of curvature

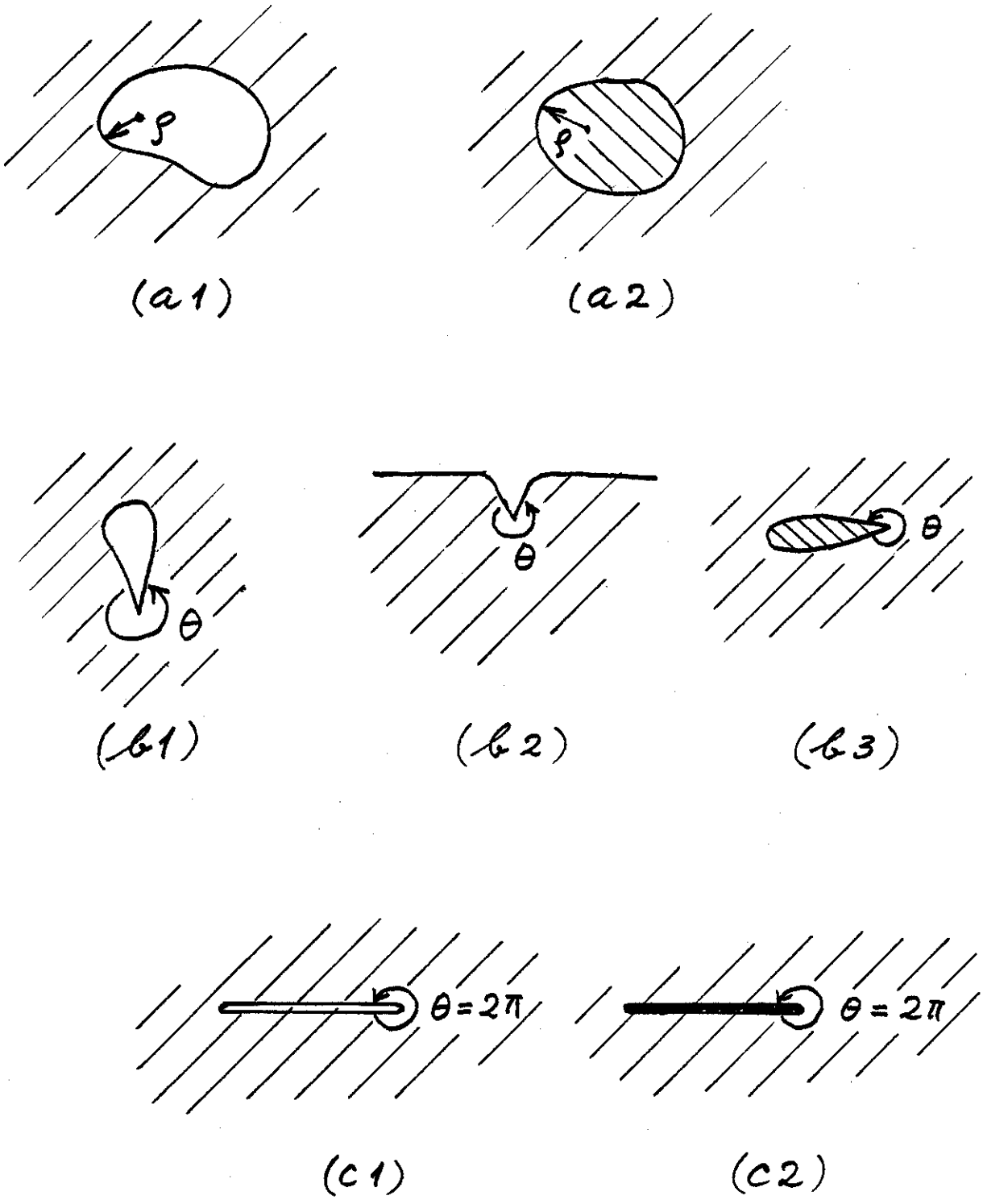

Fig. 1 Types of Flaws

of the pore. Generally K is greater than one. We note that surface notches with finite radius of curvature ρ would also come under this category.

Solid inclusions are the second phase materials in the medium also having entirely smooth surfaces. The modulus E_i of the inclusion may be greater or less than the modulus E of the matrix or the base material, the two limiting cases being the rigid inclusion ($E_i=\infty$) and the hole ($E_i=0$). If $E_i<E$, qualitatively the perturbed stress field of the inclusion is similar to that of a pore, meaning that there would be a stress concentration around the inclusion. On the other hand, if $E_i>E$ there would be a reduction in the net section stress. However, in this case there would also be a stress concentration in other planes perpendicular to the applied stress. For example, Fig. 2 shows the stress distribution in a medium containing a circular inclusion under plane strain or plane stress conditions. Note that for c>R around the inclusion there is indeed some stress concentration. In this figure, μ is the shear modulus, $\kappa = 3-4\nu$ for plane strain, and $\kappa = (3-\nu)/(1+\nu)$ for plane stress, ν being the Poisson's ratio.

2.2 Pores, Notches and Solid Inclusions with Sharp Corners

From Eq. (1) and Fig. 2 it may be seen that from a viewpoint of failure analysis a distinguishing feature of the pores, notches and solid inclusions with smooth surfaces is that the stress state around such flaws is always bounded. Eq. (1) also indicates that as the root radius ρ of the notch tends to zero, the stress state around notch tip would tend to infinity. Particularly in problems concerning brittle fracture and fatigue crack initiation such flaws may have to be treated differently. In these nonplanar flaw problems it is said that the inclusion or the notch tip is a point of stress singularity around which the stress state would have the following behavior:

$$\sigma_{ij} = \frac{k}{r^{\lambda}} \quad , \quad 0 < \mathrm{Re}(\lambda) \leq 1/2 \ , \tag{2}$$

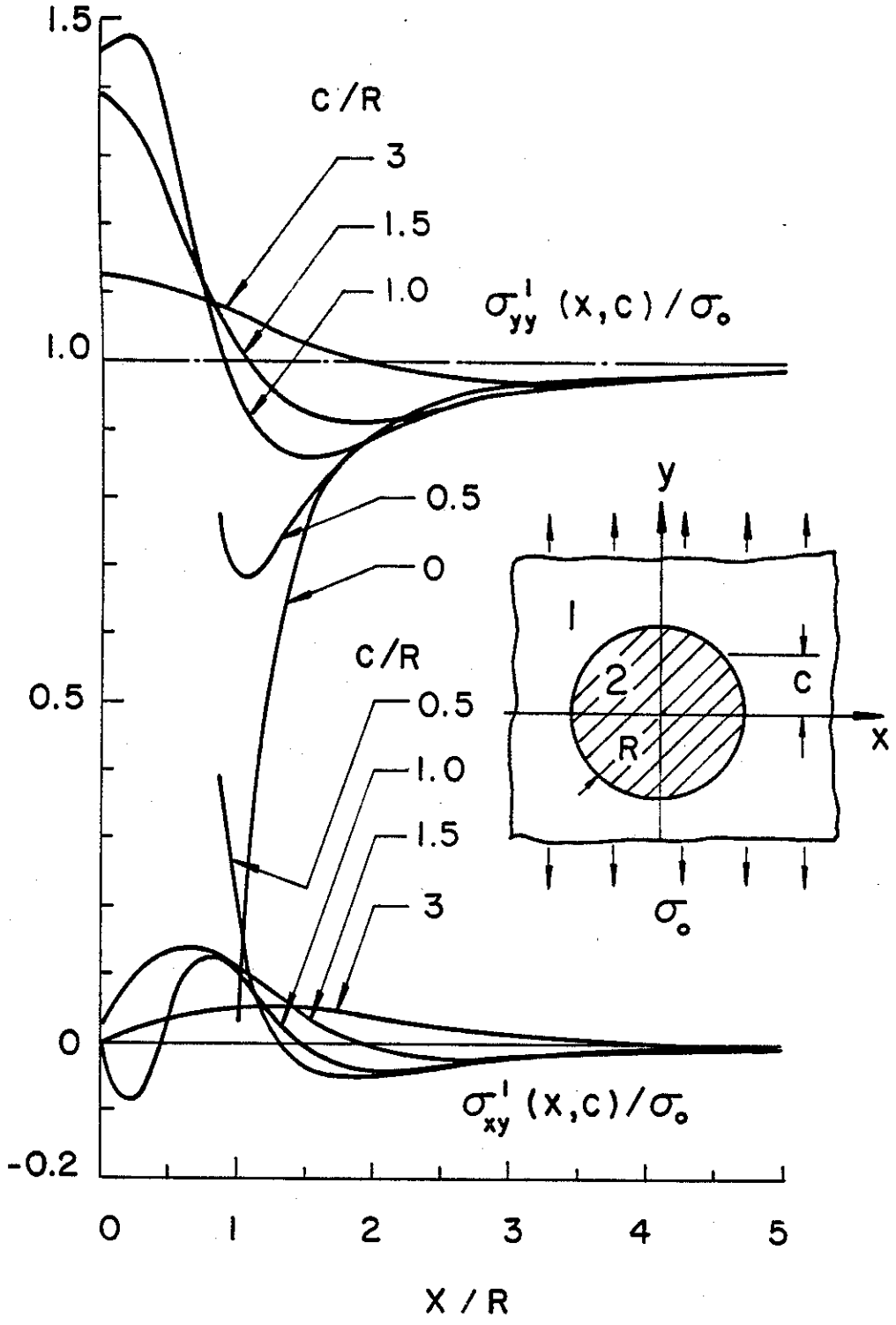

Figure 2. The stress distribution in a plate with a circular elastic inclusion ($\mu_2 = 23\mu_1$, $\kappa_1 = 1.6$, $\kappa_2 = 1.8$).

where k and λ are constants representing the strength and the power of the stress singularity and r is a (small) distance from the notch tip. Generally, Eq. (2) is valid for values of the material angle $\theta > \pi$ (Fig. 1 b1, b2, b3). Even though the term "stress intensity factor" is commonly used in relation with crack problems for which $\lambda = 0.5$, in the more general problem leading to an expression such as (2) k is also called the "stress intensity factor".

In the case of notches with a material angle $\pi < \theta < 2\pi$ the power of singularity λ is dependent on θ only and may be obtained from (see, for example, [9] where the general problem of bimaterial wedge under variety of boundary conditions are discussed)

$$\cos[2(\lambda-1)\theta] - 1 + (\lambda-1)^2(1-\cos 2\theta) = 0 \quad . \tag{3}$$

Fig. 3 shows the solution of (3) in the relevant range.

2.3 Cracks and Flat Inclusions

These are simply the planar flaws in which the material angle θ (theoretically) is 2π (Fig. 1 c1, c2). Again, the inclusion may be elastic or rigid, the crack being a limiting case with zero modulus. In all planar inclusion as well as crack problems eq. (2) is valid with $\lambda = 0.5$.

The bulk of the material in this report is devoted to the problem of interaction between two flaws or a flaw and a boundary. Since the initial phase of the fracture problem is invariably a subcritical crack growth and since the stress intensity factor is the primary fracture mechanics parameter used in analyzing the subcritical crack growth process, the quantitative results in the interaction problems considered are mostly the stress intensity factors.

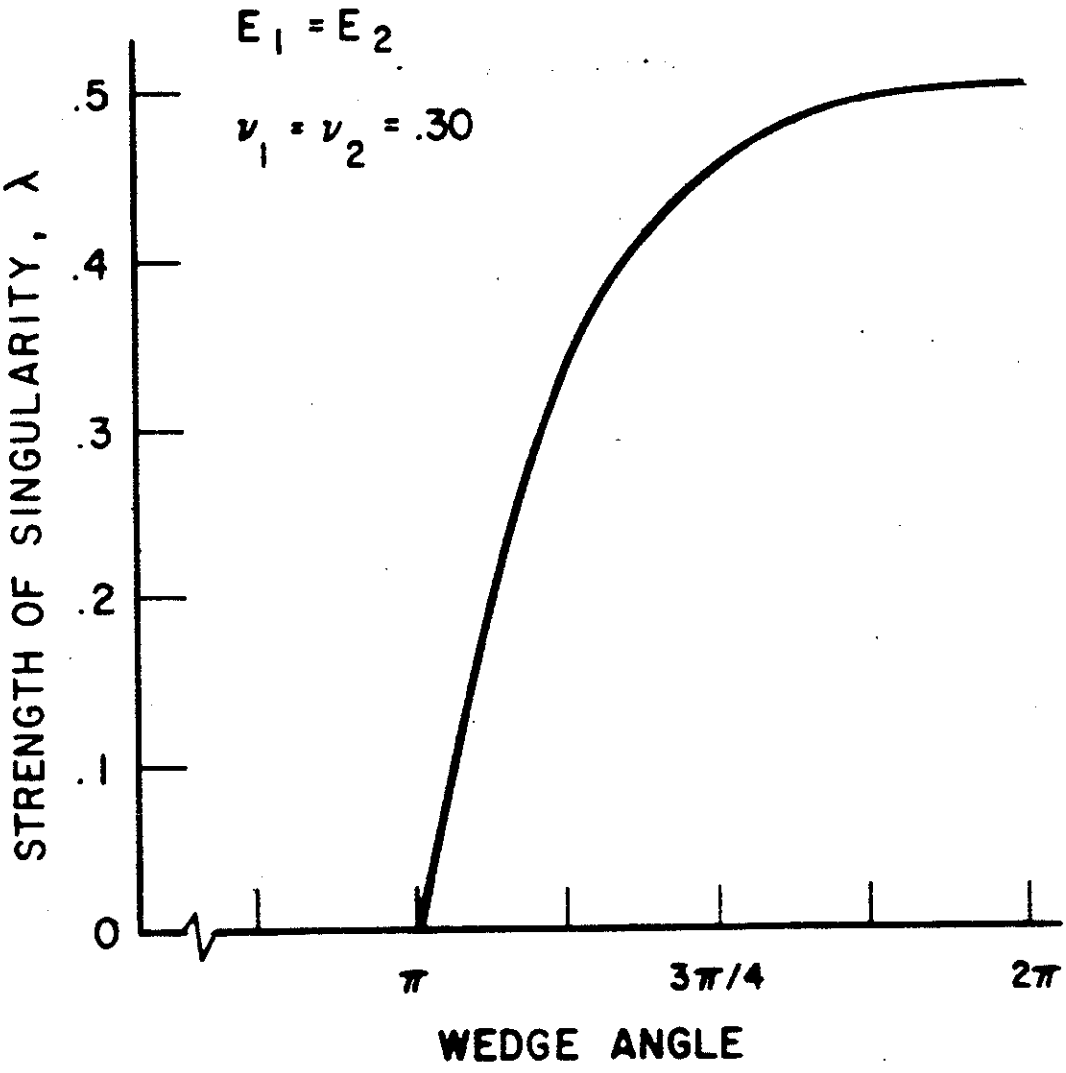

Fig. 3 STRENGTH OF STRESS SINGULARITY
($\sigma_{ij} \propto r^{-\lambda}$)

3. INTERACTION BETWEEN A CRACK AND A SOLID INCLUSION OR A PORE

In this section we will consider the problem of the interaction between a solid elastic inclusion and a line crack. It will be assumed that the inclusion and the crack are sufficiently close to each other so that their perturbed stress fields interact with each other. It will also be assumed that the crack-inclusion region is sufficiently far away from the boundaries so that their combined perturbed stress field does not interact with the boundaries. Consequently, for the purpose of calculating the perturbed stress state and the stress intensity factors it may be assumed that the domain is infinite.

3.1 Plane Strain Problem for a Circular Inclusion or Pore

Consider the general crack-inclusion problem described in Fig. 4. Assume that the composite medium is under plane strain or generalized plane stress conditions, with μ_i and κ_i, $(i=1,2)$ referring to the elastic constants (μ_i the shear modulus, $\kappa_i = 3-4\nu_i$ for plane strain, and $\kappa_i = (3-\nu_i)/(1+\nu_i)$ for plane stress, ν_i being the Poisson's ratio). Let u_t and u_w be the displacement components in t and w directions shown in Fig. 4(b). By defining

$$g_1(t) = \frac{\partial}{\partial t}\,(u_t^+ - u_t^-)\ ,\quad g_2(t) = \frac{\partial}{\partial t}\,(u_w^+ - u_w^-)\ , \tag{4}$$

and by referring to [10] for details, the problem may be formulated in terms of a pair of singular integral equations of the following form:

$$\frac{1}{\pi}\int_{t_2}^{t_1} \sum_{j=1}^{2} k_{ij}(t,t_o)g_j(t_o)dt_o = \frac{1+\kappa_1}{2\mu_1}\,p_i(t)\ ,\quad (i=1,2) \tag{5}$$

where the kernels k_{ij} are known functions and have a Cauchy type singularity. The known input functions p_1 and p_2 are given by

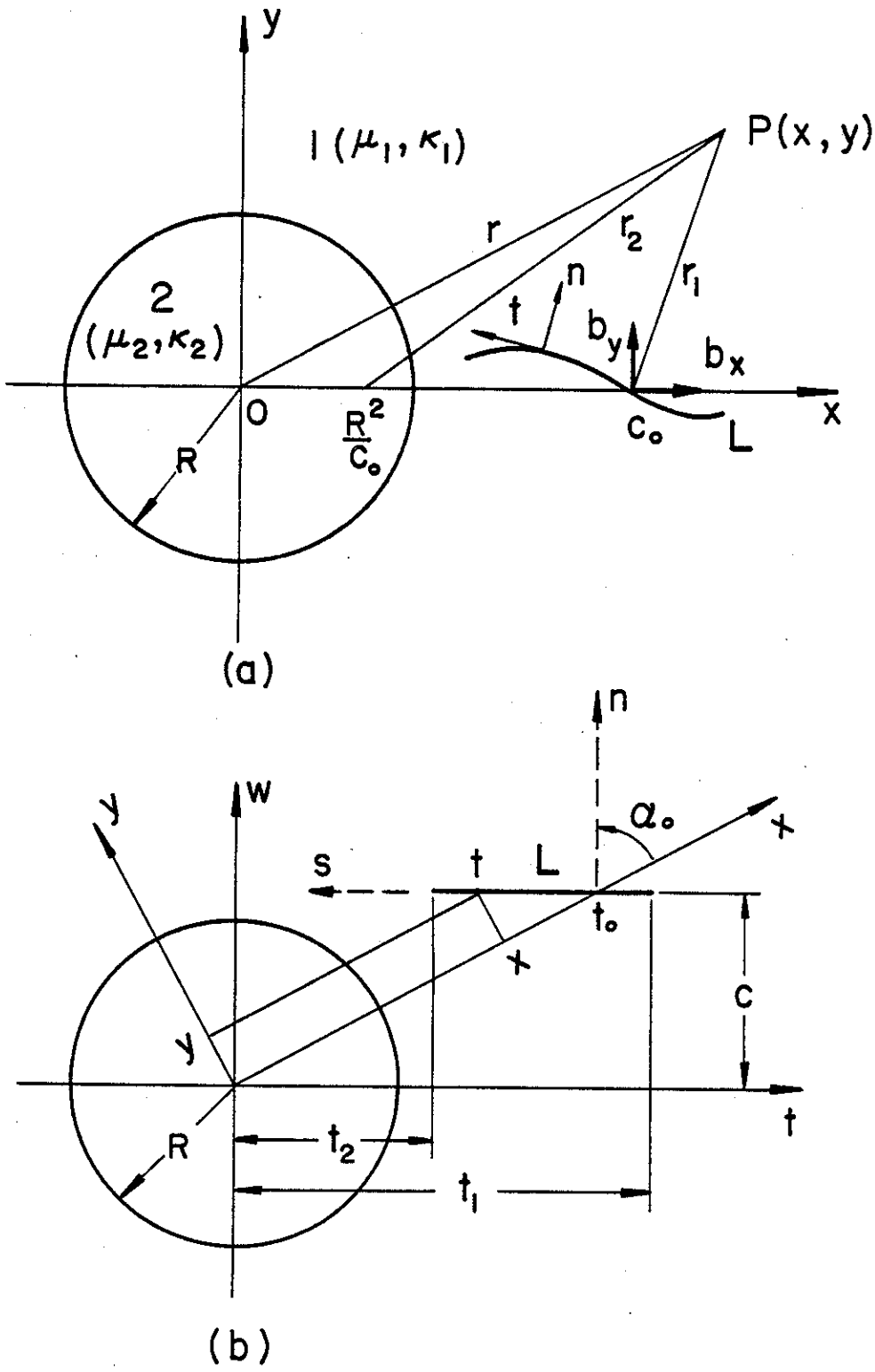

Figure 4. Geometry showing the dislocations b_x and b_y, and the crack L in the neighborhood of the inclusion 2.

$$p_1(t) = -\sigma_{ww}(t,c) \ , \ p_2(t) = -\sigma_{wt}(t,c) \ , \ (t_2<t<t_1) \ , \qquad (6)$$

σ_{ww} and σ_{wt} being the stress components at the point (t,c) in the plane with inclusion but without a crack. For example, for a plane under uniform tension σ_o away from the inclusion these stresses are given by Fig. 2. The solution of (5) is of the following form

$$g_j(t) = G_j(t)/\sqrt{(t-t_2)(t_1-t)} \ , \ (j=1,2) \qquad (7)$$

where G_1 and G_2 are unknown bounded functions. After solving the integral equations the Modes I and II stress intensity factors at the crack tips t_1 and t_2 may be defined by and obtained from the following expressions:

$$k_1(t_1) = \lim_{t\to t_1} \sqrt{2(t-t_1)} \ \sigma_{ww}(t,c) = -\frac{2\mu_1}{1+\kappa_1} \lim_{t\to t_1} \sqrt{2(t_1-t)} \ g_2(t) \ ,$$

$$k_2(t_1) = \lim_{t\to t_1} \sqrt{2(t-t_1)} \ \sigma_{wt}(t,c) = -\frac{2\mu_1}{1+\kappa_1} \lim_{t\to t_1} \sqrt{2(t_1-t)} \ g_1(t) \ ,$$

$$k_1(t_2) = \lim_{t\to t_2} \sqrt{2(t_2-t)} \ \sigma_{ww}(t,c) = \frac{2\mu_1}{1+\kappa_1} \lim_{t\ t_2} \sqrt{2(t-t_2)} \ g_2(t) \ ,$$

$$k_2(t_2) = \lim_{t\to t_2} \sqrt{2(t_2-t)} \ \sigma_{wt}(t,c) = \frac{2\mu_1}{1+\kappa_1} \lim_{t\to t_2} \sqrt{2(t-t_2)} \ g_1(t).$$

(8a-d)

In the absence of a crack the stress components on a line perpendicular to the loading direction are shown in Fig. 2 for an elastic inclusion. Similar results for a circular hole (i.e., for μ_2=0) are shown in Fig. 5.

The stress intensity factors calculated at the crack tips t_1 and t_2 are shown in Figures 6-13. The results shown in the figures are normalized with respect to $\sigma_o\sqrt{a}$ where σ_o is the tensile stress acting on the plane away from and perpendicular to the crack and a is the half crack length. Thus, the normalized stress intensity factors k_{ij} shown in the

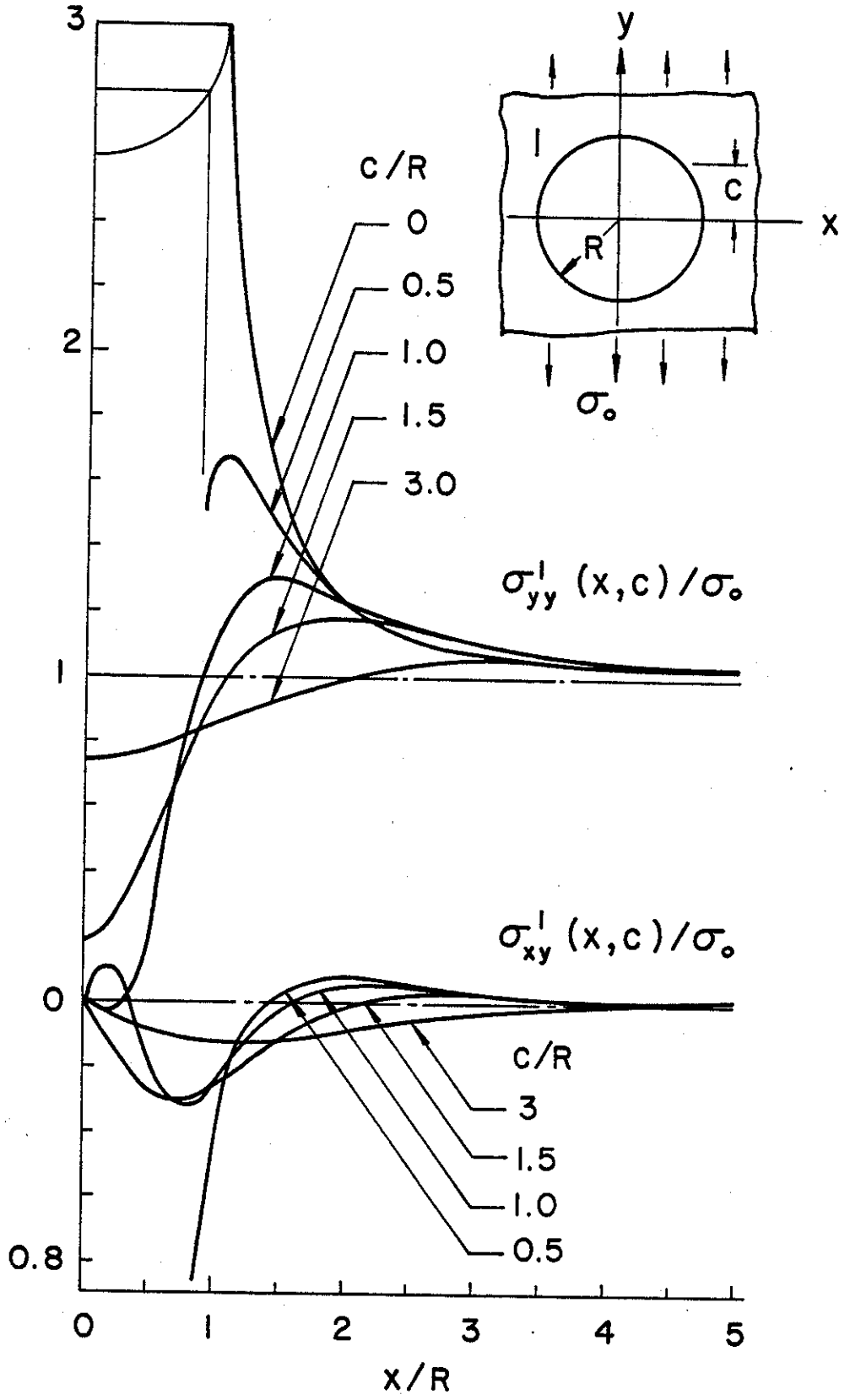

Figure 5. The stress distribution in a plate with a circular hole.

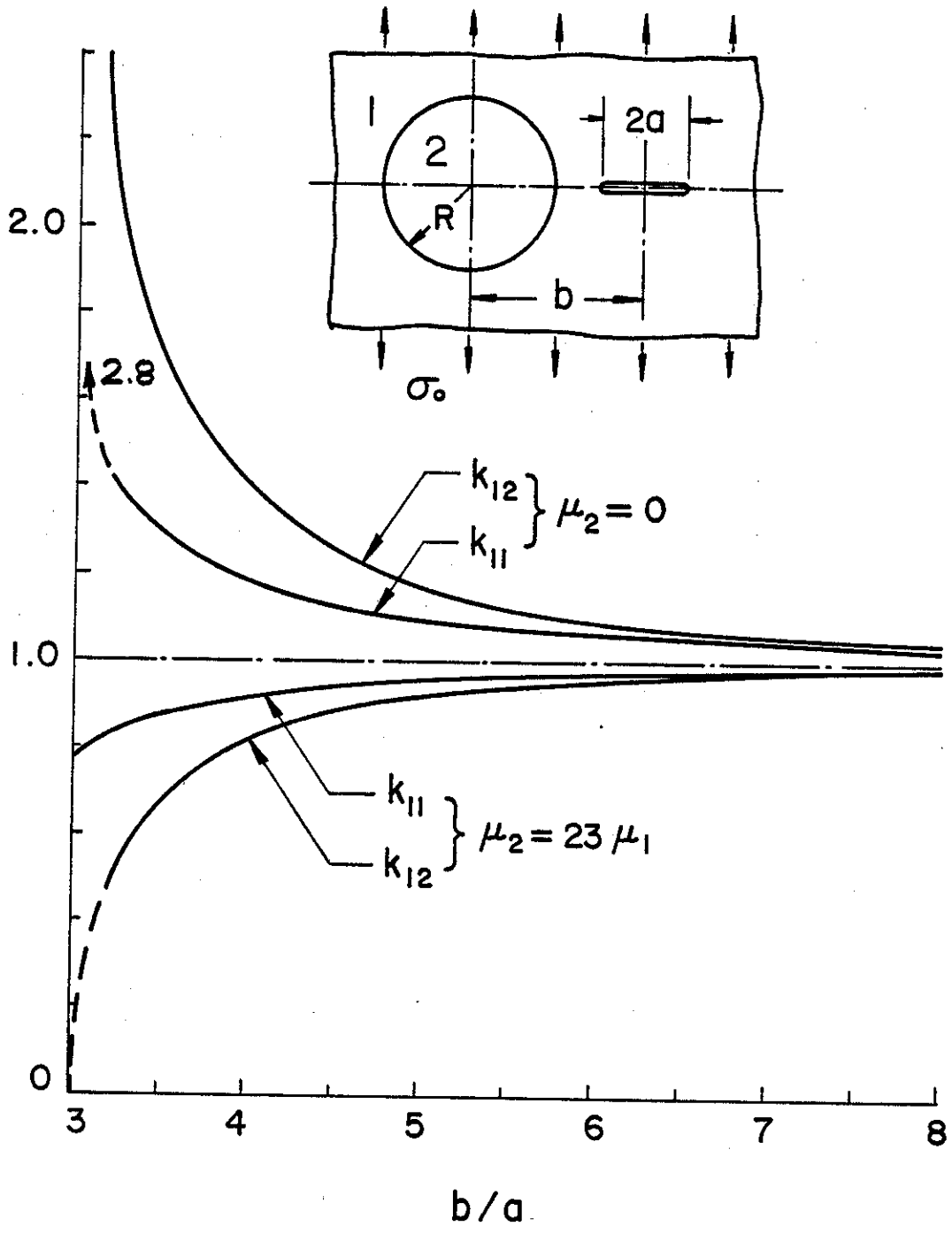

Figure 6. The stress intensity factors for a symmetrically located radial crack (R/a = 2, c = 0).

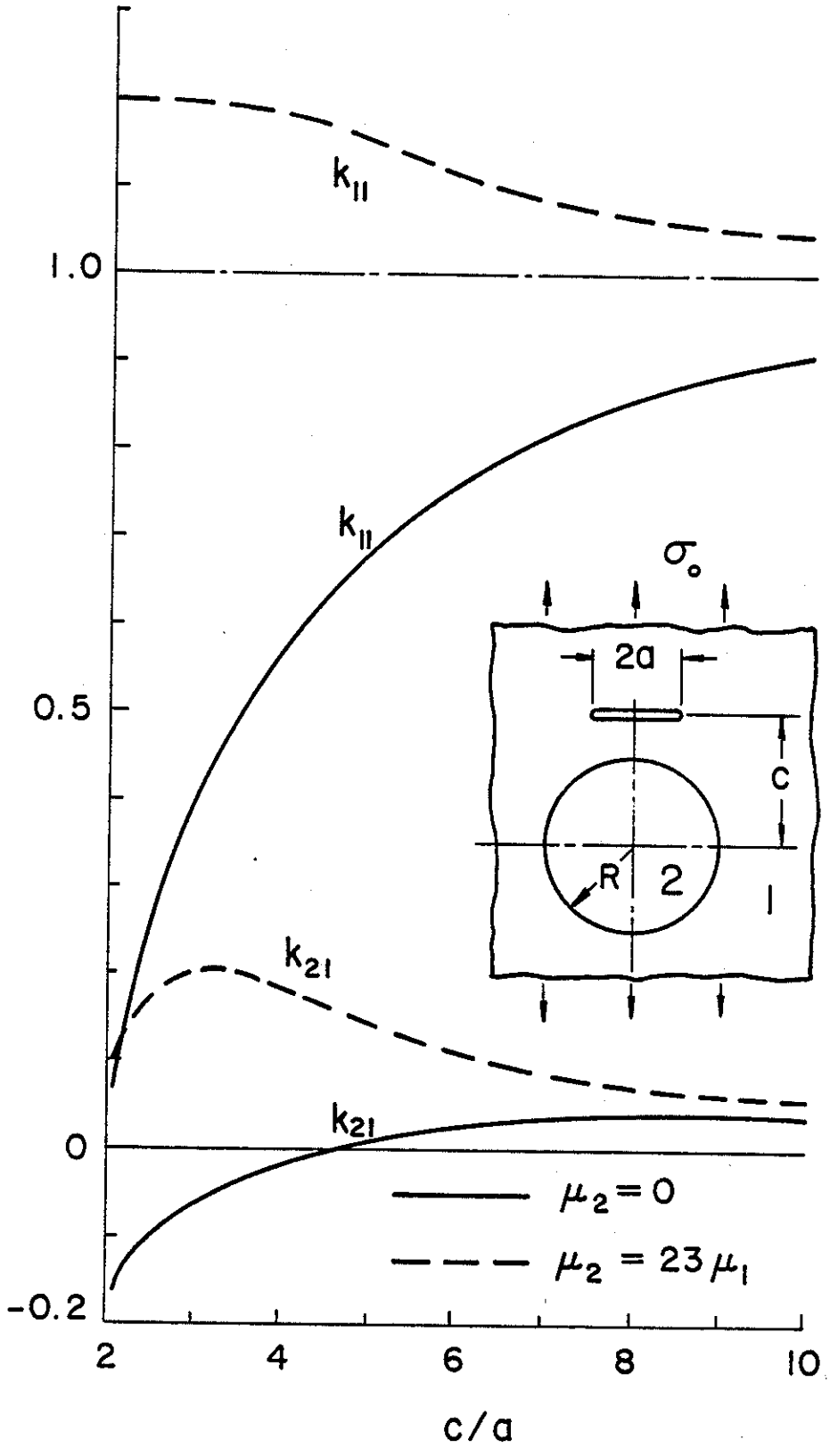

Figure 7. The stress intensity factors for a symmetrically located "tangential crack" perpendicular to the load (b = 0, R = 2a).

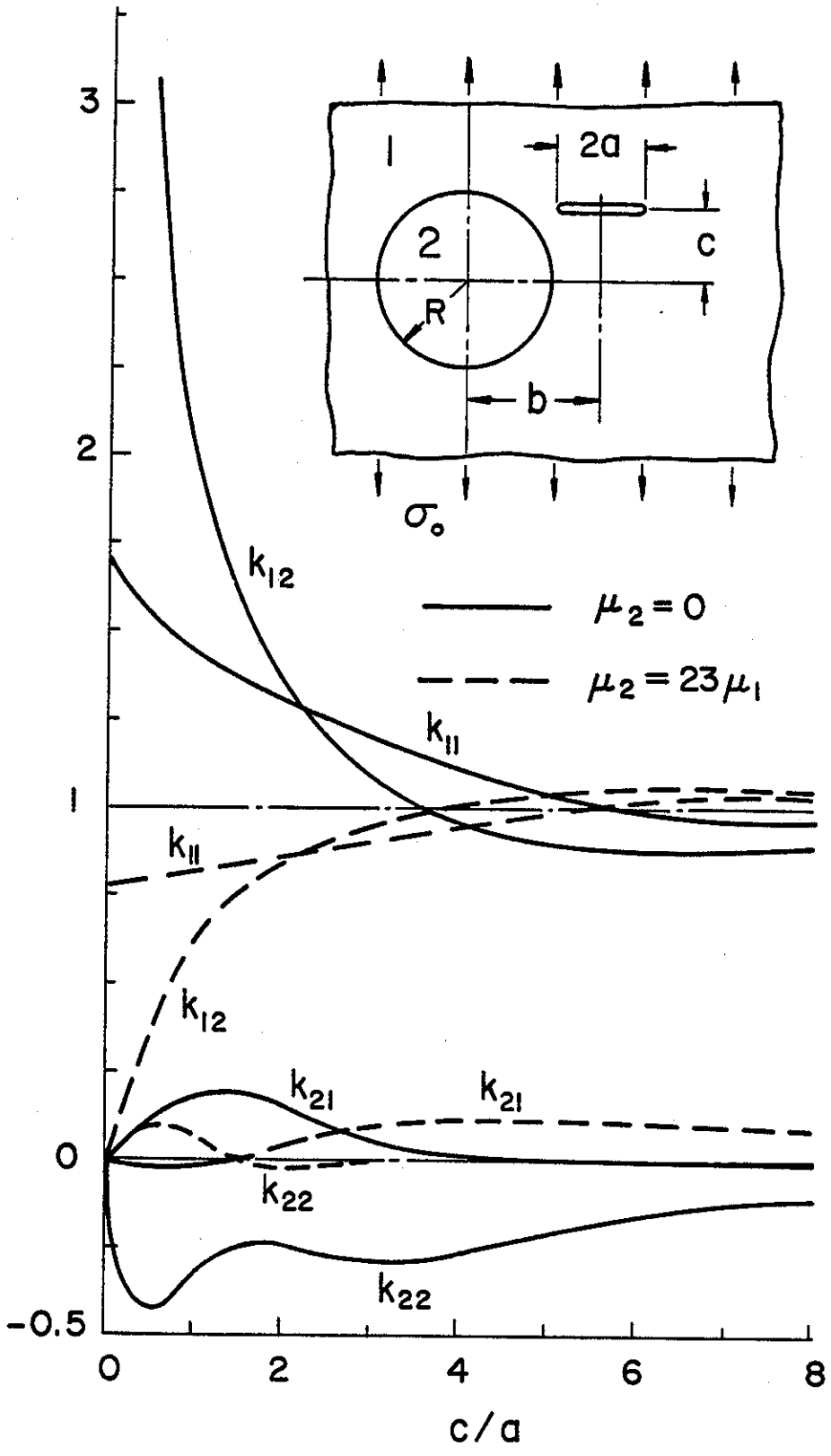

Figure 8. Stress intensity factors for a crack perpendicular to the external load (R = 2a, b = 3a).

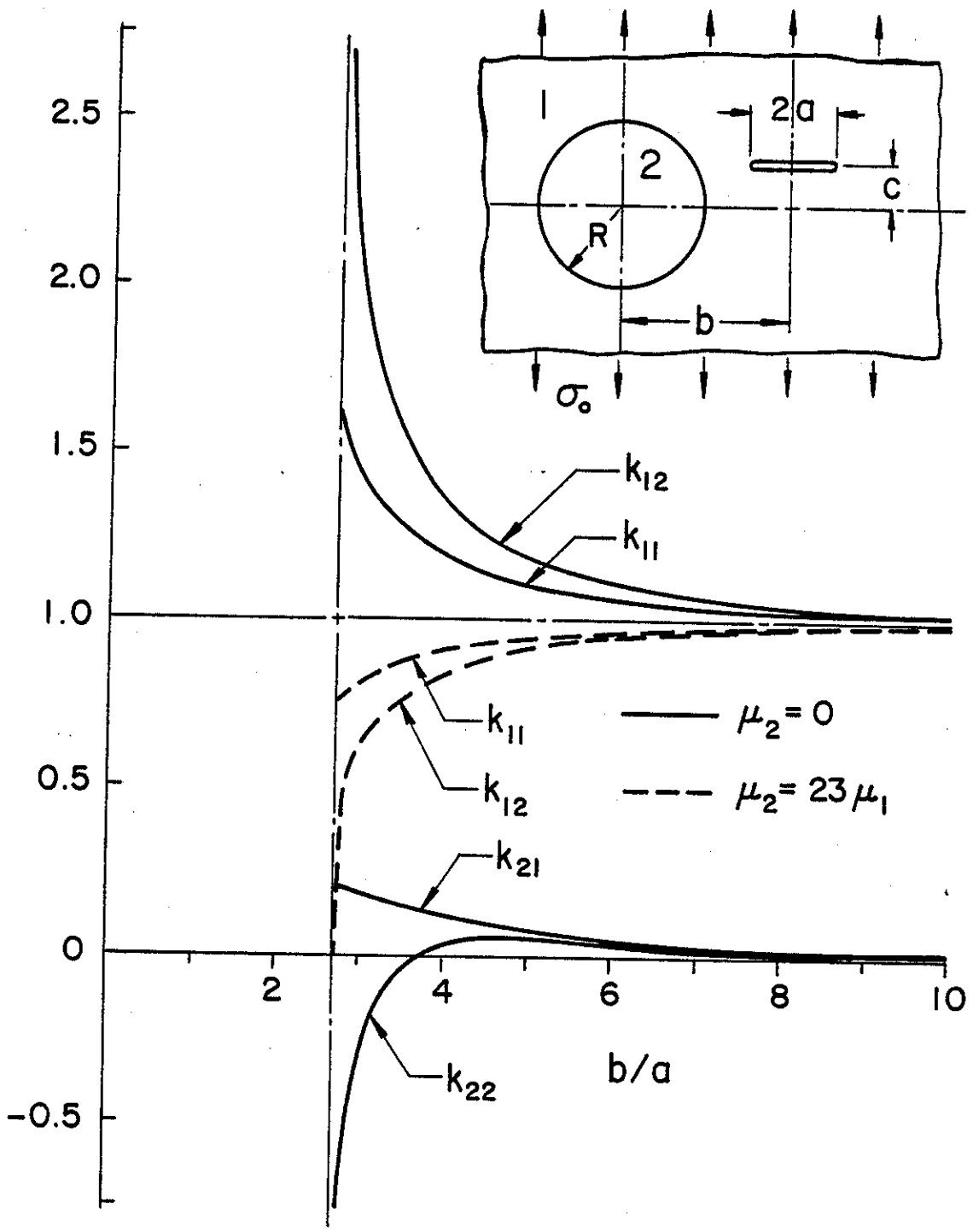

Figure 9. Stress intensity factors for a crack perpendicular to the external load (R = 2a, c = a).

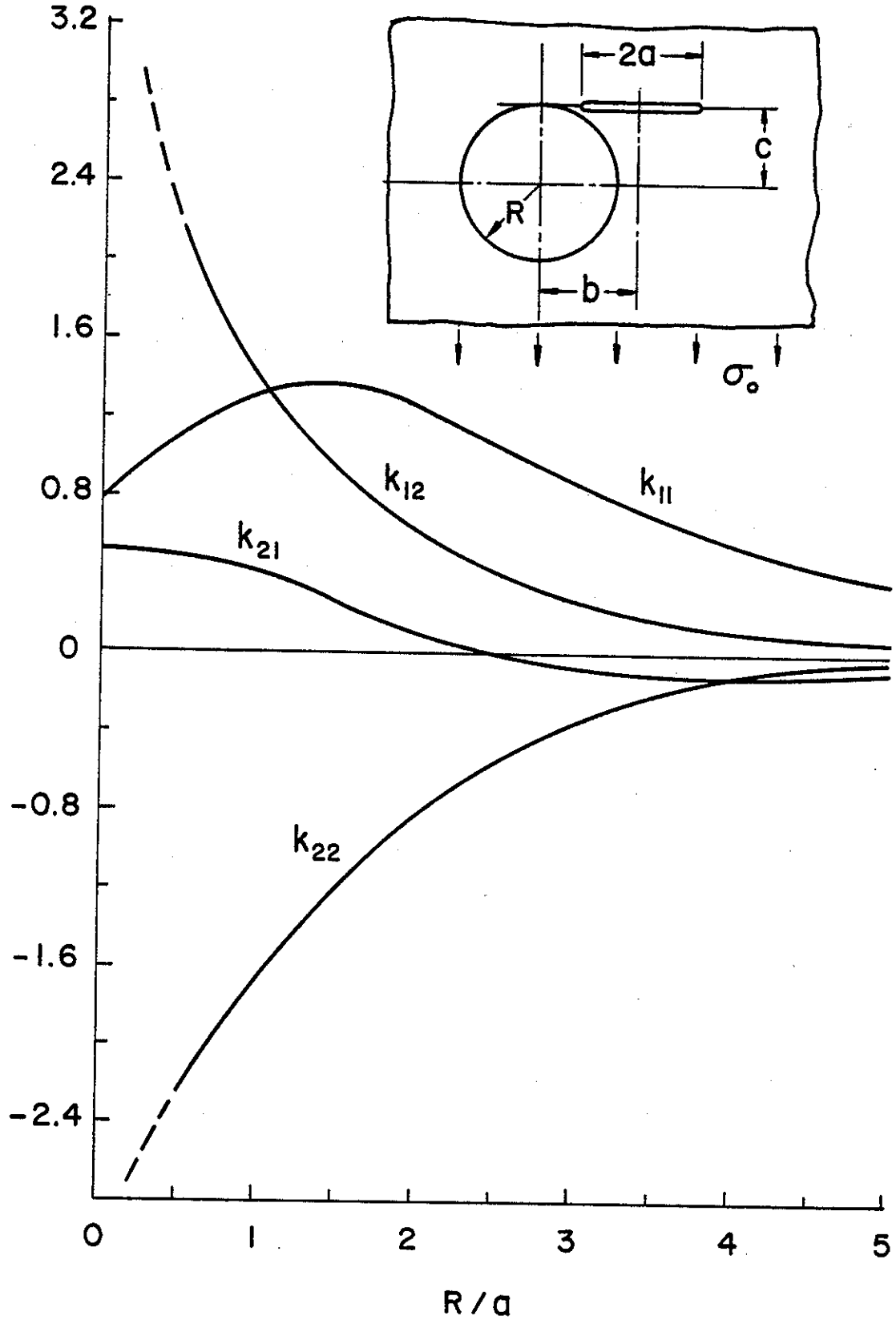

Figure 10. Stress intensity factors for a crack in the matrix containing a circular hole ($\mu_2 = 0$, $c = R$, $b-a = 0.2R$, a = constant).

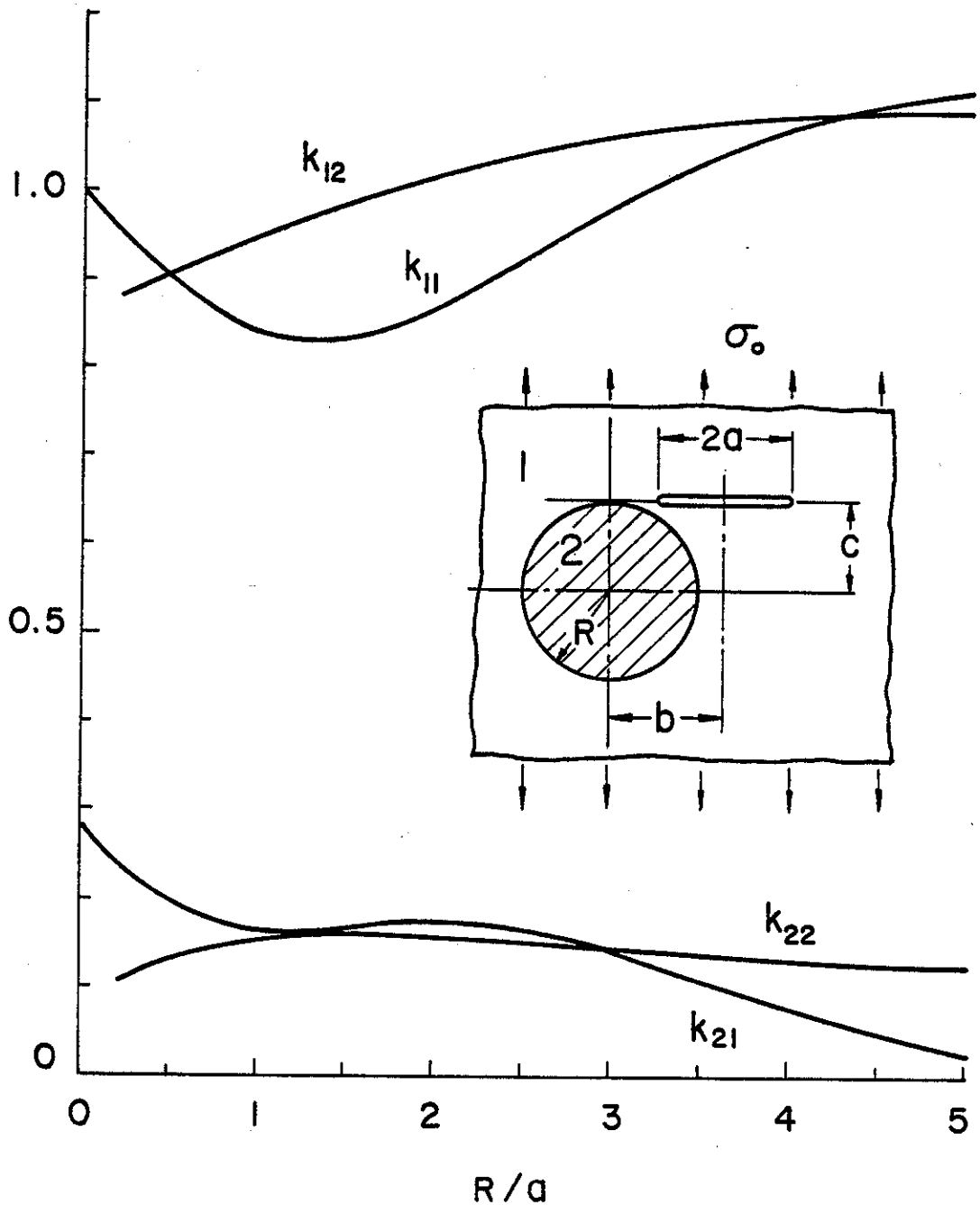

Figure 11. Stress intensity factors for a crack in the matrix containing an elastic inclusion ($\mu_2 = 23\mu_1$, c = R, b-a = 0.2R, a = constant).

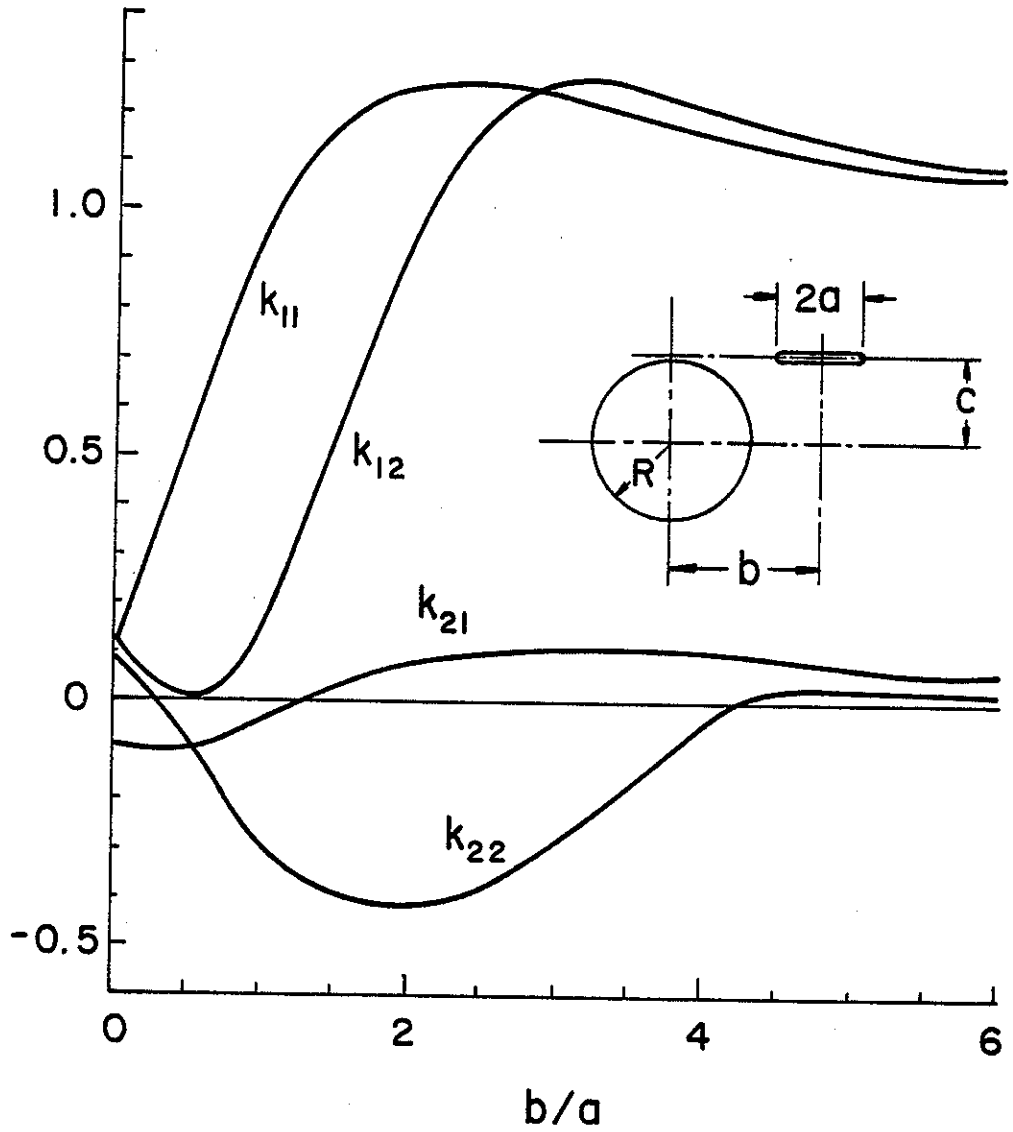

Figure 12. Stress intensity factors for a crack in the matrix containing a circular hole ($\mu_2 = 0$, $c = 2.2a$, $R = 2a$).

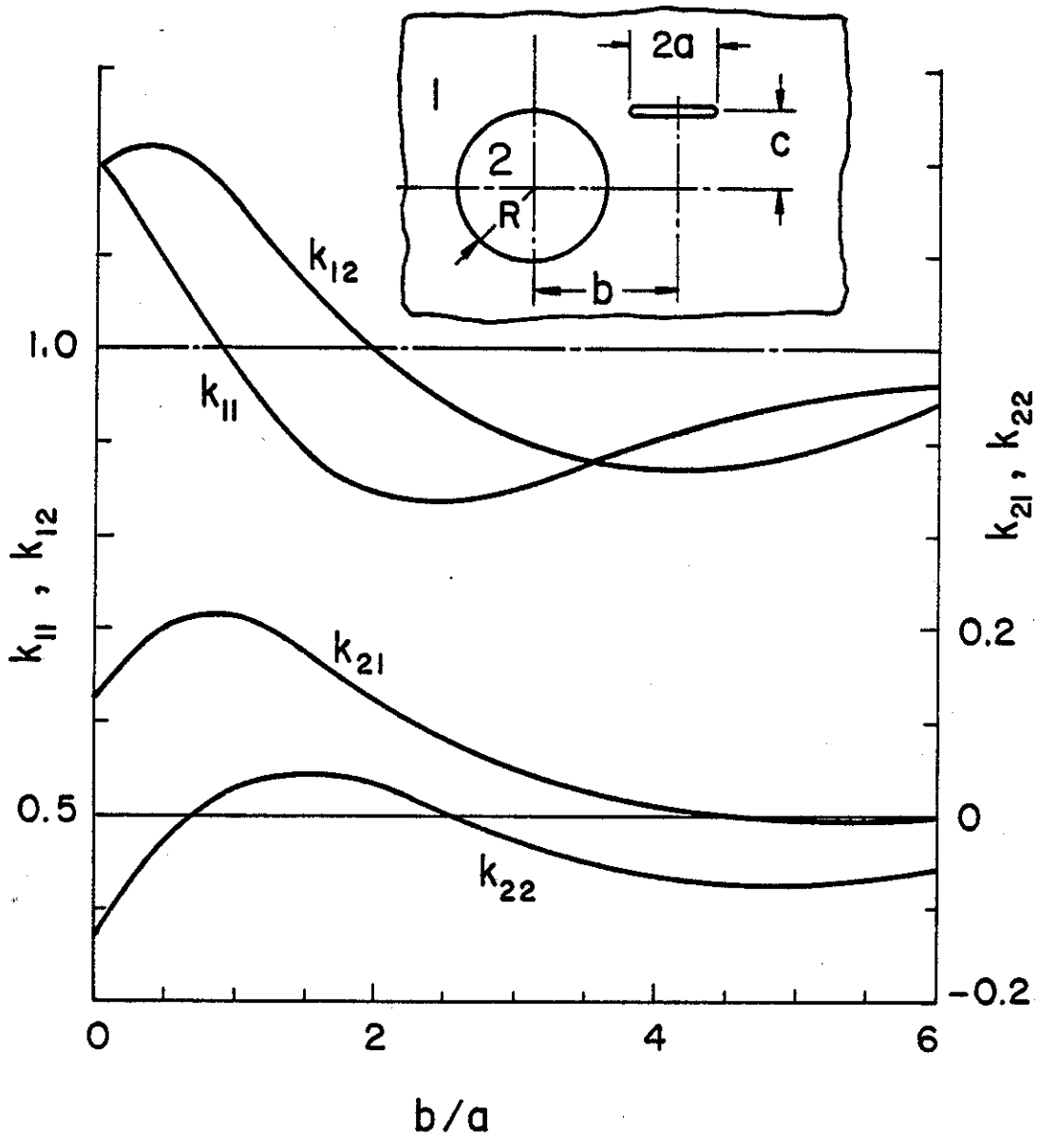

Figure 13. Stress intensity factors for a crack in the matrix containing an elastic inclusion ($\mu_2 = 23\mu_1$, $c = 2.2a$, $R = 2a$).

figures are defined by

$$k_{ij} = \frac{k_i(t_j)}{\sigma_o\sqrt{a}} \quad , \quad (i,j = 1,2) \tag{9}$$

where $k_i(t_j)$ are given in (8). Figures show the results for only two cases, namely a circular hole (i.e., $\mu_2=0$) and a stiffer elastic inclusion with elastic constants

$$(\mu_2/\mu_1) = 23 \quad , \quad \kappa_1 = 1.6 \ , \ \kappa_2 = 1.8 \quad . \tag{10}$$

Fig. 6 shows the results for a symmetrically located radial crack. Note that as the (inner) crack tip t_2 approaches the boundary (i.e., for $b \to R+a$) the stress intensity factor $k_1(t_2)$ tends to infinity for the case of hole and to zero for the case of inclusion. Qualitatively the results given in this figure are very general, that is if the perturbed stress fields of a crack and a hole (or a pore) interact, then the stress intensity factors at the crack tips would be greater than those which would be obtained for the cracked medium without the hole. For example, note that in Fig. 6 the stress intensity factors for $\mu_2=0$ are greater than $\sigma_o\sqrt{a}$, the value for the cracked plane without a hole, and approach this value as the crack moves away from the hole (i.e., as $b \to \infty$). Similar trend would be observed for an inclusion the stiffness of which is less than that of the cracked medium (i.e., for $\mu_2 < \mu_1$). On the other hand, if the plane contains a stiffer inclusion (i.e., for $\mu_2 > \mu_1$), then the stress intensity factors are smaller than $\sigma_o\sqrt{a}$.

The results shown in Figures 7-13 are self-explanatory. Depending on the location of the crack, one may observe some trends in these results which are opposite to that observed for the symmetric radial crack shown in Fig. 6. These trends, however, may easily be explained by examining the stress fields perturbed by an inclusion or a hole which are shown in figures 2 and 5. By examining the signs of the Modes I and II stress intensity factors, from the results given in these figures one may easily conclude that generally for the crack tip near the matrix-inclusion boundary the crack would propagate towards the boundary if

$\mu_2=0$ or $\mu_2<\mu_1$, and away from the boundary if $\mu_2>\mu_1$. This conclusion is based on the analysis giving the plane of the maximum cleavage stress at the crack tip. The details of the analysis and its experimental verification may be found in [12].

In another class of crack-inclusion interaction problems both the inclusion and the matrix material may contain a crack. For symmetrically located radial cracks the general problem is described by Fig. 14. The details of the analysis of this problem may be found in [11]. Figures 15-21 show some calculated results. In this problem the formulation given in [11] and Fig. 14 allow the consideration of the special cases of a crack terminating at the interface (i.e., $b=R+a$, $\mu_2\neq 0$ in Fig. 6 or $a_2=b_2$, $a_1=a$ in Fig. 14), and the crack going through the interface (i.e., $b_2=a=a_1$ in Fig. 14). In these special cases it is shown that [11] the point ($x=a$, $y=0$) (Fig. 14) is a point of stress singularity and the stress state in a close neighborhood of it has the following form:

$$\sigma_{ij}(r,\theta) = \frac{k}{r^{\beta}} g_{ij}(\theta) \quad , \quad (i,j=x,y) \ , \ (0<\beta<1) \tag{11}$$

where r and θ are the polar coordinates centered at the singular point, g_{ij} is a bounded function and the stress intensity factor k is a constant. The stress intensity factors $k = k(a)$ given in this section are defined in terms of the related cleavage stresses as follows (Fig. 14):

(i) crack in the matrix ($-a<a_2<b_2<a = a_1<b_1$):

$$k(a) = \lim_{x\to a} \sqrt{2}\,(a-x)^{\beta}\sigma_{2yy}(x,0) \ , \tag{12}$$

(ii) crack in the inclusion ($-a<a_2<b_2 = a<a_1<b_1$):

$$k(a) = \lim_{x\to a} \sqrt{2}\,(x-a)^{\alpha}\sigma_{1yy}(x,0) \tag{13}$$

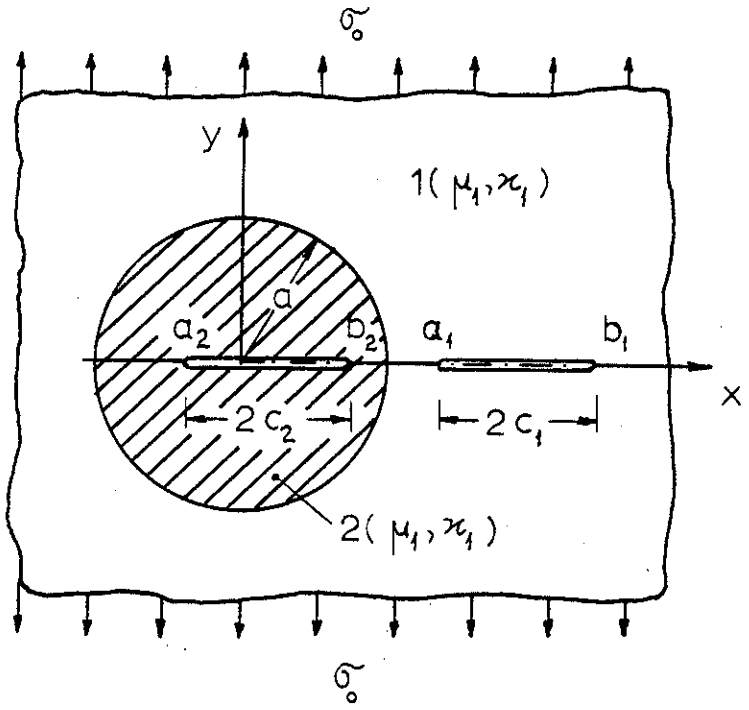

Figure 14. Inclusion-crack geometry.

(iii) crack crossing the boundary ($-a<a_2<b_2 = a = a_1<b_1$):

In this case for simplicity we define the following normal and shear cleavage stress intensity factors

$$k_{xx}(a) = \lim_{y\to 0} y^{\gamma}\, \sigma_{1xx}(a,y) \ , \text{(normal cleavage)} \ , \tag{14}$$

$$k_{xy}(a) = \lim_{y\to 0} y^{\gamma}\, \sigma_{1xy}(a,y) \ , \text{(shear cleavage)} \ . \tag{15}$$

The first special problem (i) with $a_2=b_2$ corresponds to the limiting case of the problem considered in Fig. 6. In the problem of a crack terminating at the bimaterial interface such as the cases (i) and (ii) mentioned above, the power of the stress singularity (α or β) is highly dependent on the stiffness ratio μ_2/μ_1 and is relatively insensitive to the Poisson's ratios (or κ_1 and κ_2). For the crack geometry $a_2=b_2$, $a_1=a$, $b_1>a$, Fig. 14, Table 1 shows the effect of μ_2/μ_1 on β. It may be seen that for $(\mu_2/\mu_1)<1$ the power β is greater than 0.5, meaning that if the stiffness of the inclusion is less than that of the matrix, then the stress singularity is stronger than the corresponding homogeneous case. Similarly, if $\mu_2>\mu_1$ then $\beta<0.5$. This is the reason for the asymptotic trends observed in Fig. 6 for the stress intensity factor k(a) as $b\to R+a$. Table 1 also gives the corresponding stress intensity factors calculated from (12).

For this problem, to give some idea about the nature and the relative magnitude of the crack surface displacement, Fig. 15 shows some calculated results. Here v(x,0) is the crack surface displacement in y direction.

Figures 16 and 17 show the stress intensity factors for a crack located in the inclusion. The limiting values of the stress intensity factors shown in these figures for the crack length $2c_2$ approaching zero are obtained from uniformly loaded "infinite" plane solution with the applied stress state away from the crack region given by the uncracked

Table 1. The effect of modulus ratio on the stress intensity factors for a crack terminating at the interface ($a_1 = a$, $b_1/a = 2$, $\kappa_1 = \kappa_2 = 1.8$, $c_1 = (b_1-a)/2$).

$m = \frac{\mu_2}{\mu_1}$	β	$\frac{k(b_1)}{\sigma_0\sqrt{c_1}}$	$\frac{k(a)}{\sigma_0 c_1^{\beta}}$
0		2.808	
0.05	0.81730	1.615	1.053
1/3	0.62049	1.229	0.5836
1.0	0.5	1.000	1.000
3.0	0.40074	0.8610	1.299
10.0	0.33277	0.7969	1.389
23.0	0.30959	0.7796	1.375
100	0.29387	0.7691	1.345
300	0.28883	0.7667	1.348

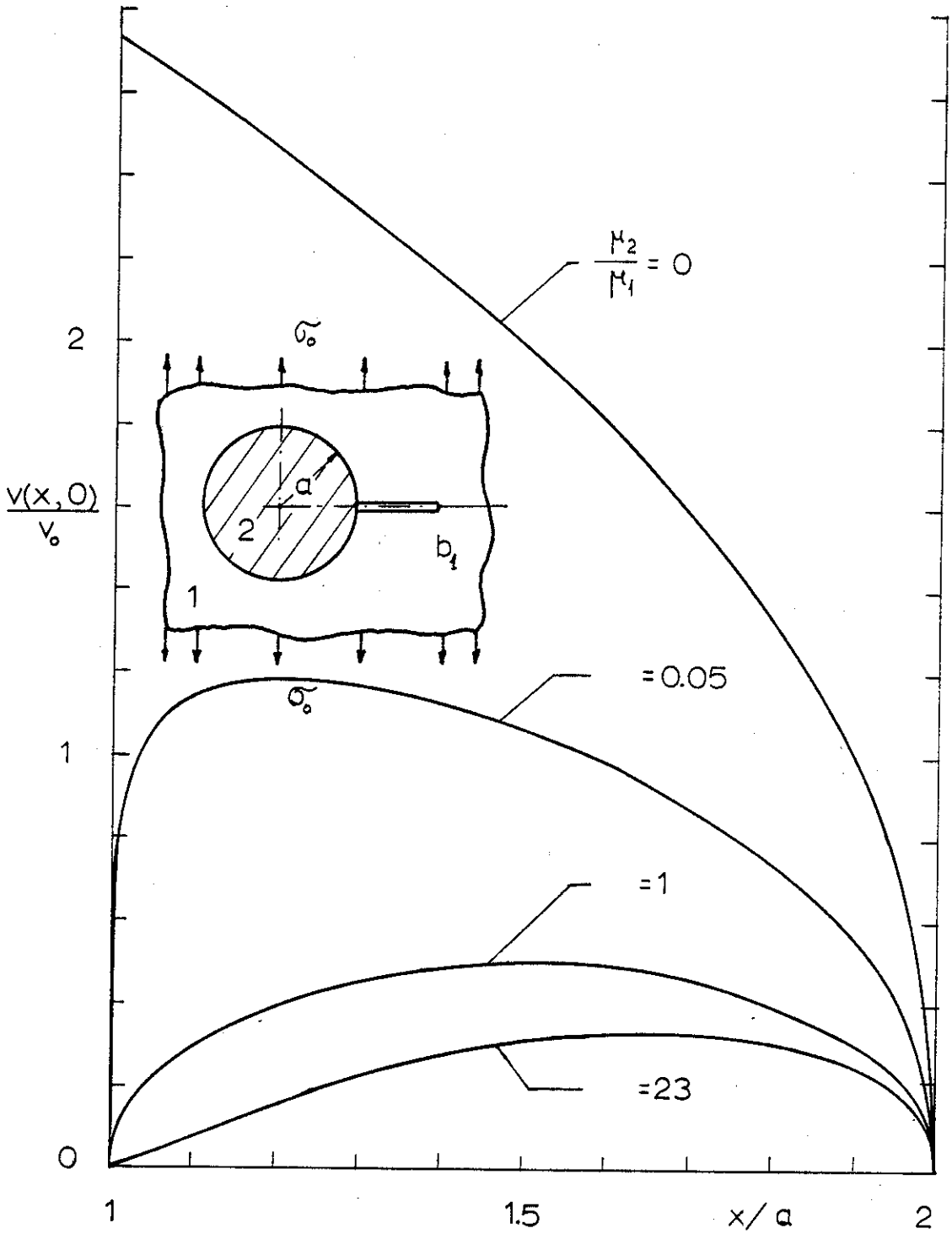

Figure 15. Crack surface displacement for a crack in the matrix with one tip on the interface ($\kappa_1 = \kappa_2 = 1.8$, $b_1/a = 2$, $v_o = (1+\kappa_1)a\sigma_o/\mu_1$).

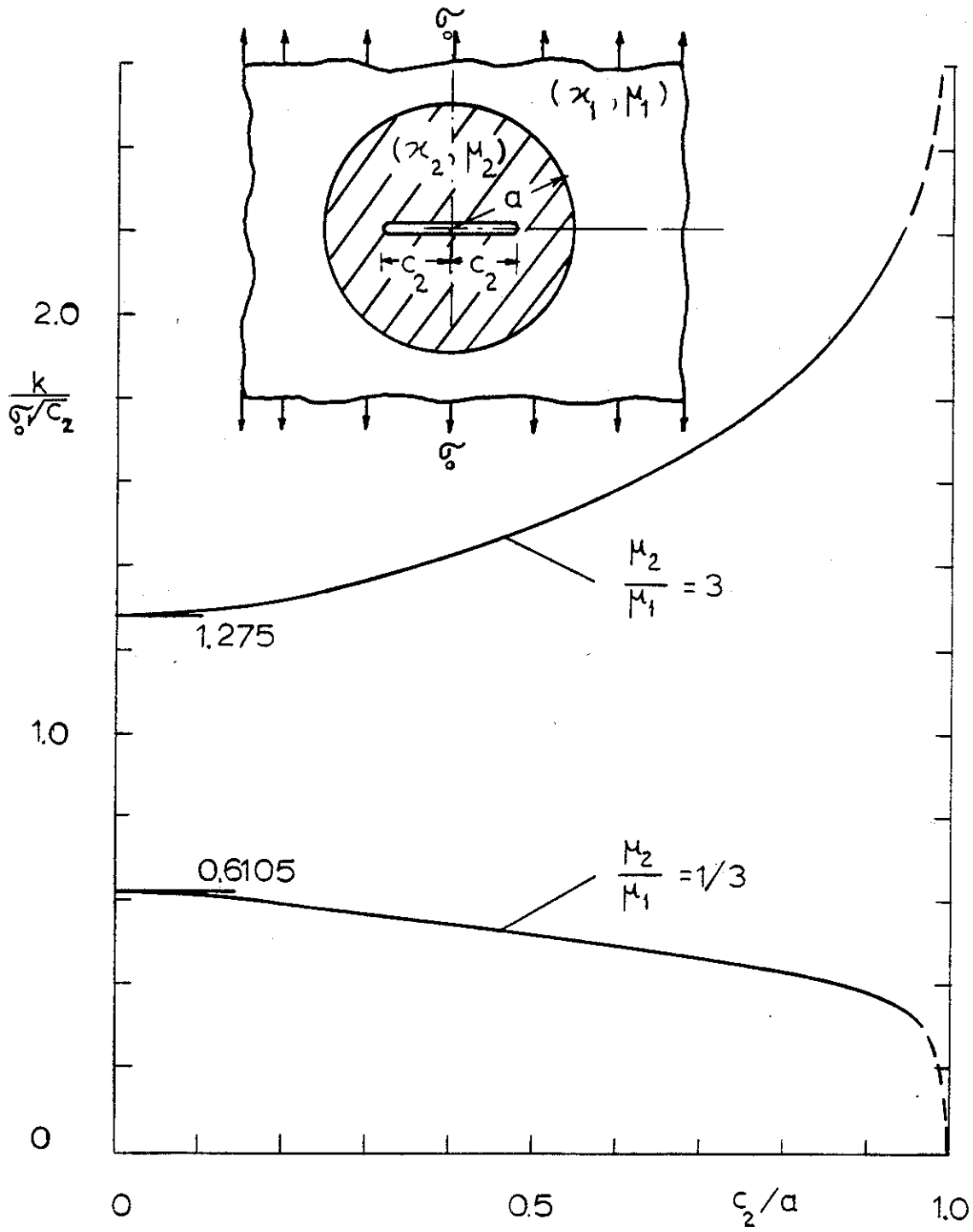

Figure16. Stress intensity factor for a symmetrically located crack in the inclusion ($\kappa_1 = \kappa_2 = 1.8$).

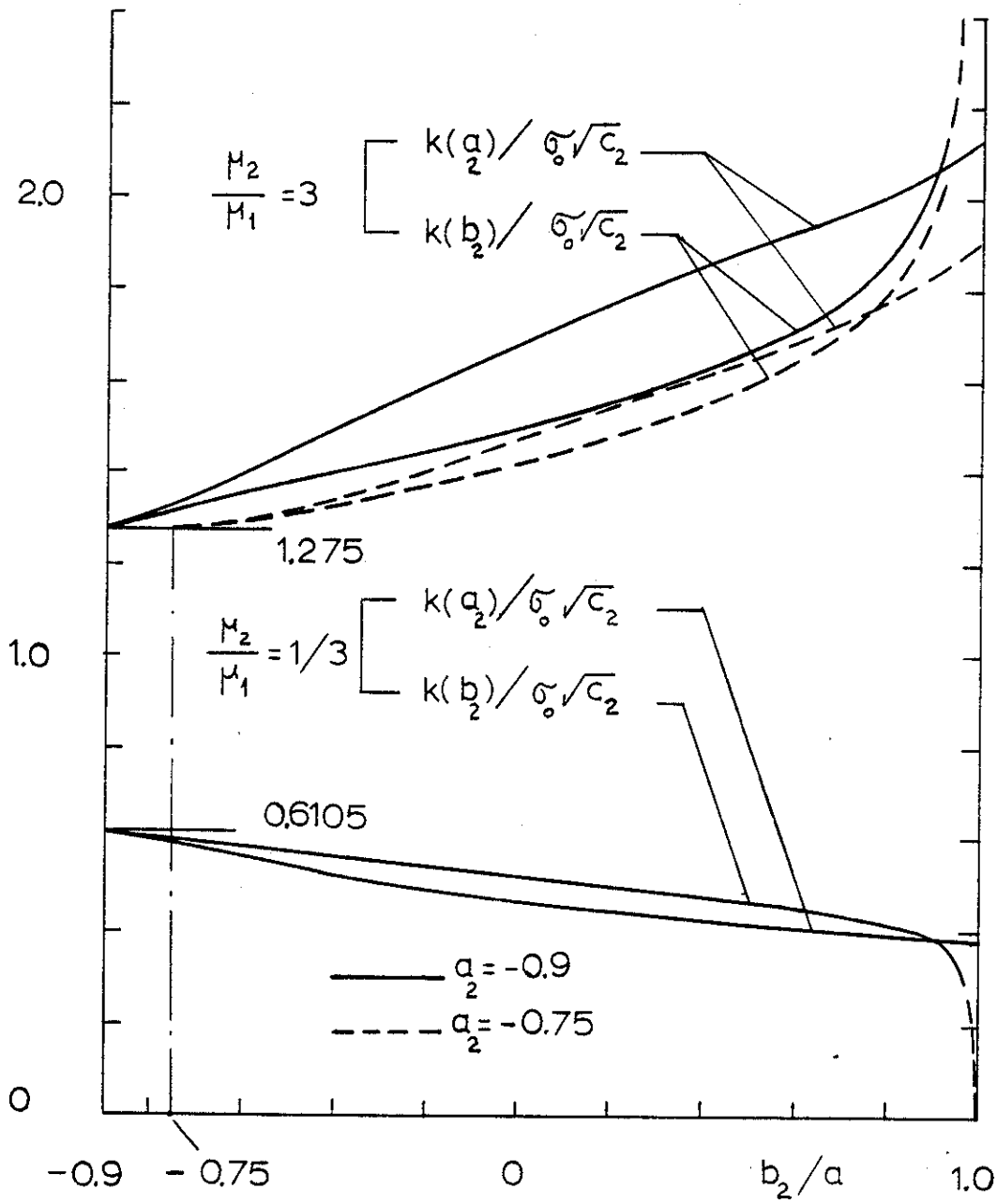

Figure 17. Stress intensity factors for a crack located in the inclusion ($\kappa_1 = \kappa_2 = 1.8$, one tip fixed at $a_2 = -0.9a$ or $a_2 = -0.75a$, b_2 variable, $c_2 = (b_2 - a_2)/2$).

inclusion solution [13], namely

$$\sigma^a_{2yy}(x,0) = \sigma_o \frac{(1+\kappa_1)\mu_2}{2\mu_1}\left(\frac{1}{\kappa_2-1+2\mu_2/\mu_1} + \frac{1}{1+\kappa_1\mu_2/\mu_1}\right) , \quad |x|<a , \tag{16}$$

$$\sigma^a_{1yy}(x,0) = \sigma_o\left[1 - \frac{a^2}{2x^2}\frac{\mu_2(\kappa_1-1)-\mu_1(\kappa_2-1)}{2\mu_2 + \mu_1(\kappa_2-1)} - \frac{a^4}{x^4}\frac{3(\mu_2-\mu_1)}{2(\mu_1+\kappa_1\mu_2)}\right], \quad |x|>a , \tag{17}$$

$$\sigma^a_{1xy}(x,0) = 0 \quad , \quad \sigma^a_{2xy}(x,0) = 0 \quad . \tag{18}$$

By using (16) it may be shown that for the crack in the inclusion the stress intensity factor has the following limit:

$$\lim_{c_2\to 0} \frac{k}{\sigma_o\sqrt{c_2}} = \frac{\mu_2(\kappa_1+1)}{2\mu_1}\left(\frac{\mu_1}{2\mu_2+\mu_1(\kappa_2-1)} + \frac{\mu_1}{\mu_1+\kappa_1\mu_2}\right) \quad . \tag{19}$$

Fig. 16 shows the results for a symmetrically located crack. The results for an eccentric crack are shown in Fig. 17 (see Fig. 14 for notation).

Some typical results for the case in which both the inclusion and the matrix or base material contain a crack are shown in Fig. 18.

The stress intensity factor for a completely cracked inclusion (i.e., for $a_2=-a$, $b_2=a$, $a_1=b_1$) is given in Table 2. The stress intensity factor k(a) given in this table is defined by (13) where α is the power of stress singularity.

The stress intensity factors for a crack crossing the interface are given by figures 19 and 20. In these figures $x=a_2$ and $x=b_1$ are conventional crack tips for which the stress state has square-root singularity (i.e., $\alpha'=\beta'=0.5$). For the point of the intersection of the crack with the boundary (x=a) the normal and shear cleavage components of the stress intensity factor k_{xx} and k_{xy} are defined by (14) and (15). The asymptotic trends of the stress intensity factors observed in these figures as a crack tip approaches the boundary x=a are again due to the change in the

Table 2. Stress intensity factor for a completely cracked inclusion.

$\frac{\mu_2}{\mu_1}$	$\kappa_1 = \kappa_2 = 1.8$		$\kappa_1 = 2.2$, $\kappa_2 = 1.8$		$\kappa_1 = 1.8$, $\kappa_2 = 2.2$		$\kappa_1 = \kappa_2 = 2.2$	
	α	$\frac{k(a)}{\sigma_0 a^{\alpha}}$	α	$\frac{k(a)}{\sigma_0 a^{\alpha}}$	α	$\frac{k(a)}{\sigma_0 a^{\alpha}}$	α	$\frac{k(a)}{\sigma_0 a^{\alpha}}$
0.2	0.36621	0.7890	0.38087	0.7848	0.32027	1.046	0.33845	1.010
0.6	0.45025	1.014	0.47028	0.9456	0.42123	1.174	0.44466	1.068
1.0	0.5	1.0	0.51991	0.9209	0.47724	1.107	0.5	1.0
2.0	0.57451	0.8843	0.59188	0.8165	0.55687	0.9465	0.57624	0.8613
5.0	0.67885	0.6555	0.69124	0.6194	0.66380	0.6940	0.67733	0.6500

power of stress singularity. For example, in Fig. 19 for $b_1 > a$ the stress components around the singular point (x=a, y=0) are (see (14) and (15))

$$\sigma_{xx}(a,y) \cong \frac{k_{xx}(a)}{y^{\gamma}} \quad , \quad \sigma_{xy}(a,y) \cong \frac{k_{xy}(a)}{y^{\gamma}} \quad , \quad \gamma = 0.27326. \tag{20}$$

On the other hand, for $b_1 = a$ (i.e., the case of a crack in the inclusion terminating at the boundary) the stress state around (x=a, y=0) is given by (see eq. (13))

$$\sigma_{ij} = \frac{k(a)}{\sqrt{2}\, r^{\alpha}} f_{ij}(\theta) \quad , \quad \alpha = 0.82580 \ , \tag{21}$$

where r and θ are the polar coordinates centered at the point (x=a, y=0) (i.e., $r=y$ for $\theta = \pi/2$). Thus, as $b_1 \to a$ from (20) and (21) it follows that

$$\sigma_{xx}(a,y) \cong \frac{k_{xx}(a)}{y^{\gamma}} \to \frac{k(a)}{\sqrt{2}\, y^{\alpha}} f_{xx}(\tfrac{\pi}{2}) \tag{22}$$

or

$$\sigma_{xx}(a,y) \to \frac{1}{y^{\gamma}} \left[\frac{k(a)}{\sqrt{2}\, y^{\alpha-\gamma}} f_{xx}(\pi/2) \right] , \tag{23}$$

and

$$k_{xx}(a) \to \frac{k(a)}{\sqrt{2}\, y^{\alpha-\gamma}} f_{xx}(\pi/2) \quad . \tag{24}$$

Since k(a) and f_{xx} are bounded and $\alpha > \gamma$, for y=0 (at which, by (14), k_{xx} must be calculated) $k_{xx}(a)$ would become unbounded. Similarly, it is seen that for $b_1 \to a$, k_{xy} tends to (negative) infinity. Also, since α (for the terminating crack tip) is greater than 0.5 (at b_1 for the embedded crack tip), by following a similar argument it may be shown that as $b_1 \to a$, $k(b_1)$ becomes unbounded.

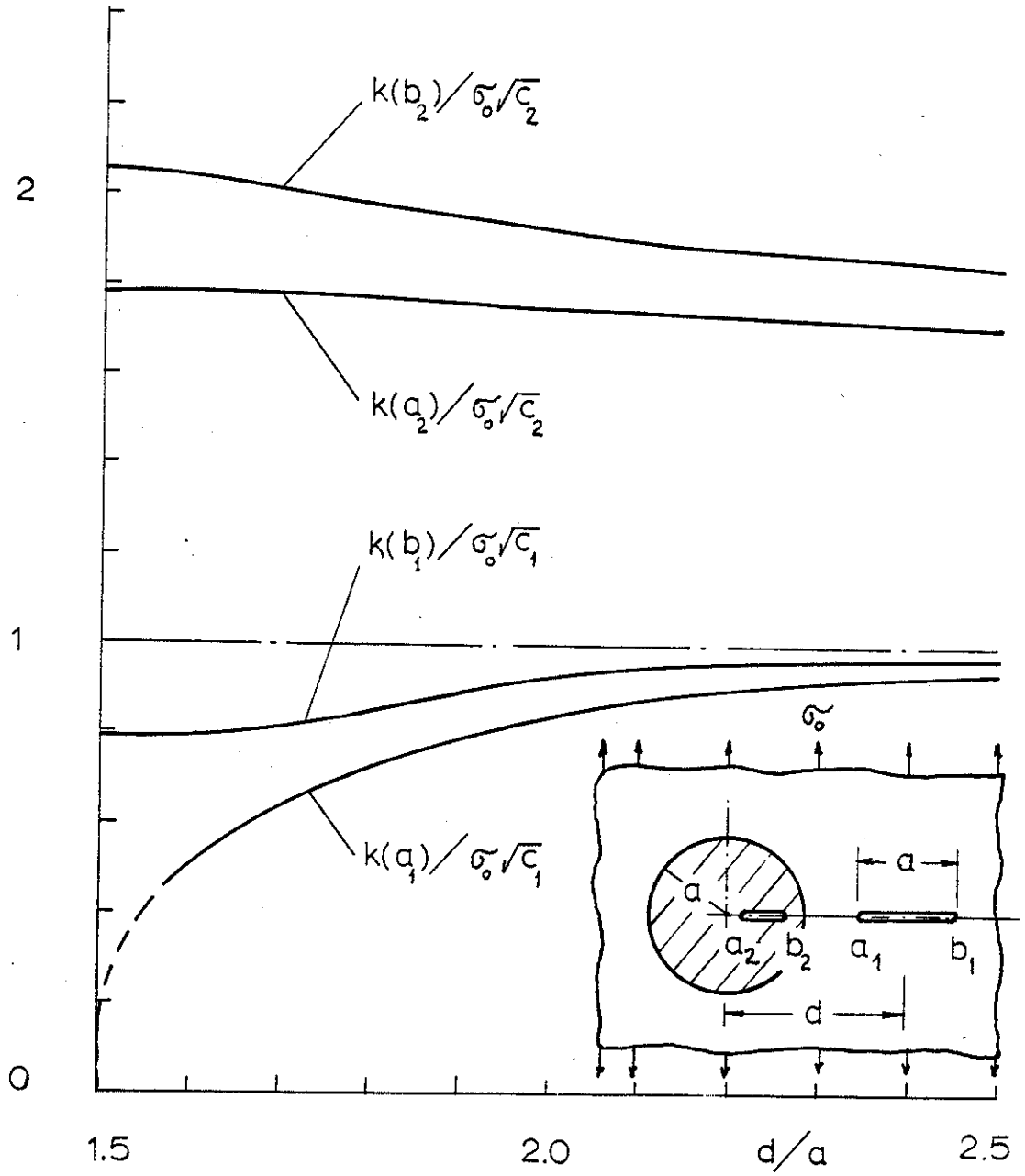

Figure 18. Stress intensity factors for a crack in the matrix (epoxy) and a crack in the inclusion (aluminum) ($\kappa_1 = 1.6$, $\kappa_2 = 1.8$, $\mu_2/\mu_1 = 23.077$; $a_2 = 0.3a$, $b_2 = 0.8a$, $2c_1 = (b_1 - a_1) = a$ fixed, $d = (b_1 + a_1)/2$ variable).

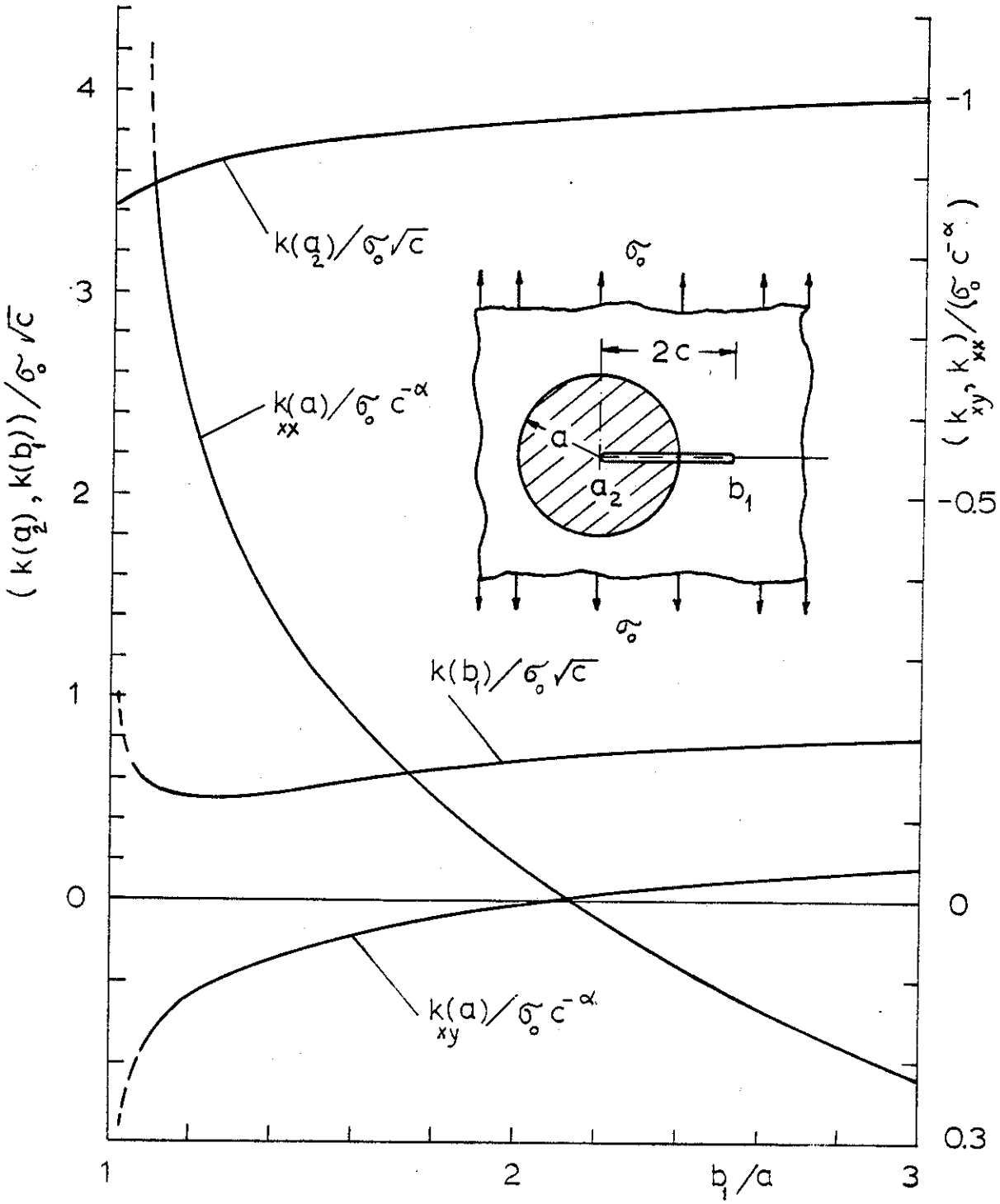

Figure 19. Stress intensity factors for a crack going through the matrix-inclusion interface ($\kappa_1 = 1.6$, $\kappa_2 = 1.8$, $\mu_2/\mu_1 = 23.077$, $\alpha' = \beta' = -0.5$, $\alpha = \beta = 0.27326$, $c = (b_1 - a_2)/2$, $a_2 = 0$ fixed, b_1 variable).

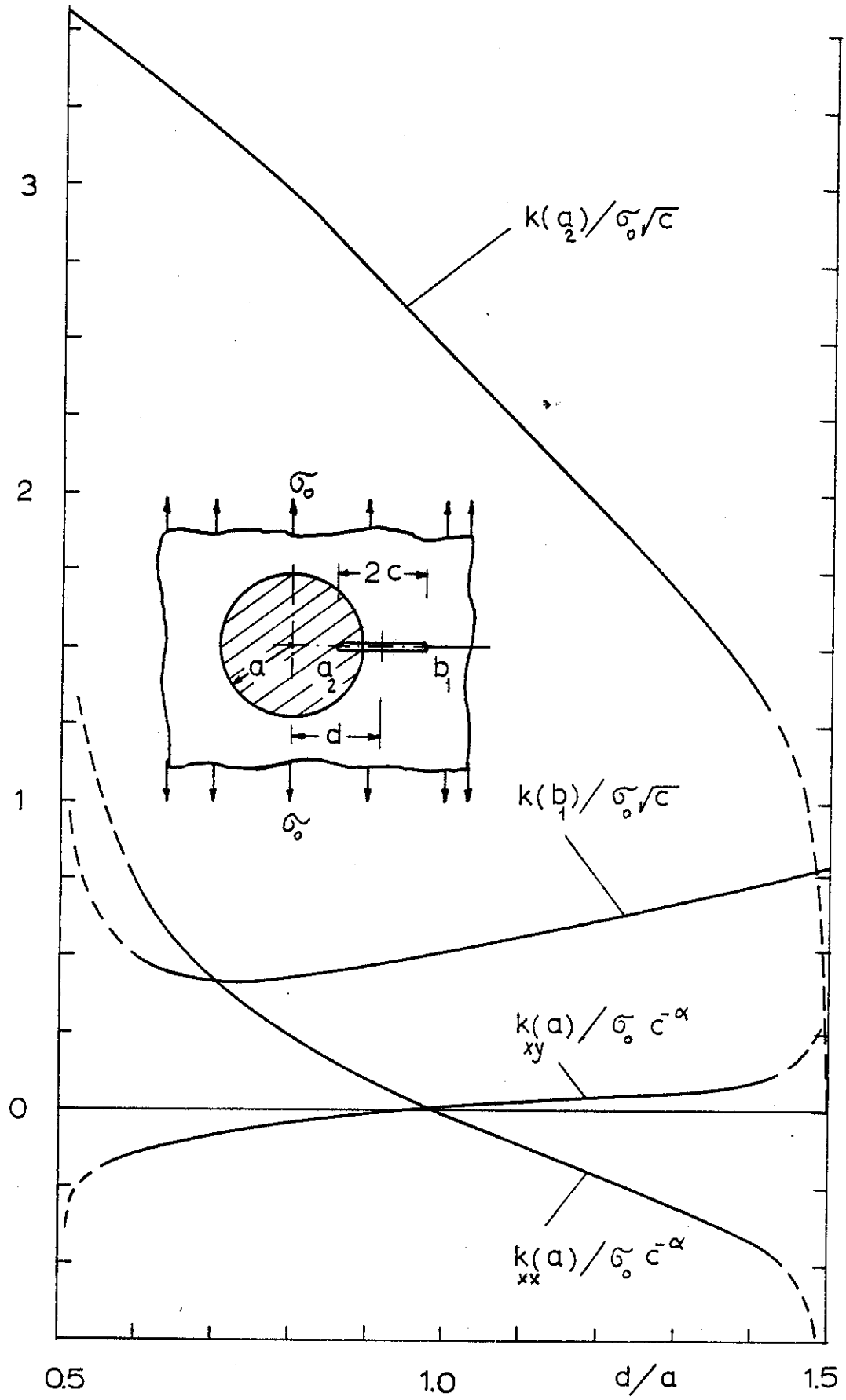

Figure 20. Stress intensity factors for a crack going through the interface ($\kappa_1 = 1.6$, $\kappa_2 = 1.8$, $\mu_2/\mu_1 = 23.077$, $\gamma = \alpha = \beta = 0.27326$, $2c = (b_1 - a_2) = a$ fixed, $d = (b_1 + a_2)/2$ variable).

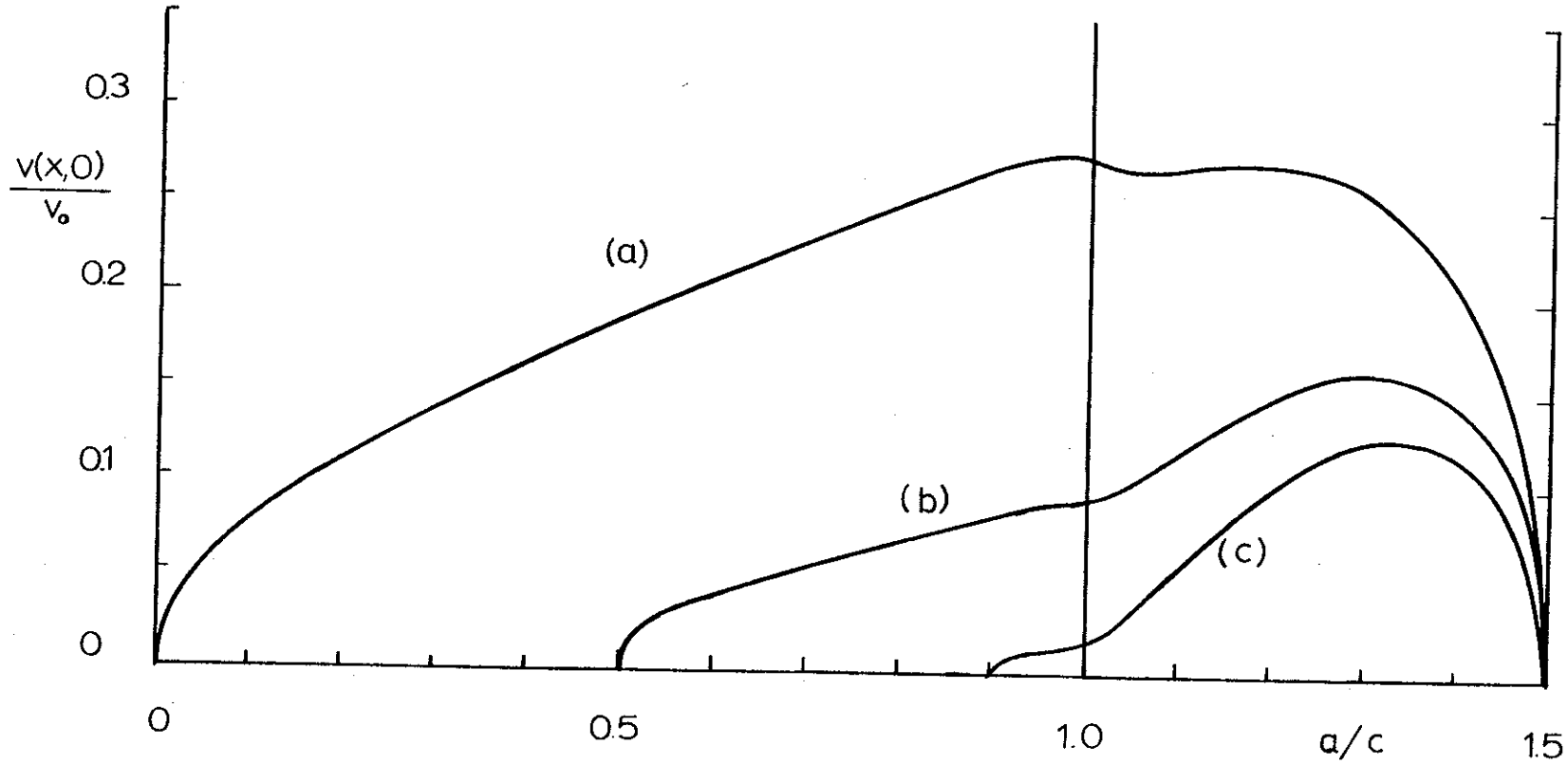

Figure 21. Crack surface displacement for cracks going through the interface ($\kappa_1 = 1.6$, $\kappa_2 = 1.8$, $\mu_2/\mu_1 = 23.077$, $v_0 = (1+\kappa_1)a\sigma_0/\mu_1$, $b_2 = a$ fixed, a_2 variable: (a) $a_2 = 0$, (b) $a_2 = a/2$, (c) $a_2 = 0.9a$).

The asymptotic trends in Fig. 20 can be explained by observing that $\gamma=\alpha=0.27326$ for the crack crossing the boundary ($a_2<b_2=a=a_1<b_1$), $\alpha=0.5$ for the crack tip embedded in the matrix, $\beta=0.33811$ for the crack in the matrix terminating at the boundary ($a_1=a$, $d/a=1.5$) and $\alpha=0.82580$ for the crack in the inclusion terminating at the boundary ($b_2=a$, $d/a = 0.5$).

Figure 21 shows some sample results for the crack surface displacements of a crack crossing the boundary.

For a crack terminating at the boundary to study the further crack propagation the details of the angular variation of the stresses, that is the functions $f_{ij}(\theta)$ in (21) may be needed. Sample results giving the distribution of these functions are shown in Figures 22-24. From the definitions (12), (13) and (21) we note that $f_{\theta\theta}(0) = 1$. The functions G_{ij} shown in Figures 22-24 are obtained from

$$\sigma_{ij}(r,\theta) \cong \frac{G_{ij}(\theta)}{\sqrt{2}\, r^{\alpha}} \quad , \quad (i,j=r,\theta),\ (-\pi<\theta<\pi). \tag{25}$$

Thus, $G_{\theta\theta}(0) = k(a)$ and $f_{ij}(\theta)$ is given by

$$f_{ij}(\theta) = \frac{G_{ij}(\theta)}{G_{\theta\theta}(0)} \ , \ (i,j=r,\theta) \ , \ (-\pi<\theta<\pi) \quad . \tag{26}$$

The analytical details of a crack terminating at and crossing the boundary in a two-phase nonhomogeneous elastic medium may be found in [14] and [15].

3.2 Anti-Plane Shear Problem for a Crack Interacting with a Circular Inclusion

The simpler problem for a medium containing a crack and a circular elastic inclusion or a hole shown in Fig. 4 and subjected to a uniform anti-plane shear loading

$$\sigma_{yz}(x, \mp \infty) = p_o \tag{27}$$

can also be treated in a manner similar to the plane strain problem

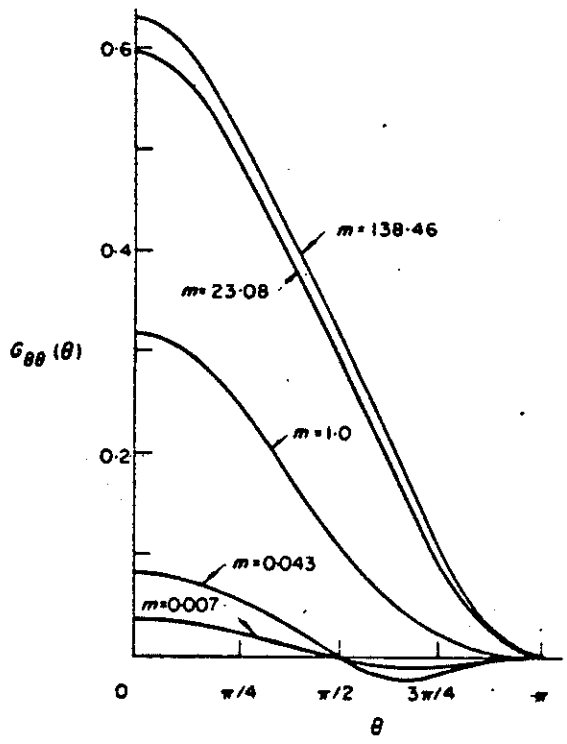

Fig. 22. Angular variation of $\sigma_{\theta\theta}$ around a crack tip touching the interface.

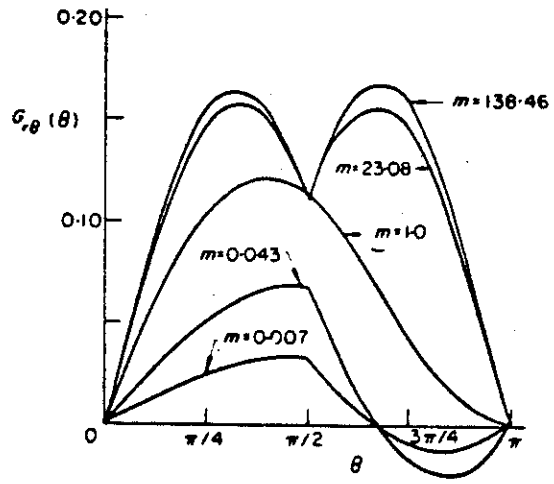

Fig. 23. Angular variation of $\sigma_{r\theta}$ around a crack tip touching the interface.

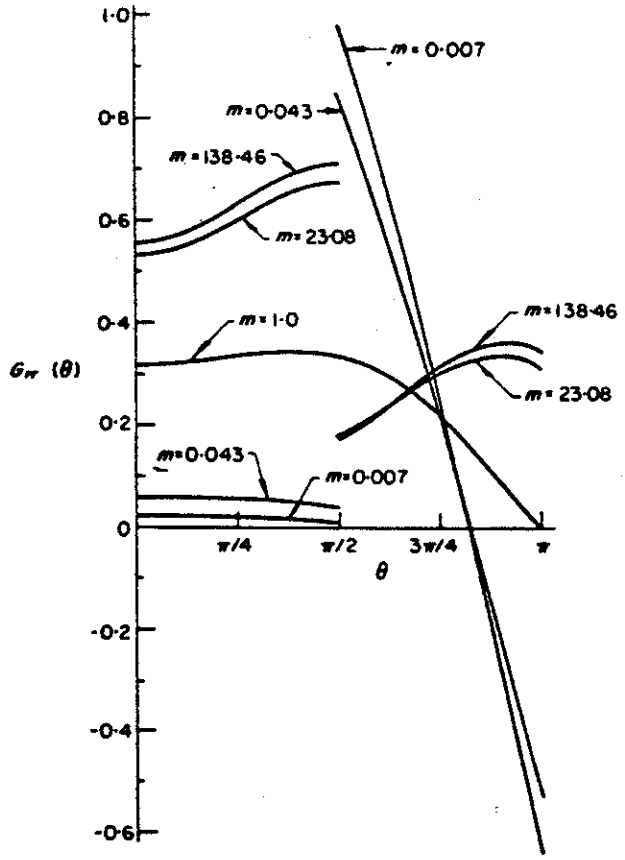

Fig. 24. Angular variation of σ_{rr} around a crack tip touching the interface.

discussed in the previous section. In this case the crack surface tractions for the perturbation problem are obtained by solving the problem of inclusion or hole without a crack. Some sample results giving the stress distribution $\sigma_{yz}(x,y)$ (for various fixed values of y) are shown in Figures 25 and 26. Again note that qualitatively these results are very similar to the plane strain results shown in figures 2 and 5. For this problem some sample results giving the Mode III stress intensity factors k_3 at the crack tips $x = \mp a$ are defined by

$$k(a)p_0\sqrt{a} = k_3(a) = \lim_{x\to a} \sqrt{2(x-a)}\, \sigma_{1yz}(x,c) \ , \tag{28}$$

$$k(-a)p_0\sqrt{a} = k_3(-a) = \lim_{x\to -a} \sqrt{2(x+a)}\, \sigma_{1yz}(x,c) \ . \tag{29}$$

Figure 27 shows the results for the radial crack in a medium containing an inclusion or a hole. Similar results for an arbitrarily located crack are shown in Figures 28 and 29. Figure 30 gives some comparative results showing the influence of the crack length-to-radius ratio on the stress intensity factors where m is the modulus ratio $m = \mu_2/\mu_1$ and $k(\mp a) = k_3(\mp a)/p_0\sqrt{R}$. For $m = 1$ we have a homogeneous plane with a crack of length 2a for which $k_3(\mp a) = p_0\sqrt{a}$. Consequently

$$k(\mp a) = \frac{k_3(\mp a)}{p_0\sqrt{R}} = \frac{p_0\sqrt{a}}{p_0\sqrt{R}} = \sqrt{a/R} \ , \tag{30}$$

giving the straight line shown in the figure. For m=0, m=1 and m=23.3 the slopes of $k(\mp a)$ vs. $\sqrt{a/R}$ curves as $(a/R)\to 0$ are 1.47, 1 and 0.57, respectively. The results for m=0 and m>0 are obtained from the solution of an "infinite" plane with a central crack subjected to the crack surface tractions $\sigma_{yz}(x,0)$ which are equal and opposite to the corresponding stresses given in figures 25 and 26 at x=b=1.5R.

The singular behavior of the stresses terminating at and crossing the boundary is discussed in [16] and [17].

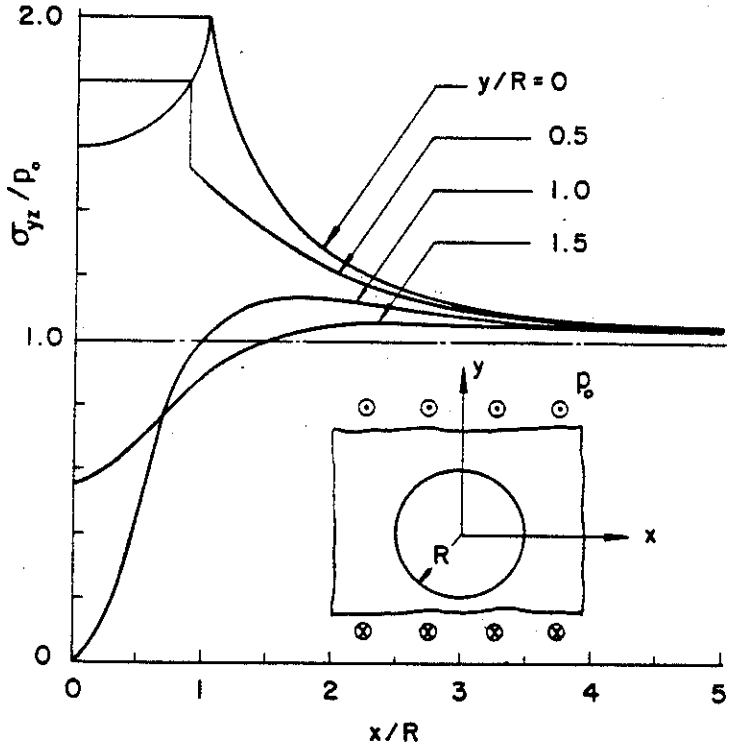

Fig. 25. The shear stress τ_{yz} in a matrix with a circular hole.

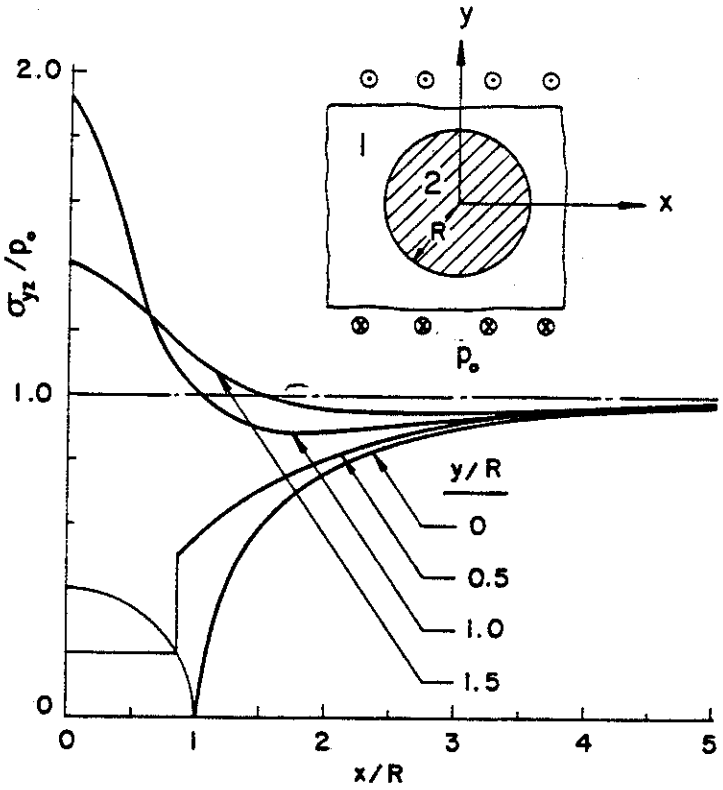

Fig. 26. The shear stress τ_{yz} in a matrix with a circular inclusion ($\mu_2 = 23.3\ \mu_1$).

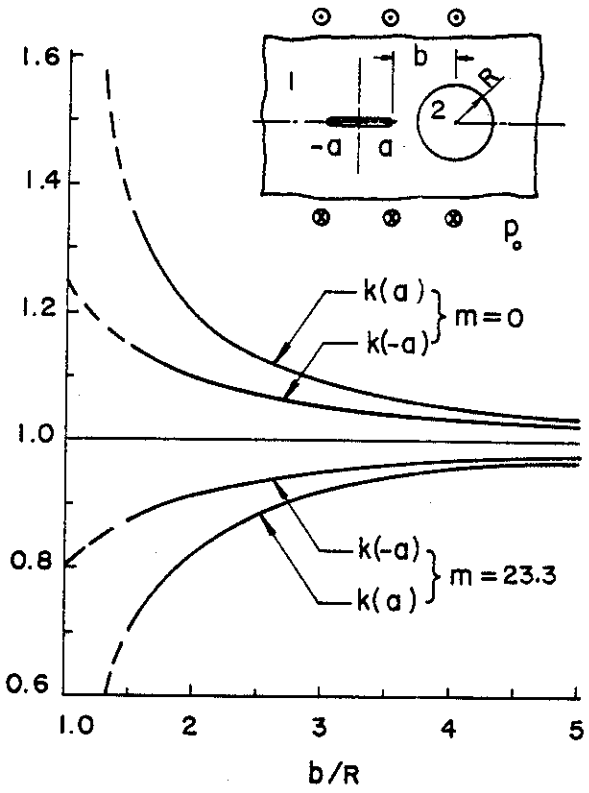

Fig. 27. Stress intensity factors for the antiplane shear problem ($k = k_3/p_o\sqrt{a}$, $R = a$).

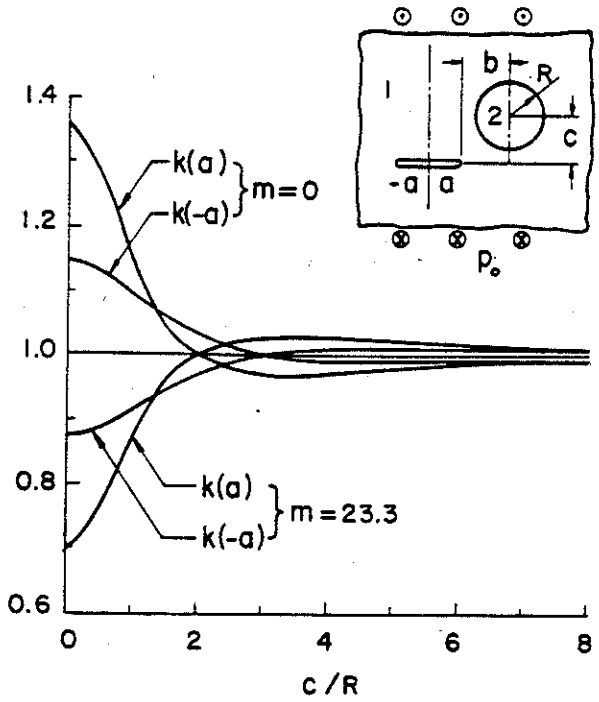

Fig. 28. Stress intensity factors for the antiplane shear problem ($k=k_3/p_o\sqrt{a}$, R=a, b=1.5R).

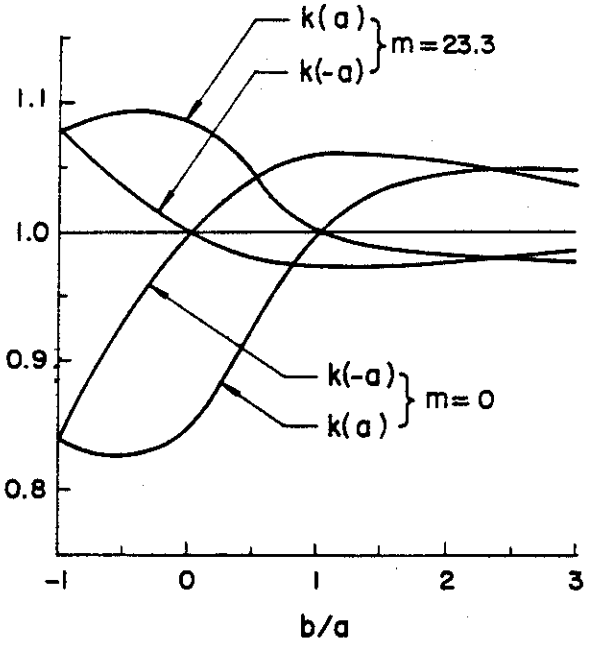

Fig. 29. Stress intensity factors for the antiplane shear problem ($k=k_3/p_o\sqrt{a}$, R=a, c=1.5R).

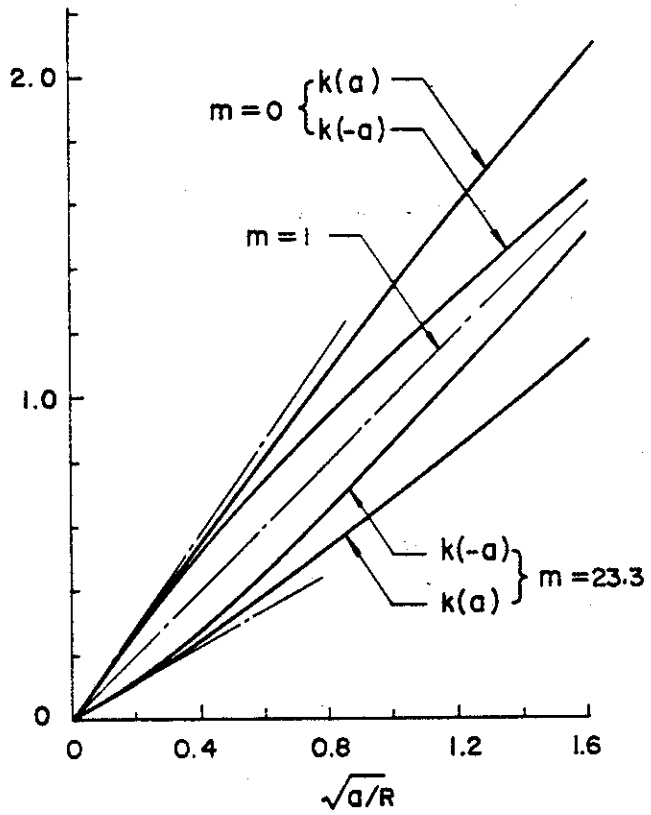

Fig. 30. Stress intensity factors for the antiplane shear problem ($k=k_3/p_0\sqrt{R}$, c=0, b=1.5R).

4. INTERACTION BETWEEN CRACKS

In this section the problem of interaction between cracks on the surface and inside a plate with finite thickness is considered.

4.1 Interaction Between Parallel Internal Cracks

The basic geometry of the problem is shown in Fig. 31. In this section we will consider various special cases relating two or three cracks on the surface of a plate under uniform tension.

For two symmetrically located parallel cracks the stress intensity factors are given in Table 3. Referring to Fig. 31, for this problem we have a=b (i.e., no crack on x axis) c = H-d, P = 0 (no concentrated force) 2B is the distance between the cracks, 2ℓ is the crack length and $\sigma_{yy} = \sigma_0$ for $y \to \mp\infty$. In this section too the Modes I and II stress intensity factors k_1 and k_2 are defined by

$$k_1 = \lim_{r\to 0} \sqrt{2r}\, \sigma_{yy}(r,0) \ , \quad k_2 = \lim_{r\to 0} \sqrt{2r}\, \sigma_{xy}(r,0) \ , \tag{31}$$

where r,ϕ are the polar coordinates at the crack tip, the crack being along $\phi = \pi$. Note that as the distance 2B between the cracks decreases k_1 also decreases and k_2 becomes more significant. The angle θ shown in this table is an (approximate) direction of a probable crack growth which is obtained from a simple assumption that along this radial line at the crack tip the cleavage stress $\sigma_{\theta\theta}(r,\theta)$ is maximum [12], where r<<H-d. Here $\theta>0$ indicates that the cracks would grow away from each other.

4.2 Interaction Between Parallel Surface Cracks

The stress intensity factors and the angle of probable crack growth direction in a plate containing two parallel and equal surface cracks under uniform tension or pure bending are shown in Figures 32-35. In this problem we have a=b, c=0 and d<H. The figures also show the Mode I

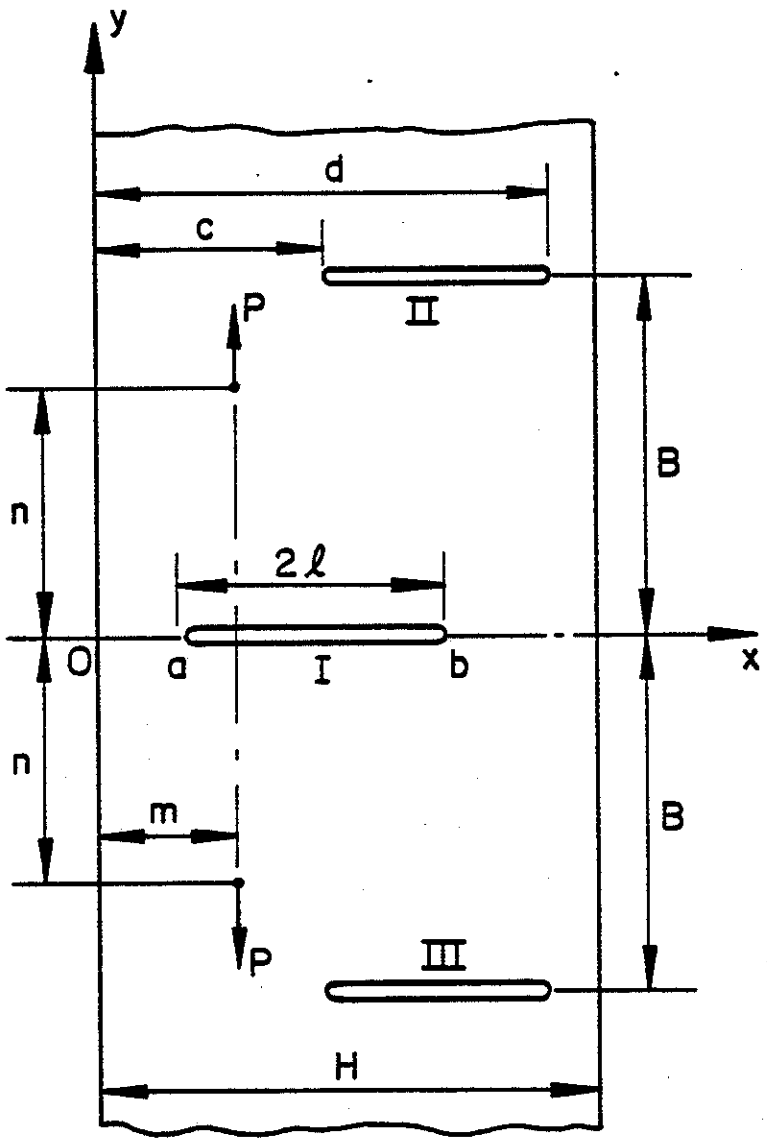

Figure 31. The basic crack geometry.

Table 3. Stress intensity factors in a strip containing two symmetric internal cracks, $\ell=(d-c)/2$.

ℓ/H	B/ℓ	$k_1/\sigma_0\sqrt{\ell}$	$k_2/\sigma_0\sqrt{\ell}$	$\theta(°)$
0.05	0.5	0.7797	-0.1175	16.430
	1.0	0.8512	-0.0616	8.194
	1.5	0.9052	-0.0308	3.887
	2.0	0.9395	-0.0163	1.992
	5.0	0.9953	-0.0001	0.157
	10.0	1.0053	-0.00001	0.014
	20.0	1.0060	0.0000	0.000
0.1	0.5	0.7992	-0.1199	16.363
	1.0	0.8749	-0.0624	8.076
	1.5	0.9310	-0.0307	3.774
	2.0	0.9660	-0.0162	1.920
	5.0	1.0219	-0.0001	0.106
	10.0	1.0247	-0.00001	0.003
	20.0	1.0248	0.0000	0.000
0.2	0.5	0.8846	-0.2570	15.578
	1.0	0.9749	-0.0656	7.634
	1.5	1.0437	-0.0330	3.648
	2.0	1.0839	-0.0155	1.641
	5.0	1.1096	-0.0001	0.019
	10.0	1.1097	0.0000	0.000

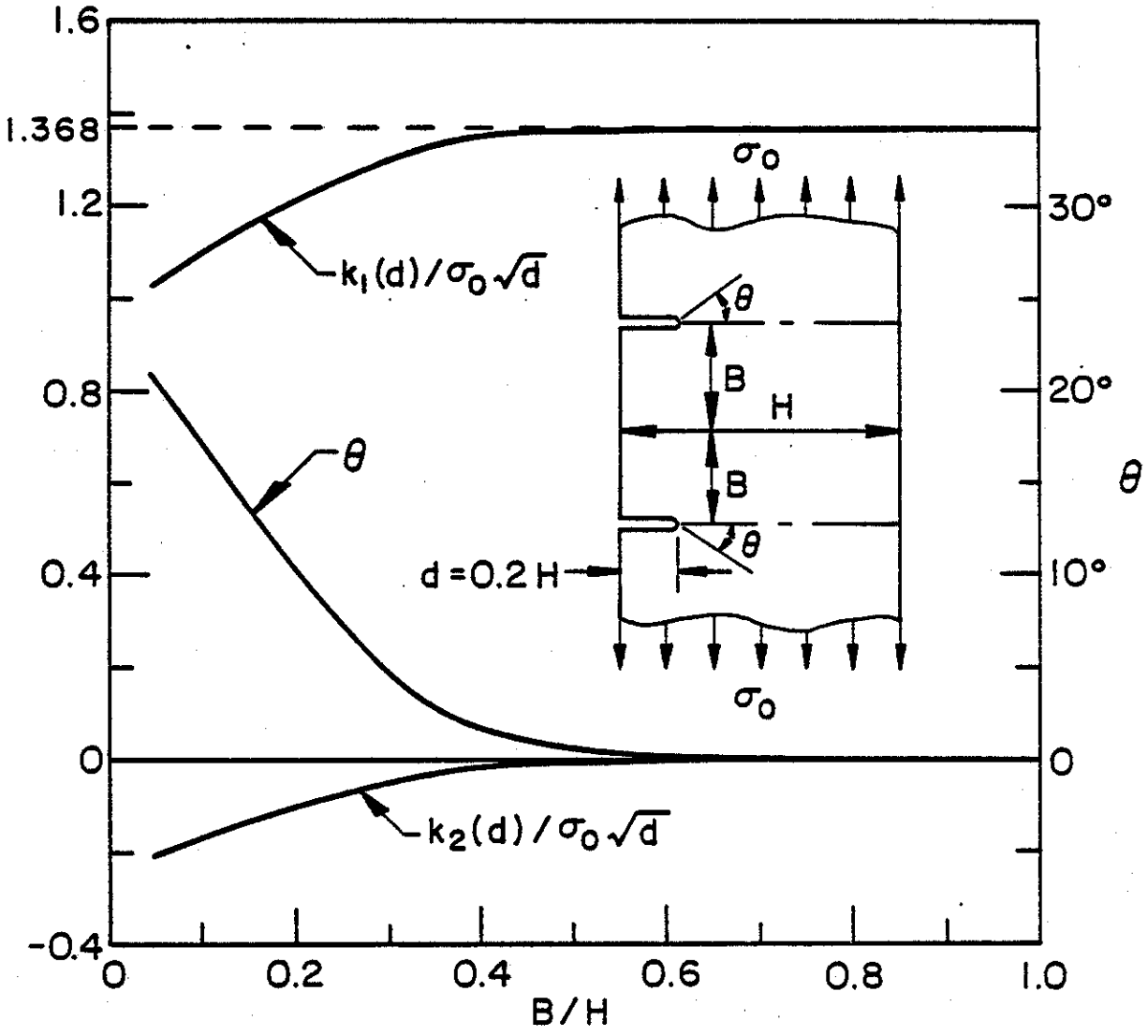

Figure 32. Stress intensity factors and probable crack propagation angle in an infinite strip containing two edge cracks under uniform tension, d=0.2H.

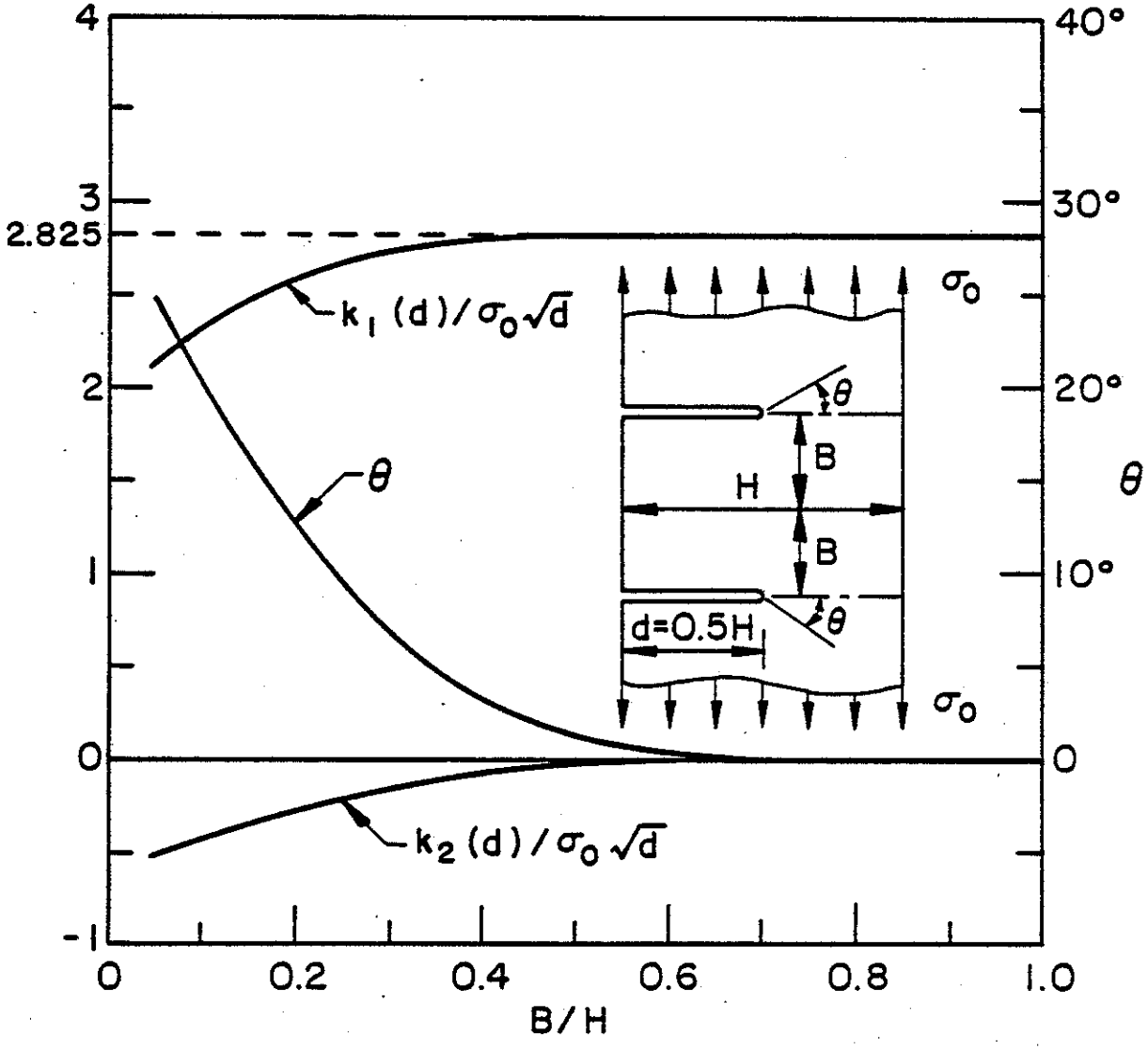

Figure 33. Same as Figure 2, d=0.5H.

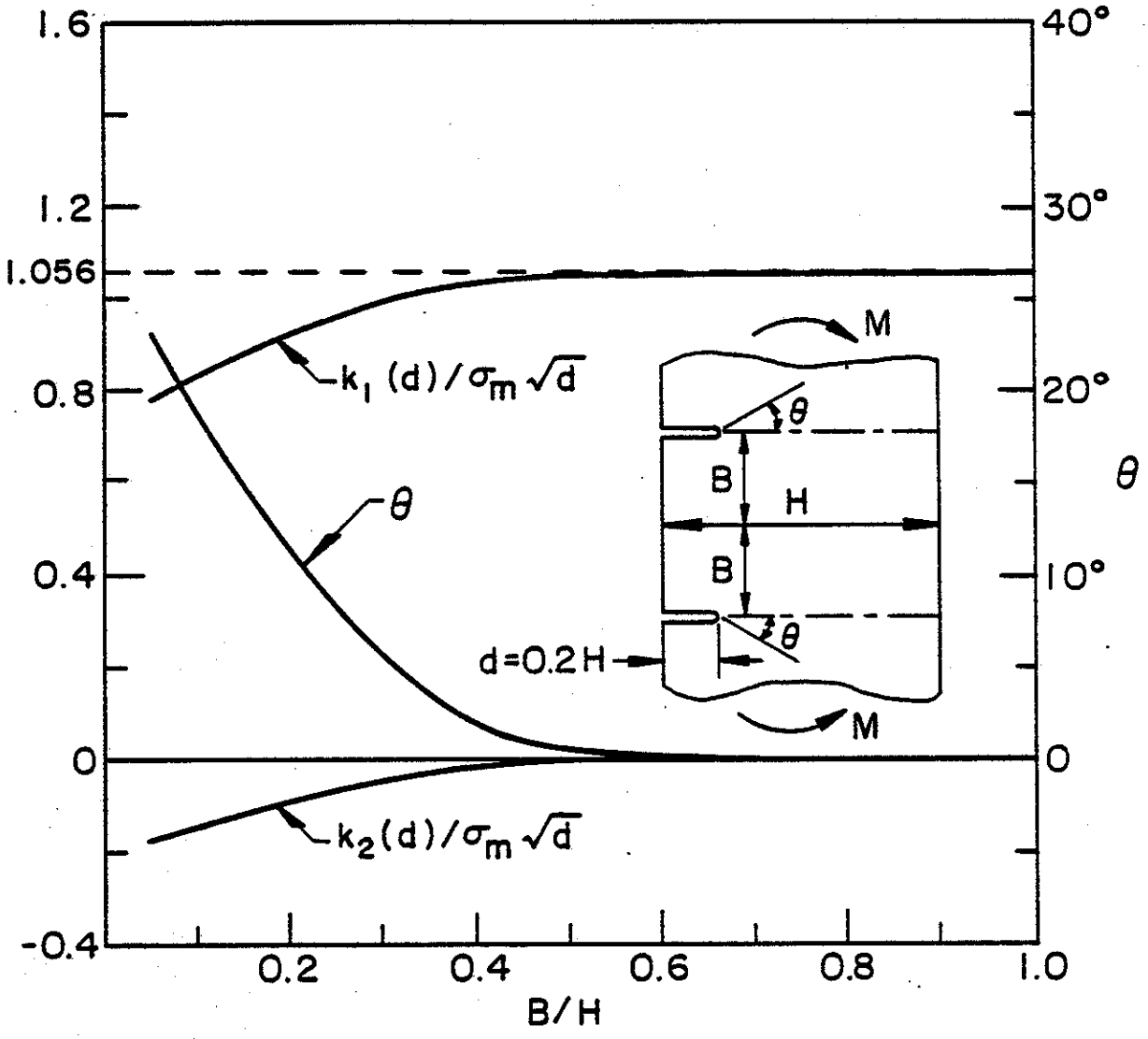

Figure 34. Stress intensity factors and probable crack propagation angle in an infinite strip with two edge cracks under bending, d=0.2H.

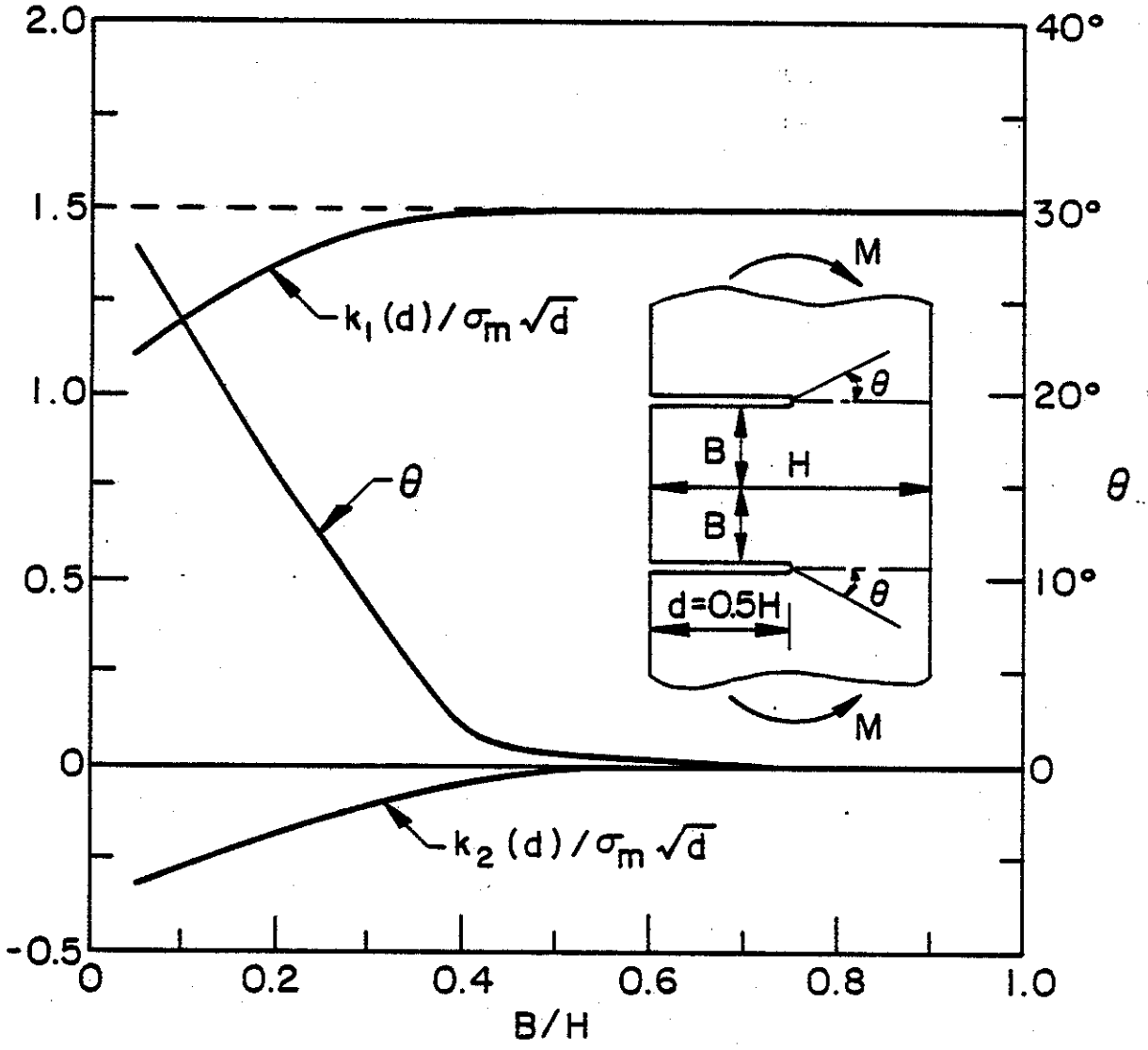

Figure 35. Same as Figure 4, d=0.5H.

stress intensity factor k_1 for a single surface crack for comparison (the dashed line). For the single crack k_2 is 0. Again note that k_1 is smaller than the corresponding single crack value, k_2 becomes more significant as B decreases, and cracks would tend to propagate away from each other. For the bending problem shown in Figures 34 and 35 the normalizing stress σ_m is given by

$$\sigma_m = \frac{6M}{H^2} \tag{32}$$

where M is the moment for unit thickness.

Figures 36-41 show the results for a plate containing three parallel surface cracks under uniform tension or bending. In this case, too, $k_2<0$, meaning that the outside cracks would grow away from the middle crack. Comparison of the two and three crack results shows that the introduction of the middle crack "relaxes" the stress intensity factors in the outer cracks. Fig. 40 shows that for short cracks the interaction and for longer cracks the back surface effect would dominate. Figure 41 shows the results for three point bending. In this problem, too, σ_m is the surface stress in the plate under bending, namely

$$\sigma_m = \frac{6M}{H} = \frac{24P}{H} \quad . \tag{33}$$

The stress intensity factor k(d) for the outer cracks approaches zero as $B \to 4H$ (for which the moment is zero).

4.3 Cracks Parallel to the Boundary

The basic geometry for the plate containing a crack parallel to the boundary is shown by the insert in Fig. 42. The problem considered in this section also takes into account the material orthotropy. Thus, the material constants shown in Fig. 42 are related to the elastic constants of an orthotropic plate as follows:

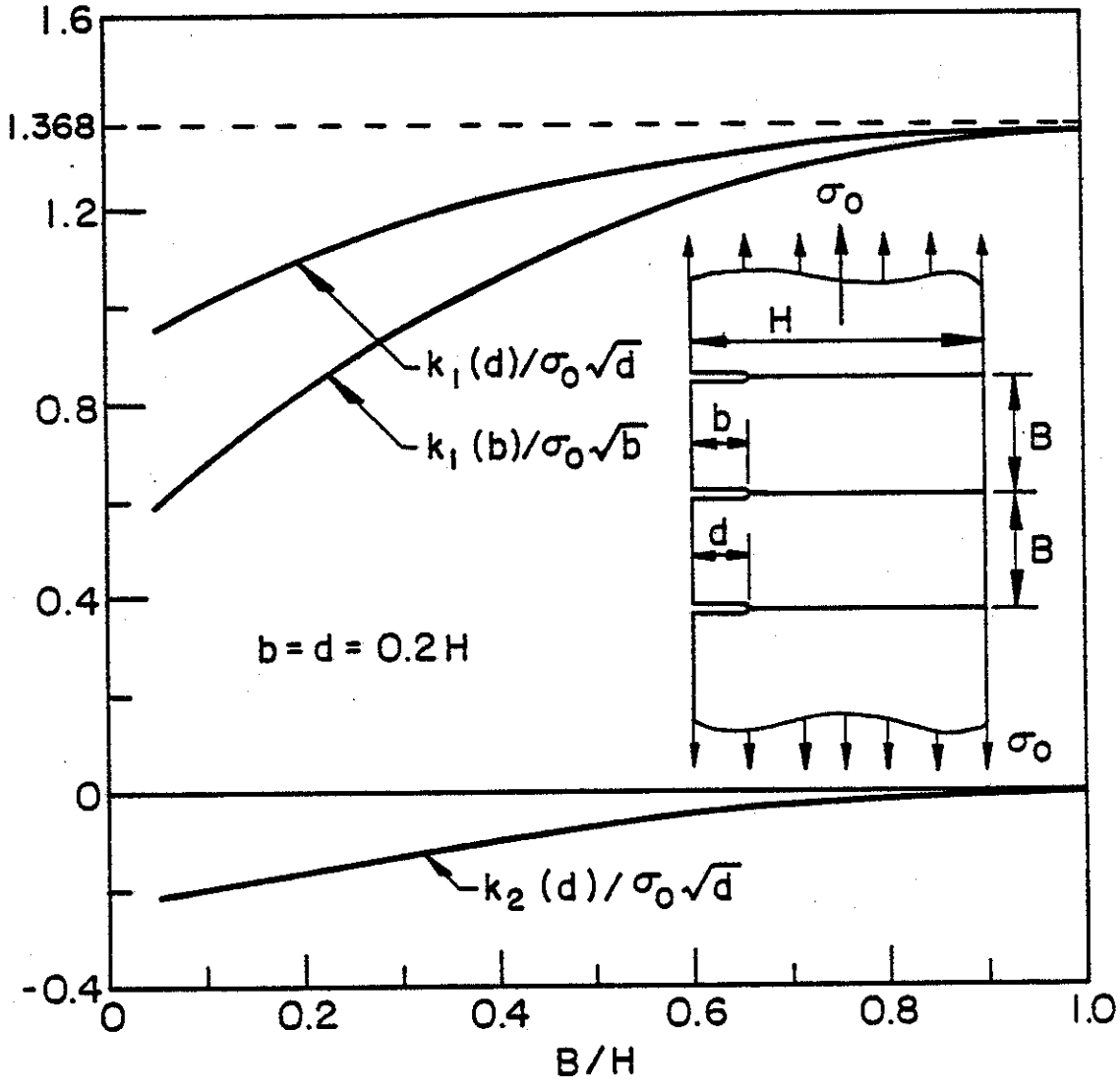

Figure 36. Stress intensity factors in an infinite strip containing three edge cracks under uniform tension, d=b=0.2H.

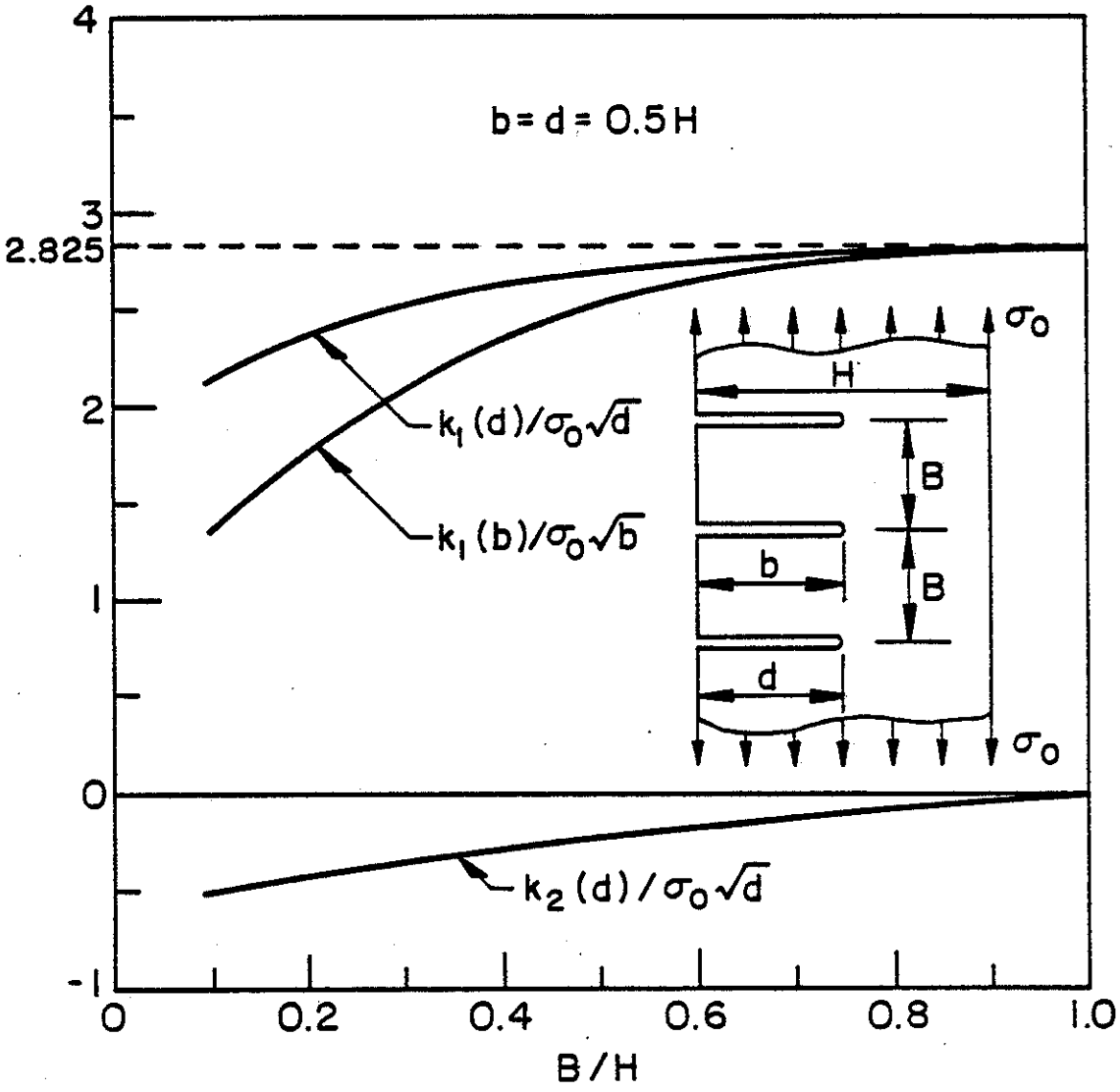

Figure 37. Same as Figure 6, d=b=0.5H.

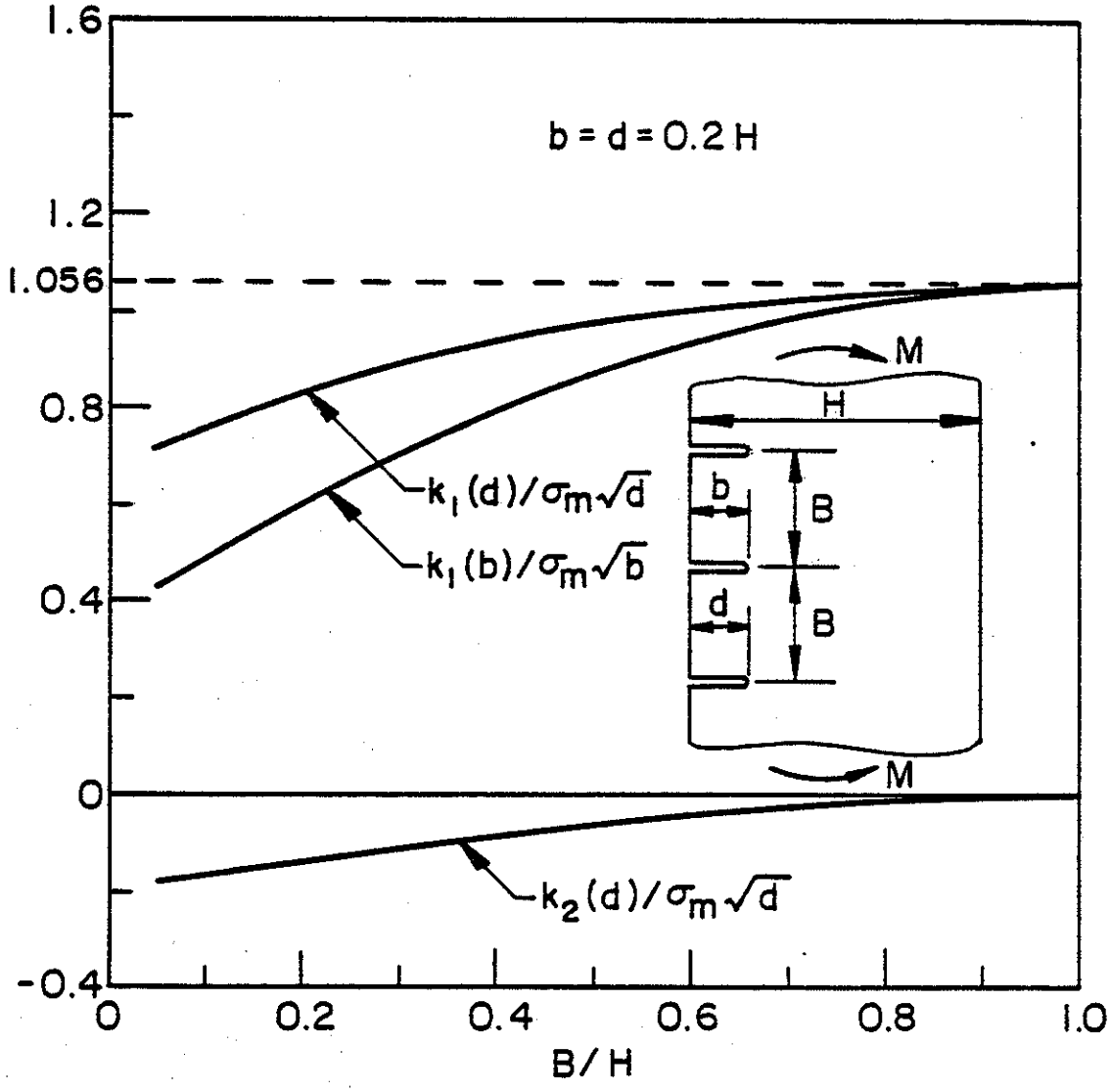

Figure 38. Stress intensity factors in an infinite strip containing three edge cracks under bending, d=b=0.2H, $\sigma_m=6M/H^2$.

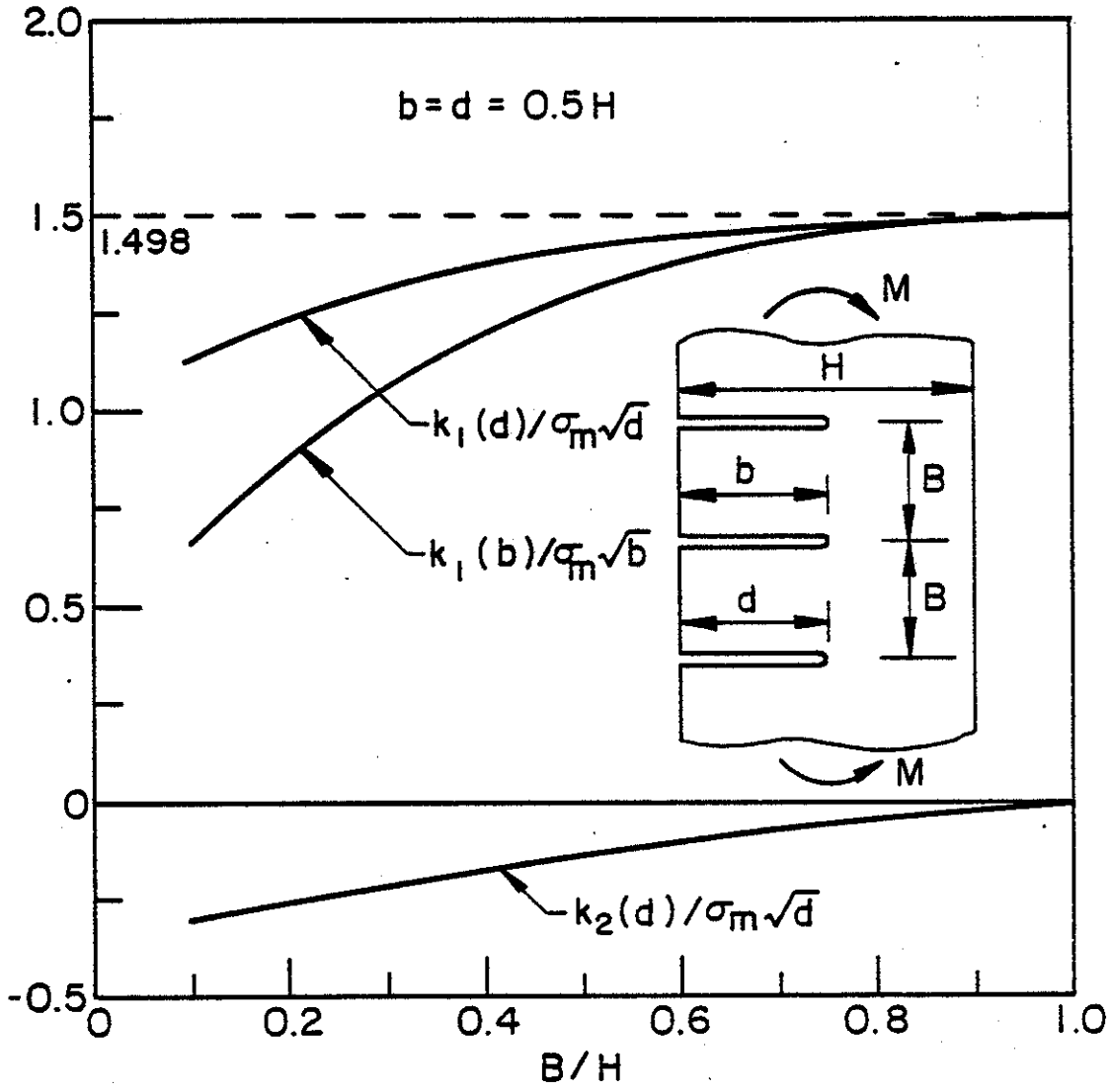

Figure 39. Same as Figure 8, d=b=0.5H, $\sigma_m=6M/H^2$.

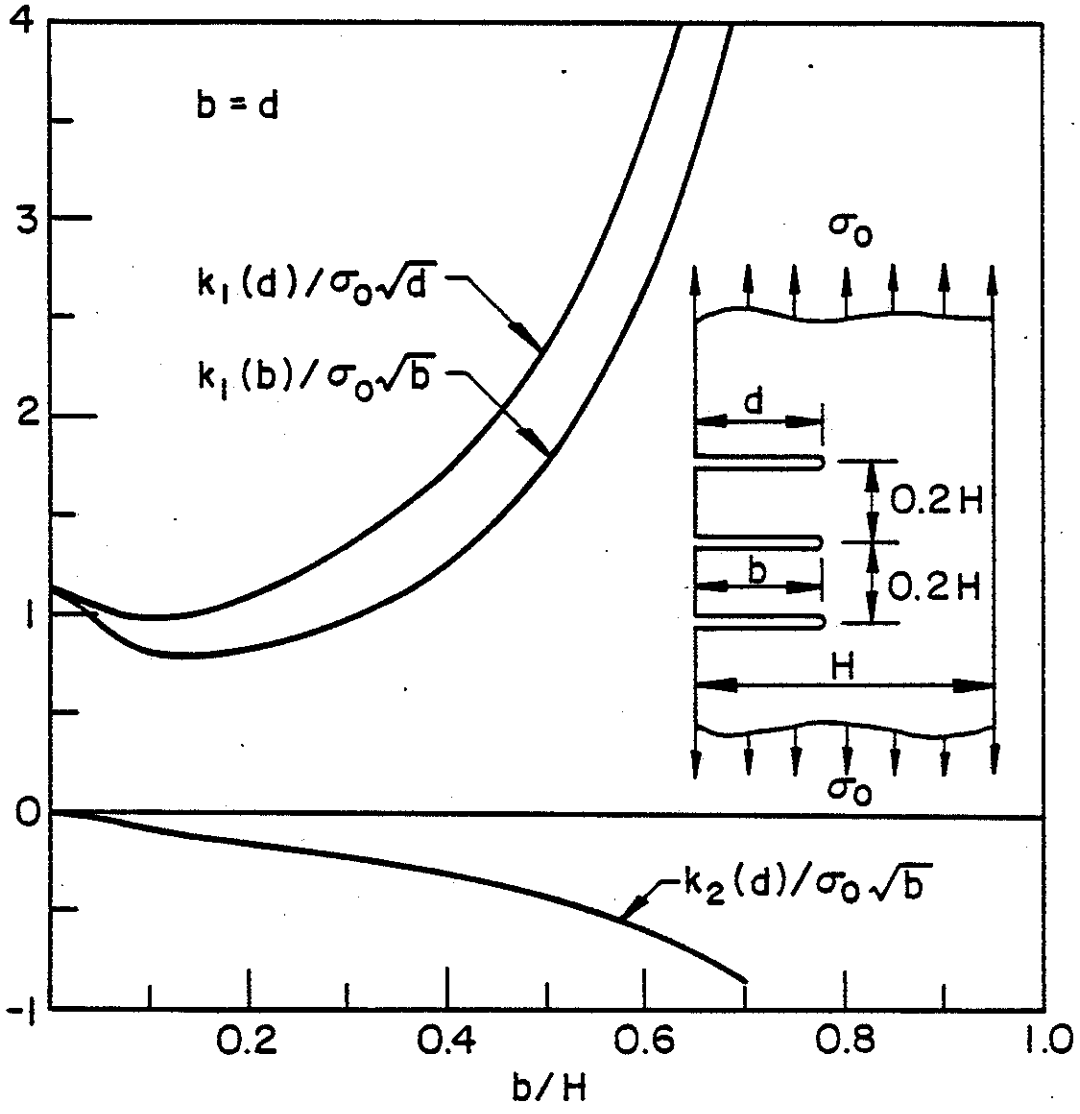

Figure 40. The effect of the crack depth on the stress intensity factors in an infinite strip under tension, B=0.2H.

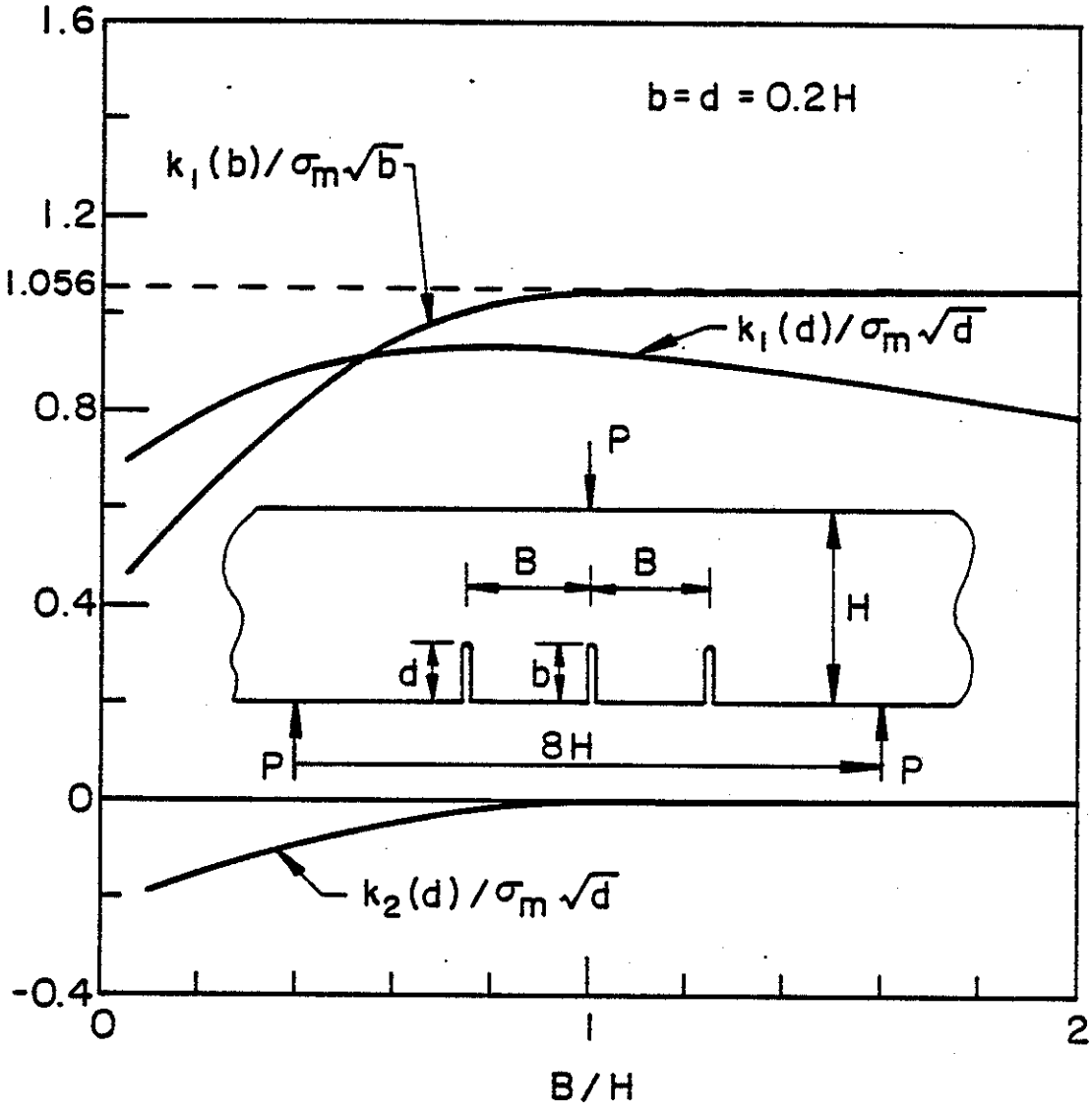

Figure 41. Stress intensity factors in an infinite strip containing edge cracks and subjected to three point bending, $\sigma_m = 6M/H^2 = 24P/H$.

$$\delta^4 = E_{11}/E_{22} \quad , \quad \kappa = \frac{\sqrt{E_{11}E_{22}}}{2G_{12}} - \sqrt{\nu_{12}\nu_{21}} \quad . \tag{34}$$

The engineering material constants which appear in (34) are defined by the following stress-strain relations

$$\begin{aligned} \varepsilon_{11} &= \frac{1}{E_{11}} (\sigma_{11} - \nu_{12}\sigma_{22} - \nu_{13}\sigma_{33}) \ , \ \cdots \\ 2\varepsilon_{12} &= \frac{1}{G_{12}} \sigma_{12} \ , \ \cdots \end{aligned} \tag{35}$$

In Fig. 42 and the subsequent figures the coordinate axes 1 and 2 are respectively parallel and are perpendicular to the crack. The main result of Fig. 42 is that as the crack approaches the boundary the stress intensity factors become unbounded. Also, the analysis of the mixed mode stress state at the crack tip would indicate that the direction along which the cleavage stress is maximum is inclined toward the nearest boundary, meaning that any further propagation of the crack would be toward the nearest boundary. The corresponding results for a crack loaded under pure shear are shown in Fig. 43. The peculiarity of these results is that the Mode II stress intensity factor is relatively insensitive to the location of the crack, in fact it somewhat decreases as the crack approaches the boundary before becoming unbounded.

Figures 44 and 45 show the effect of the relative crack length for a symmetrically located crack under Modes I and II loading conditions.

The results for two collinear cracks loaded under Mode I conditions are shown in Fig. 46. The figure also shows the stress intensity factors for an infinite plate (H=∞) which are given by

$$k_1(b) = p\sqrt{(b-a)/2} \left(\frac{2b}{b-a}\right)^{1/2} [1 - \frac{E(k)}{K(k)}]/k \tag{36}$$

$$k_1(a) = p\sqrt{(b-a)/2} \left(\frac{2b^2}{a(b-a)}\right)^{1/2} [\frac{E(k)}{K(k)} - \left(\frac{a}{b}\right)^2]/k \tag{37}$$

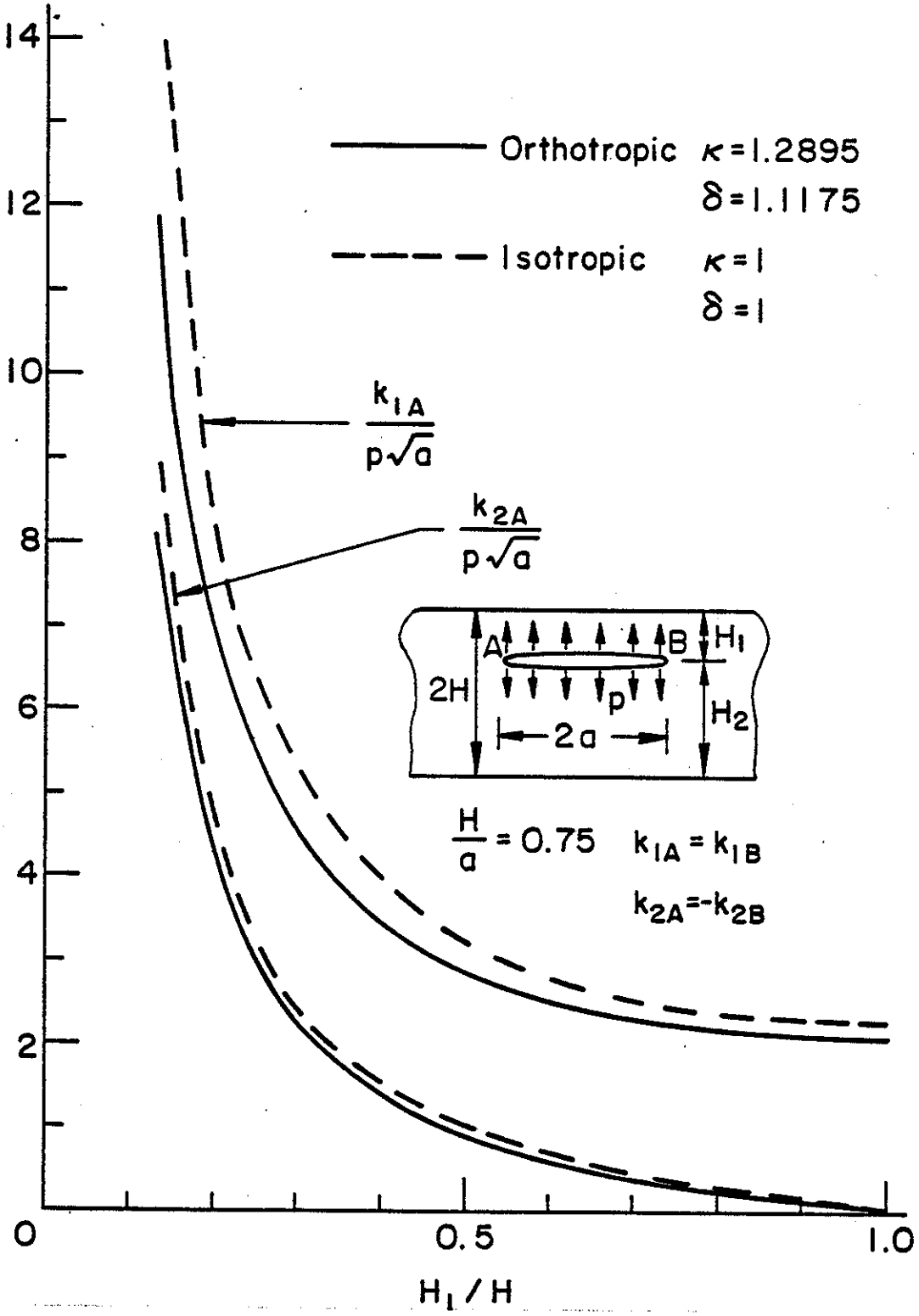

Figure 42. The effect of the crack location on the stress intensity factors for uniform surface pressure. $H = 0.75a$, $\delta = 1 = \kappa$ for the isotropic materials and $\delta = 1.1175$, $\kappa = 1.2895$ for the orthotropic material (yellow birch).

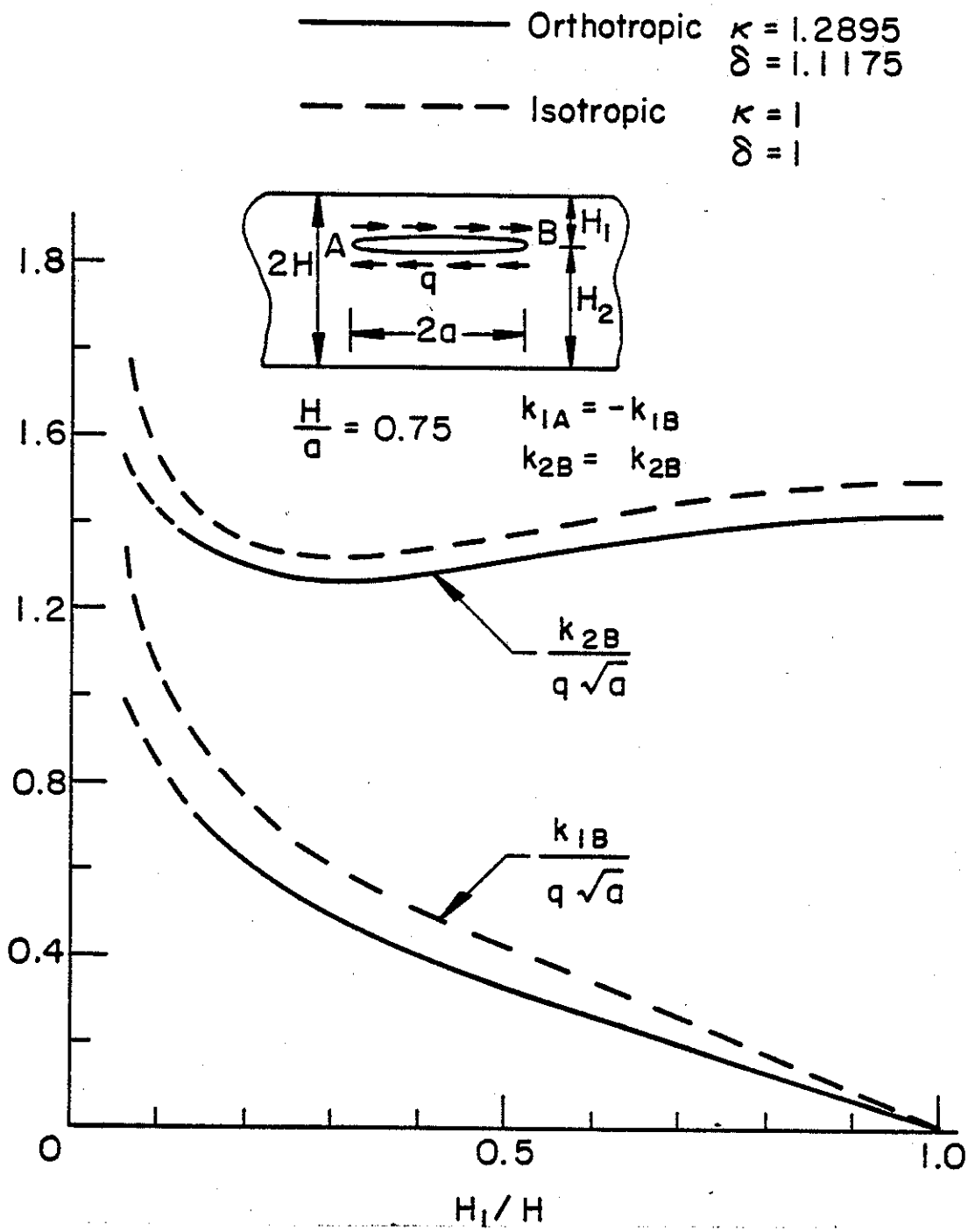

Figure 43. Same as figure 2 for uniform shear applied to the crack surface.

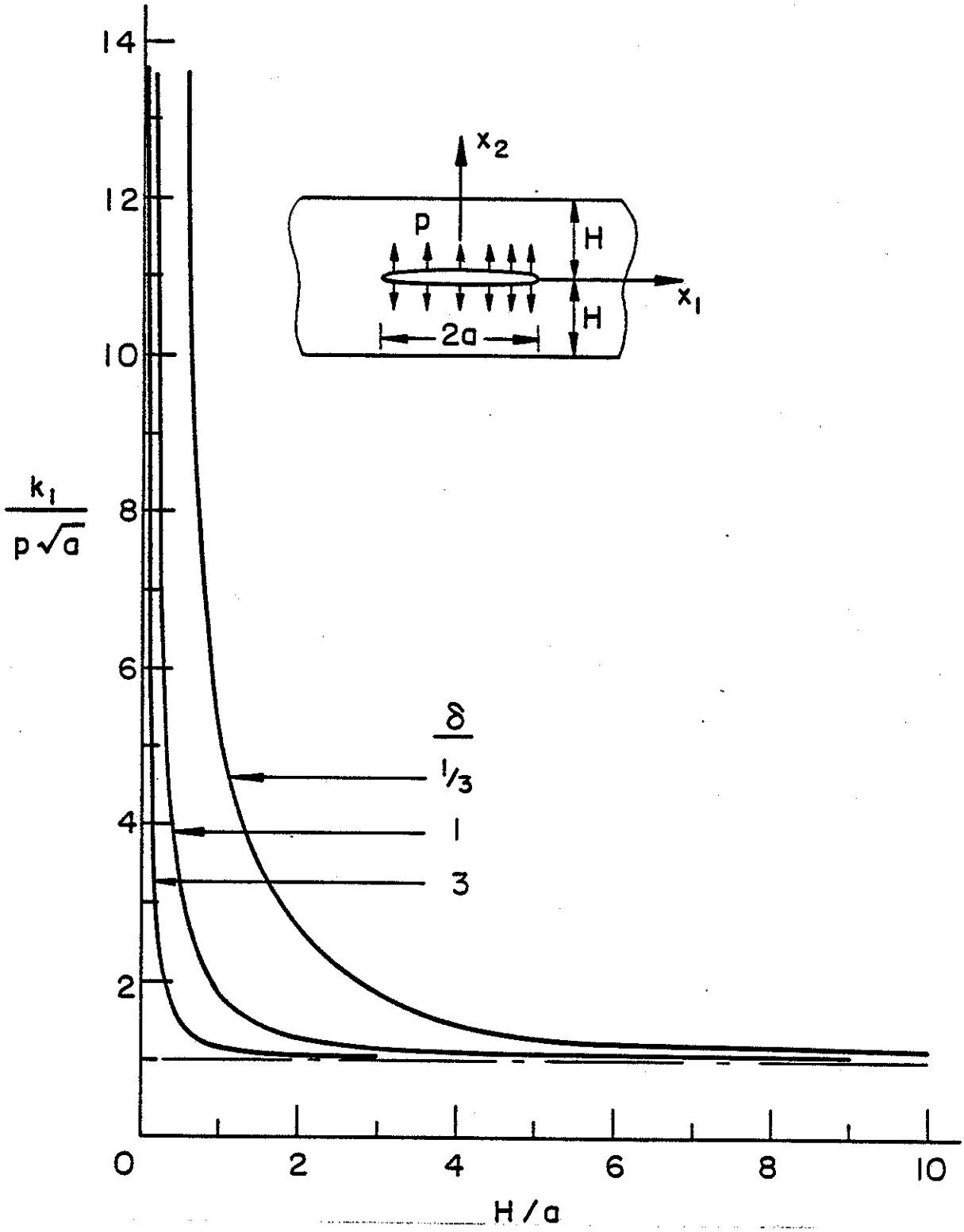

Figure 44. Effect of the crack length on the stress intensity factor for a symmetrically located crack under uniform pressure, $\kappa = 1$.

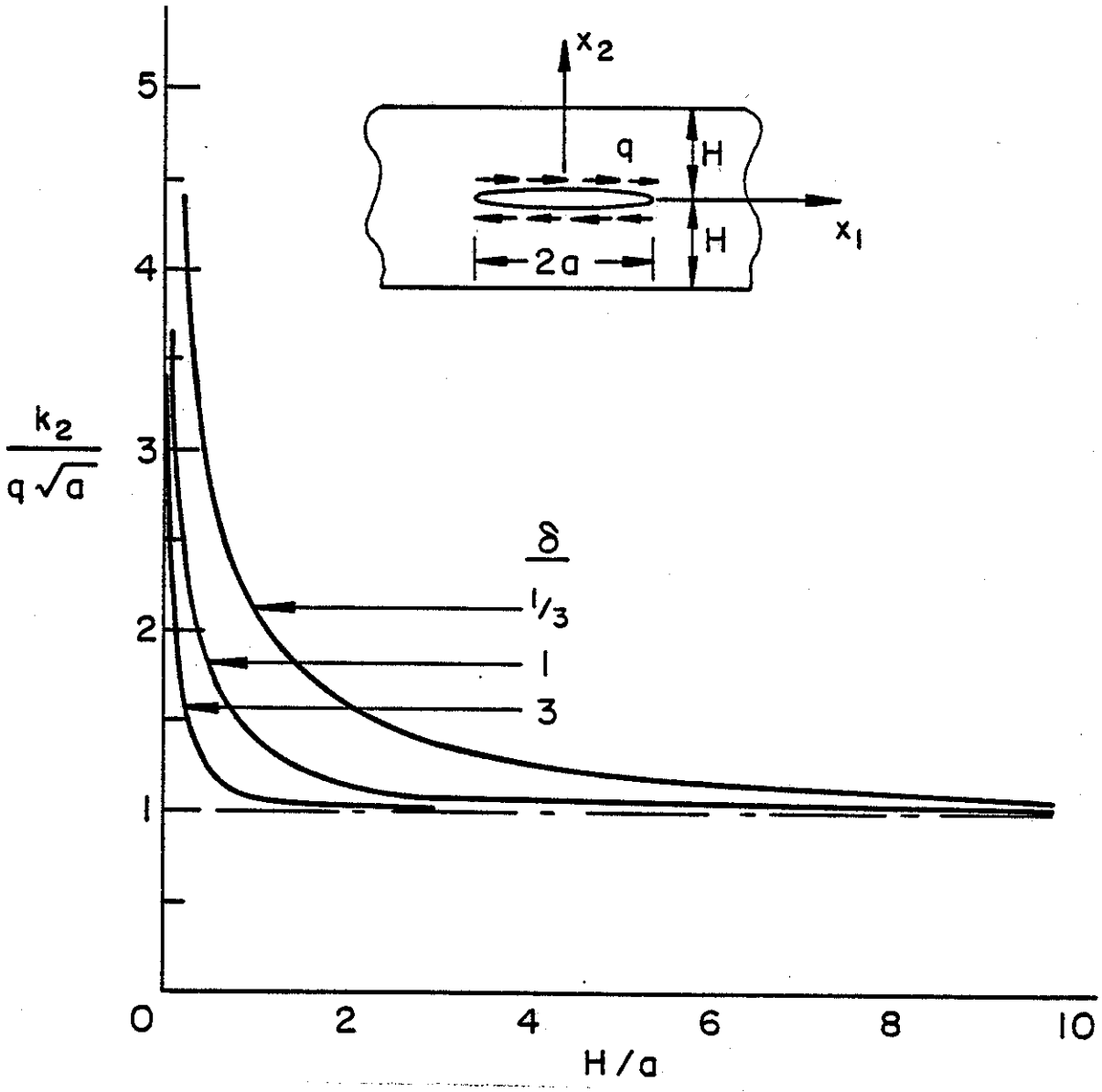

Figure 45. Same as figure 4 for uniform shear applied to crack surface.

where K(k) and E(k) are complete elliptic integrals of respectively first and second kind, and the modulus k is defined by

$$k = \sqrt{1-a^2/b^2} \quad . \tag{37}$$

For convenience a table giving the elliptic integrals (Table 4) is included in this report where the angle α is related to k by $\sin\alpha=k$.

Further results for collinear cracks under Mode II loading condition are given in Table 5. In these results the half crack length (b-a)/2 is used in normalizing stress intensity factor. (a/b) = 0 and (a/b) = 1 correspond to the two limiting cases of a single crack of length 2b and b-a, respectively. As expected $k_1(a)$ becomes unbounded for $a\to 0$ and both $k_1(a)$ and $k_1(b)$ approach the corresponding single crack value for $(a/b)\to 1$ (i.e., for $a\to\infty$). An interesting result observed in Fig. 46 and Table 5, however, is that generally for smaller plate thicknesses as a approaches zero the stress intensity factor $k_1(a)$ goes through a minimum before becoming unbounded. This reduction is apparently due to the interaction of the stress fields of the two cracks as the distance 2a decreases. For example, from Fig. 47 it may clearly be seen that even though the cleavage stress $\sigma_{22}(x_1,0)$ perpendicular to and on the line of the crack is tensile near the crack and becomes unbounded at the crack tip, it becomes compressive in a certain interval away from the crack. This is largely due to the "bending" effect of the two halves of the plate. Thus after the interaction of stress fields of the two cracks it is seen that the inner crack tips would be in compressive region and consequently there would be some decrease in the stress intensity factor.

4.4 Collinear Cracks Perpendicular to the Boundary

From a viewpoint of interaction between two cracks or between cracks and free boundaries another geometry of great deal of practical interest is that of collinear cracks perpendicular to the plate boundary described in Fig. 48. A special case of this problem is the two surface

4. Tables of Complete Elliptic Integrals K(k) and E(k), k = sinα.

V. Vollständige elliptische Integrale.
V. Complete elliptic integrals.

α	K	E	α	K	E	α	K	E
0°	1,5708	1,5708	50°	1,9356	1,3055	82° 0′	3,3699	1,0278
1°	1,5709	1,5707	51°	1,9539	1,2963	82° 12′	3,3946	1,0267
2°	1,5713	1,5703	52°	1,9729	1,2870	82° 24′	3,4199	1,0256
3°	1,5719	1,5697	53°	1,9927	1,2776	82° 36′	3,4460	1,0245
4°	1,5727	1,5689	54°	2,0133	1,2682	82° 48′	3,4728	1,0234
5°	1,5738	1,5678	55°	2,0347	1,2587	83° 0′	3,5004	1,0223
6°	1,5751	1,5665	56°	2,0571	1,2492	83° 12′	3,5288	1,0213
7°	1,5767	1,5650	57°	2,0804	1,2397	83° 24′	3,5581	1,0202
8°	1,5785	1,5632	58°	2,1047	1,2301	83° 36′	3,5884	1,0192
9°	1,5805	1,5611	59°	2,1300	1,2206	83° 48′	3,6196	1,0182
10°	1,5828	1,5589	60°	2,1565	1,2111	84° 0′	3,6519	1,0172
11°	1,5854	1,5564	61°	2,1842	1,2015	84° 12′	3,6853	1,0163
12°	1,5882	1,5537	62°	2,2132	1,1921	84° 24′	3,7198	1,0153
13°	1,5913	1,5507	63°	2,2435	1,1826	84° 36′	3,7557	1,0144
14°	1,5946	1,5476	64°	2,2754	1,1732	84° 48′	3,7930	1,0135
15°	1,5981	1,5442	65°	2,3088	1,1638	85° 0′	3,8317	1,0127
16°	1,6020	1,5405	66°	2,3439	1,1546	85° 12′	3,8721	1,0118
17°	1,6061	1,5367	67°	2,3809	1,1454	85° 24′	3,9142	1,0110
18°	1,6105	1,5326	68°	2,4198	1,1362	85° 36′	3,9583	1,0102
19°	1,6151	1,5283	69°	2,4610	1,1273	85° 48′	4,0044	1,0094
20°	1,6200	1,5238	70° 0′	2,5046	1,1184	86° 0′	4,0528	1,0087
21°	1,6252	1,5191	70° 30′	2,5273	1,1140	86° 12′	4,1037	1,0079
22°	1,6307	1,5142	71° 0′	2,5507	1,1096	86° 24′	4,1574	1,0072
23°	1,6365	1,5090	71° 30′	2,5749	1,1053	86° 36′	4,2142	1,0065
24°	1,6426	1,5037	72° 0′	2,5998	1,1011	86° 48′	4,2746	1,0059
25°	1,6490	1,4981	72° 30′	2,6256	1,0968	87° 0′	4,3387	1,0053
26°	1,6557	1,4924	73° 0′	2,6521	1,0927	87° 12′	4,4073	1,0047
27°	1,6627	1,4864	73° 30′	2,6796	1,0885	87° 24′	4,4812	1,0041
28°	1,6701	1,4803	74° 0′	2,7081	1,0844	87° 36′	4,5609	1,0036
29°	1,6777	1,4740	74° 30′	2,7375	1,0804	87° 48′	4,6477	1,0031
30°	1,6858	1,4675	75° 0′	2,7681	1,0764	88° 0′	4,7427	1,0026
31°	1,6941	1,4608	75° 30′	2,7998	1,0725	88° 12′	4,8479	1,0022
32°	1,7028	1,4539	76° 0′	2,8327	1,0686	88° 24′	4,9654	1,0017
33°	1,7119	1,4469	76° 30′	2,8669	1,0648	88° 36′	5,0988	1,0014
34°	1,7214	1,4397	77° 0′	2,9026	1,0611	88° 48′	5,2527	1,0010
35°	1,7313	1,4323	77° 30′	2,9397	1,0574	89° 0′	5,4349	1,0008
36°	1,7415	1,4248	78° 0′	2,9786	1,0538	89° 6′	5,5402	1,0006
37°	1,7522	1,4171	78° 30′	3,0192	1,0502	89° 12′	5,6579	1,0005
38°	1,7633	1,4092	79° 0′	3,0617	1,0468	89° 18′	5,7914	1,0005
39°	1,7748	1,4013	79° 30′	3,1064	1,0434	89° 24′	5,9455	1,0003
40°	1,7868	1,3931	80° 0′	3,1534	1,0401	89° 30′	6,1278	1,0002
41°	1,7992	1,3849	80° 12′	3,1729	1,0388	89° 36′	6,3509	1,0001
42°	1,8122	1,3765	80° 24′	3,1928	1,0375	89° 42′	6,6385	1,0001
43°	1,8256	1,3680	80° 36′	3,2132	1,0363	89° 48′	7,0440	1,0000
44°	1,8396	1,3594	80° 48′	3,2340	1,0350	89° 54′	7,7371	1,0000
45°	1,8541	1,3506	81° 0′	3,2553	1,0338	90°	∞	1,0000
46°	1,8692	1,3418	81° 12′	3,2771	1,0326			
47°	1,8848	1,3329	81° 24′	3,2995	1,0313			
48°	1,9011	1,3238	81° 36′	3,3223	1,0302			
49°	1,9180	1,3147	81° 48′	3,3458	1,0290			

Jahnke & Emde, "Tables of Functions"

Table 5. Stress intensity factors in an orthotropic strip containing two identical collinear cracks loaded by uniform crack surface pressure p or shear q; $H_1=H_2=H$, $\kappa=1$, $H\delta/(b-a)/2 = 0.4$.

$\frac{2a}{b-a}$	$\sigma_{22}(x_1,0)=-p$		$\sigma_{12}(x_1,0)=-q$	
	$\frac{k_1(b)}{p(\frac{b-a}{2})^{1/2}}$	$\frac{k_1(a)}{p(\frac{b-a}{2})^{1/2}}$	$\frac{k_2(b)}{q(\frac{b-a}{2})^{1/2}}$	$\frac{k_2(a)}{q(\frac{b-a}{2})^{1/2}}$
0	9.376	∞	2.629	∞
.01	3.693	6.996	2.106	5.837
.1	3.788	2.837	1.952	2.300
.2	3.962	3.113	1.935	1.989
.3	4.074	3.642	1.933	1.939
.4	4.124	3.971	1.933	1.933
.5	4.138	4.103	1.933	1.932
.6	4.141	4.138	1.933	1.933
.7	4.140	4.143	1.933	1.933
.8	4.140	4.142	1.933	1.933
.9	4.139	4.140	1.933	1.933
1	4.139	4.140	1.933	1.933
2	4.142	4.142	1.933	1.933

cracks simulating weld defects on both surfaces.

Some sample results for the stress intensity factors k(a) and k(b) for two symmetrically located collinear cracks are given in Table 6. Fig. 49 shows the results for two (collinear) surface cracks. For very shallow surface cracks (i.e., for a→h), as seen from the figure k(a) approaches the stress intensity factor in a semi-infinite plane containing an edge crack of depth $2a_o$, namely

$$k_1(a) \to 1.586\ \sigma_o\sqrt{a_o} \quad . \tag{38}$$

In the other limiting case for which a→0, k(a) approaches the stress intensity factor in a symmetrically loaded infinite plane containing

Table 6. Stress intensity factors for collinear internal cracks in a strip (Figure 1, $a_o = (b-a)/2$).

a/h	b/h	$\frac{k(a)}{\sigma_o\sqrt{a_o}}$	$\frac{k(b)}{\sigma_o\sqrt{a_o}}$
0	0.4	(→ ∞)	1.5690
0.1	0.5	1.1746	1.1169
0.2	0.6	1.1102	1.0961
0.4	0.8	1.0984	1.1250
0.5	0.9	1.1290	1.2278
0.6	1.0	1.6080	(→ ∞)
0	0.8	(→ ∞)	2.5680
0.1	0.9	1.6730	1.7451
0.2	1.0	2.1769	(→ ∞)
0.5	0.95	1.1960	1.4711
0.5	0.98	1.2713	1.9008
0.5	1.0	1.6228	(→ ∞)

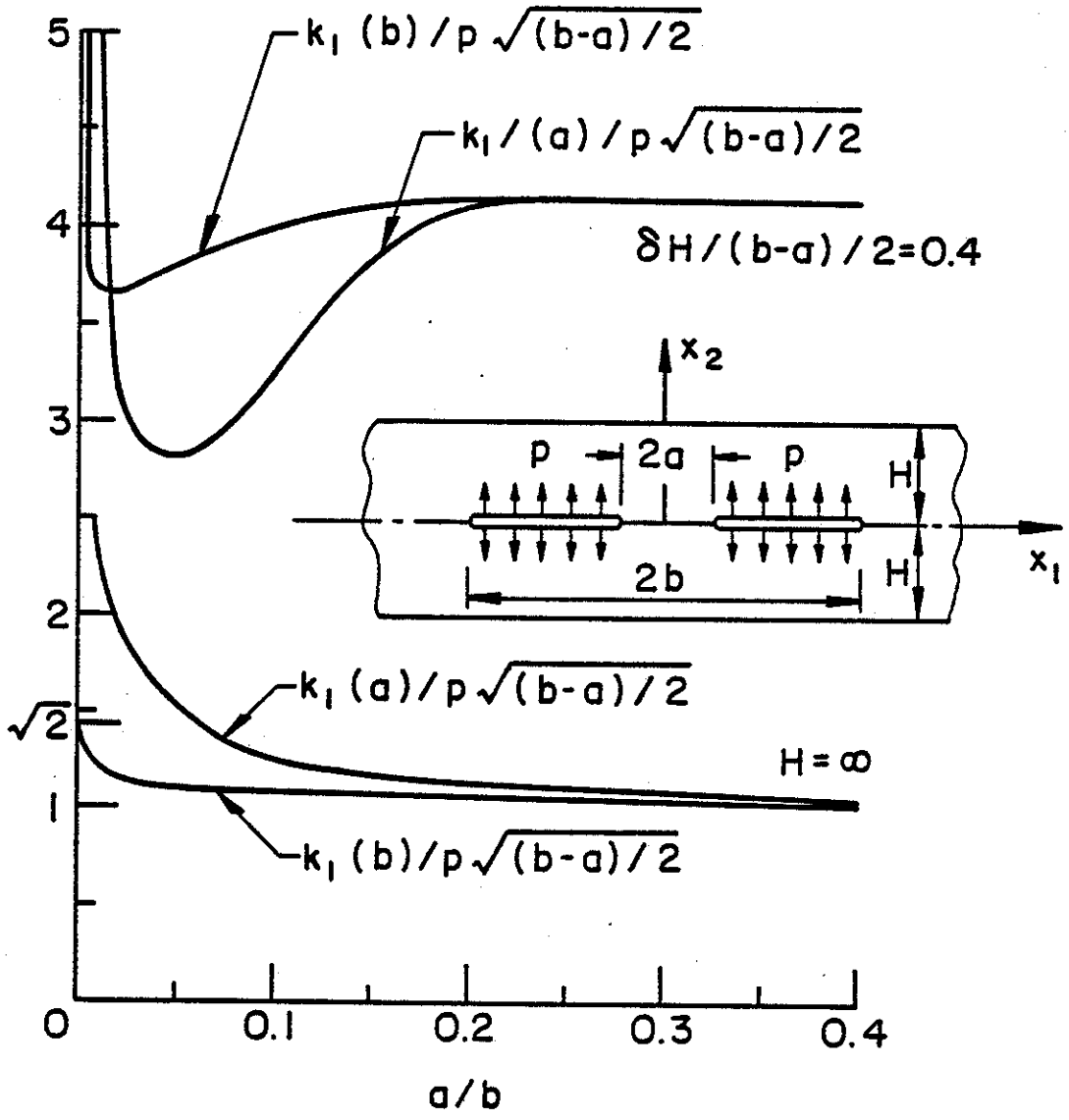

Figure 46. Stress intensity factors for two collinear cracks in an orthotropic strip.

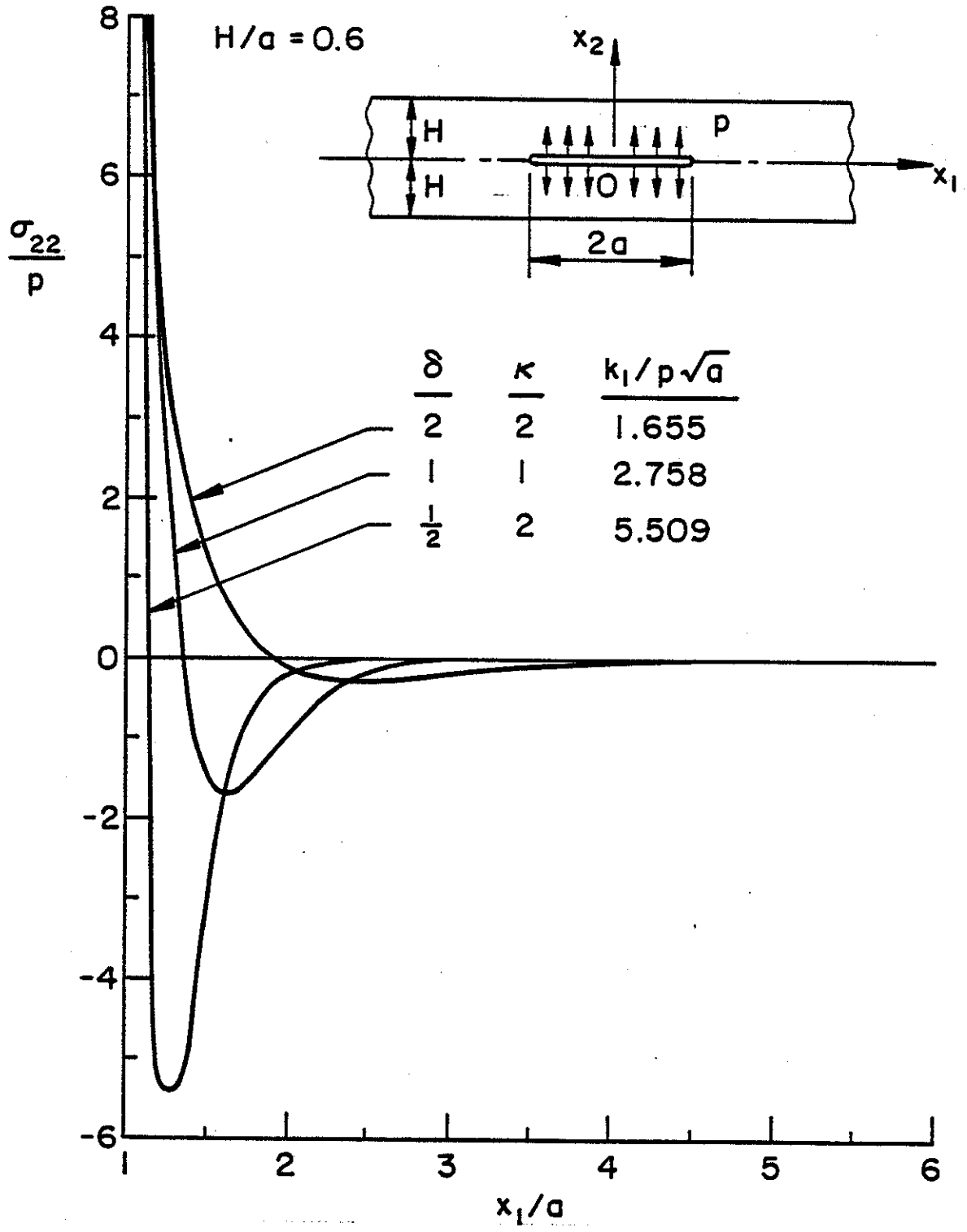

Figure 47. The effect of material orthotropy on the normal stress $\sigma_{22}(x_1,0)$ in a strip containing a pressurized crack ($\delta=\kappa=1$ isotropic strip).

two edge cracks. In this case, if the resultant force perpendicular to the cracks is P, and the length of the net ligament is 2a, it can be shown that the stress state in the net ligament is given by

$$\sigma_{yy}(x,0) = \frac{P}{\pi\sqrt{a^2-x^2}} \quad , \quad \sigma_{xy}(x,0) = 0 \quad . \tag{39}$$

Thus, by observing that

$$P = 2h\sigma_o = 2a\sigma_1 \tag{40}$$

and

$$k(a) = \lim_{x\to a} \sqrt{2(a-x)}\ \sigma_{yy}(x,0) \ , \tag{41}$$

we obtain

$$k(a) = \frac{2}{\pi}\ \sigma_1\ \sqrt{a} \quad . \tag{42}$$

These two limiting results are also shown in Fig. 49.

5. INTERACTION BETWEEN FLAT INCLUSIONS AND CRACKS

Few unusual results aside, the problem of interaction between two cracks is relatively well-understood in the sense that the resulting stress field or the stress intensity factors would either be amplified or reduced as the distance between the cracks decreases. Almost in all cases the qualitative nature of the result could be predicted intuitively. For example, if the cracks are parallel then they would be in each other's shadow and there would be a reduction in the stress intensity factors. On the other hand if the cracks are co-planar then one would expect an amplification in the stress intensity factors. The exception or the unusual result in this case is the reduction in the stress

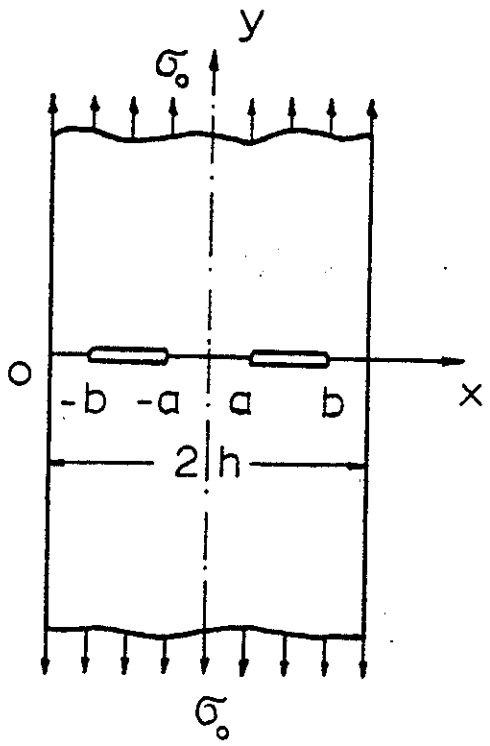

Figure 48. Infinite strip with two internal cracks.

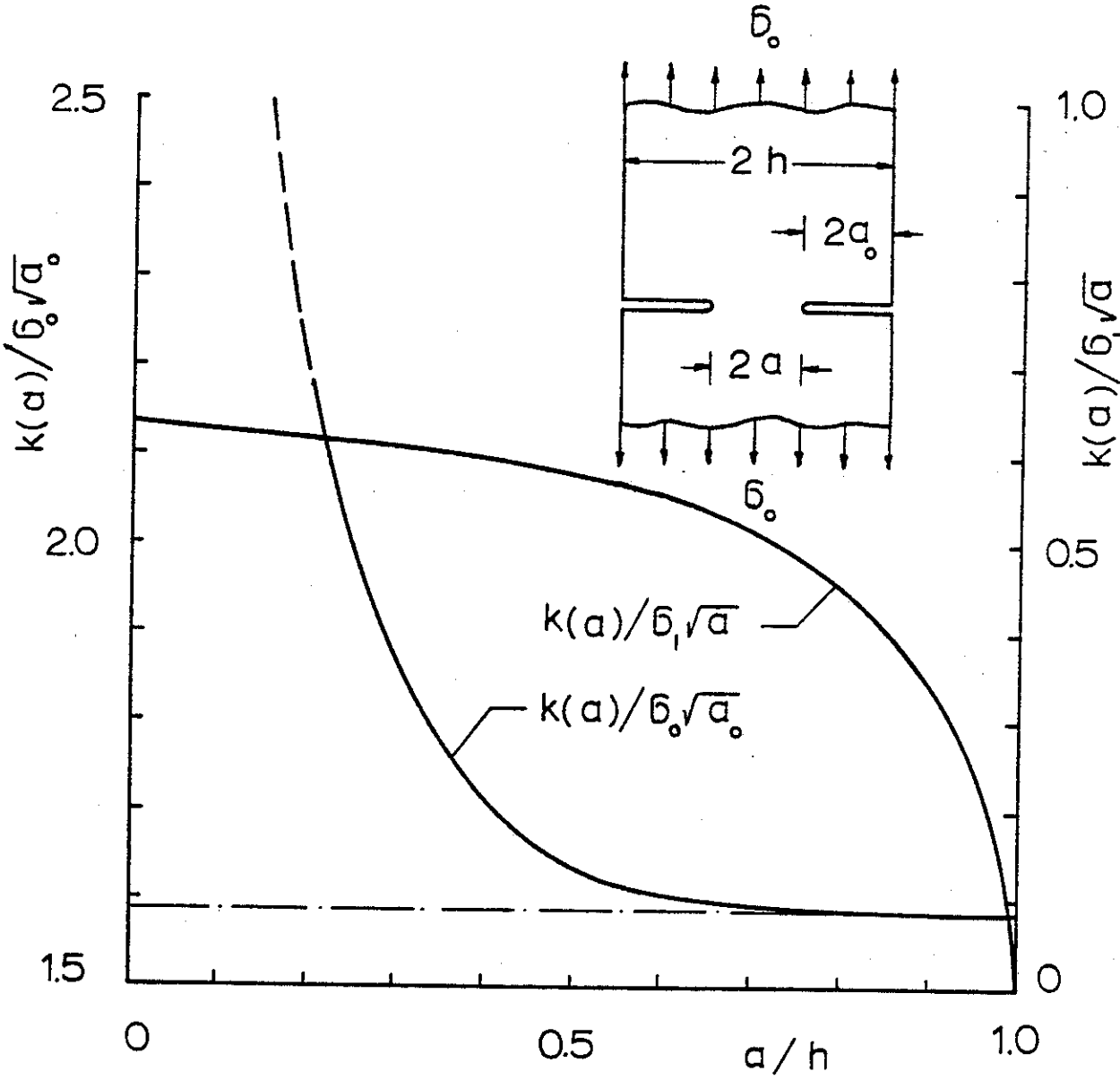

Figure 49. The stress intensity factor for the edge cracks in an infinite strip ($\sigma_1 = \sigma_0 h/a$).

intensity factors at the inner crack tips for certain relative crack locations in plates with relatively smaller thicknesses. Some specific problems relating to interaction between cracks were discussed in the previous sections.

Intuitively what is not as well understood is the problem of interaction between cracks and flat inclusions. Separately both flaws have singular stresses and consequently are locations for potential fracture initiation. However, the inclusions are also "stiffeners" and therefore, properly oriented, they should tend to arrest crack propagation. For this reason in this study it is found to be worthwhile to undertake a detailed investigation of the problem on which the technical literature seems to be extremely weak. Particularly interesting in this problem is the behavior of the stress state around the ends of the inclusions and at the points of intersection between inclusions and cracks. The details of the analysis of this crack-inclusion interaction problem and very detailed results are given in Appendix A of this report.

6. PLANAR CRACKS OF FINITE SIZE

Referring to Fig. 50 which is reproduced from API Standard 1104 and which describes a set of empirical rules regarding the interaction between planar cracks it may be seen that somewhat more quantitative results are needed. The general method to provide such results is described in Appendix B of this report. The appendix gives the results only for a single internal crack. However, the method is general and will be used for the interaction of coplanar surface cracks, and coplanar internal cracks located parallel or in series.

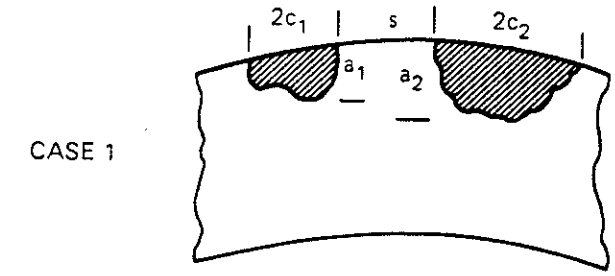

CASE 1

INTERACTION EXISTS IF: $s < c_1 + c_2$

IF INTERACTION EXISTS EFFECTIVE FLAW SIZE IS:

$a_e = a_2$

$2c_e = 2c_1 + s + 2c_2$

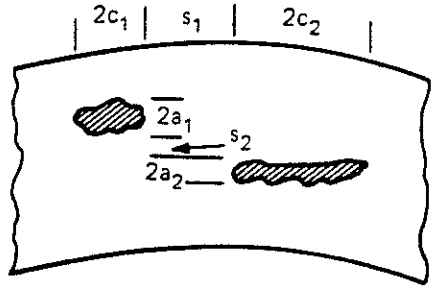

CASE 2

$s_1 < c_1 + c_2$ and $s_2 < a_1 + a_2$

$2a_e = 2a_1 + s_2 + 2a_2$

$2c_e = 2c_1 + s_1 + 2c_2$

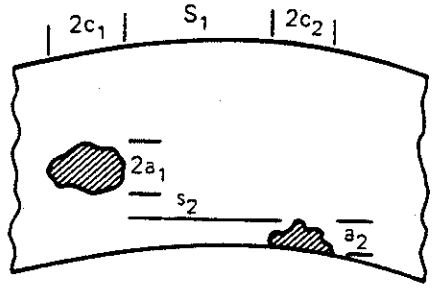

CASE 3

$s_1 < c_1 + c_2$ and $s_2 < a_1 + \frac{a_2}{2}$

$a_e = 2a_1 + s_2 + a_2$

$2c_e = 2c_1 + s_1 + 2c_2$

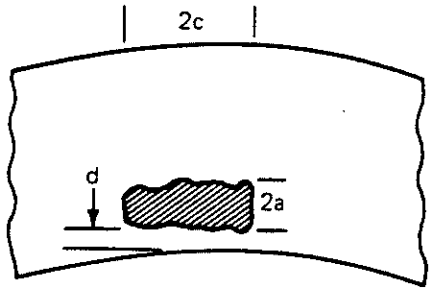

CASE 4

$d < a$

$a_e = d + 2a$

$2c_e = 2c$

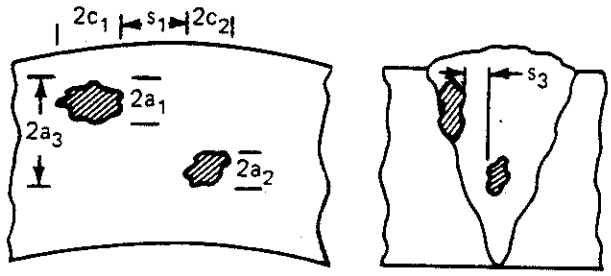

CASE 5

$s_1 < c_2 + c_2$ and $s_3 < a_1 + a_2$

$2a_e = 2a_3$

$2c_e = 2c_1 + s_1 + 2c_2$

Fig. 50. RULES FOR EVALUATION OF FLAW INTERACTION

7. REFERENCES FOR PART I

1. C.D. Lundin, "The Significance of Weld Discontinuities - A Review of Current Literature", W.R.C. Bulletin, No. 222, Dec. 1976.

2. "Proposed Assessment Methods for Flaws with Respect to Failure by Brittle Fracture", Welding in the World, Vol. 13, No. 1/2, 1975.

3. S.T. Rolfe and J.M. Barsom, Fracture and Fatigue Control in Structures, Prentice Hall, 1977.

4. Fatigue Crack Propagation, ASTM-STP 415, 1967.

5. M.S. Kamath, "The COD Design Curve: An Assessment of Validity Using Wide Plate Tests", The Welding Institute Research Report 71/1978/E, Sept. 1978.

6. J.D. Harrison, "The 'State-of-the-Art' in Crack Tip Opening Displacement Testing and Analysis", the Welding Institute Research Report 108/1980, April 1980.

7. J.D. Harrison, M.G. Dawes, G.L. Archer, and M.S. Kamath, "The COD Approach and Its Application to Welded Structures", ASTM-STP668, 1979.

8. F. Erdogan, "Theoretical and Experimental Study of Fracture in Pipelines Containing Circumferential Flaws", Final Report, DOT-RSPA-DMA-50/83/3, Sept. 1982.

9. V.L. Hein and F. Erdogan, "Stress Singularities in a Two-Material Wedge", Int. J. of Fracture Mechanics, Vol. 7, pp. 317-330, 1971.

10. F. Erdogan, G.D. Gupta and M. Ratwani, "Interaction Between a Circular Inclusion and an Arbitrarily Oriented Crack", J. Appl. Mech., Vol. 41, Trans. ASME, pp. 1007-1013, 1974.

11. F. Erdogan and G.D. Gupta, "The Inclusion Problem with a Crack Crossing the Boundary", Int. J. of Fracture, Vol. 11, pp. 13-27, 1975.

12. F. Erdogan and G.C. Sih, "On the Crack Extension in Plates Under Plane Loading and Transverse Shear", J. Basic Engng., Trans. ASME, Vol. 85, pp. 519-526, 1963.

13. N.I. Muskhelishvili, Some Basic Problems of the Mathematical Theory of Elasticity, P. Noordhoff Ltd. Groningen-Holland, 1953.

14. T.S. Cook and F. Erdogan, "Stresses in Bonded Materials with a Crack Perpendicular to the Interface", Int. J. Engng. Sci., Vol. 10, pp. 667-697, 1972.

15. F. Erdogan and V. Biricikoglu, "Two Bonded Half Planes with a Crack Going Through the Interface", Int. J. Engng. Sci., Vol. 11, pp. 745-766, 1973.

16. F. Erdogan and T.S. Cook, "Antiplane Shear Crack Terminating at and Going Through a Bimaterial Interface", Int. J. of Fracture, Vol. 10, pp. 227-240, 1974.

17. J.L. Bassani and F. Erdogan, "Stress Intensity Factors in Bonded Half Planes Containing Inclined Cracks and Subjected to Antiplane Shear Loading", Int. J. Fracture, Vol. 15, pp. 145-158, 1979.

PART II

MECHANISMS OF CORROSION FATIGUE IN PIPELINE STEELS

In this part, the initial results of studies, designed for developing mechanistic understanding of corrosion fatigue, are described. These studies provide the scientific bases for guiding the development of methodology for assessing safety and durability of pipelines in service, and for guiding the development of improved materials and protection systems. The results are not intended for use directly in design and rule-making.

1. INTRODUCTION

Transmission and distribution pipelines are exposed to a broad range of chemical environments, both in terms of corrosive species that are present in soils (such as carbonates, chlorides and nitrates) and of deleterious species that may be transported within the lines (such as hydrogen and ammonia, and hydrogen sulfide and water/water vapor as impurities in natural gas and oil). These environments, acting in concert with operating stresses (both static and cyclic stresses) and residual stresses, can cause cracks to initiate and grow, and result in subsequent failure (leakage or rupture). In addition to these external environments, hydrogen that might be present in the steel (introduced during fabrication, processing or field installation, or by corrosion or cathodic charging during service) can also lead to cracking. Quantitative information and understanding are needed, therefore, to assess the safety and reliability of pipelines during service, and to guide in the development of improved materials and protection systems.

Although a considerable amount of research has been devoted to the problems of environmentally assisted cracking in pipeline steels, most of this effort, however, has been directed to the study of stress corrosion cracking (or cracking under static loading) and of corrosion per se. For a range of reasons, quantitative understanding of the phenomenological and mechanistic aspects of environmentally assisted cracking is yet to be fully developed. Research during recent years, at Lehigh University and elsewhere, has shown that environmentally assisted cracking results from

the interaction of clean metal surfaces (produced by cracking or by deformation) with the environment, and that the very early stages (i.e., the first few milliseconds to few seconds) of reactions are responsible for the enhanced cracking. Fatigue (associated with cyclic loading from a variety of sources), being a proficient mechanical process for creating new surfaces, acting in concert with corrosion, therefore, may be a more serious failure mechanism than stress corrosion cracking.

The need to consider corrosion fatigue as a potentially significant failure mechanism in pipelines is based on the recognition that the operating pressure (or stresses) do not remain truly constant and minor fluctuations in stresses can significantly alter cracking response [1-4]. Indeed, it has been difficult to reconcile service failures and laboratory stress corrosion cracking data without allowing for the possibility for corrosion fatigue [4,5]. To properly address the problems of corrosion fatigue, it is essential to recognize the multi-faceted nature of the phenomenon which reflects the synergism of chemistry/electrochemistry, mechanics and metallurgy. The cracking response reflects both the nature and the kinetics of chemical reactions between the environment and the fresh crack surfaces, and the interactions of hydrogen that is produced by these reactions with the microstructure [6]. Significant advances in understanding and in placing corrosion fatigue analysis on a fundamentally sound and quantitative basis depends on the understanding of the mechanisms for and various processes that control corrosion fatigue.

2. PROGRAM OBJECTIVE AND SCOPE

In this part of the program, a multi-disciplinary research is being undertaken to investigate the mechanisms of corrosion fatigue crack initiation and propagation in pipeline steels exposed to aqueous environments. The program is directed at (1) the development of quantitative understanding of the early stage of chemical reactions in relation to the crack initiation and propagation, (2) elucidating the mechanisms for corrosion fatigue crack initiation and propagation, including the influences of chemical, mechanical and metallurgical variables, and

(3) the formulation and evaluation of models for predicting cracking response and service performance. A combined fracture mechanics, surface chemistry and material science approach is used.

The specific areas of research are as follows:

(1) Determination of the kinetics of passivation (viz., initial reactions) as functions of temperature, pH, ion concentration, and other factors.

(2) Determination of the kinetics of fatigue crack initiation as a function of temperature for selected environmental conditions, and correlation with the chemical data.

(3) Determination of the kinetics of fatigue crack propagation as a function of temperature for selected environmental conditions, and correlation with the chemical data.

(4) Examination of the influences of loading variables (such as cyclic load frequency, waveform, and load ratio) on corrosion fatigue crack initiation and propagation.

(5) Synthesis of chemical, mechanical and metallurgical data to develop quantitative understanding of the mechanisms for corrosion fatigue crack initiation and propagation. Formulation and verification of models for predicting cracking response and service performance.

The research program is planned for a period of three (3) years, and complements an ongoing study on the mechanisms for corrosion fatigue in high-strength steels and titanium alloys sponsored by the Office of Naval Research. Principal efforts during the first year are being directed towards the measurements of the kinetics of passivation and of the kinetics of fatigue crack growth in one electrolyte over a range of temperatures from 10°C to 90°C. Cyclic load frequencies from 10^{-2} to 10 Hz. will be used for the fatigue crack growth experiments. X-70 steel (in plate form) and 1N Na_2CO_3 - 1N $NaHCO_3$ solution are used in these initial studies. Other environments will be considered for later studies.

3. PROGRESS TO DATE

Because of the relatively late starting date of this program with respect to Lehigh's academic calendar, a suitable graduate student was assigned at the beginning of the spring semester (that is, in January,

1983). Principal effort has been directed towards the exploration and development of electrochemical measurement techniques for determining the kinetics of passivation or surface reaction of clean surfaces. Studies of the kinetics of corrosion fatigue crack growth in the X-70 steel have been initiated also. The results are summarized briefly here.

3.1 Electrochemical Measurement Techniques

Two electrochemical measurement techniques are being considered. The first one (the potential step technique) involves cathodically polarizing a "clean" surface at a suitable potential in the electrolyte of interest, suddenly switching to another potential, and monitoring the current transient under potentiostatic conditions at the new potential. The second technique, proposed by Gunchoo Shim as a part of an ONR sponsored program, measures the galvanic current between a cathodically "cleaned" surface and a surface that has been "oxidized" in the electrolyte. The current flow in each of these cases is expected to contain information on the reactions of a clean surface with the electrolyte.

Since the second technique more closely simulates the reactions at the crack tip, under open circuit conditions, further evaluation of this technique is being made (in part by Professor Wei in conjunction with his sabbatical leave at EXXON Corporate Research Laboratories during the 1982-83 academic year). The essential elements of this technique are illustrated in Fig. 1. Figure 1a illustrates the cleaning arrangement, and Fig. 1b, the measurement configuration. Evaluation of the technique was carried out using a borate solution, containing an equivolume mixture of 0.15N $Na_2B_4O_7 \cdot 10H_2O$ and 0.15N H_3BO_3 solutions, with pH = 8.8 at room temperature.

An idealized galvanic current transient is illustrated in Fig. 2. The initial rapid decay represents dissipation of charges in the Helmholtz (or double) layer formed during cathodic cleaning. The slower decay represents charge transfer associated with the surface reactions. A simple, linear relationship in log (current) versus time coordinates would suggest a simple first order reaction of the Langmuir type. A typical current transient for iron in a deaerated buffered borate

solution (pH = 8.8) at room temperature is shown in Fig. 3. With increases in test temperature, the current decay becomes more rapid and is consistent with the expected increase in the rates of reactions. It is clear, however, that the processes are much more complex.

To better understand the processes that might contribute to the galvanic current transient, experiments were carried out using only graphite electrodes. In a well-deaerated solution, the current decays rapidly, Fig. 4. This rapid decay is consistent with the expected rapid initial dissipation of the double layer. With the presence of dissolved oxygen, dissipation of the double layer is followed by a much slower current decay, Fig. 5. This slower decay is believed to result from the reduction of oxygen in solution. Other processes, such as the oxidation of iron from Fe^{2+} to Fe^{3+}, are also expected to contribute to the current flow.

Nevertheless, the results are very encouraging. Additional experiments using gold electrodes in 3% NaCl solution have been carried out to attempt to identify the various reactions. Analysis of these data are in progress. Measurements of the reactions of X-70 steel with 1N Na_2CO_3 - 1N $NaHCO_3$ solution will be made to correlate the kinetics of these reactions to corrosion fatigue crack growth response.

3.2 Fatigue Crack Growth

Fatigue crack growth experiments have been carried out on X-70 steel in distilled water, under constant-K conditions at four temperatures from about 20°C to 90°C (Fig. 6). The results clearly show the influence of test frequency and temperature on the rate of corrosion fatigue crack growth. The observed response is similar to that of HY130 steel in distilled water [6]. A stronger temperature dependence for the mechanical component of fatigue crack growth, however, is suggested by these data. Room temperature fatigue crack growth data, obtained in 1N Na_2CO_3 - 1N $NaHCO_3$ solution, are shown in Fig. 7. The result indicates no effect of frequency over the range 0.03 to 10 Hz in this environment. Additional tests at higher temperatures are in progress. The results

will be correlated with the planned electrochemical measurements to develop an understanding of corrosion fatigue crack growth response in this steel.

4. PLANNED RESEARCH

Further development and evaluation of the electrochemical measurement techniques and measurements of the kinetics of reactions of X70 steel with 1N Na_2CO_3 - 1N $NaHCO_3$ and 3.5% NaCl solutions will be made during the coming year. Corrosion fatigue crack growth experiments will be continued to assess the influences of frequency and temperature in the same solutions.

REFERENCES FOR PART II

1. R.R. Fessler and T.J. Barlo, "The Effect of Cyclic Loading on the Threshold Stress for Stress Corrosion Cracking in Mild and HSLA Steels", presented at the ASME Third National Congress on Pressure Vessel and Piping Technology, San Francisco, 1979.

2. O. Vosikovsky and R.J. Cooke, Int. J. Pres. Ves. & Piping, Vol. 6, 1978, pp. 113-129.

3. R.N. Parkins and B.S. Greenwell, Aug./Sept. Metal Science, 1977, pp. 405-413.

4. "Environmentally Induced Cracking of Natural Gas and Liquid Pipelines", Vols. 1 & 2, Final Report, Contract #DOT-OS-60519, ASL Engineering, Inc., 495 South Fairview Ave., Goleta, CA 33017, Dec. 1977.

5. "Proceedings - 5th Symposium on Line Pipe Research", American Gas Association, Cat. No. L30174, 1974.

6. R.P. Wei and Gunchoo Shim, "Fracture Mechanics and Corrosion Fatigue", in Corrosion Fatigue, ASTM STP 801, T.W. Crooker and B.N. Leis,eds., American Society for Testing and Materials, Philadelphia, Pa, 1983, pp. 5-25.

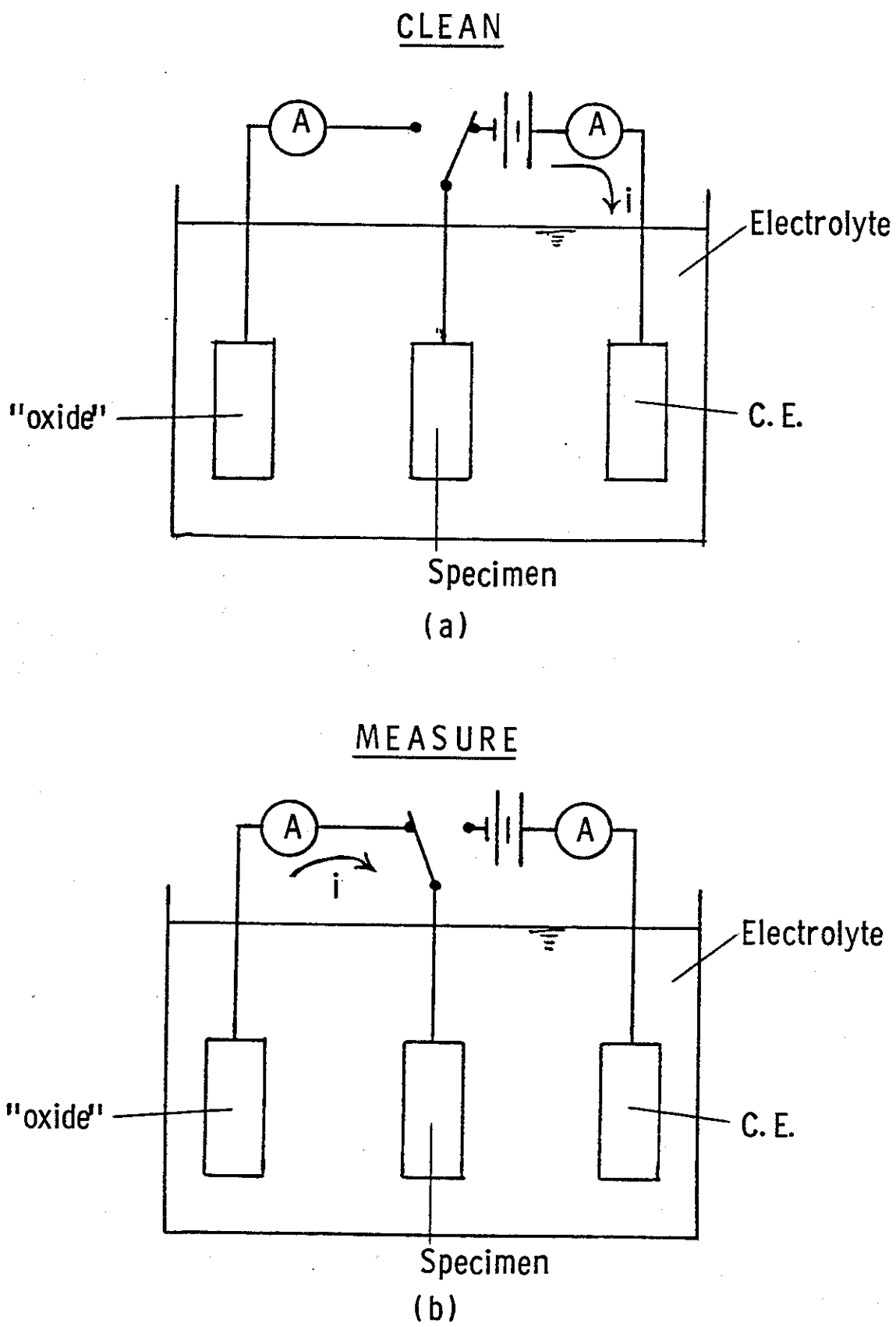

Fig. 1: Schematic illustration of technique for measuring galvanic current transient between "clean" and "oxidized" metal surfaces.

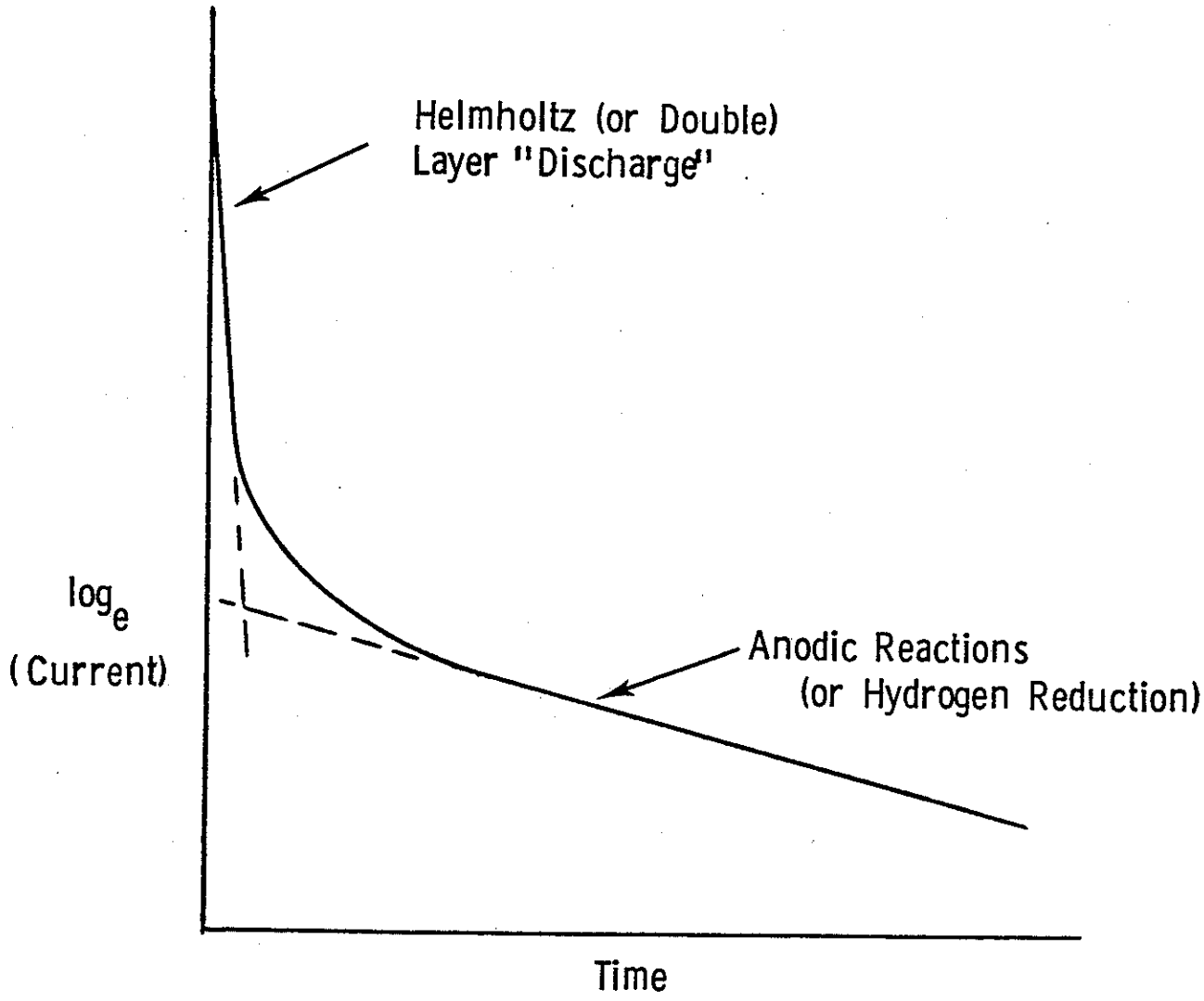

Fig. 2: Idealized galvanic current transient.

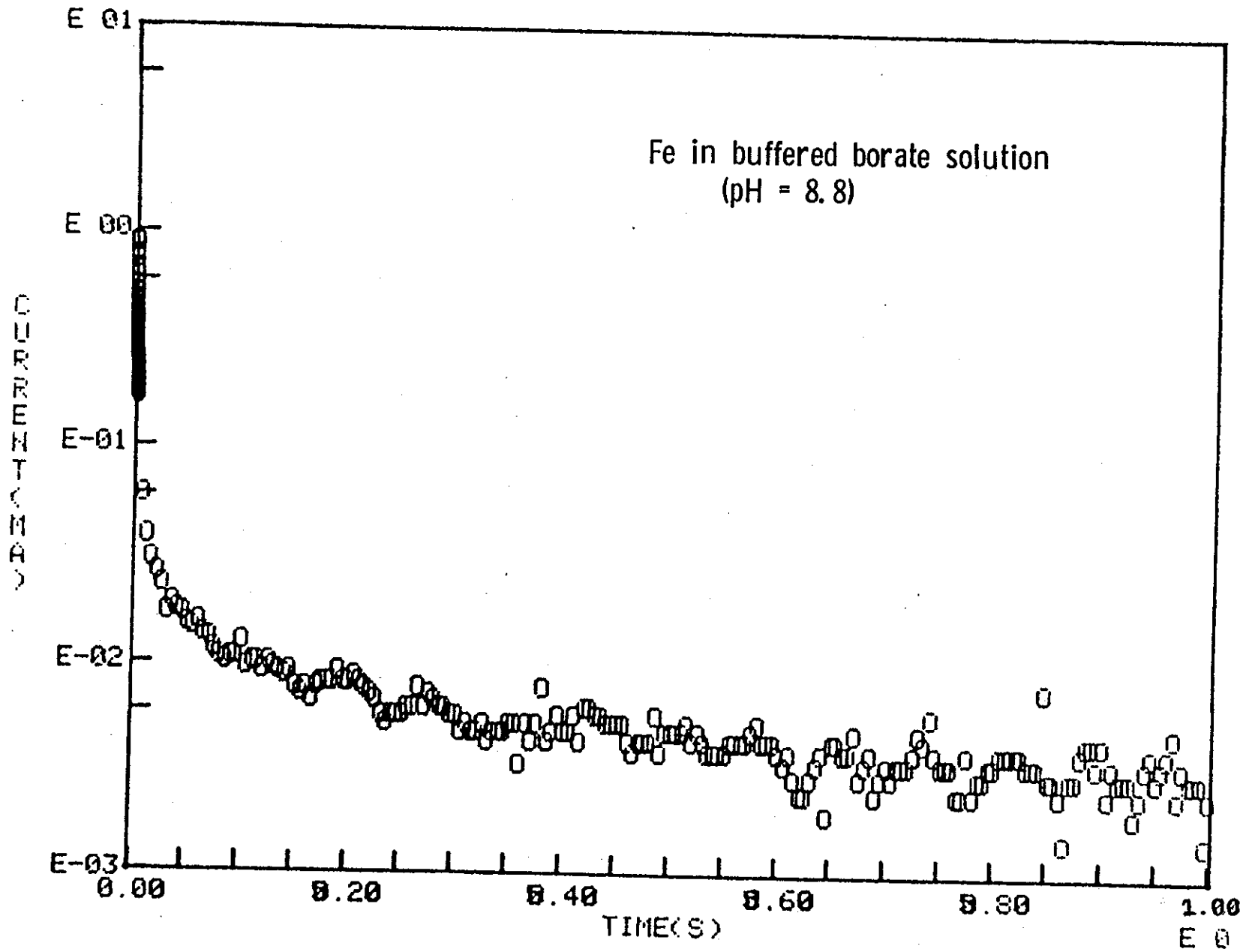

Fig. 3: Typical galvanic current transient for iron in a deaerated buffered borate solution (pH = 8.8) at room temperature.

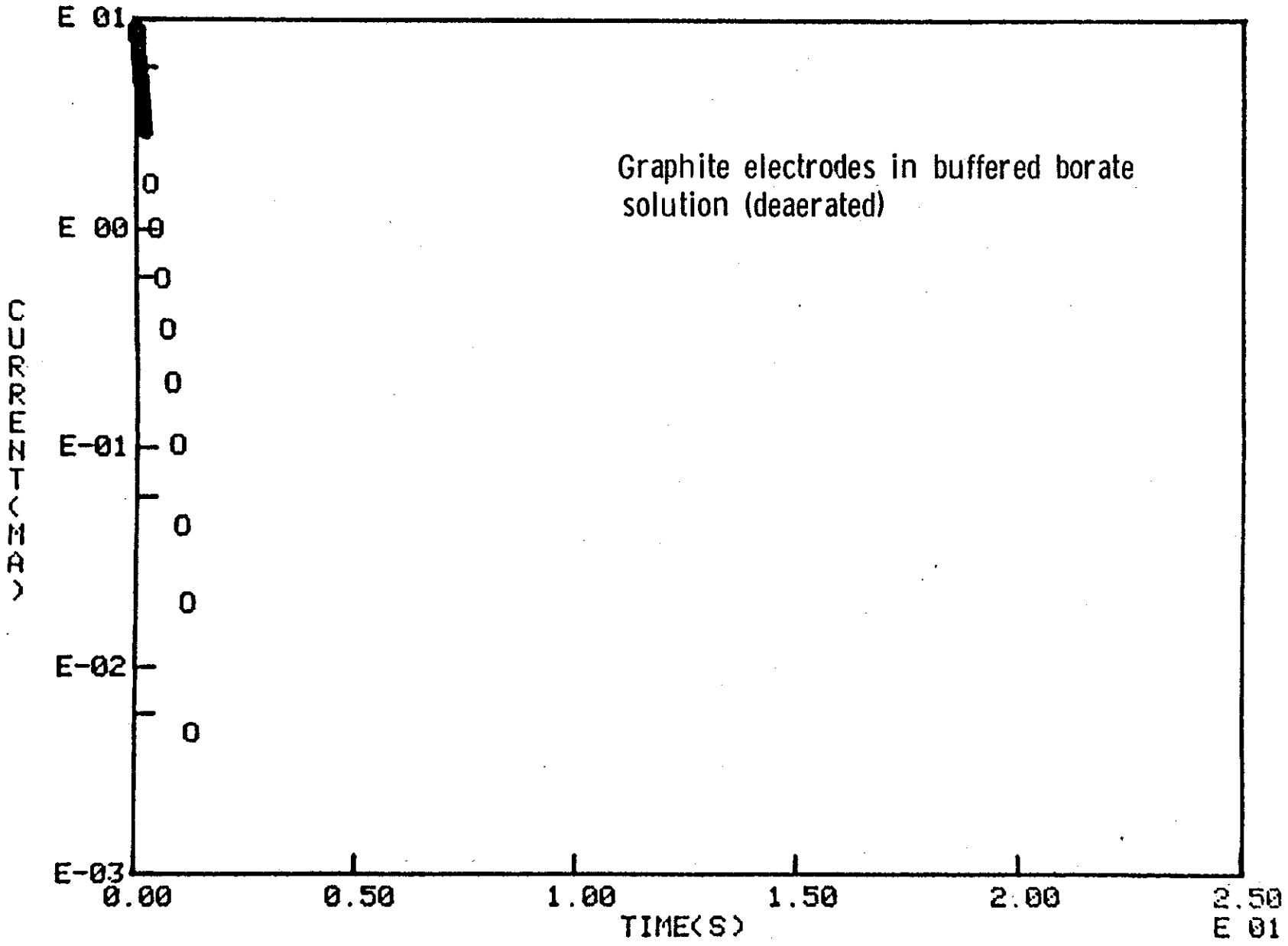

Fig. 4: Typical galvanic current transient between graphite electrode in a deaerated buffered borate solution (pH = 8.8) at room temperature. The transient is associated with dissipation of the Helmholtz (double) layer.

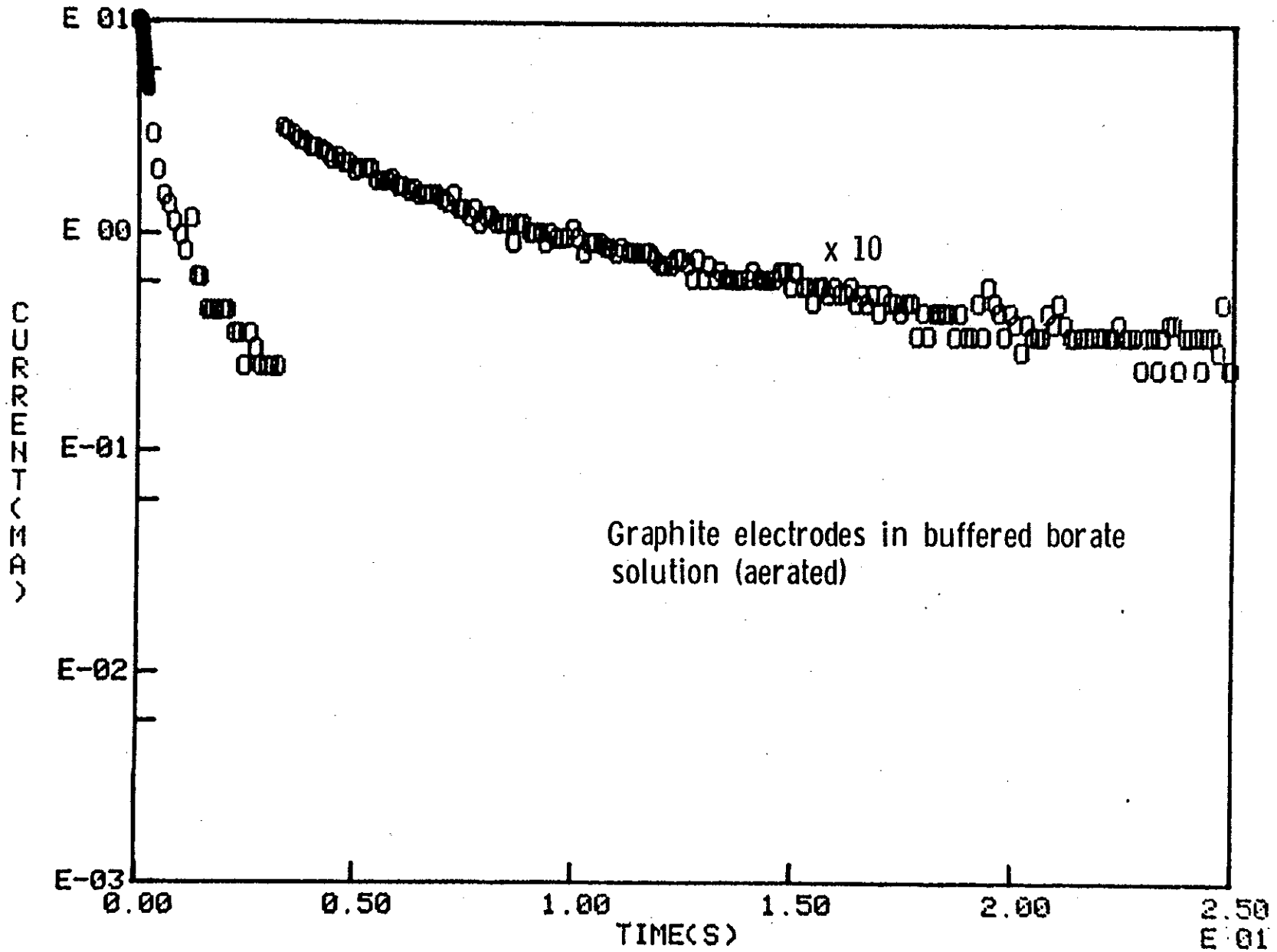

Fig. 5: Typical galvanic current transient between graphite electrode in an aerated buffered solution (pH = 8.8) at room temperature showing the effect of dissolved oxygen.

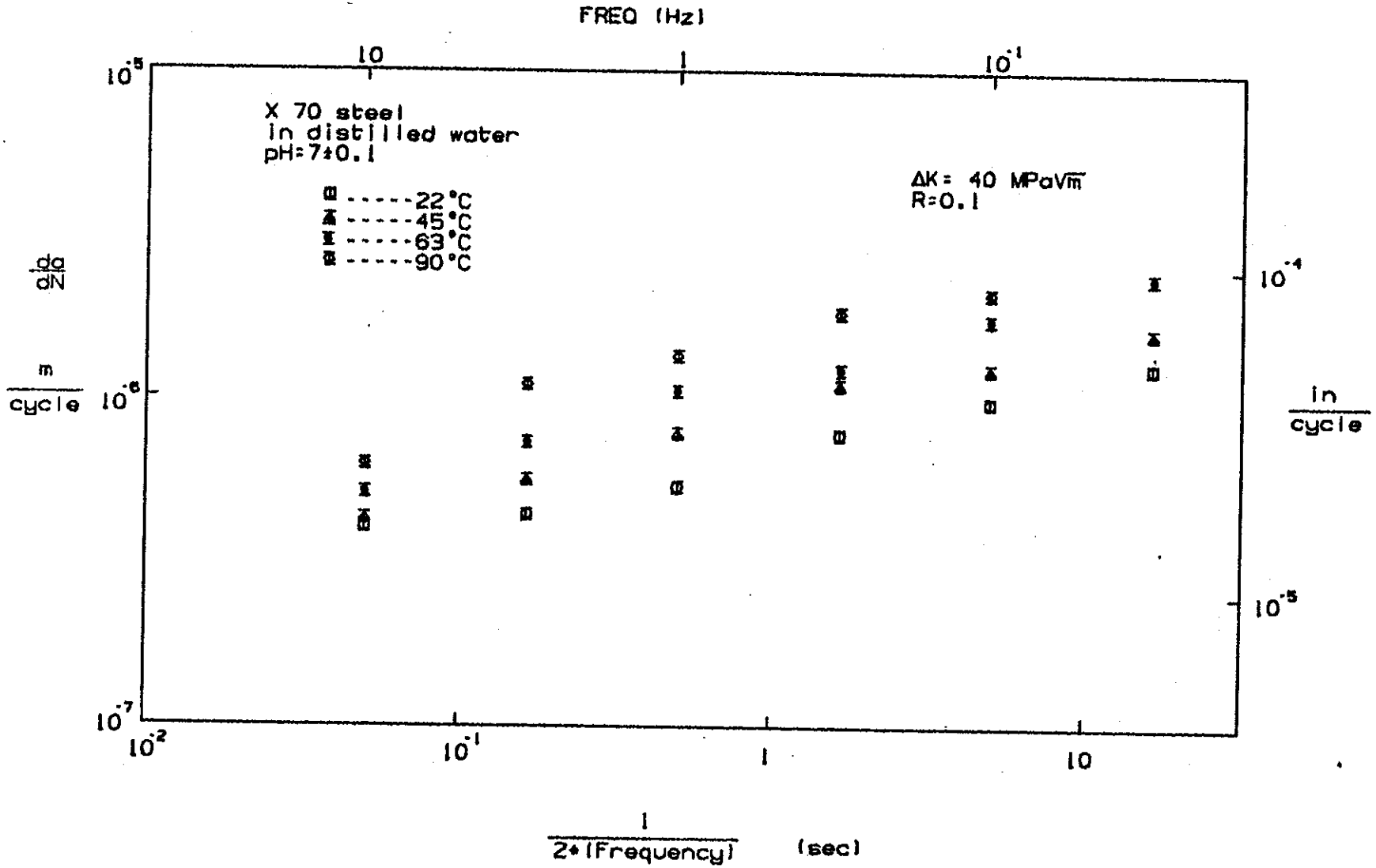

Fig. 6: The influence of frequency on fatigue crack growth for an X-70 steel plate in distilled water at different temperatures (R = 0.1).

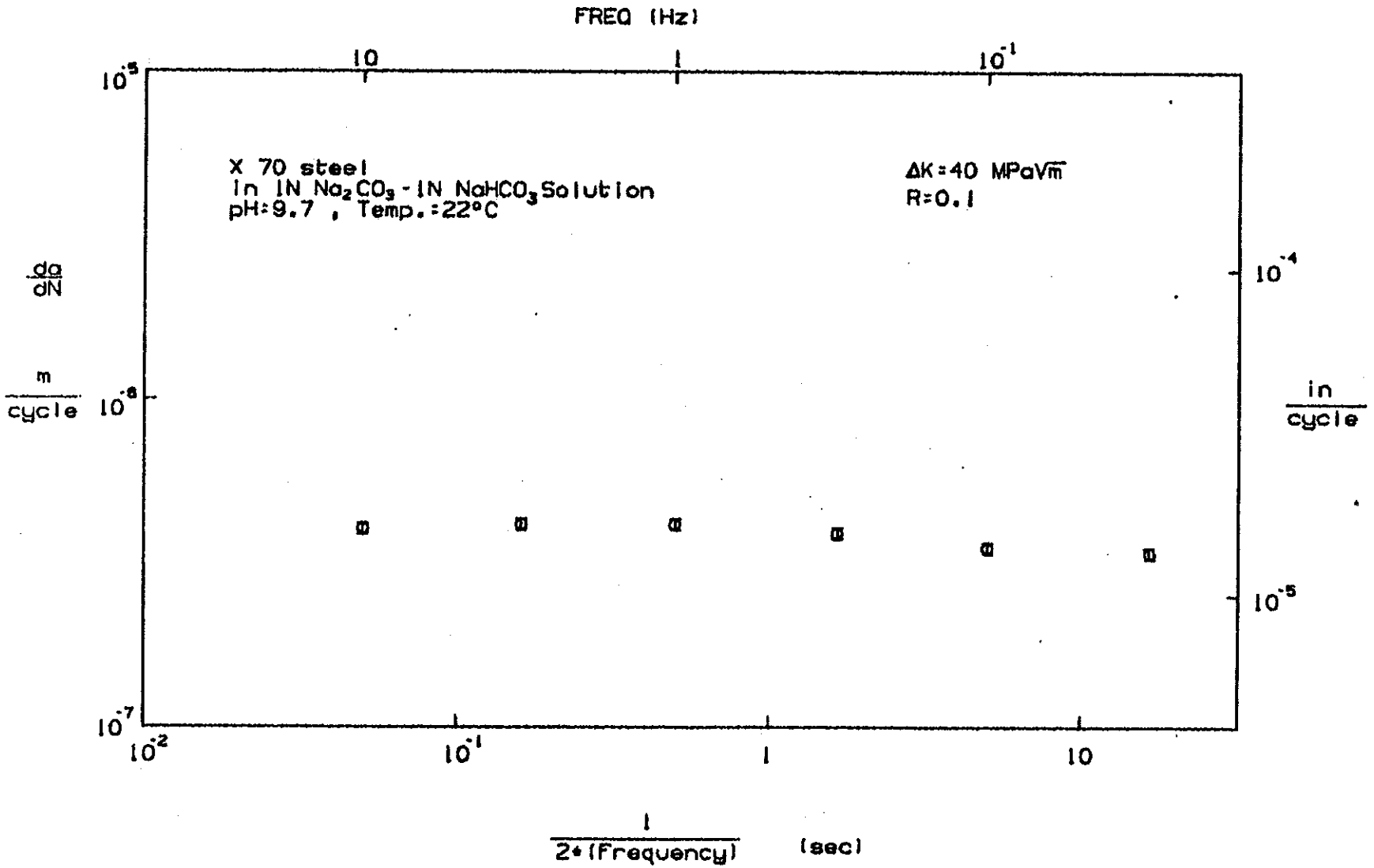

Fig. 7: The influence of frequency on fatigue crack growth for an X-70 steel plate in 1N Na_2CO_3 - 1N $NaHCO_3$ solution at room temperature (R = 0.1).

APPENDIX A

THE CRACK-INCLUSION INTERACTION PROBLEM

1. Introduction

In studying the fracture of multi-phase materials, structures composed of bonded dissimilar solids, and welded joints it is necessary to take into account the effect of the imperfections in the medium. Generally such imperfections are in the form of either geometric discontinuities or material inhomogeneities. For example, in welded joints various shapes of voids, cracks, notches and regions of lack of fusion may be mentioned as examples for the former and variety of inclusions for the latter. From the viewpoint of fracture mechanics two important classes of imperfections are the planar flaws which may be idealized as cracks and relatively thin inhomogeneities which may be idealized as flat inclusions with "sharp" boundaries. In both cases the edges of the defects are lines of stress singularity and, consequently, regions of potential crack initiation and propagation.

The technical literature on cracks, voids and inclusions which exist in the material separately is quite extensive. However, the problems concerning the interaction of cracks, voids and inclusions do not seem to be as widely studied (see, for example, [1] for the results of crack-circular inclusion or void interaction problem and for some references). In this paper the relatively simple problem of an elastic plane containing a crack and an arbitrarily oriented flat elastic inclusion is considered. Of special interest is the examination of the asymptotic stress field in the neighborhood of inclusion ends and the problems of intersecting cracks and inclusions. The basic dislocation and concentrated force solutions are used to formulate the problem [2]. Hence, the formulation can easily be extended to study problems involving multiple cracks and inclusions.

2. Integral Equations of the Problem

The geometry of the crack-inclusion interaction problem under consideration is shown in Figure 1. It is assumed that the medium is under a state of plane strain or generalized plane stress and the in-plane dimensions of the medium are large compared to the lengths of and the distance between the crack and the inclusion so that the effect of the remote boundaries on the

perturbed stress state may be neglected. Thus, the Green's functions for the concentrated forces and dislocations in an infinite plane may be used to formulate the problem. It is further assumed that the inclusion is sufficiently "thin" so that its bending stiffness may also be neglected.

Referring to Figure 1 we consider the stresses and displacements due to a pair of edge dislocations on the x axis, a pair of concentrated forces on the line θ=constant and the applied loads acting on the medium away from the crack-inclusion region. Let the subscripts d, p and a designate these three stress and deformation states, i.e., let σ_{dij}, σ_{pij} and σ_{aij}, $(i,j) = (x,y)$ or $(i,j) = (r,\theta)$, be the stress components due to dislocations, concentrated forces, and applied loads, respectively. The total stress state in the elastic plane may, therefore, be expressed as

$$\sigma_{ij}(x,y) = \sigma_{dij}(x,y) + \sigma_{pij}(x,y) + \sigma_{aij}(x,y), \quad (i,j = x,y) \tag{1}$$

Let us now assume that the dislocations are distributed along $a<x<b$, $y=0$ forming a crack. If $g(x)$ and $h(x)$ refer to the dislocation densities defined by

$$\frac{\partial}{\partial x}[u_y(x,+0) - u_y(x,-0)] = g(x) \ , \ a < x < b \ ,$$

$$\frac{\partial}{\partial x}[u_x(x,+0) - u_x(x,-0)] = h(x) \ , \ a < x < b \ , \tag{2a,b}$$

the corresponding stress components at a point (x,y) in the plane may be expressed as

$$\sigma_{dxx}(x,y) = \int_a^b [G_{xx}(x,y,t)g(t) + H_{xx}(x,y,t)h(t)]dt \ ,$$

$$\sigma_{dyy}(x,y) = \int_a^b [G_{yy}(x,y,t)g(t) + H_{yy}(x,y,t)h(t)]dt \ , \tag{3a-c}$$

$$\sigma_{dxy}(x,y) = \int_a^b [G_{xy}(x,y,t)g(t) + H_{xy}(x,y,t)h(t)]dt \ ,$$

where

$$G_{xx} = \frac{2\mu}{\pi(\kappa+1)} \cdot \frac{(t-x)[(t-x)^2 - y^2]}{[(t-x)^2 + y^2]^2} ,$$

$$G_{yy} = \frac{2\mu}{\pi(\kappa+1)} \cdot \frac{(t-x)[3y^2 + (t-x)^2]}{[(t-x)^2 + y^2]^2} ,$$

$$G_{xy} = \frac{2\mu}{\pi(\kappa+1)} \cdot \frac{y[y^2 - (t-x)^2]}{[(t-x)^2 + y^2]^2} ,$$

$$H_{xx} = \frac{2\mu}{\pi(\kappa+1)} \cdot \frac{y[y^2 + 3(t-x)^2]}{[(t-x)^2 + y^2]^2} , \qquad (4a\text{-}f)$$

$$H_{yy} = \frac{2\mu}{\pi(\kappa+1)} \cdot \frac{y[y^2 - (t-x)^2]}{[(t-x)^2 + y^2]^2} ,$$

$$H_{xy} = \frac{2\mu}{\pi(\kappa+1)} \cdot \frac{(t-x)[(t-x)^2 - y^2]}{[(t-x)^2 + y^2]^2} .$$

In (4) μ and κ are the elastic constants of the medium, μ the shear modulus, $\kappa = 3-4\nu$ for plane strain and $\kappa = (3-\nu)/(1+\nu)$ for plane stress ν being the Poisson's ratio.

Similarly, from the concentrated force solution as given, for example, in [2] the stress components $\sigma_{pij} = S_{ij}$ due to a pair of forces P_x and P_y acting at the point (x_o, y_o) may be written as

$$S_{xx}(x,y,x_o,y_o) = \frac{1}{2\pi(\kappa+1)} \frac{(A_1+A_2)P_x + (B_1+B_2)P_y}{[(x-x_o)^2 + (y-y_o)^2]^2} ,$$

$$S_{yy}(x,y,x_o,y_o) = \frac{1}{2\pi(\kappa+1)} \frac{(A_1-A_2)P_x + (B_1-B_2)P_y}{[(x-x_o)^2 + (y-y_o)^2]^2} , \qquad (5a\text{-}c)$$

$$S_{xy}(x,y,x_o,y_o) = \frac{1}{2\pi(\kappa+1)} \frac{A_3P_x + B_3P_y}{[(x-x_o)^2 + (y-y_o)^2]^2} ,$$

$$A_1 = -2(x-x_o)[(x-x_o)^2 + (y-y_o)^2]$$

$$A_2 = -\kappa(x-x_o)[(x-x_o)^2 + (y-y_o)^2] - (x-x_o)[(x-x_o)^2 - (y-y_o)^2] + 2(y-y_o)^2(x-x_o)$$

$$B_1 = -2(y-y_o)[(x-x_o)^2 + (y-y_o)^2]$$

$$B_2 = +\kappa(y-y_o)[(x-x_o)^2+ (y-y_o)^2]-(y-y_o)[(x-x_o)^2-(y-y_o)^2]-2(x-x_o)^2(y-y_o)$$

$$A_3 = -\kappa(y-y_o)[(x-x_o)^2+(y-y_o)^2]-(y-y_o)[(x-x_o)^2-(y-y_o)^2]-2(x-x_o)^2(y-y_o)$$

$$B_3 = -\kappa(x-x_o)[(x-x_o)^2+(y-y_o)^2]+(x-x_o)[(x-x_o)^2-(y-y_o)^2]-2(y-y_o)^2(x-x_o)$$

(6a-f)

If the inclusion is located along the line $c < r < d$, θ = constant, and if its bending stiffness is neglected, then the following conditions are valid:

$$u_r(r,\theta+0) = u_r(r,\theta-0),\ u_\theta(r,\theta+0) = u_\theta(r,\theta-0)\ ,$$

$$-P_\theta(r,\theta) = \sigma_{\theta\theta}(r,\theta+0) - \sigma_{\theta\theta}(r,\theta-0) = 0\ , \qquad (7a\text{-}d)$$

$$-P_r(r,\theta) = -p(r) = \sigma_{r\theta}(r,\theta+0) - \sigma_{r\theta}(r,\theta-0)\ ,\ (c<r<d).$$

Thus, to formulate the problem it is sufficient to consider only the radial component $P_r=p$ of the concentrated force. For $P_\theta=0$ and $P_r=p$ observing that

$$P_x = p\cos\theta\ ,\ P_y = p\sin\theta\ , \qquad (8a,b)$$

and substituting $x_o = r_o\cos\theta$, $y_o = r_o\sin\theta$, by using the kernels S_{ij} given by (5) the stress components σ_{pij} are found to be

$$\sigma_{pxx}(x,y) = \frac{1}{2\pi(\kappa+1)}\int_c^d \frac{(A_1'+A_2')\cos\theta+(B_1'+B_2')\sin\theta}{[(x-r_o\cos\theta)^2+(y-r_o\sin\theta)^2]^2}\,p(r_o)dr_o\ ,$$

$$\sigma_{pyy}(x,y) = \frac{1}{2\pi(\kappa+1)}\int_c^d \frac{(A_1'-A_2')\cos\theta+(B_1'-B_2')\sin\theta}{[(x-r_o\cos\theta)^2+(y-r_o\sin\theta)^2]^2}\,p(r_o)dr_o\ , \qquad (9a\text{-}c)$$

$$\sigma_{pxy}(x,y) = \frac{1}{2\pi(\kappa+1)}\int_c^d \frac{A_3'\cos\theta + B_3'\sin\theta}{[(x-r_o\cos\theta)^2+(y-r_o\sin\theta)^2]^2}\,p(r_o)dr_o\ ,$$

where the functions A_i', B_i', (i=1,2,3) are obtained from (6) by substituting $x_o = r_o\cos\theta$ and $y_o = r_o\sin\theta$, e.g.,

$$A_1'(x,y,r_o) = -2(x-r_o\cos\theta)[(x-r_o\cos\theta)^2 + (y-r_o\sin\theta)^2] \ . \qquad (10)$$

Since the stresses σ_{aij} due to the applied loads are known, from (1), (3) and (9) it is seen that once the functions g(x), h(x) and p(r) are determined the problem is solved. These unknown functions may be determined by expressing the stress boundary conditions on the crack surfaces and the displacement compatibility condition along the inclusion, namely

$$\sigma_{yy}(x,0) = \sigma_{dyy}(x,0) + \sigma_{pyy}(x,0) + \sigma_{ayy}(x,0) = 0 \ , \quad (a<x<b),$$

$$\sigma_{xy}(x,0) = \sigma_{dxy}(x,0) + \sigma_{pxy}(x,0) + \sigma_{axy}(x,0) = 0 \ , \quad (a<x<b), \qquad (11a\text{-}c)$$

$$\varepsilon_{rr}(r,\theta) = \varepsilon_{drr}(r,\theta) + \varepsilon_{prr}(r,\theta) + \varepsilon_{arr}(r,\theta) = \varepsilon_i(r), \ (c<r<d)$$

where $\varepsilon_i(r)$ is the (longitudinal) strain in the inclusion. If, for example, the stress state away from the crack inclusion region is given by σ^{∞}_{ij}, (i,j) = (x,y), then the applied quantities in (11) may be expressed as

$$\sigma_{ayy}(x,0) = \sigma^{\infty}_{yy} \ , \ \sigma_{axy}(x,0) = \sigma^{\infty}_{xy} \ ,$$

$$\varepsilon_{arr}(r,\theta) = \frac{1+\kappa}{8\mu}\left[\sigma^{\infty}_{xx}\left(\cos^2\theta - \frac{3-\kappa}{1+\kappa}\sin^2\theta\right)\right.$$

$$\left. + \sigma^{\infty}_{yy}\left(\sin^2\theta - \frac{3-\kappa}{1+\kappa}\cos^2\theta\right) + \frac{4}{1+\kappa}\sigma^{\infty}_{xy}\sin 2\theta\right] . \qquad (12a\text{-}c)$$

We now note that if p(r) is the body force acting on the elastic medium then -p(r) would be the force acting on the inclusion distributed along its length. Thus, the strain in the inclusion may be obtained as

$$\varepsilon_i(r) = -\frac{1+\kappa_s}{8\mu_s A_s}\int_r^d p(r_o)dr_o \qquad (13)$$

where μ_s and κ_s are the elastic constants, and A_s is the cross-sectional area of the inclusion corresponding to unit thickness of the medium in z-direction. From the expression of ε_{rr} given by the Hooke's law

$$\varepsilon_{rr} = \frac{1+\kappa}{8\mu}\left(\sigma_{rr} - \frac{3-\kappa}{1+\kappa}\sigma_{\theta\theta}\right) , \tag{14}$$

from (9) and the corresponding stress transformation it can be shown that

$$\varepsilon_{prr}(r,\theta) = \frac{\kappa}{2\pi(1+\kappa)\mu}\int_c^d \frac{p(r_o)}{r_o - r}\, dr_o . \tag{15}$$

Similarly, from (3), (4) and (14) we find

$$\varepsilon_{drr}(r,\theta) = \frac{1+\kappa}{8\mu}\int_a^b [G_\varepsilon(r,t)g(t) + H_\varepsilon(r,t)h(t)]dt \tag{16}$$

where

$$\begin{aligned} G_\varepsilon(r,t) = {} & \frac{2\mu}{\pi(1+\kappa)}\frac{1}{R^4}\{\cos^2\theta - \frac{3-\kappa}{1+\kappa}\sin^2\theta)(t - r\cos\theta) \times \\ & \times[(t-r\cos\theta)^2 - r^2\sin^2\theta] + (\sin^2\theta - \frac{3-\kappa}{1+\kappa}\cos^2\theta) \times \\ & \times(t-r\cos\theta)[3r^2\sin^2\theta + (t-r\cos\theta)^2] \\ & + \frac{4}{1+\kappa}\sin 2\theta\; r\sin\theta[r^2\sin^2\theta - (t-r\cos\theta)^2]\} , \end{aligned} \tag{17}$$

$$\begin{aligned} H_\varepsilon(r,t) = {} & \frac{2\mu}{\pi(1+\kappa)}\frac{1}{R^4}\{(\cos^2\theta - \frac{3-\kappa}{1+\kappa}\sin^2\theta) r\sin\theta[r^2\sin^2\theta \\ & + 3(t-r\cos\theta)^2] + (\sin^2\theta - \frac{3-\kappa}{1+\kappa}\cos^2\theta) r\sin\theta \times \\ & \times[r^2\sin^2\theta - (t-r^2\cos^2\theta)^2] + \frac{4}{1+\kappa}\sin 2\theta \times \\ & \times(t-r\cos\theta)[(t-r\cos\theta)^2 - r^2\sin^2\theta] , \end{aligned} \tag{18}$$

$$R^2 = (t - r\cos\theta)^2 + r^2\sin^2\theta \quad . \tag{19}$$

Finally, by substituting from (3), (4), (9), (12), (13), (15) and (16) into (11), the integral equations of the problem may be obtained as follows:

$$\frac{1}{\pi}\int_a^b \frac{g(t)dt}{t-x} + \frac{1}{4\pi\mu}\int_c^d \frac{(A_1'-A_2')\cos\theta+(B_1'-B_2')\sin\theta}{[(x-r_o\cos\theta)^2+(r_o\sin\theta)^2]^2}\, p(r_o)dr_o = -\frac{1+\kappa}{2\mu}\sigma_{yy}^{\infty} ,$$

$$(a<x<b) ,$$

$$\frac{1}{\pi}\int_a^b \frac{h(t)dt}{t-x} + \frac{1}{4\pi\mu}\int_c^d \frac{(A_3'\cos\theta+B_3'\sin\theta)p(r_o)}{[(x-r_o\cos\theta)^2+(r_o\sin\theta)^2]^2}\, dr_o = -\frac{1+\kappa}{2\mu}\sigma_{xy}^{\infty} ,$$

$$(a<x<b) ,$$

$$\frac{c_o}{\pi}\int_a^b G_\varepsilon(r,t)g(t)dt + \frac{c_o}{\pi}\int_a^b H_\varepsilon(r,t)h(t)dt + \frac{1}{\pi}\int_c^d \frac{p(r_o)}{r_o-r}\, dr_o$$

$$+ \frac{\gamma c_o}{\pi}\int_c^d H(r_o-r)p(r_o)dr_o = -\frac{c_o}{\pi}[(\cos^2\theta - \frac{3-\kappa}{1+\kappa}\sin^2\theta)\sigma_{xx}^{\infty}$$

$$+ (\sin^2\theta - \frac{3-\kappa}{1+\kappa}\cos^2\theta)\sigma_{yy}^{\infty} + \frac{4}{1+\kappa}\sigma_{xy}^{\infty}\sin 2\theta], \quad (c<r<d) , \qquad (20a\text{-}c)$$

where

$$c_o = \frac{\pi(1+\kappa)^2}{4\kappa} , \quad \gamma = \frac{\mu(1+\kappa_s)}{A_s\mu_s(1+\kappa)} . \qquad (21a,b)$$

From the definition of g and h given by (2) it follows that

$$\int_a^b g(t)dt = 0 , \quad \int_a^b h(t)dt = 0 . \qquad (22a,b)$$

Also, the static equilibrium of the inclusion requires that

$$\int_c^d p(r)dr = 0 . \qquad (23)$$

Thus, the system of singular integral equations must be solved under the conditions (22) and (23). From the function-theoretic examination of the integral equations (20) it can be shown that the unknown functions g, h and p are of the following form [2]:

$$g(t) = \frac{F_1(t)}{(b-t)^{\frac{1}{2}}(t-a)^{\frac{1}{2}}} , \quad h(t) = \frac{F_2(t)}{(b-t)^{\frac{1}{2}}(t-a)^{\frac{1}{2}}} , \quad p(r) = \frac{F_3(r)}{(d-r)^{\frac{1}{2}}(r-c)^{\frac{1}{2}}} ,$$

(24a-c)

where F_1, F_2 and F_3 are bounded functions. The solution of (20) subject to (22) and (23) may easily be obtained by using the numerical method described in [3].

3. Stress Singularities

After solving (20) the Modes I and II stress intensity factors k_1 and k_2 at the crack tips x=a and x=b, y=0 which are defined by

$$k_1(a) = \lim_{x\to a} \sqrt{2(a-x)}\, \sigma_{yy}(x,0) , \quad k_1(b) = \lim_{x\to b} \sqrt{2(x-b)}\, \sigma_{yy}(x,0) ,$$

$$k_2(a) = \lim_{x\to a} \sqrt{2(a-x)}\, \sigma_{xy}(x,0) , \quad k_2(b) = \lim_{x\to b} \sqrt{2(x-b)}\, \sigma_{xy}(x,0) ,$$

(25a-d)

may be obtained as follows:

$$k_1(a) = \frac{2\mu}{1+\kappa} \lim_{x\to a} \sqrt{2(x-a)}\, g(x) , \quad k_1(b) = -\frac{2\mu}{1+\kappa} \lim_{x\to b} \sqrt{2(b-x)}\, g(x) ,$$

$$k_2(a) = \frac{2\mu}{1+\kappa} \lim_{x\to a} \sqrt{2(x-a)}\, h(x) , \quad k_2(b) = -\frac{2\mu}{1+\kappa} \lim_{x\to b} \sqrt{2(b-x)}\, h(x) .$$

(26a-d)

The constants k_1 and k_2 are related to the asymptotic stress fields near the crack tips through the well-known expressions (see, for example, [4] and [5]). However, not so well-known is the asymptotic behavior of the stress fields near the inclusions having sharp edges. From (24c) and (7d) it is seen that the shear stress $\sigma_{r\theta}$ has a square-root singularity at the

tip of the inclusion. However, if one is interested in crack initiation around such singular points, one needs to know the direction and the magnitude of the maximum local cleavage stress. This, in turn, requires the investigation of the complete asymptotic stress field near the singular points. By using the basic form of the solution of the related density functions given by (24) and going back to the original stress expressions, the asymptotic stress fields may be developed by following the general techniques described in, for example, [6] or [7].

In an elastic medium containing an elastic line inclusion under plane strain or generalized plane stress conditions, the asymptotic analysis gives the near tip stress field as follows [7](*):

$$\sigma_{yy}(r,\theta) \cong \frac{k_1}{\sqrt{2r}} \cos\frac{\theta}{2} ,$$

$$\sigma_{xx}(r,\theta) \cong -\frac{3+\kappa}{\kappa-1} \frac{k_1}{\sqrt{2r}} \cos\frac{\theta}{2} ,$$

$$\sigma_{xy}(r,\theta) \cong -\frac{\kappa+1}{\kappa-1} \frac{k_1}{\sqrt{2r}} \sin\frac{\theta}{2} , \qquad (27a\text{-}c)$$

where x,y and r,θ are the standard rectangular and polar coordinates, the origin of coordinate axes is at the inclusion tip and the inclusion lies along the negative x axis or along $\theta=\pi$, $r>0$. Equations (27) suggest that similar to crack problems one may define a (Mode I) "stress intensity factor" in terms of the (tensile) cleavage stress as follows:

$$k_1 = \lim_{r\to 0} \sqrt{2r}\, \sigma_{yy}(r,0) . \qquad (28)$$

From (7) by observing that (at the right end of the inclusion)

$$\sigma_{xy}(r,+\pi) - \sigma_{xy}(r,-\pi) = -p(r) , \qquad (29)$$

(*) Note the misprints in (4.6) of [7].

in terms of the function $p(x)$ k_1 may be expressed as

$$k_1 = -\lim_{r\to 0} \frac{1}{2}\frac{\kappa-1}{\kappa+1}\sqrt{2r}\, p(r) \ . \tag{30}$$

It should be noted that in the case of flexible elastic line inclusions there is no antisymmetric singular stress field. For example, in a plane under pure shear (σ^{∞}_{xy}) parallel to the inclusion, the perturbed stress field is zero. Physically this of course follows from the fact that the normal strain (ε_{xx}) parallel to the plane of shear is zero.

Similarly, for a rigid line inclusion (i.e., for an inclusion having infinite bending as well as tensile stiffness) it can be shown that for small values of r the asymptotic stress field is given by

$$\sigma_{yy}(r,\theta) \cong \frac{1}{\sqrt{2r}}\left(k_1 \cos\frac{\theta}{2} + \frac{\kappa+1}{\kappa-1} k_2 \sin\frac{\theta}{2}\right) ,$$

$$\sigma_{xx}(r,\theta) \cong \frac{1}{\sqrt{2r}}\left(-\frac{3+\kappa}{\kappa-1} k_1 \cos\frac{\theta}{2} + \frac{3-\kappa}{\kappa-1} k_2 \sin\frac{\theta}{2}\right) , \tag{31a-c}$$

$$\sigma_{xy}(r,\theta) \cong \frac{1}{\sqrt{2r}}\left(-\frac{\kappa+1}{\kappa-1} k_1 \sin\frac{\theta}{2} + k_2 \cos\frac{\theta}{2}\right) \ .$$

Again, the stress intensity factors k_1 and k_2 are defined in terms of the tensile and shear cleavage stresses at $\theta=0$ plane as follows:

$$k_1 = \lim_{r\to 0} \sqrt{2r}\, \sigma_{yy}(r,0) \ , \ k_2 = \lim_{r\to 0} \sqrt{2r}\, \sigma_{xy}(r,0) \ . \tag{32a,b}$$

As in the crack problems, the antiplane shear component of the asymptotic stress field around flat elastic and rigid inclusions is uncoupled. Defining a Mode III stress intensity factor by

$$k_3 = \lim_{r\to 0} \sqrt{2r}\, \sigma_{xz}(r,0) \ , \tag{33}$$

the asymptotic stress field may be expressed as

$$\sigma_{xz}(r,\theta) \cong \frac{k_3}{\sqrt{2r}} \cos\frac{\theta}{2} ,$$

$$\sigma_{yz}(r,\theta) \cong \frac{k_3}{\sqrt{2r}} \sin\frac{\theta}{2} , \qquad (34a,b)$$

where again the inclusion lies along $\theta=\pi$ plane(*).

4. Crack-Inclusion Intersection

Analytically as well as from a practical viewpoint intersection of cracks and inclusions presents some interesting problems. In these problems the point of intersection is a point of irregular singularity with a power other than 1/2. Even though the general intersection problems for an arbitrary value of θ may be treated in a relatively straightforward manner, in this paper only some special cases will be considered.

4.1 The case of $\theta = \frac{\pi}{2}$, a = 0, c = 0

In this case the system of singular integral equations (20) becomes

$$\frac{1}{\pi}\int_0^b \frac{g(t)}{t-x}\,dt + \frac{1}{\pi}\int_0^d \left[\frac{c_1 t}{x^2+t^2} - \frac{c_2 t x^2}{(x^2+t^2)^2}\right]p(t)dt = f_1(x) , \quad (0<x<b) ,$$

$$\frac{1}{\pi}\int_0^b \frac{h(t)}{t-x}\,dt + \frac{1}{\pi}\int_0^d \left[\frac{c_2 x^3}{(x^2+t^2)^2} - \frac{c_1 x}{x^2+t^2}\right]p(t)dt = f_2(x) , \quad (0<x<b) ,$$

(*) Note that in this case if the remote stress is decomposed into σ^{∞}_{xz} and σ^{∞}_{yz}, the perturbed stress field due to σ^{∞}_{yz} would be zero. For the cleavage plane θ the shear cleavage stress may be written as $\sigma_{\theta_0}(r,\theta)=\sigma_{xz}\sin\theta-\sigma_{yz}\cos\theta= -(k_3/\sqrt{2r})\sin(\theta/2)$, $\theta_0 = \theta+\pi/2$, indicating that $\theta=\mp\pi/2$ is the maximum cleavage planes.

$$\frac{1}{\pi}\int_0^b \left[\frac{c_3 t}{t^2+r^2} + \frac{c_4 t r^2}{(t^2+r^2)^2}\right] g(t)dt + \frac{1}{\pi}\int_0^b \left[\frac{c_3 r}{t^2+r^2} - \frac{c_4 r t^2}{(t^2+r^2)^2}\right] h(t)dt$$

$$+ \frac{1}{\pi}\int_0^d \frac{p(t)}{t-r}\,dt + \frac{c_5}{\pi}\int_0^d H(t-r)p(t)dt = f_3(r)\ ,\ (0<r<d), \qquad (35a\text{-}c)$$

where

$$c_1 = \frac{3+\kappa}{4\mu}\ ,\ c_2 = \frac{1}{\mu}\ ,\ c_3 = \frac{\mu(\kappa-1)}{\kappa}\ ,$$

$$c_4 = \frac{4\mu}{\kappa}\ ,\ c_5 = \frac{\pi(1+\kappa)(1+\kappa_s)\mu}{4A_s\kappa\mu_s}\ , \qquad (36)$$

and f_1, f_2 and f_3 are known input functions (see, for example, the right hand side of (20)). Note that aside from the simple Cauchy kernels, (35) has kernels which become unbounded as the variables (t,x,r) approach the point of irregular singularity (x=0=t=r). Thus, defining the unknown functions by

$$g(t) = \frac{F_1(t)}{t^\alpha(b-t)^{\beta_1}}\ ,\ h(t) = \frac{F_2(t)}{t^\alpha(b-t)^{\beta_2}}\ ,\ p(t) = \frac{F_3(t)}{t^\alpha(c-t)^{\beta_3}}\ ,$$

$$0<\mathrm{Re}(\alpha,\beta_k)<1,\ (k=1,2,3)\ , \qquad (37a\text{-}c)$$

and by using the function-theoretic technique described in [3], the characteristic equations for β_1, β_2, β_3 and α may be obtained as follows:

$$\cot\pi\beta_k = 0\ ,\ (k = 1,2,3) \qquad (38)$$

$$b_1\cos^2\pi\alpha - (b_2+8\alpha-b_3\alpha^2)\cos^2\frac{\pi\alpha}{2}$$

$$-(b_4-b_5\alpha+b_3\alpha^2)\sin^2\frac{\pi\alpha}{2} = 0\ , \qquad (39)$$

where

$$b_1 = 8\kappa/(1+\kappa)\ ,\ b_2 = 2(3+\kappa)(\kappa-1)/(\kappa+1)\ ,$$
$$b_3 = 8/(\kappa+1)\ ,\ b_4 = 2(3-\kappa)\ ,\ b_5 = 16/(1+\kappa)\ . \qquad (40)$$

Note that the properties of the inclusion (as expressed by the constant c_5 in (36)) enter the integral equations (35) only through a Fredholm kernel and, therefore, have no influence on the singular behavior of the solution, and α is dependent on κ or on the Poisson's ratio of the medium only. From (38) it is seen that the acceptable roots are $\beta_k = 0.5$, (k = 1,2,3). The numerical examination of (39) indicates that in this special case of $\theta = \frac{\pi}{2}$ we have $0.5<\alpha<1$, meaning that the stress state at r=0=x has a stronger singularity than the conventional crack tip singularity of $1/\sqrt{r}$. This may be due to the fact that in this problem two singular stress fields are combined at r=0. Also, it turns out that for $0<\nu\leq 5$ the characteristic equation (39) has two roots in $0<\mathrm{Re}(\alpha)<1$ and both are real. These roots are given in Table 1 for various values of the Poisson's ratio.

Table 1. Powers of stress singularity α for a crack and an inclusion: a = 0, c = 0, $\theta = \pi/2$ (Fig. 1).

ν	plane strain		plane stress	
	α_1	α_2	α_1	α_2
0.0	0.63627093	0	0.63627093	0
0.1	0.64489401	0.09571474	0.64408581	0.08990596
0.2	0.65405762	0.14825371	0.65095281	0.13249000
0.3	0.66352760	0.18953334	0.65695651	0.16176440
0.4	0.67270080	0.22567265	0.66217253	0.18404447
0.5	0.67996342	0.26027940	0.66666667	0.20196313

The stress intensity factors at the crack tip x=b, y=0 and at the end of the inclusion x=0, y=d may be obtained by using the relations (26) and (30). At the singular point x=0, y=0 the following useful stress intensity factors are defined;

$$k_1(0) = \lim_{x\to -0} \sqrt{2}\, x^{\alpha}\, \sigma_{yy}(-0,0) \ ,$$

$$k_2(0) = \lim_{x\to -0} \sqrt{2}\, x^{\alpha}\, \sigma_{xy}(-0,0) \ , \qquad (41a,b)$$

for the crack, and

$$k_1(0) = \lim_{y\to +0} \frac{\sqrt{2}}{2}\, y^{\alpha}\, p(0,+0) \qquad (42)$$

for the inclusion.

4.2 The Special Case of $\theta = \frac{\pi}{2}$, $c = -d$, $a = 0$.

In this case the problem is further simplified by assuming "symmetric" external loads (for example, $\sigma_{xy}^{\infty}=0$ in (20)). Thus, the plane of the crack is a plane of symmetry, $h(x) = 0$, and (20) would reduce to

$$\frac{1}{\pi}\int_0^b \frac{g(t)}{t-x}\,dt + \frac{2}{\pi}\int_0^d \left[\frac{c_1 t}{t^2+x^2} - \frac{c_2 t x^2}{(t^2+x^2)^2}\right]p(t)dt = f_1(x), \ (0<x<b) \ ,$$

$$\frac{1}{\pi}\int_0^b \left[\frac{c_3 t}{t^2+y^2} + \frac{c_4 t y^2}{(t^2+y^2)^2}\right]g(t)dt + \frac{1}{\pi}\int_0^d \left[\frac{1}{t-y} + \frac{1}{t+y}\right.$$

$$\left. + c_5 H(t-y)\right]p(t)dt = f_3(y) \ , \ (0<y<d) \ , \qquad (43a,b)$$

where, again the input functions f_1 and f_3 are known and, for example, are given in (20) (with $\sigma_{xy}^{\infty} = 0$) and the constants $c_1,\ldots,c_5$ are defined by (36).

By defining

$$g(t) = \frac{G_1(t)}{t^{\alpha}(b-t)^{\beta_1}} \ , \ p(t) = \frac{G_2(t)}{t^{\alpha}(d-t)^{\beta_2}} \ , \ 0<\mathrm{Re}(\alpha,\beta_1,\beta_2)<1 \qquad (44)$$

from (43) it may be shown that

$$\cot\beta_k = 0 \ , \ (k=1,2) \ , \qquad (45)$$

$$\cos\pi\alpha-(c_3 + \frac{1}{2} c_4\alpha)(c_1 - \frac{1}{2} c_2\alpha) = 0 . \qquad (46)$$

From (45) it is seen that $\beta_k = 0.5$. A close examination of (46) shows that it has only one root for which $0<Re(\alpha)<1$. Furthermore, this root turns out to be real and highly dependent on the Poisson's ratio (see Table 2). The characteristic equation (46) and the roots given in Table 2 are identical to those found in [8] where an infinitely long stringer in cracked plate was considered.

Table 2. Power of stress singularity α at the crack-inclusion intersection for $\theta=\pi/2$, $c=-d$, $a=0$ and for symmetric loading.

ν	α	
	plane strain	plane stress
0	0	0
0.1	0.10964561	0.10263043
0.2	0.17432137	0.15468088
0.3	0.22678790	0.19132495
0.4	0.27392547	0.21972274
0.5	0.31955800	0.24288552

In this problem, too, the stress intensity factors for the crack and the inclusion may be defined as in (41) and (42).

4.3 The Special Case of $\theta=\pi$, $a=0$, $c=0$

In this case the crack and the inclusion are on the x axis and occupy $(y=0, 0<x<b)$ and $(y=0, -d<x<0)$, respectively. Restricting our attention again to the symmetric loading for which $h(x) = 0$ and observing that for the variables along the inclusion $r = -x$, $r_o = -t$, $p(r_o) = -p_x(t)$, the integral equations of the problem may be expressed as

$$\frac{1}{\pi}\int_0^b \frac{g(t)}{t-x}\,dt - \frac{1}{\pi}\frac{\kappa-1}{4\mu}\int_{-d}^0 \frac{p_x(t)}{t-x}\,dt = f_1(x)\ ,\ (0<x<b)$$

$$\frac{c_3}{\pi}\int_0^b \frac{g(t)}{t-x}\,dt + \frac{1}{\pi}\int_{-d}^0 \frac{p_x(t)}{t-x}\,dt - \frac{c_5}{\pi}\int_{-d}^x p_x(t)dt = f_3(x),\ (-d<x<0) \qquad (47a,b)$$

where the constants c_3 and c_5 are defined by (36) and the known functions f_1 and f_3 are given by the right hand sides of (20a) and (20c) (with $\sigma_{xy}^{\infty}=0$). If we now let

$$g(t) = \frac{H_1(t)}{t^{\alpha}(b-t)^{\beta_1}}\ ,\ p_x(t) = \frac{H_2(t)}{(-t)^{\alpha}(t+d)^{\beta_2}}\ ,\ 0<\mathrm{Re}(\alpha,\beta_1,\beta_2)<1\ , \qquad (48)$$

from (47) the characteristic equations for α, β_1 and β_2 may be obtained as follows:

$$\cot\pi\beta_k = 0\ ,\ (k = 1,2)\ , \qquad (49)$$

$$\cos 2\pi\alpha = -\left(\frac{\kappa-1}{2\sqrt{\kappa}}\right)^2\ . \qquad (50)$$

Equation (49) again gives $\beta_1 = \beta_2 = 0.5$. From (50) it may easily be seen that α is complex and its value for which $0<\mathrm{Re}(\alpha)<1$ is found to be

$$\alpha = \frac{1}{2} + i\left(\frac{\log\kappa}{2\pi}\right)\ . \qquad (51)$$

This value of α turns out to be identical to the power of singularity for a perfectly rough rigid stamp with a sharp corner pressed against an elastic half plane having κ as an elastic constant [2] (e.g., $\kappa = 3-4\nu$ for the plane strain case). At first this result may be somewhat unexpected. However, upon closer examination of the problem first, from (47b) it may be seen that the elasticity of the inclusion (i.e., the term containing the constant c_5) has no effect on the nature of the stress singularity. Thus, if one assumes the inclusion to be inextensible, for the symmetric problem under consideration it can be shown that the conditions in the neighborhood of the

crack tip x=0, y=0, for example, for y<0, are identical to the conditions around the corner of the stamp in the elastic half plane occupying y<0. It, therefore, appears that for the elastic inclusion collinear with a crack, the stress state around the common end point would have the standard complex singularity found in the rigid stamp problem.

5. The Results

The crack-inclusion problem described in previous sections is solved for a uniform stress state σ_{ij}^{∞}, (i,j=x,y), away from the crack-inclusion region. For simplicity the results are obtained by assuming one stress component (σ_{xx}^{∞} or σ_{yy}^{∞} or σ_{xy}^{∞}) to be nonzero at a time. The solution for a more general loading may then be obtained by superposition. Even though the stress state everywhere in the plane can be calculated after solving the integral equations (e.g., (20)) and determining the density functions g, h, and p, only the stress intensity factors are given in this section. For nonintersecting cracks and inclusions the stress intensity factors defined by (26) and (28) are normalized as follows:

$$k_i'(x_j) = \frac{k_i(x_j)}{\sigma_a^{\infty}\sqrt{(b-a)/2}} \quad , \quad (i=(1,2);\ x_j=(a,b);\ \sigma_a^{\infty}=(\sigma_{yy}^{\infty},\sigma_{xx}^{\infty},\sigma_{xy}^{\infty})), \tag{52}$$

for the crack and

$$k_1'(r_j) = \frac{k_1(r_j)}{k_o} \ , \ k_o = \frac{1-\kappa}{2(1+\kappa)}\ \sigma_a^{\infty}\ \sqrt{(d-c)/2} \ ,$$

$$(r_j = (c,d) \ , \ \sigma_a^{\infty} = (\sigma_{yy}^{\infty},\ \sigma_{xx}^{\infty},\ \sigma_{xy}^{\infty})) \tag{53}$$

for the inclusion.

Referring to Figure 1, for c=a, d=b, and (b/a)=5 the effect of the angle θ on the stress intensity factors is shown in Table 3. These results are given for two values of the stiffness parameter γ defined by (21), namely γ=0 (the inextensible inclusion) and γ=10.

Table 3. Normalized stress intensity factors in a plane containing a crack and an inclusion subjected to a uniform stress state σ^{∞}_{ij} away from the crack-inclusion region (c=a,d=b,a=b/5,Fig. 1).

γ	k'	θ						
		1°	30°	60°	90°	120°	150°	180°
		(a) $\sigma^{\infty}_{yy} \neq 0$, $\sigma^{\infty}_{xx} = 0$, $\sigma^{\infty}_{xy} = 0$						
0	$k'_1(a)$	.8905	1.0083	1.0298	1.0049	.9912	1.0001	1.0076
	$k'_2(a)$	-.2152	-.0098	-.0661	-.0830	-.0367	.0004	.0000
	$k'_1(b)$	1.0221	.9967	.9570	.9617	.9857	1.0001	1.0033
	$k'_2(b)$	.4327	-.0065	-.0002	.0007	-.0001	.0001	.0000
	$k'_1(c)$	.9570	-.3273	-1.1324	-1.3970	-.8879	-.0310	.3850
	$k'_1(d)$	.8012	.1552	-.6989	-1.1134	-.7336	.0428	.4320
10	$k'_1(a)$	.9691	.9999	1.0016	.9988	.9978	1.0000	1.0014
	$k'_2(a)$	-.0517	-.0047	-.0136	-.0153	-.0066	.0001	.0000
	$k'_1(b)$	.9862	.9997	.9919	.9928	.9973	1.0000	1.0006
	$k'_2(b)$	.0742	-.0020	.0001	.0005	.0002	.0000	.0000
	$k'_1(c)$	.2619	-.1277	-.3979	-.4735	-.2989	-.0220	.1106
	$k'_1(d)$	-.0269	.1001	-.1848	-.3269	-.2177	.0171	.1354
		(b) $\sigma^{\infty}_{xx} \neq 0$, $\sigma^{\infty}_{yy} = 0$, $\sigma^{\infty}_{xy} = 0$						
0	$k'_1(a)$	.1237	.0704	-.0034	-.0034	.0008	-.0117	-.0203
	$k'_2(a)$	.2355	.0122	.0052	.0310	.0036	-.0161	.0000
	$k'_1(b)$	-.0806	-.0365	.0036	.0142	.0014	-.0072	-.0086
	$k'_2(b)$	-.5321	-.0140	.0001	.0001	.0000	-.0003	.0000
	$k'_1(c)$	-1.1068	-.6949	.0766	.4620	.0774	-.6988	-1.0877
	$k'_1(d)$	-1.4785	-.6941	.0772	.4644	.0776	-.6994	-.0884
10	$k'_1(a)$	.0385	.0106	-.0005	-.0001	.0002	-.0023	-.0038
	$k'_2(a)$	.0587	.0004	.0010	.0056	.0006	.0029	.0000
	$k'_1(b)$	-.0252	-.0068	.0007	.0026	.0003	-.0013	-.0016
	$k'_2(b)$	-.1128	-.0030	.0000	.0000	.0000	.0000	.0000
	$k'_1(c)$	-.3440	-.2152	.0239	.1432	.0239	-.2151	-.3346
	$k'_1(d)$	-.3885	-.2154	.0239	.1434	.0239	-.2151	-.3347

Table 3 - cont.

γ	k'	θ						
		1°	30°	60°	90°	120°	150°	180°
		(c) $\sigma^{\infty}_{yy} \neq 0$, $\sigma^{\infty}_{xx} = 0$, $\sigma^{\infty}_{xy} = 0$						
0	$k'_1(a)$	.1289	.1428	.0669	.0028	.0134	.0223	0.0000
	$k'_2(a)$	1.0849	1.0180	.9054	.9950	1.0599	1.0304	1.0000
	$k'_1(b)$	.1641	-.0754	-.0670	-.0021	0.0231	.0136	0.0000
	$k'_2(b)$	1.4055	.9685	.9974	.9995	1.0005	1.0005	1.0000
	$k'_1(c)$	-1.0246	-1.6348	-1.3085	.0533	1.3767	1.3606	0.0000
	$k'_1(d)$	2.0539	-1.3808	-1.4661	-.1076	1.2735	.3117	.0000
10	$k'_1(a)$	.0858	.0198	.0100	.0010	.0032	.0043	.0000
	$k'_2(a)$	1.0527	.9967	.9826	.9992	1.0108	1.0054	1.0000
	$k'_1(b)$	.1044	-.0140	-.0121	-.0003	.0043	.0025	.0000
	$k'_2(b)$	1.1662	.9929	.9994	.9998	.9999	1.0000	1.0000
	$k'_1(c)$	-.6916	-.5492	-.3731	.0557	.4513	-.4316	.0000
	$k'_1(d)$	1.1639	-.4179	-.4533	-.0342	.3912	-.4029	.0000

Some sample results for an inclusion collinear with a crack (i.e, for $\theta=0$) are given in Table 4. Note that for this configuration under the

Table 4. Normalized stress intensity factors for an inclusion collinear with a crack. Relative dimensions: $\theta=0$, d-c = b-a, c = b+s. Applied loads: σ^{∞}_{ij}, (i,j=x,y) (Fig. 1).

σ^{∞}_{ij}	k'	s = (b-a)/100		s = (b-a)/2	
		γ = 0	γ = 10	γ = 0	γ = 10
σ^{∞}_{xx}	$k_1'(a)$	-0.0202	-0.0040	-0.0019	-0.0004
	$k_1'(b)$	-0.1338	-0.0300	-0.0027	-0.0005
	$k_1'(c)$	-1.0482	-0.3296	-1.0889	-0.3347
	$k_1'(d)$	-1.0845	-0.3345	-1.0889	-0.3347
σ^{∞}_{yy}	$k_1'(a)$	1.0047	1.0006	1.0008	1.0002
	$k_1'(b)$	1.0200	0.9987	1.0011	1.0002
	$k_1'(c)$	-0.0861	-0.1571	0.4559	0.1397
	$k_1'(d)$	0.3841	0.1273	0.4590	0.1413

loads shown in the table, that is, for σ^{∞}_{yy} and σ^{∞}_{xx}, because of symmetry the Mode II stress intensity factors $k_2(a)$ and $k_2(b)$ are zero. Also, for the shear loading σ^{∞}_{xy} it is found that $k_2'(a) = 1$, $k_2'(b) = 1$ and $k_1(a) = k_1(b) = k_1(c) = k_1(d) = 0$. This follows from the fact that in the cracked plane under pure shear σ^{∞}_{xy} the strain component $\varepsilon_{xx}(x,0)$ is zero and hence an inextensible inclusion on the x axis would have no effect on the stress distribution.

Another special configuration is an inclusion parallel to the crack for which Table 5 shows some sample results. In the two special configurations considered in Tables 4 and 5 the effect of the crack-inclusion interaction on the stress intensity factors does not seem to be very significant.

The results for an elastic medium for which xz plane is a plane of symmetry with respect to the crack-inclusion geometry as well as the

Table 5. Normalized stress intensity factors in a plane containing an inclusion parallel and equal in length to a crack, both symmetrically located with respect to the y axis. The crack is along the x axis and H is the distance between the crack and the inclusion in y direction (Fig. 1).

σ^{∞}_{ij}	k'	H = b-a		H = 10(b-a)	
		γ = 0	γ = 10	γ = 0	γ = 10
σ^{∞}_{xx}	$k'_1(a)=k'_1(b)$	-0.0182	-0.0070	-0.0007	-0.0002
	$k'_2(a)=-k'_2(b)$	0.0281	-0.0011	0.0006	0.0000
	$k'_1(c)=k'_1(d)$	-1.0834	-1.0887	-0.0683	-0.0683
σ^{∞}_{yy}	$k'_1(a)=k'_1(b)$	1.0063	1.0028	1.0004	1.0001
	$k'_2(a)=-k'_2(b)$	-0.0060	0.0004	-0.0001	0.0000
	$k'_1(c)=k'_1(d)$	0.3917	0.4387	0.0411	0.0276
σ^{∞}_{xy}	$k'_1(a)=-k'_1(b)$	-0.0042	0.0000	-0.0002	0.0000
	$k'_2(a)=k'_2(b)$	0.9965	1.0000	0.9998	1.0000
	$k'_1(c)$	-0.1131	0.0033	-0.0123	0.0004
	$k'_1(d)$	0.1129	-0.0052	0.0123	-0.0006

applied loads are given in Figures 2-12. In this example the crack is perpendicular to the inclusion and the external load is a uniform tension parallel or perpendicular to the crack and away from the crack-inclusion region (see the insert in the figures). The results shown in the figures are self-explanatory. However, the solution also has some unusual features among which, for example, one may mention the tendency of the crack tip stress intensity factors k'(a) and k'(b) to "peaking" as γ decreases and as d/ℓ increases (where 2d and 2ℓ are the lengths of the inclusion and the crack, respectively and $\gamma = 0$ corresponds to an inextensible inclusion).

The results for the limiting case of the crack touching the inclusion are given in Figures 8-12. In this case at the singular point x=0, y=0 the stress intensity factor $k_1(a)$ and the normalized stress intensity factor $k_1'(a)$ are defined by

$$k_1(a) = \lim_{x\to 0-} \sqrt{2}\, x^{\alpha}\sigma_{yy}(x,0) \ , \ (x < 0) \ , \tag{54}$$

$$k_1'(a) = k(a)/\sigma_{ii}^{\infty}\sqrt{\ell} \ , \ (i=(x,y);\ \ell=b/2) \tag{55}$$

where the power of singularity α is given in Table 2. The results shown in Figures 8-12 are obtained for $\nu = 0.3$.

The stress intensity factors for the other symmetric crack inclusion problem, namely for the problem in which y axis is the line of symmetry with regard to loading and geometry are given in Figures 13-28. In this problem $a=-\ell$, $b=\ell$, $d>c>0$ and the external load is either σ_{yy}^{∞} or σ_{xx}^{∞} (see the insert in Figure 13). Note that the figures show the crack tip stress intensity factors at $x=a=-\ell$ and $k_1(b)=k_1(a)$, $k_2(b)=-k_2(a)$. Generally the magnitude of $k_1(a)$ and $k_2(a)$ seem to increase with increasing length and stiffness of the inclusion (i.e., with increasing $(d-c)/2\ell$ and decreasing $\gamma = \mu(1+\kappa_s)/A_s\mu_s(1+\kappa)$, where μ_s is the shear modulus of the inclusion). Also, as expected, $k_1(c)$ and $k_1(d)$ describing the intensity of the stress field at inclusion ends tend to increase as the stiffness of the inclusion increases. However, their dependence on the relative length parameters is somewhat more complicated (see, for example, Figure 16 for change in behavior of the variation of $k_1(d)$ at $(d-c)/2\ell=5$). Figures 13-20 show the effect

of the inclusion length for constant crack length 2ℓ and constant distance c (Figure 13). The effect of the distance c for constant inclusion and crack lengths is shown in Figures 13-28.

The results of the nonsymmetric problem showing the effect of the relative location of the inclusion are shown in Table 6. Referring to Figure 1, in these calculations it is assumed that $\theta = \frac{\pi}{2}$, $d-c = 2\ell$, $c/2\ell = 0.1$ and $a/2\ell$ is variable.

Finally, the stress intensity factors for the crack-inclusion intersection problem considered in Section 4.1 are given in Figures 29-43. The normalized stress intensity factors shown in these figures are defined by (see (41), (52) and (53))

$$k'_{1B} = \frac{1}{\sigma^{\infty}_{ij}\sqrt{\ell}} \lim_{x\to b} \sqrt{2(x-b)}\, \sigma_{yy}(x,0) ,$$

$$k'_{2B} = \frac{1}{\sigma^{\infty}_{ij}\sqrt{\ell}} \lim_{x\to b} \sqrt{2(x-b)}\, \sigma_{xy}(x,0) ,$$

$$k'_{1A} = \frac{1}{\sigma^{\infty}_{ij}\sqrt{\ell}} \lim_{x\to -0} \sqrt{2}\, x^{\alpha}\, \sigma_{yy}(-0,0) ,$$

$$k'_{2A} = \frac{1}{\sigma^{\infty}_{ij}\sqrt{\ell}} \lim_{x\to -0} \sqrt{2}\, x^{\alpha}\, \sigma_{xy}(-0,0) , \qquad (56)$$

$$k'_{1D} = \frac{1}{k_o} \lim_{y\to d} \sqrt{2(y-d)}\, \sigma_{xx}(0,y) ,$$

$$k_o = \frac{1-\kappa}{2(1+\kappa)}\, \sigma^{\infty}_{ij}\, \sqrt{d/2} \quad .$$

In this case too, generally the magnitude of the stress intensity factors increases with increasing length and stiffness of the inclusion. However, since the crack and the inclusion are located in each other's "shadow", the relative dimensions seem to have considerable influence on the variation as well as the magnitude of the stress intensity factors.

Table 6. The effect of the relative location of inclusion on the stress intensity factors; $\theta = \pi/2$, $(d-c)/2\ell = 1$, $c/2\ell = 0.1$ (Figure 1).

σ^{∞}_{ij}	$\frac{a}{2\ell}$	$k_1'(a)$	$k_2'(a)$	$k_1'(b)$	$k_2'(b)$	$k_1'(c)$	$k_1'(d)$
	0.1	-0.0202	0.0490	0.0161	0.0003	0.4450	0.4471
	0.0	-0.1033	0.0425	0.0133	0.0039	0.4192	0.4402
σ^{∞}_{xx}	-0.1	-0.0849	-0.0044	0.0076	0.0081	0.3538	0.4285
	-0.3	-0.0349	-0.0308	0.0023	0.0060	0.3348	0.4163
	-0.5	-0.0363	-0.0114	-0.0363	0.0114	0.3195	0.4109
	+0.1	1.0458	-0.1396	0.9545	0.0012	-1.5217	-1.0543
	0.0	1.2652	-0.1090	0.9667	-0.0078	-1.2922	-0.9497
σ^{∞}_{yy}	-0.1	1.1548	0.0064	0.9865	-0.0150	-0.5345	-0.8136
	-0.3	1.0448	0.0294	1.0013	-0.0102	-0.2308	-0.6378
	-0.5	1.0313	0.0129	1.0313	-0.0129	-0.1959	-0.5801
	0.1	0.0098	0.9905	-0.0033	0.9992	0.1050	-0.1338
	0.0	0.0493	0.9796	-0.0065	0.9983	-0.1734	-0.1675
σ^{∞}_{xy}	-0.1	0.0463	1.0019	-0.0041	0.9960	-0.1054	-0.1648
	-0.3	0.0123	1.0066	-0.0007	0.9971	-0.0236	-0.0977
	-0.5	0	1	0	1	0	0

References

1. F. Erdogan and G.D. Gupta, "The Inclusion Problem with a Crack Crossing the Boundary", Int. J. of Fracture, Vol. 11, pp. 13-27, 1975.

2. I.N. Muskhelishvili, Some Basic Problems of the Mathematical Theory of Elasticity, Noordhoff, Groningen, The Netherlands, 1953.

3. F. Erdogan, "Mixed Boundary Value Problems in Mechanics", Mechanics Today, Vol. 4, S. Nemat-Nasser, ed. pp. 1-86, Pergamon Press Inc., 1978.

4. G.R. Irwin, "Analysis of Stresses and Strains Near the End of a Crack Traversing a Plate", J. Appl. Mech., Vol. 24, Trans. ASME, pp. 361-364, 1957.

5. M.L. Williams, "On the Stress Distribution at the Base of a Stationary Crack", J. Appl. Mech., Vol. 24, Trans. ASME, pp. 109-114, 1957.

6. F. Delale and F. Erdogan, "Transverse Shear Effect in a Circumferentially Cracked Cylindrical Shell", Quarterly of Applied Mathematics, Vol. 37, pp. 239-258, 1979.

7. F. Erdogan and G.D. Gupta, "Stresses near a Flat Inclusion in Bonded Dissimilar Materials", Int. J. Solids Structures, Vol. 8, pp. 533-547, 1972.

8. O.S. Yahsi and F. Erdogan, "A Note on the Cracked Plates Reinforced by a Line Stiffener", Engineering Fracture Mechanics, (to appear) 1984.

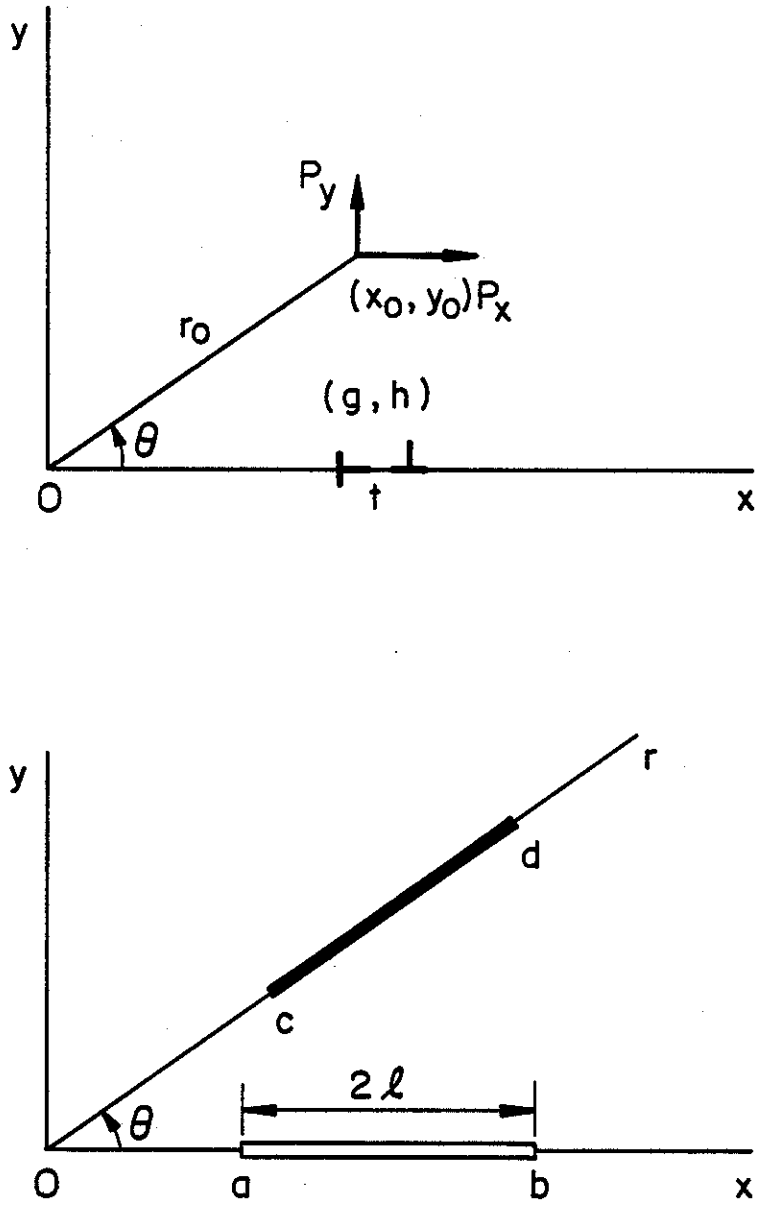

Figure 1. The geometry and notation for the crack-inclusion problem.

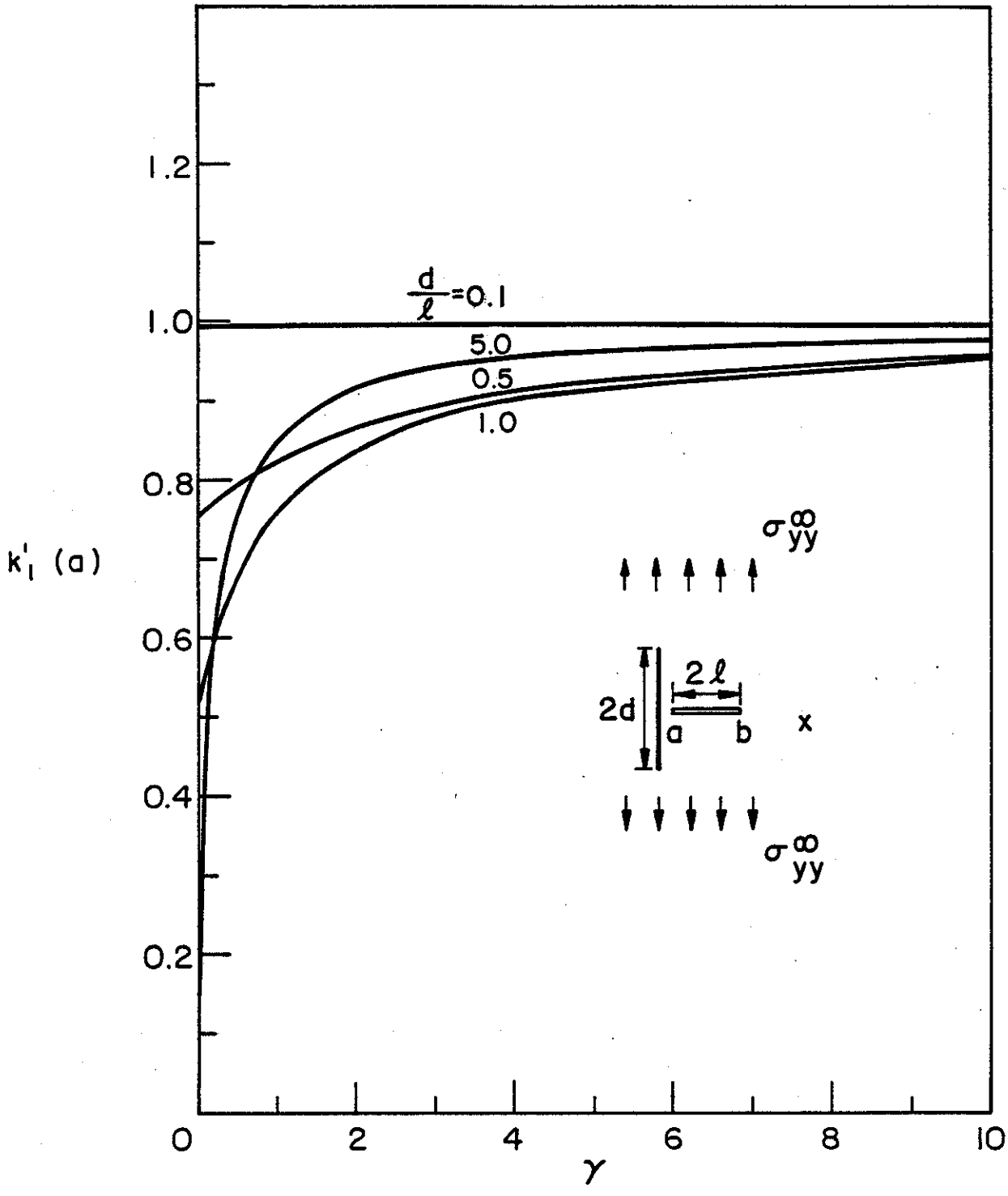

Figure 2. The effect of the stiffness and the relative length of the inclusion on the normalized stress intensity factor $k_I'(a)$; $\sigma^{\infty}_{yy} \neq 0$, $\sigma^{\infty}_{xx} = 0$, $\sigma^{\infty}_{xy} = 0$; $a/\ell = 0.5$, $\nu = 0.3$.

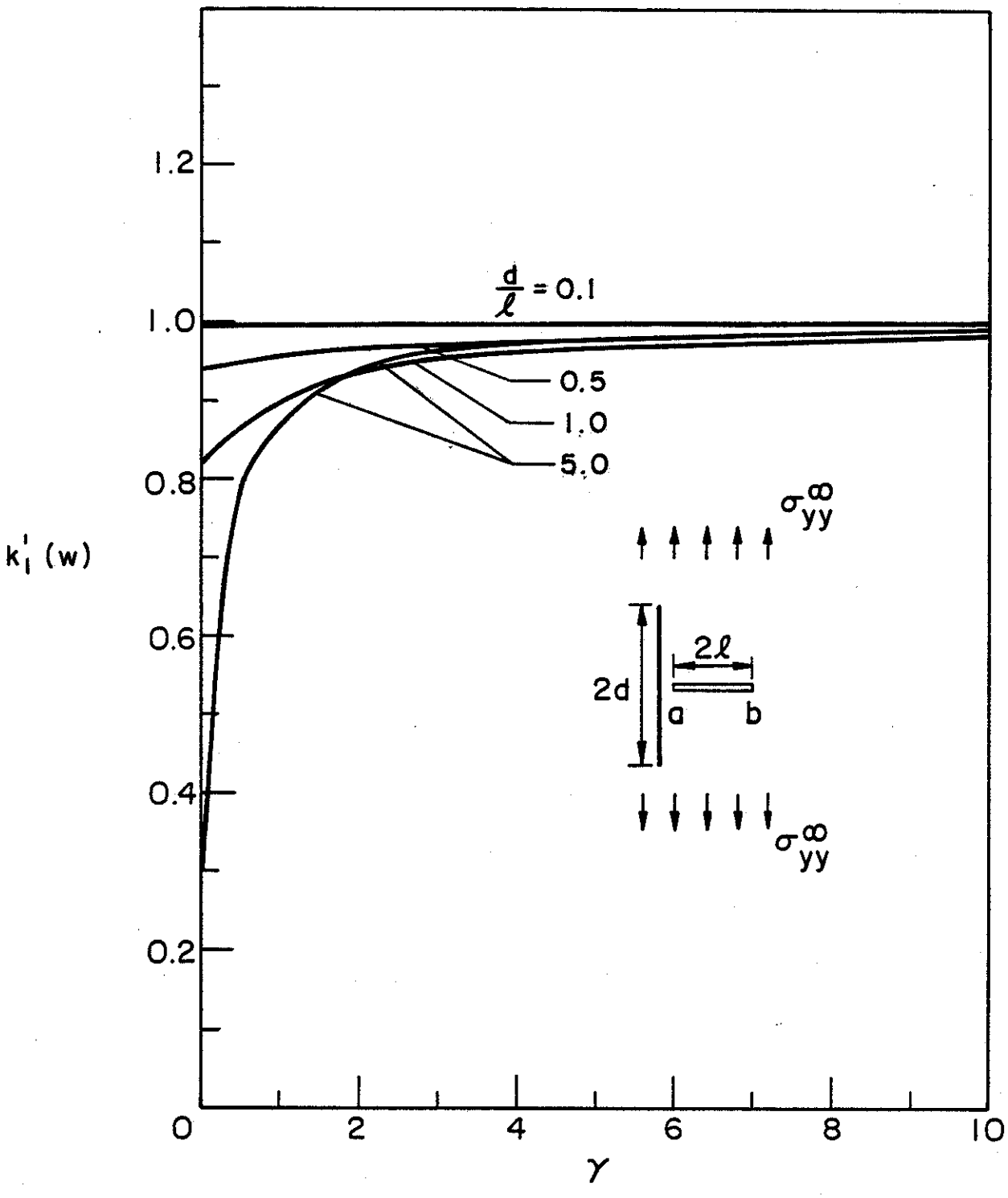

Figure 3. Normalized stress intensity factor $k_I'(b)$; $\sigma_{yy}^{\infty} \neq 0$, $\sigma_{xx}^{\infty} = 0 = \sigma_{xy}^{\infty}$, $a/\ell = 0.5$, $\nu = 0.3$.

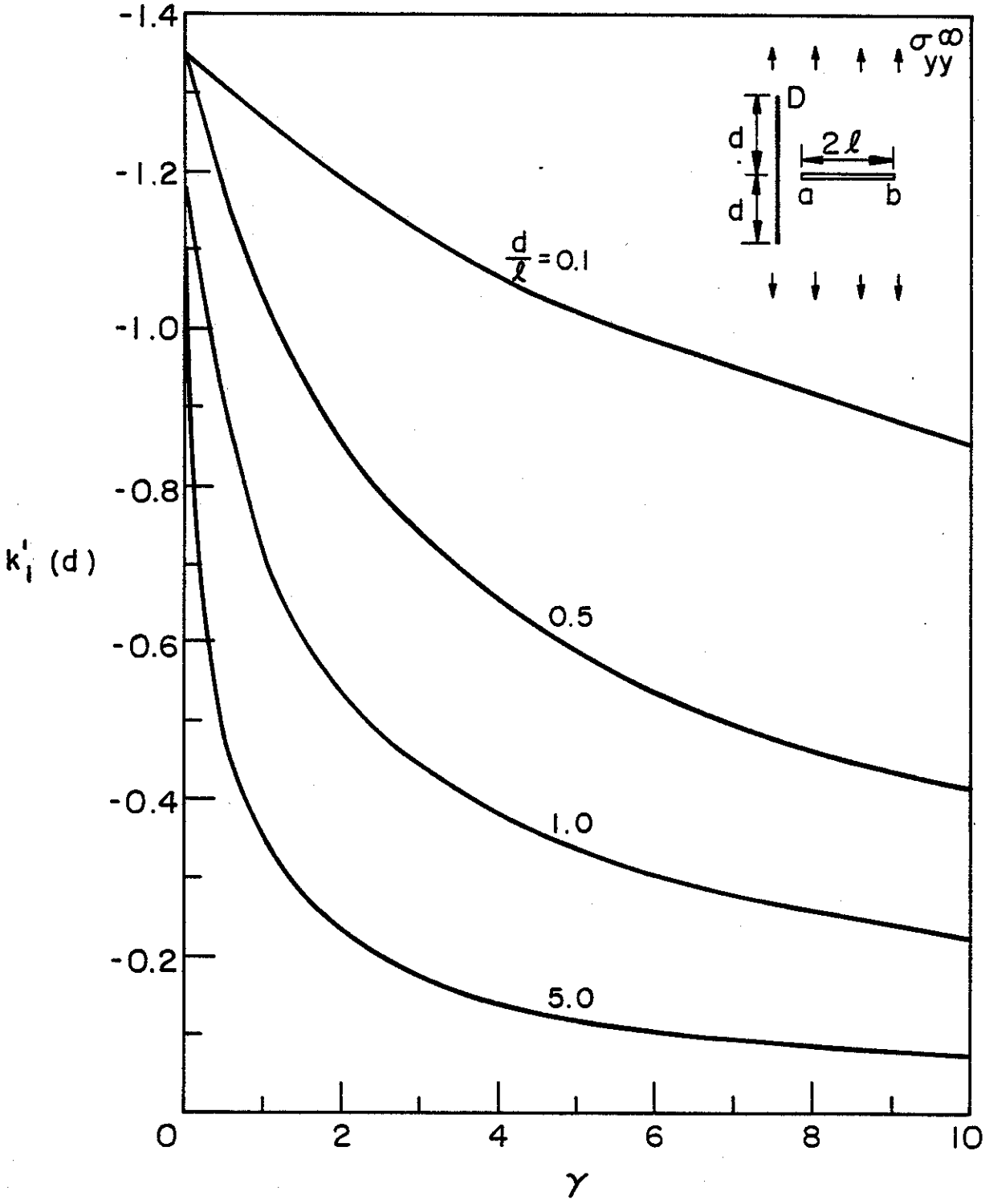

Figure 4. Normalized stress intensity factor at the inclusion end y=d; $\sigma_{yy}^{\infty} \neq 0$, $\sigma_{xx}^{\infty} = \sigma_{xy}^{\infty} = 0$, $a/\ell = 0.5$, $\nu = 0.3$.

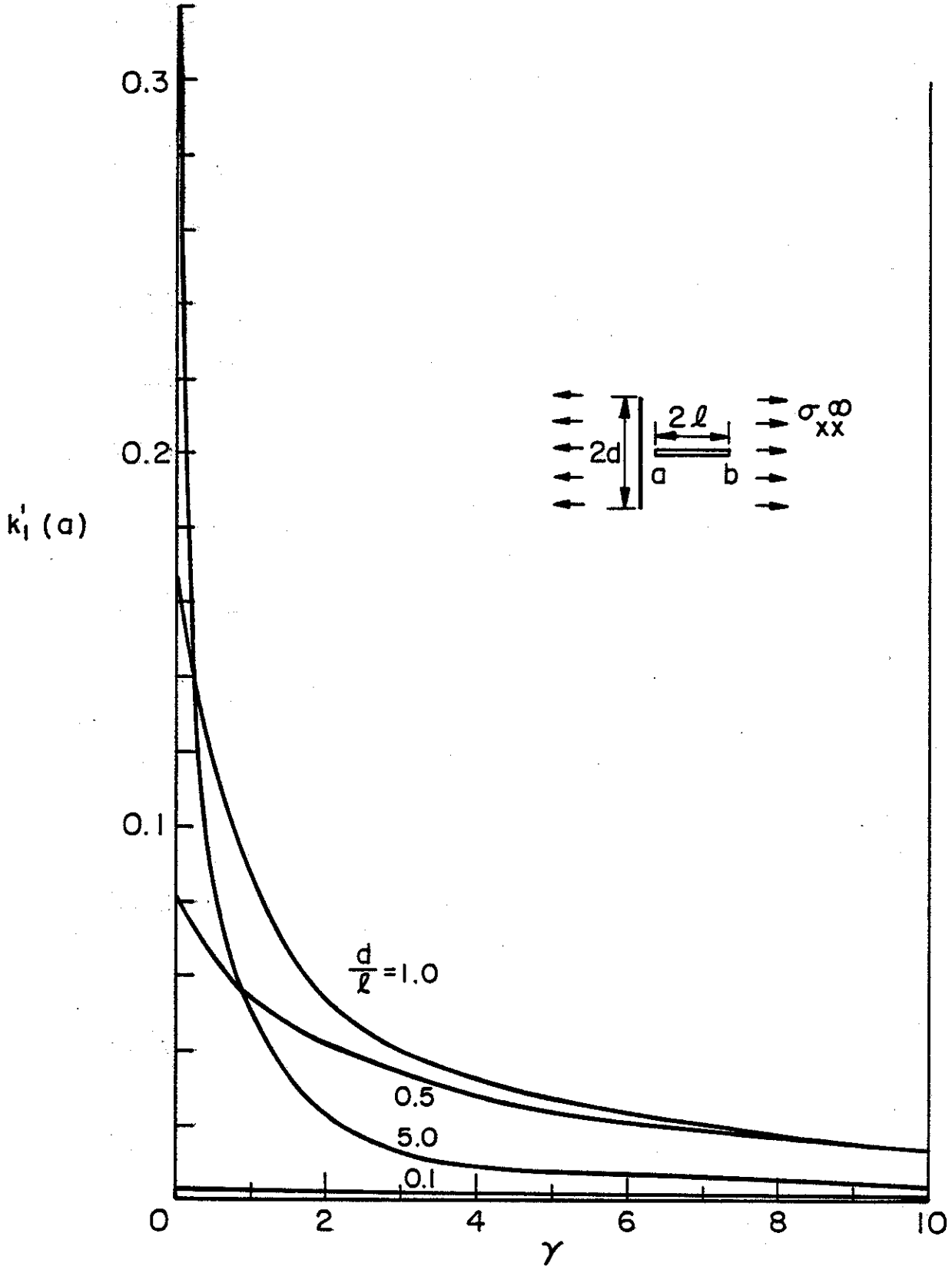

Figure 5. Normalized stress intensity factor at the crack tip x=a; $\sigma_{xx}^{\infty} \neq 0$, $\sigma_{yy}^{\infty} = \sigma_{xy}^{\infty} = 0$, $a/\ell = 0.5$, $\nu = 0.3$.

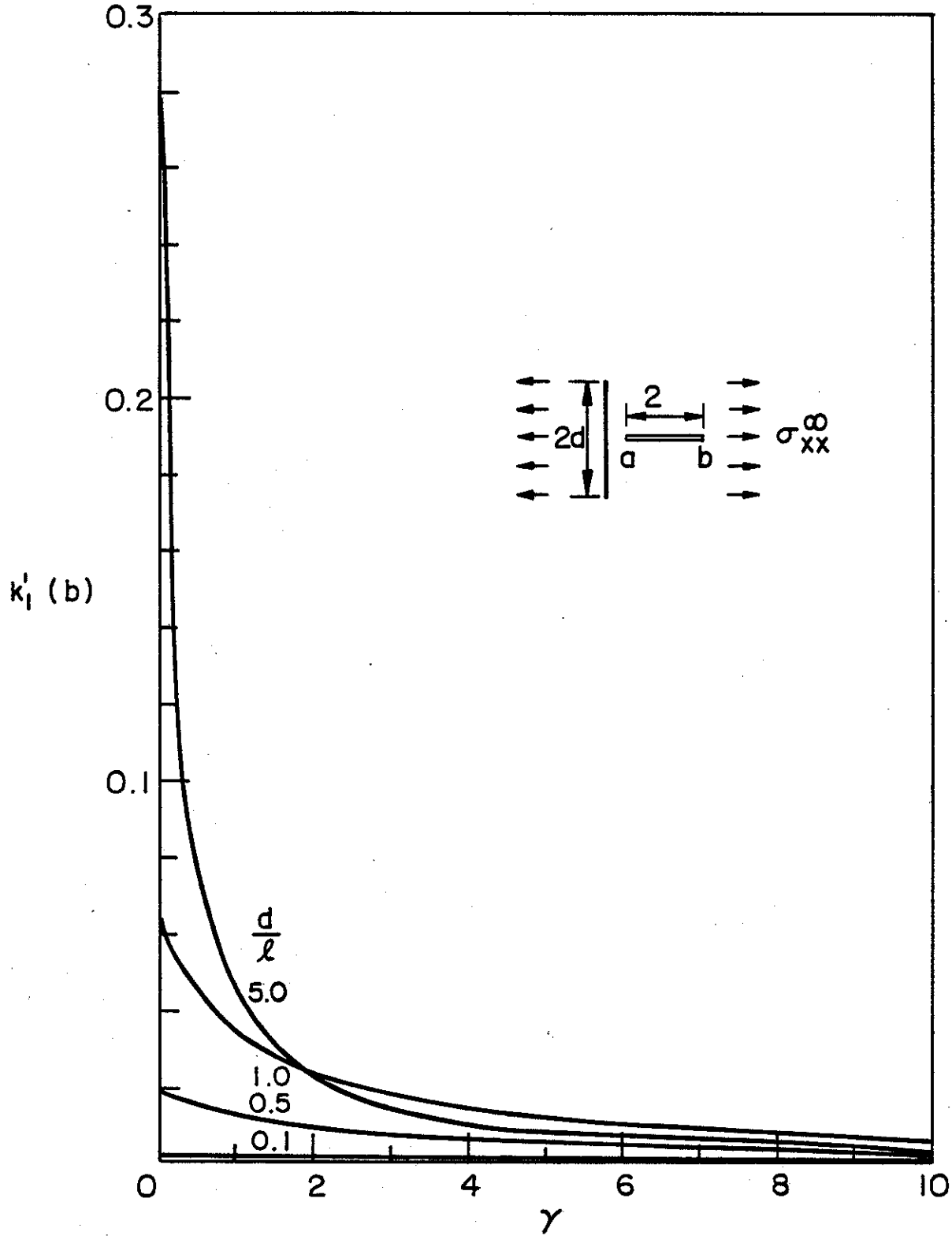

Figure 6. Normalized stress intensity factor at the crack tip x=b; $\sigma_{xx}^{\infty} \neq 0$, $\sigma_{yy}^{\infty} = \sigma_{xy}^{\infty} = 0$, $a/\ell = 0.5$, $\nu = 0.3$.

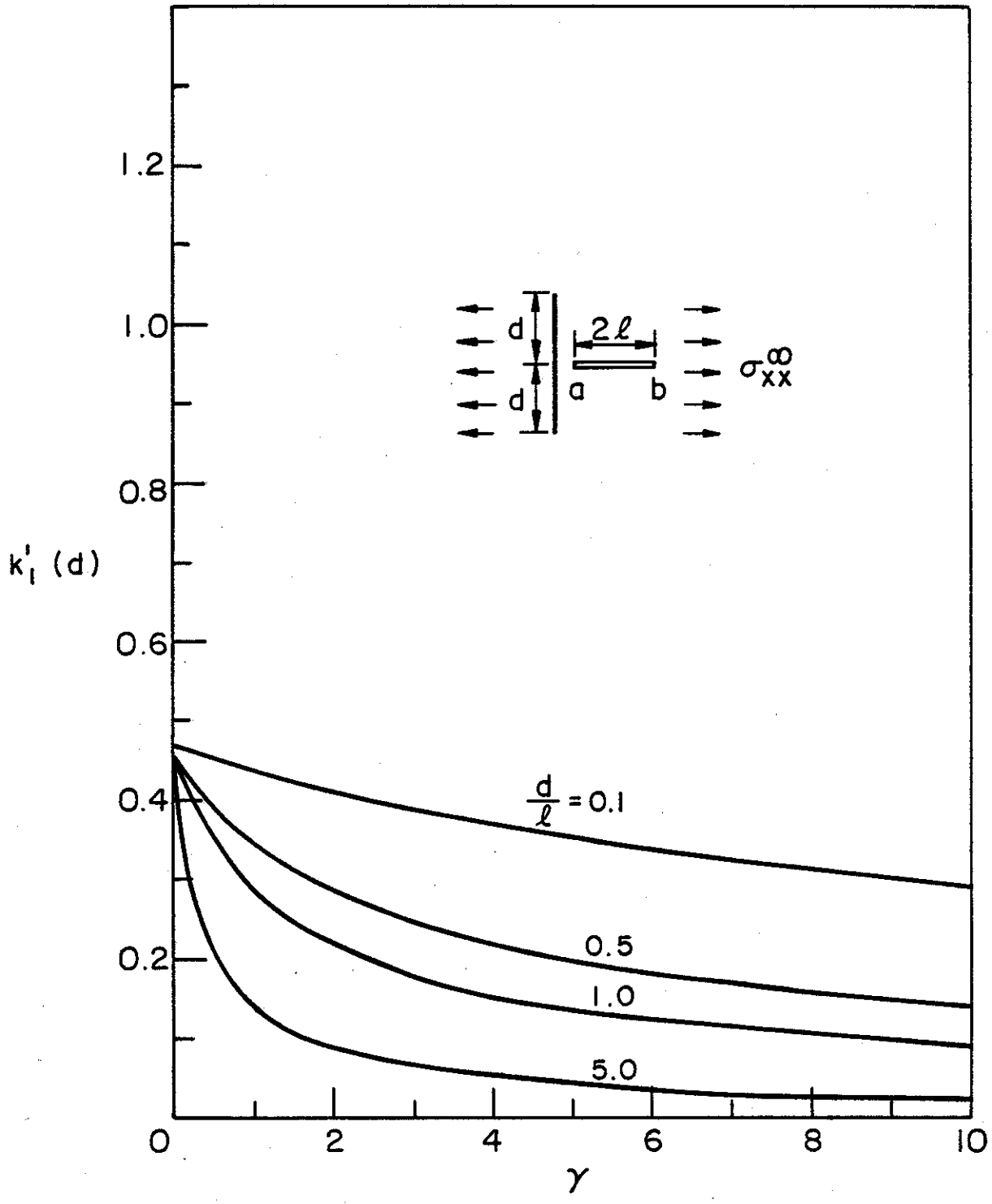

Figure 7. Normalized stress intensity factor at the inclusion end y=d; $\sigma_{xx}^{\infty} \neq 0$, $\sigma_{yy}^{\infty} = \sigma_{xy}^{\infty} = 0$, $a/\ell = 0.5$, $\nu = 0.3$.

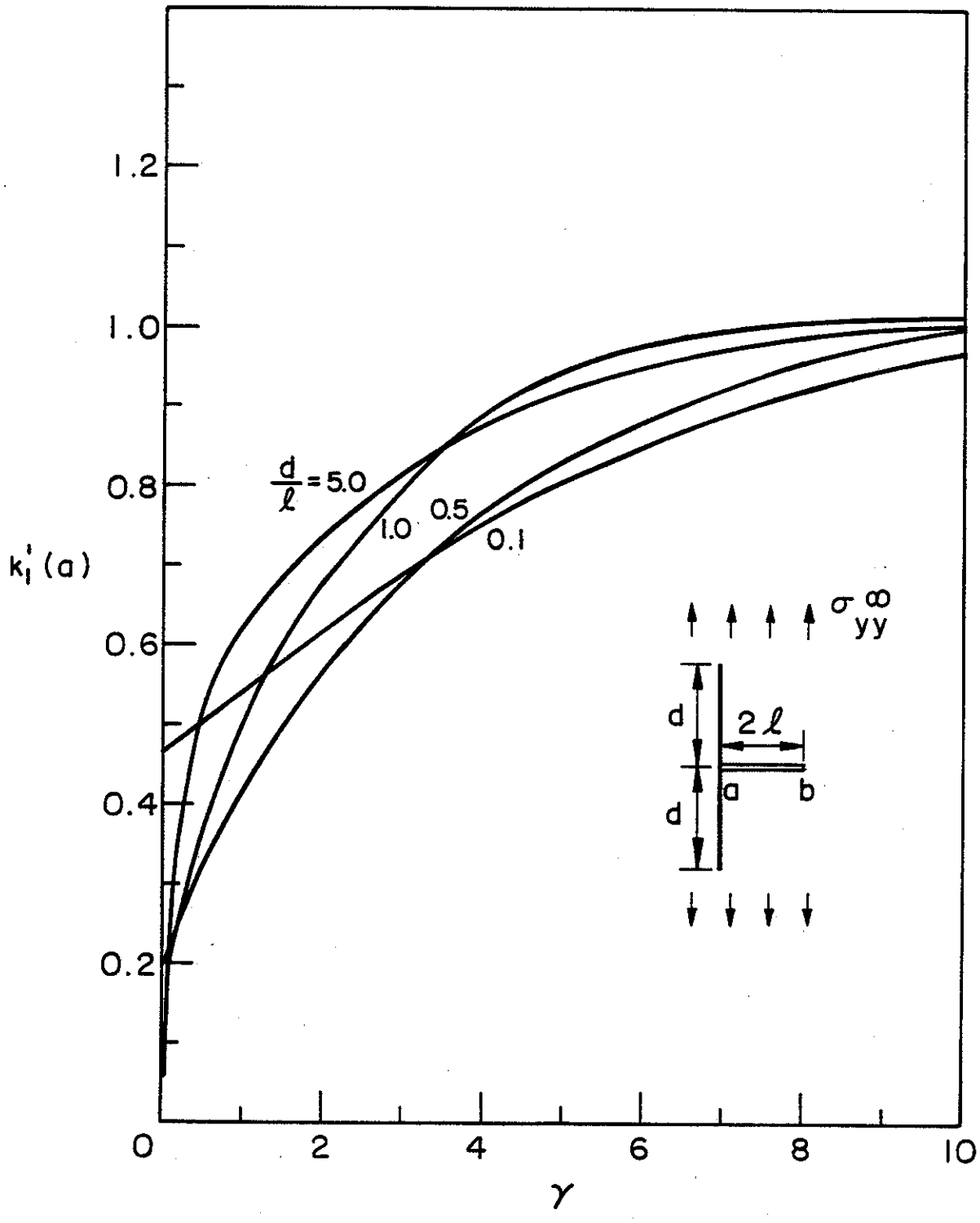

Figure 8. Normalized stress intensity factor at the crack tip x=a=0, $\sigma_{yy}^{\infty} \neq 0$, $\sigma_{xx}^{\infty} = \sigma_{xy}^{\infty} = 0$, $\nu = 0.3$.

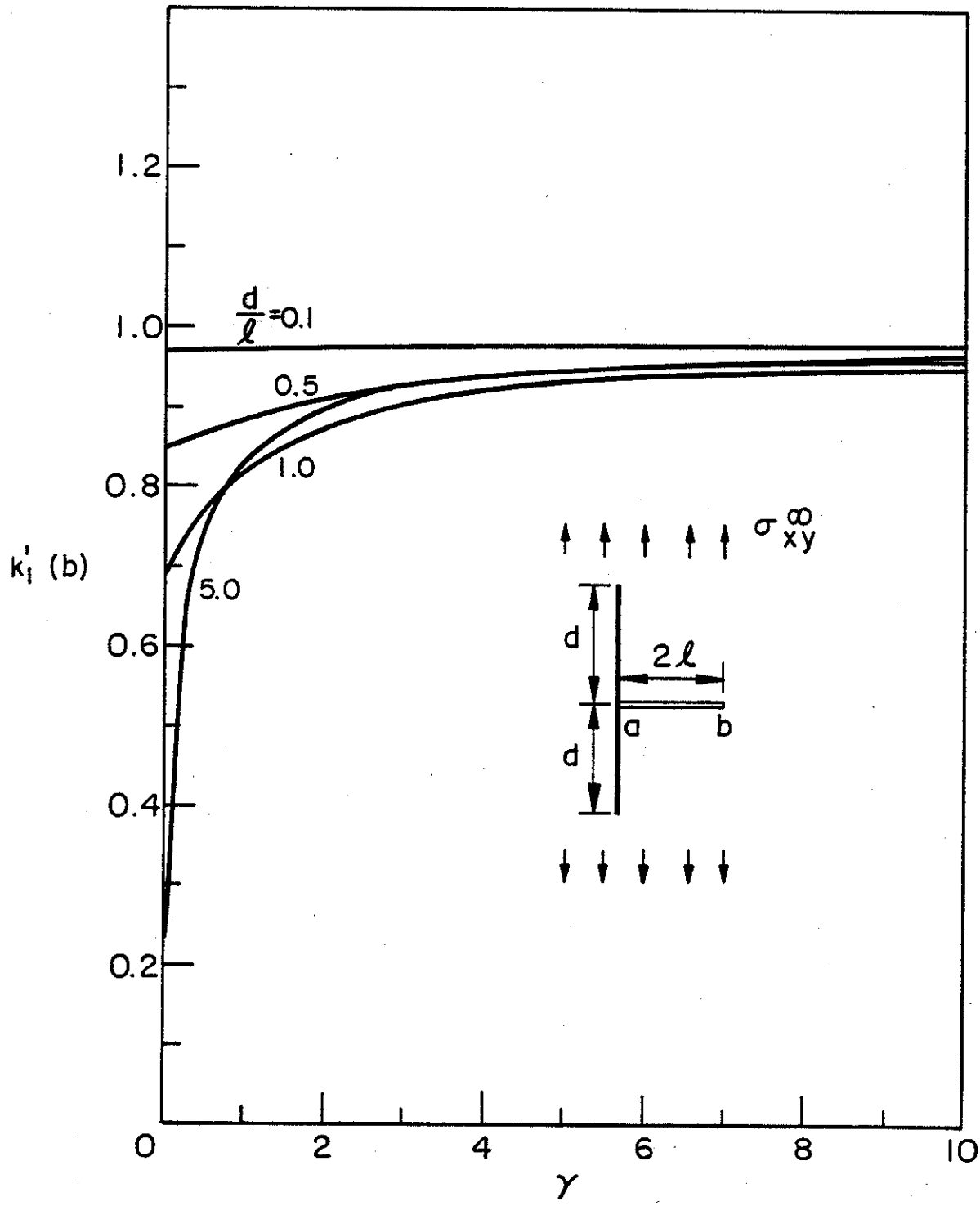

Figure 9. Normalized stress intensity factor at the crack tip x=b, $\sigma_{yy}^{\infty} \neq 0$, $\sigma_{xx}^{\infty} = \sigma_{xy}^{\infty} = 0$, $\nu = 0.3$, a = 0.

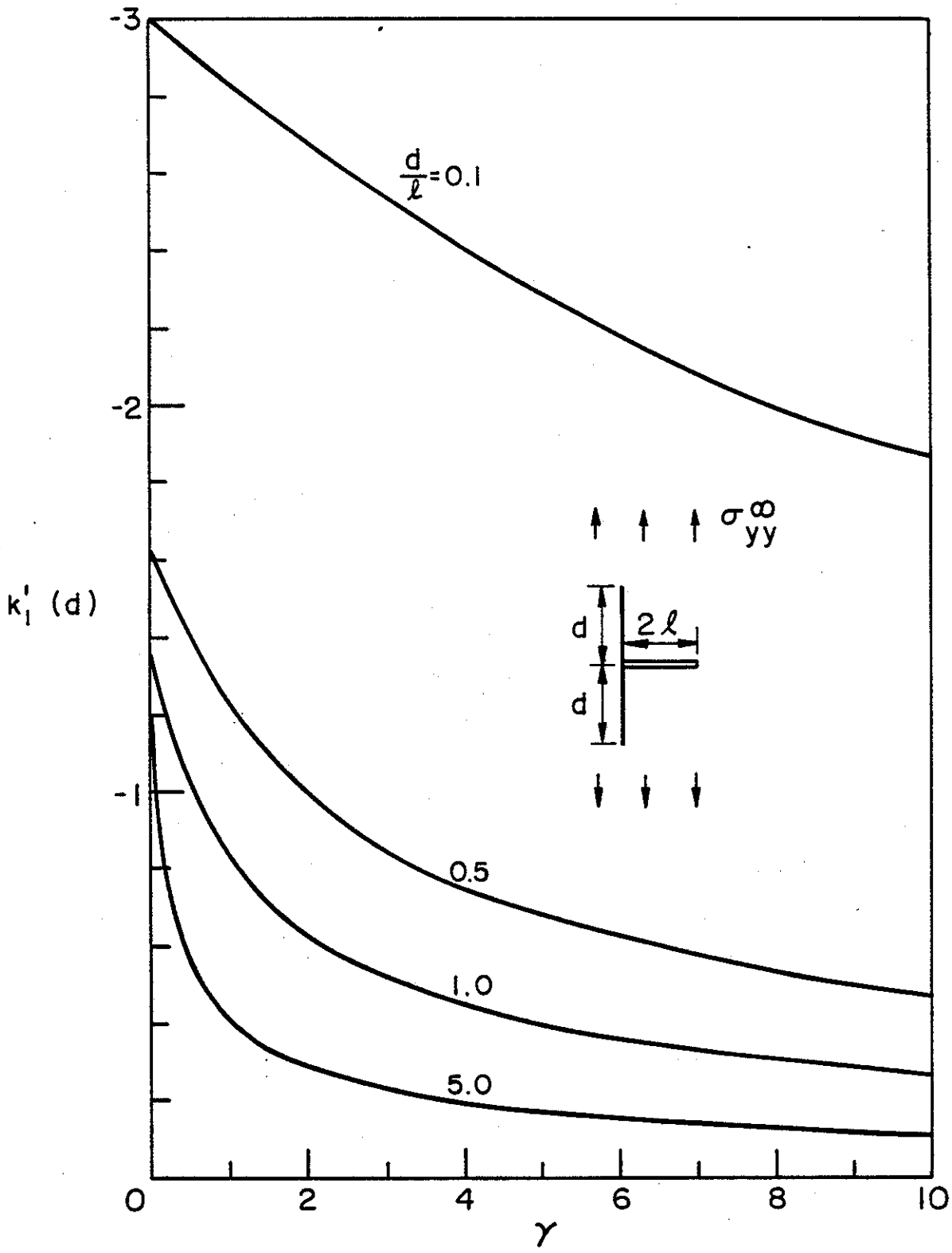

Figure 10. Normalized stress intensity factor at the inclusion end y=d, $\sigma^{\infty}_{yy} \neq 0$, $\sigma^{\infty}_{xx} = \sigma^{\infty}_{xy} = 0$, $\nu = 0.3$, $a = 0$.

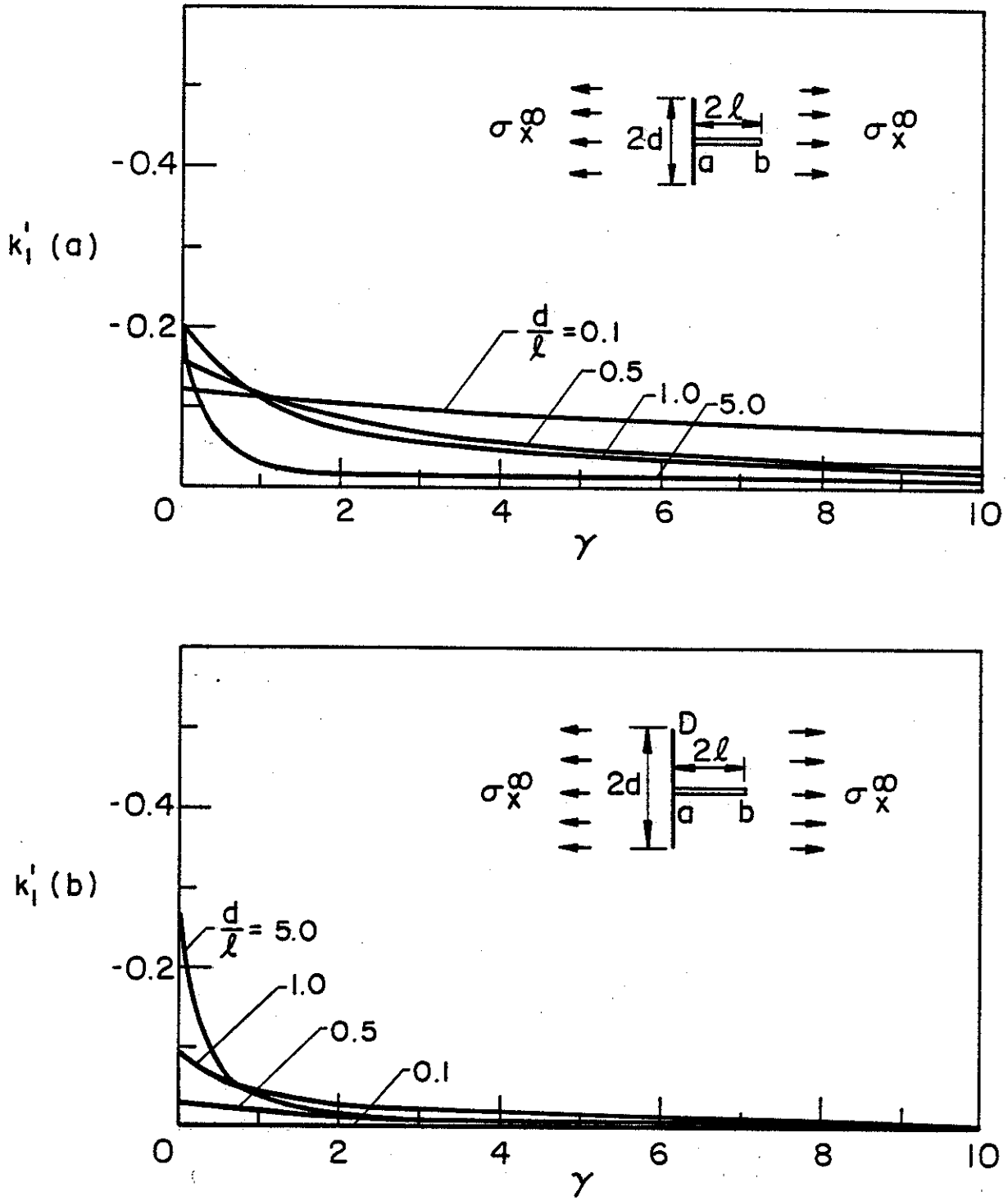

Figure 11. Normalized stress intensity factors at the crack tips x=a=0 and x=b; $\sigma_{xx}^\infty \neq 0$, $\sigma_{yy}^\infty = \sigma_{xy}^\infty = 0$, a = 0, ν = 0.3.

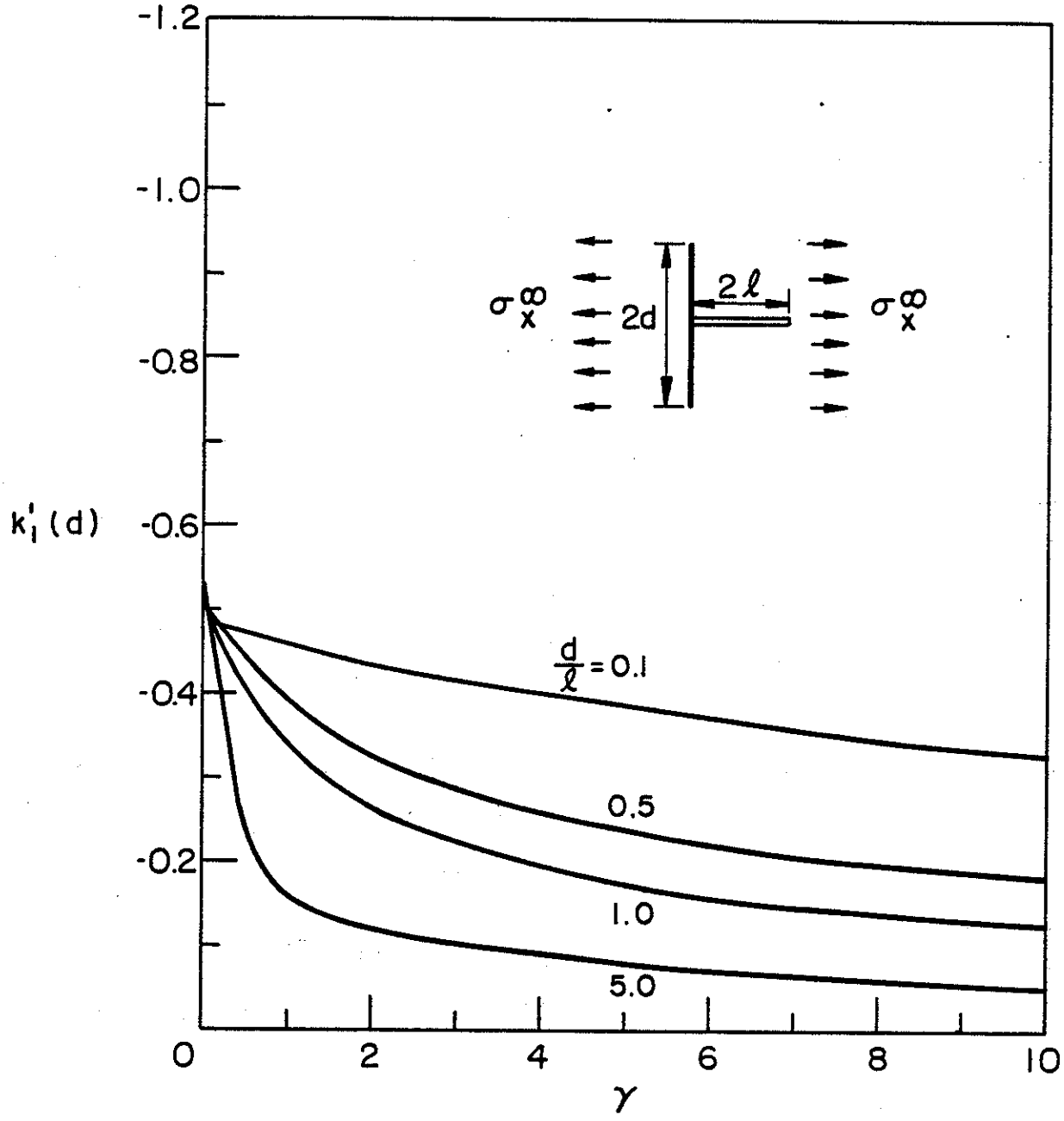

Figure 12. Normalized stress intensity factor at the inclusion end y=d; $\sigma_{xx}^\infty \neq 0$, $\sigma_{yy}^\infty = \sigma_{xy}^\infty = 0$, a = 0, ν = 0.3.

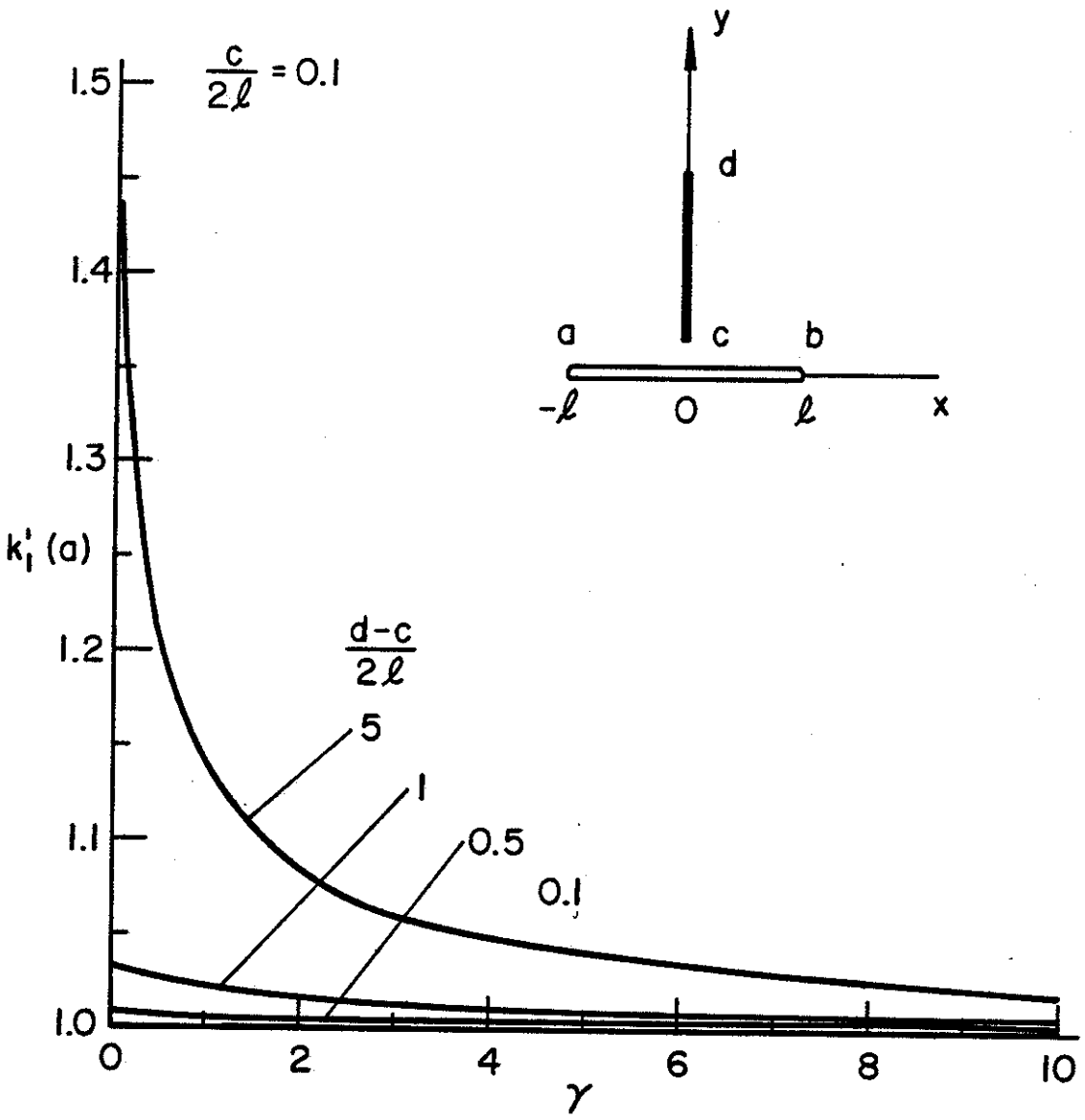

Figure 13. Mode I stress intensity factor at the crack tip $x=a=-\ell$; $\sigma_{yy}^{\infty} \neq 0$, $\sigma_{xx}^{\infty} = 0$, $\sigma_{xy}^{\infty} = 0$, $\theta = \pi/2$, $c = 0.2\ell$, $b = \ell$, $\nu = 0.3$.

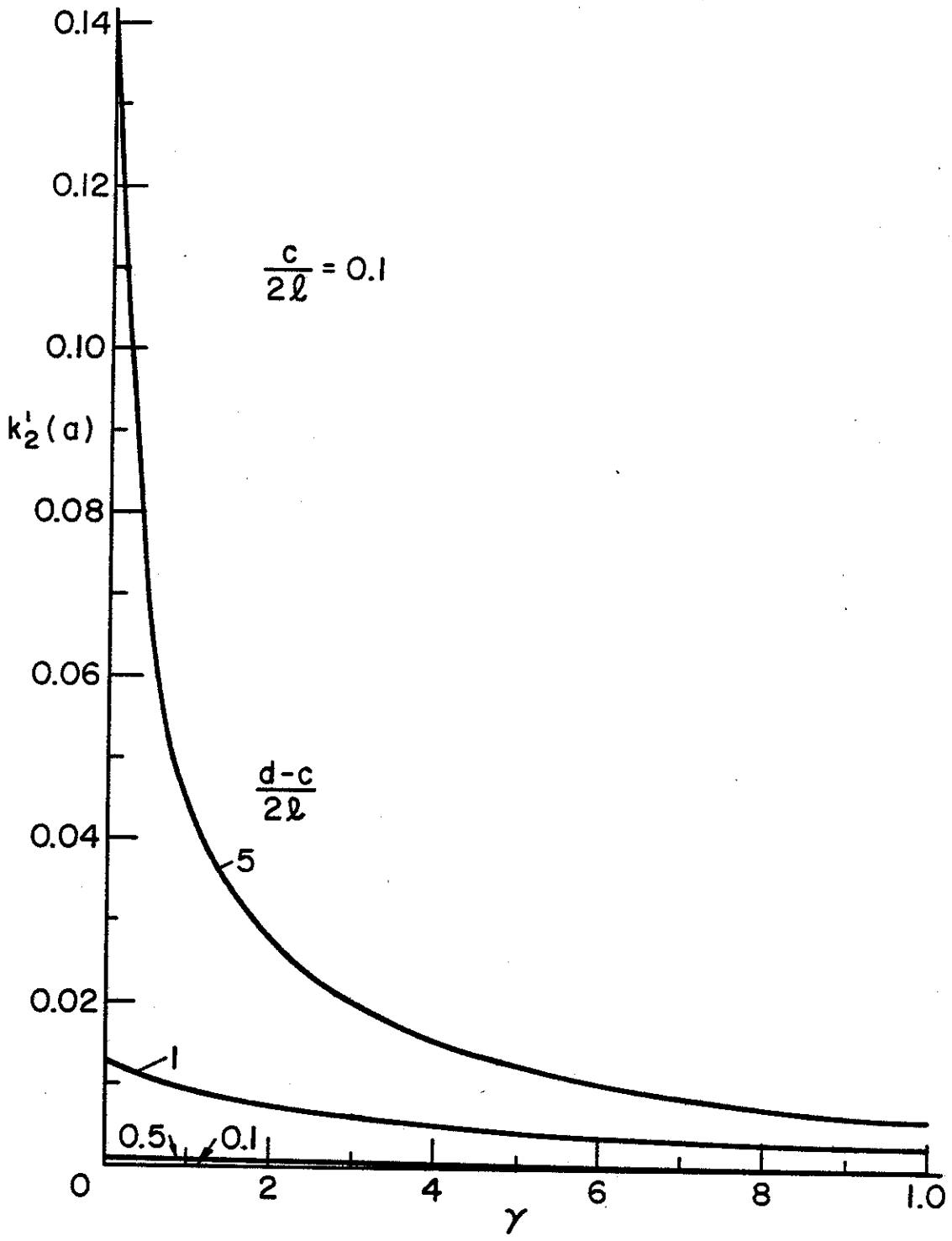

Figure 14. Mode II stress intensity factor at the crack tip $x=a=-\ell$; $\sigma_{yy}^{\infty} \neq 0$, $\sigma_{xx}^{\infty} = \sigma_{xy}^{\infty} = 0$, $\theta = \pi/2$, $c = 0.2\ell$, $b = \ell$, $\nu = 0.3$.

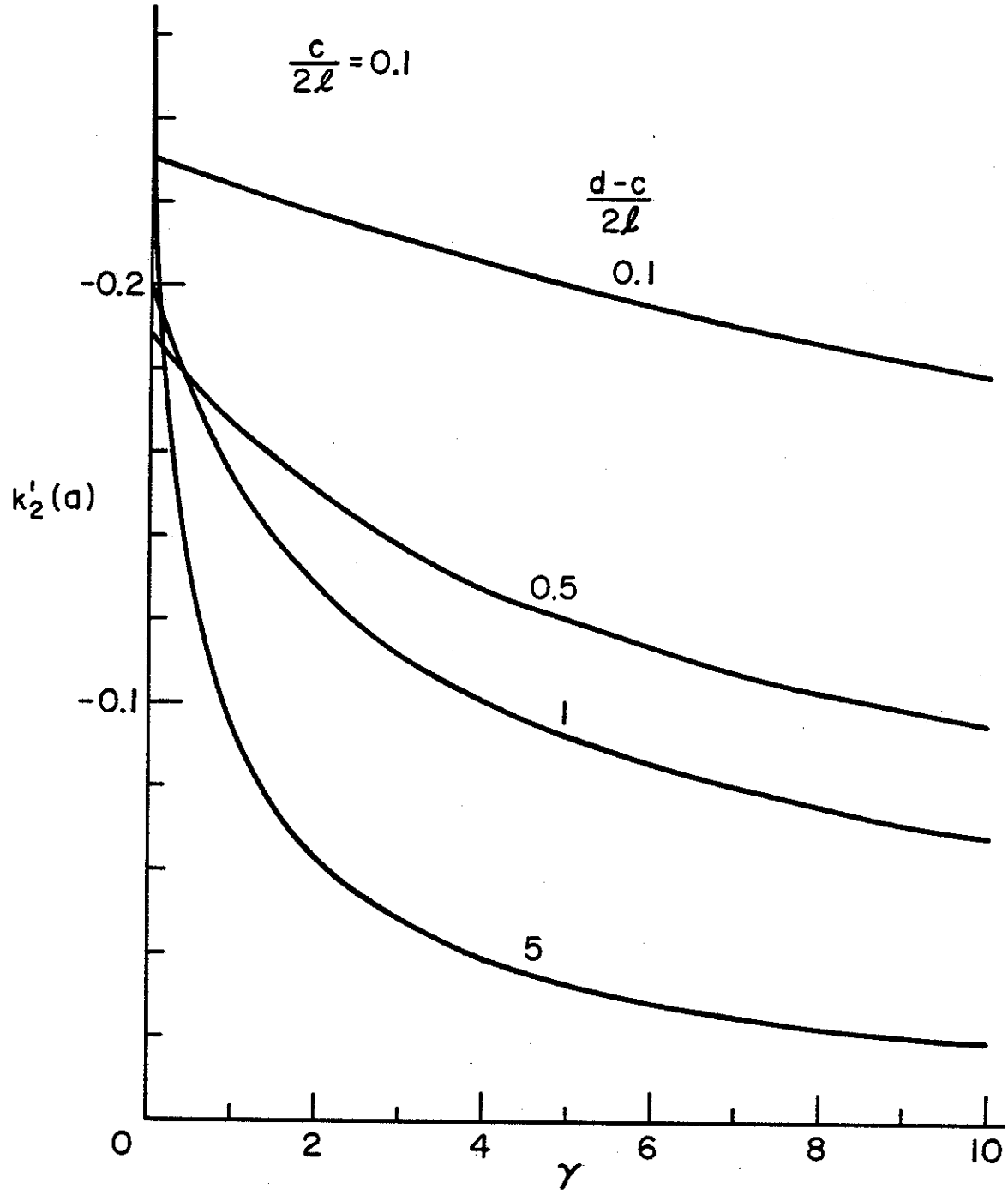

Figure 15. Stress intensity factor at the inclusion end y=c; $\sigma^{\infty}_{yy} \neq 0$, $\sigma^{\infty}_{xx} = \sigma^{\infty}_{xy} = 0$, $\theta = \pi/2$, $c = 0.2\ell$, $\nu = 0.3$, $b = \ell$.

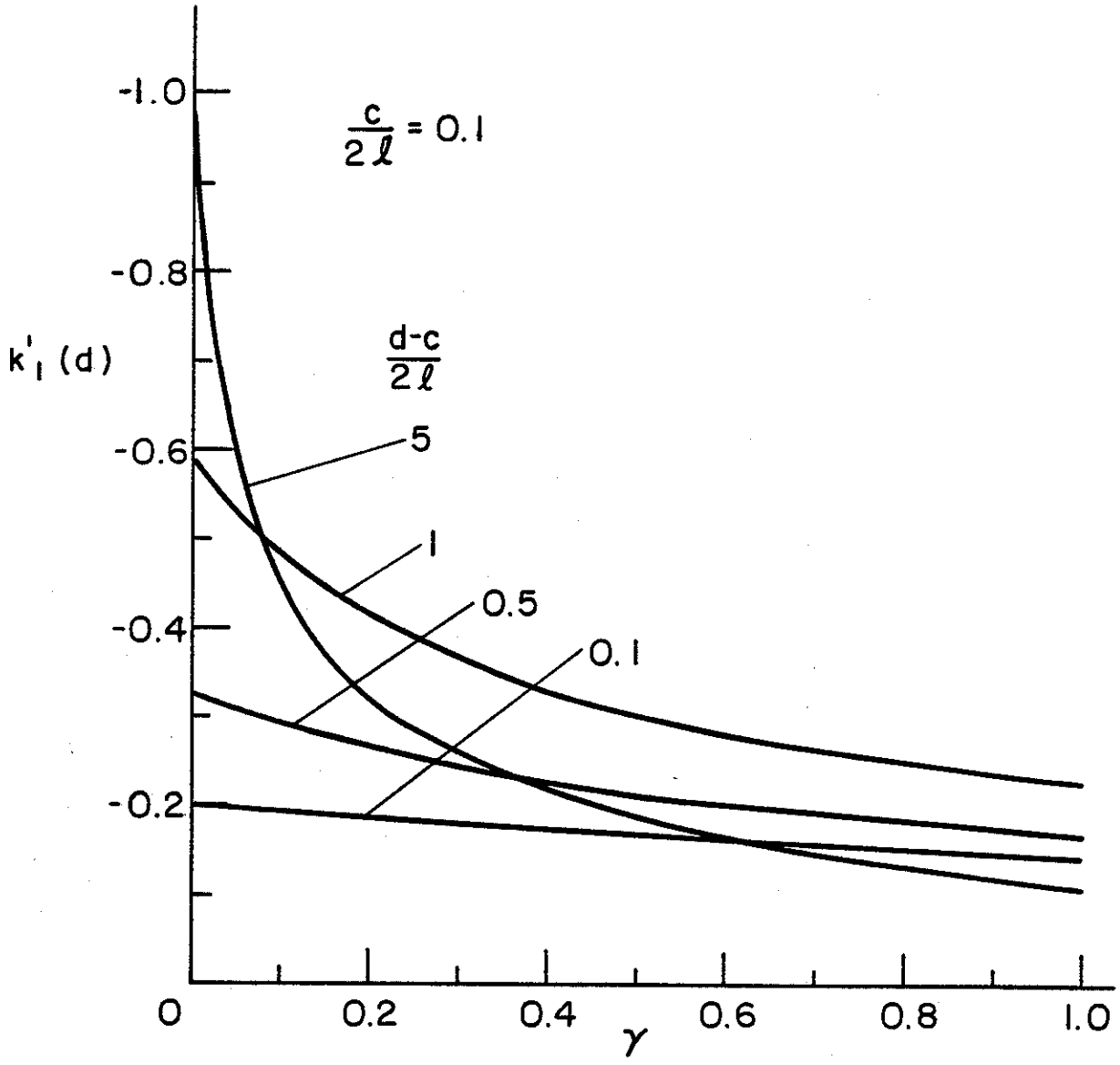

Figure 16. Stress intensity factor at the inclusion end y=d; $\sigma^{\infty}_{yy} \neq 0$, $\sigma^{\infty}_{xx} = \sigma^{\infty}_{xy} = 0$, $\nu = 0.3$, $\theta = \pi/2$, $c = 0.2\ell$, $b = \ell = -a$.

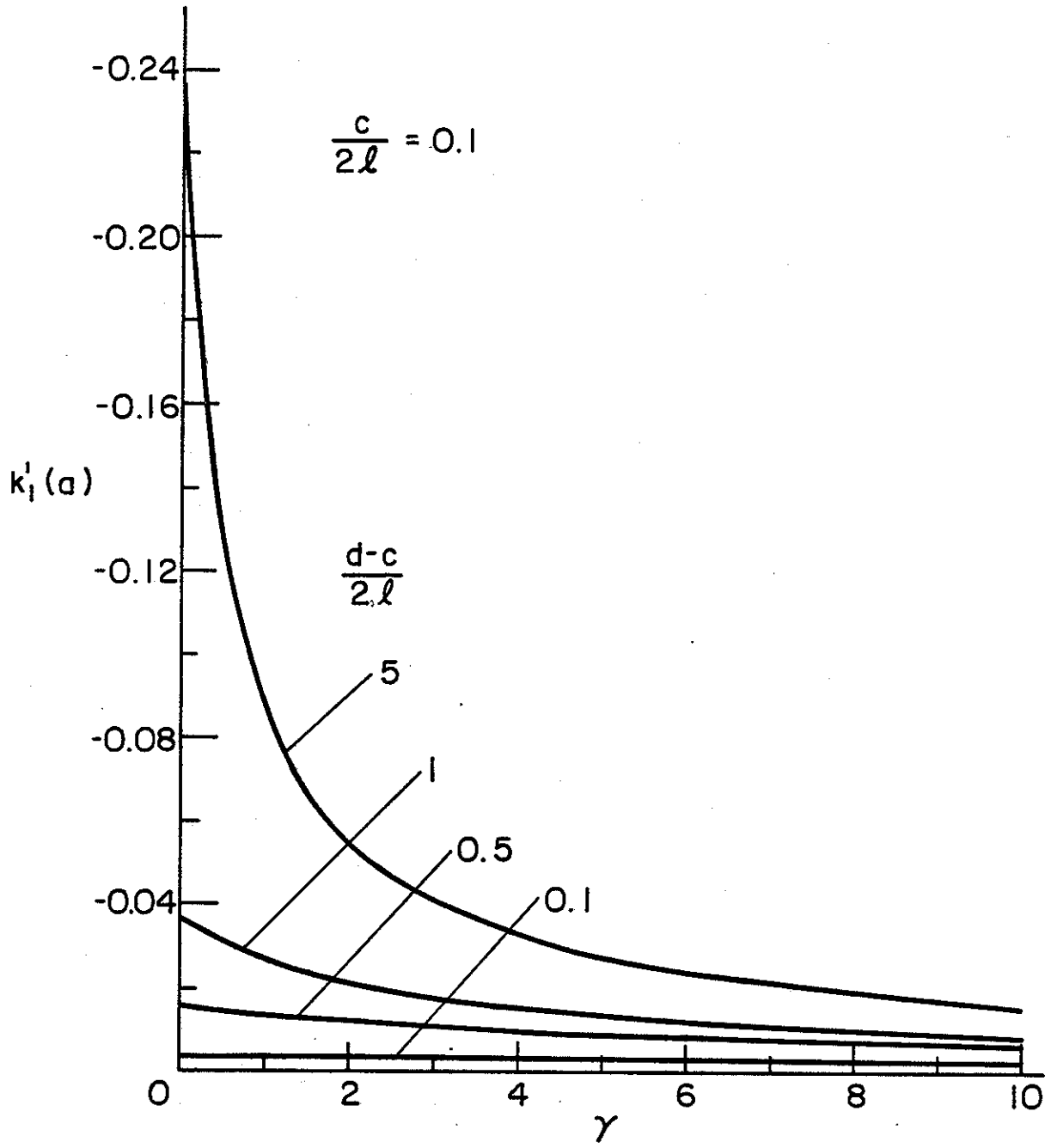

Figure 17. Mode I stress intensity factor at the crack tip $x=a=-\ell$; $\sigma_{xx}^{\infty} \neq 0$, $\sigma_{yy}^{\infty} = \sigma_{xy}^{\infty} = 0$, $\theta = \pi/2$, $\nu = 0.3$, $c = 0.2\ell$, $b = \ell$.

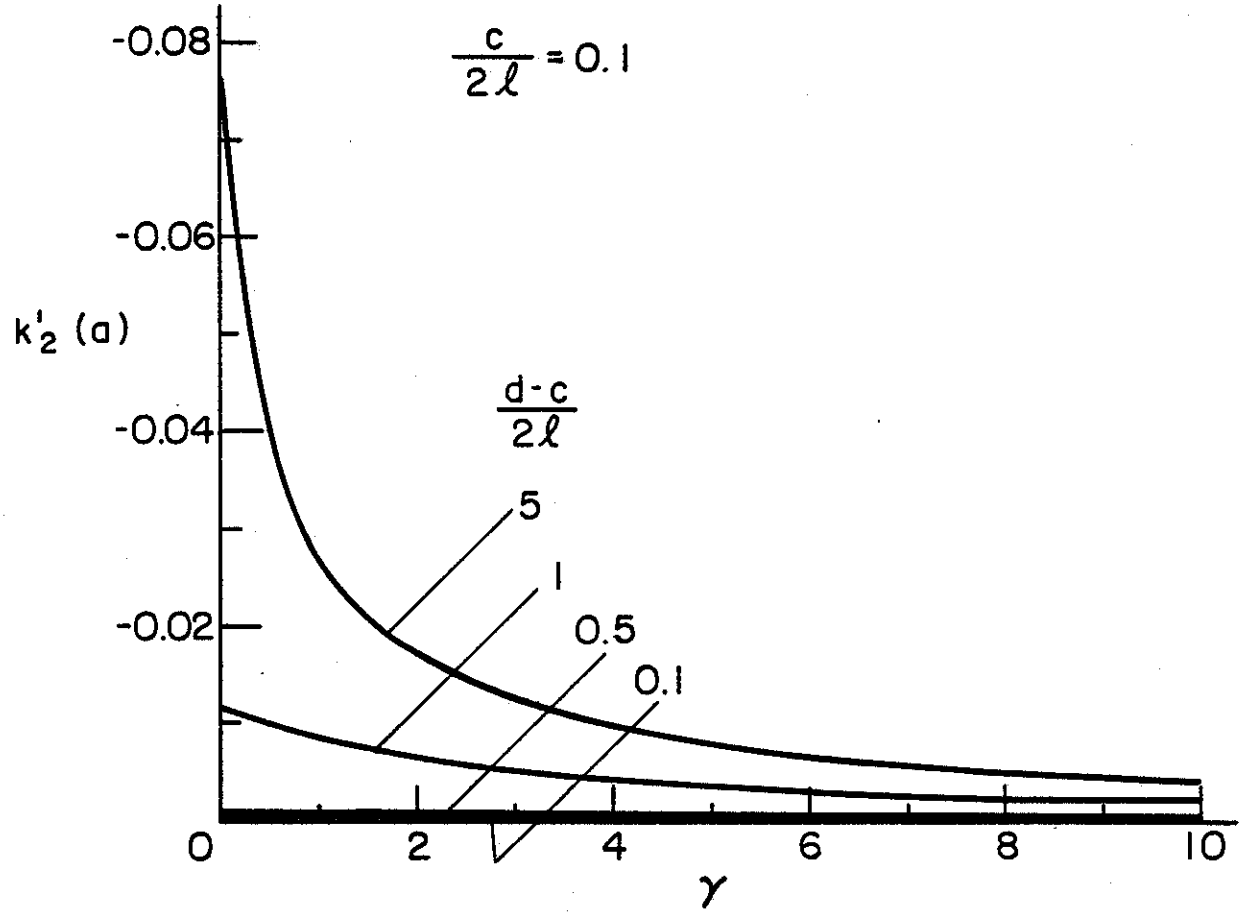

Figure 18. Mode II stress intensity factor at the crack tip $x=a=-\ell$; $\sigma_{xx}^{\infty} \neq 0$, $\sigma_{yy}^{\infty} = \sigma_{xy}^{\infty} = 0$, $\nu = 0.3$, $\theta = \pi/2$, $c = 0.2\ell$, $b = \ell$.

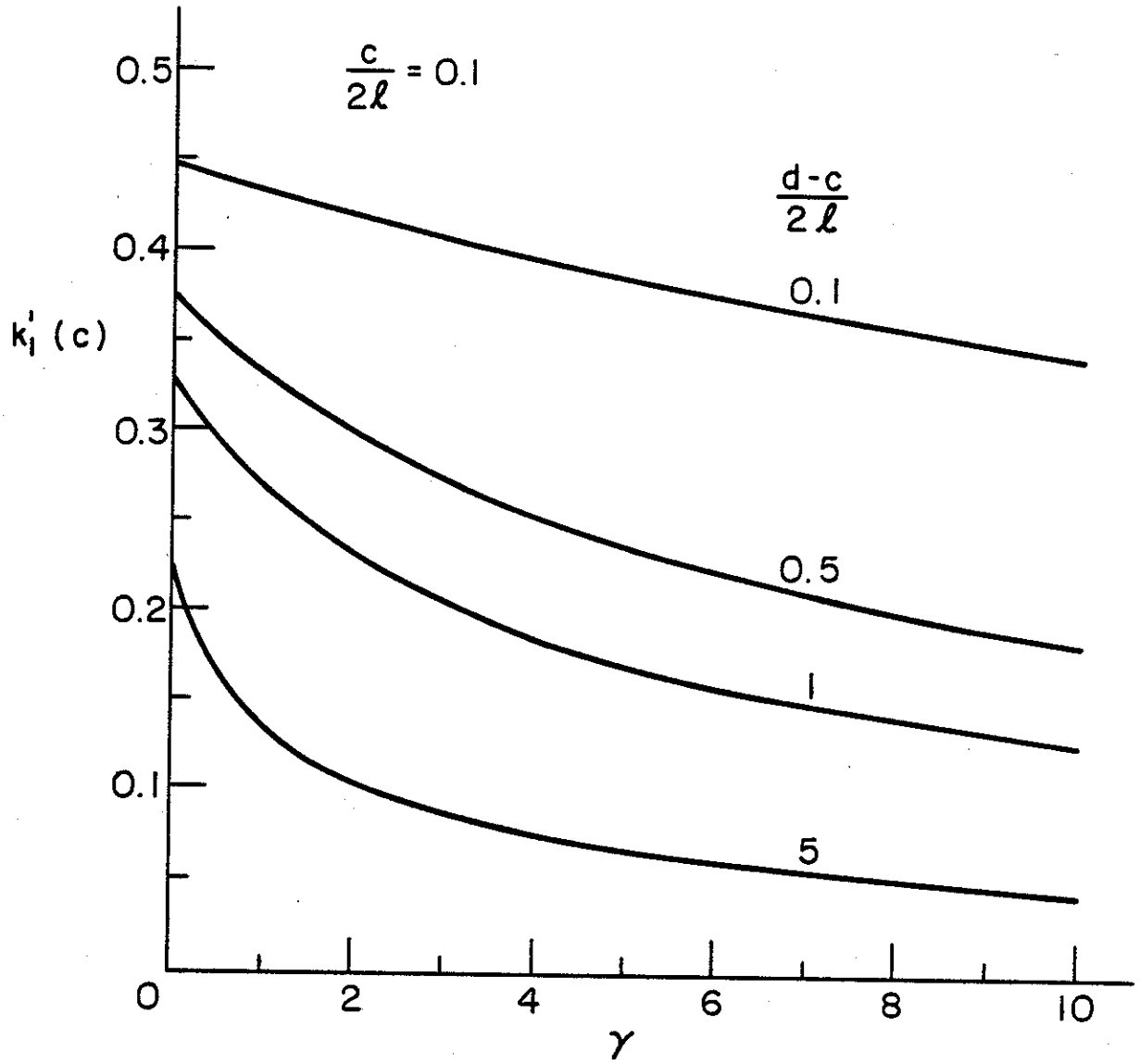

Figure 19. Stress intensity factor at the inclusion end $y = c$; $\sigma_{xx}^{\infty} \neq 0$, $\sigma_{yy}^{\infty} = \sigma_{xy}^{\infty} = 0$, $\nu = 0.3$, $c = 0.2\ell$, $\theta = \pi/2$, $b = \ell = -a$.

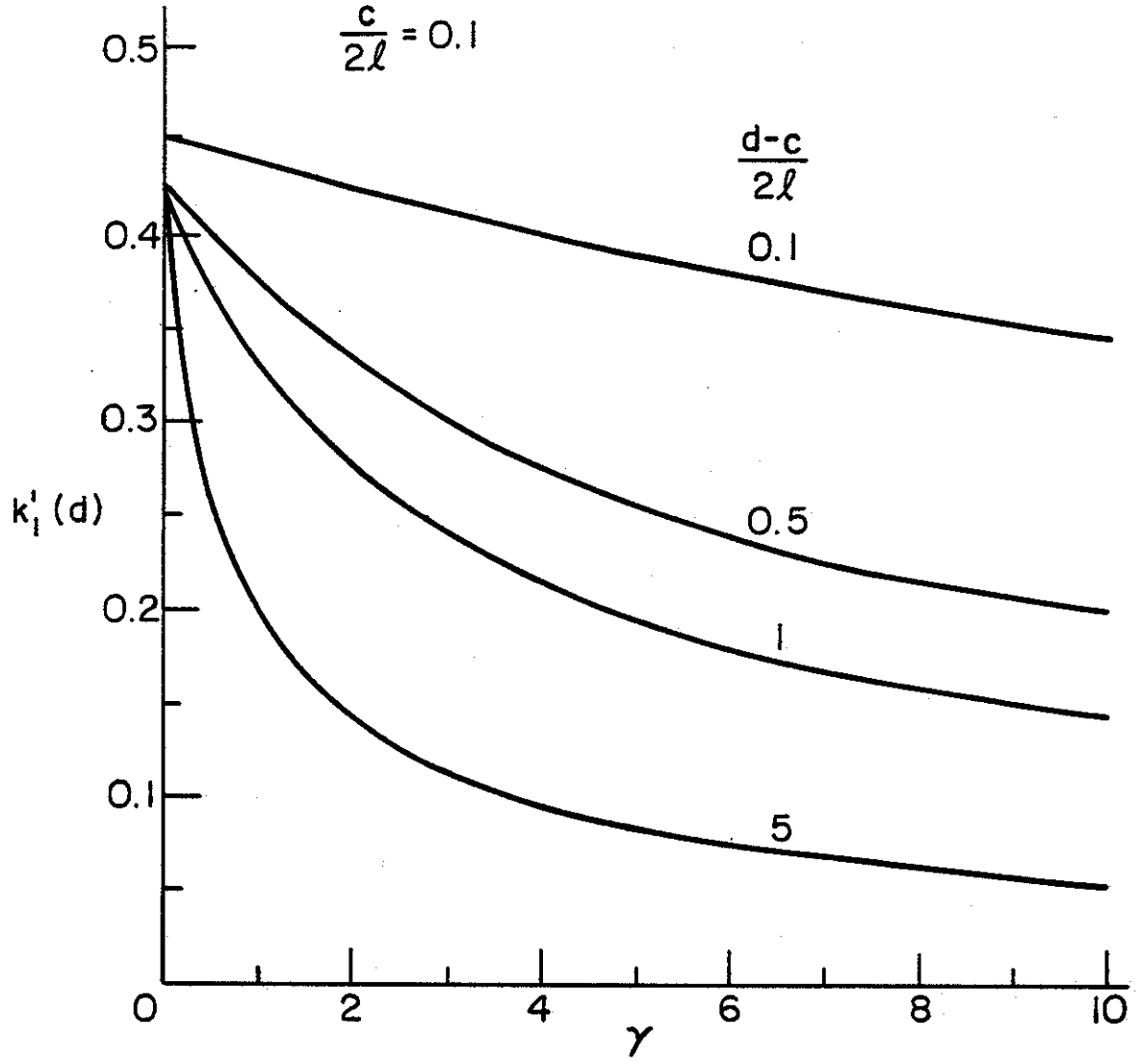

Figure 20. Stress intensity factor at the inclusion end y = d; $\sigma_{xx}^{\infty} \neq 0$, $\sigma_{yy}^{\infty} = \sigma_{xy}^{\infty} = 0$, $\nu = 0.3$, $\theta = \pi/2$, $c = 0.2\ell$, $b = \ell = -a$.

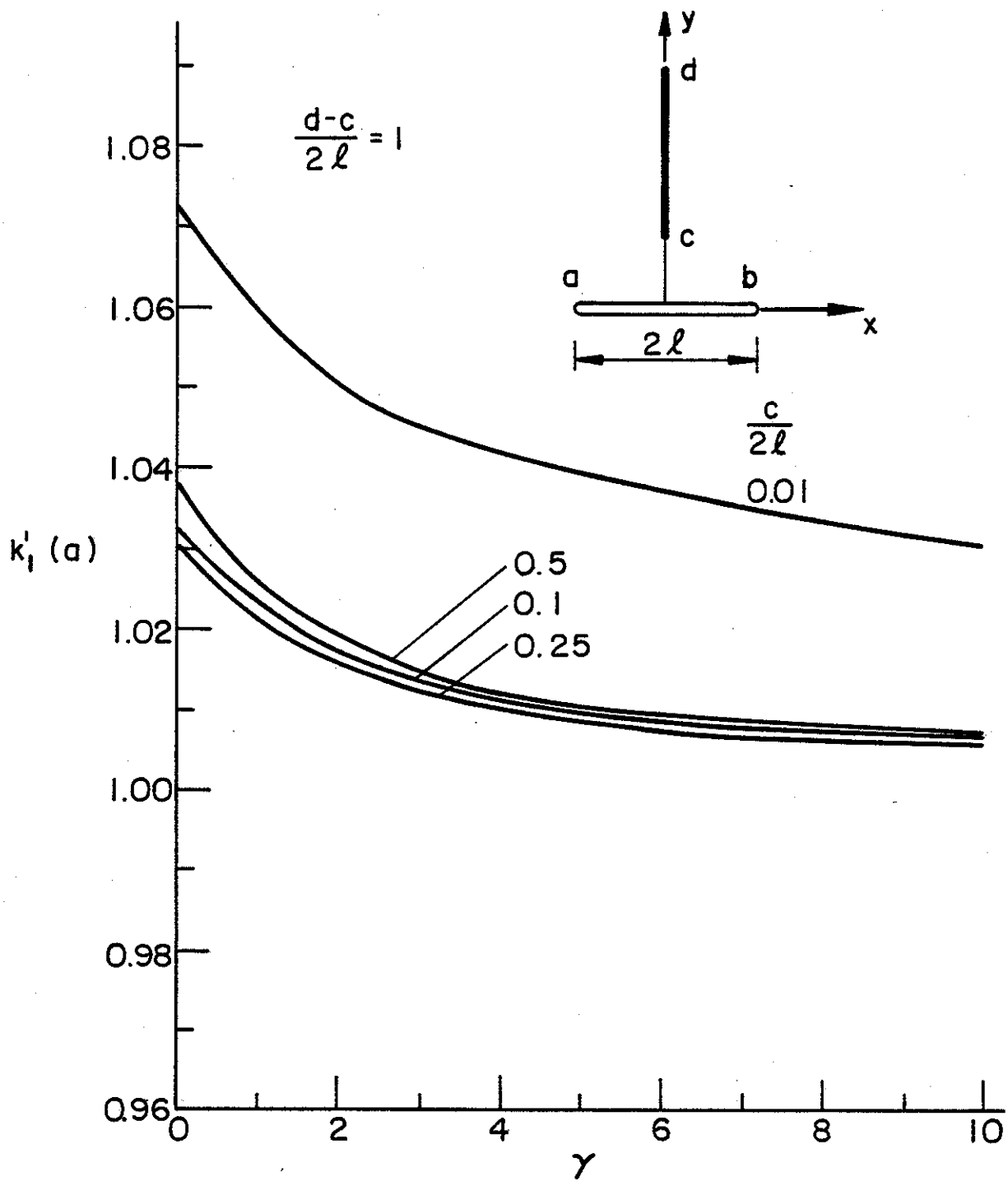

Figure 21. Mode I stress intensity factor at the crack tip $x = a = -\ell$; $\sigma^{\infty}_{yy} \neq 0$, $\sigma^{\infty}_{xx} = \sigma^{\infty}_{xy} = 0$, $\theta = \pi/2$, $\nu = 0.3$, $d-c = 2\ell$, $b = \ell$.

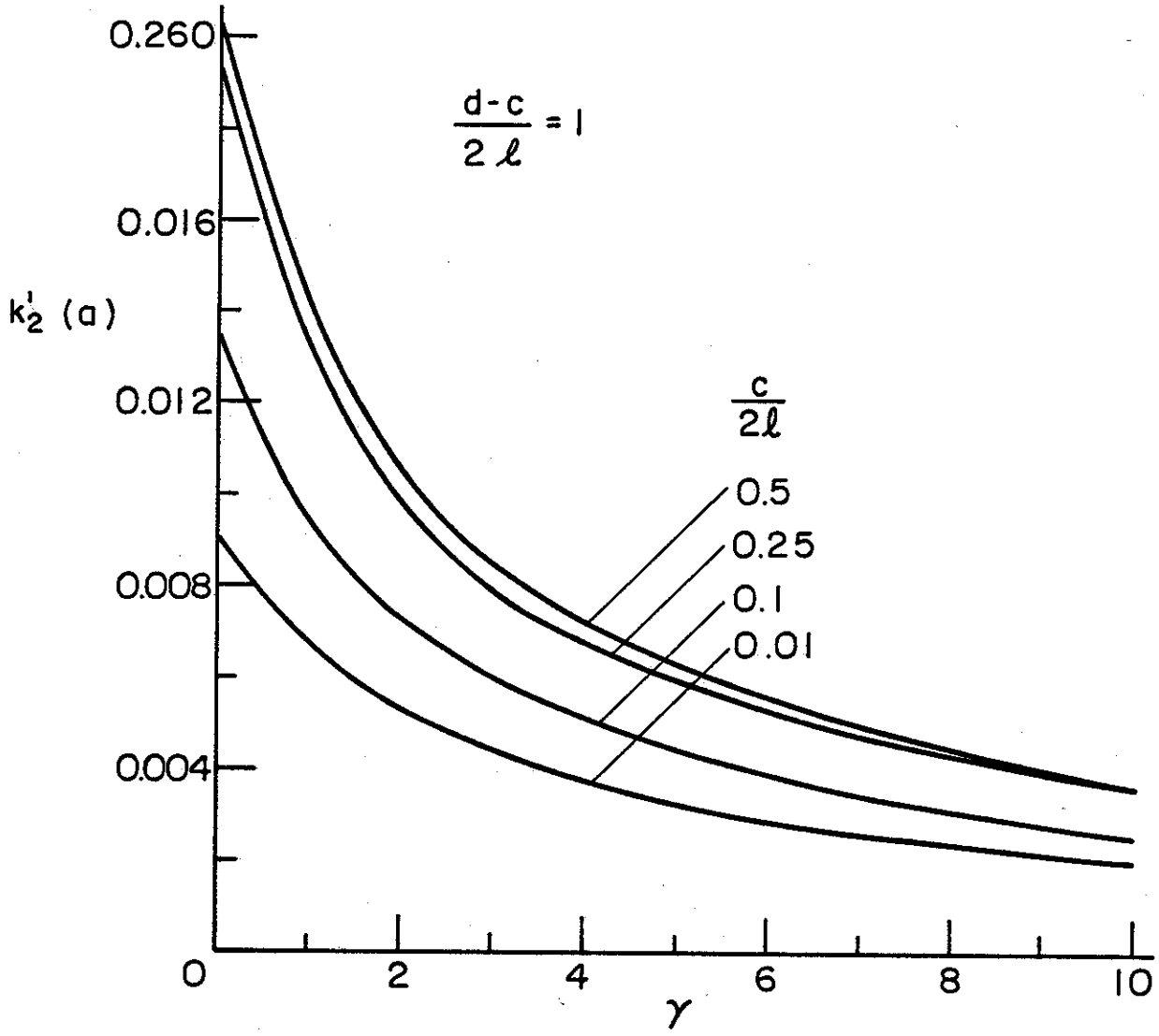

Figure 22. Mode II stress intensity factor at the crack tip $x = a = -\ell$; $\sigma^{\infty}_{yy} \neq 0$, $\sigma^{\infty}_{xx} = \sigma^{\infty}_{xy} = 0$, $\nu = 0.3$, $\theta = \pi/2$, $d-c = 2\ell$, $b = \ell$.

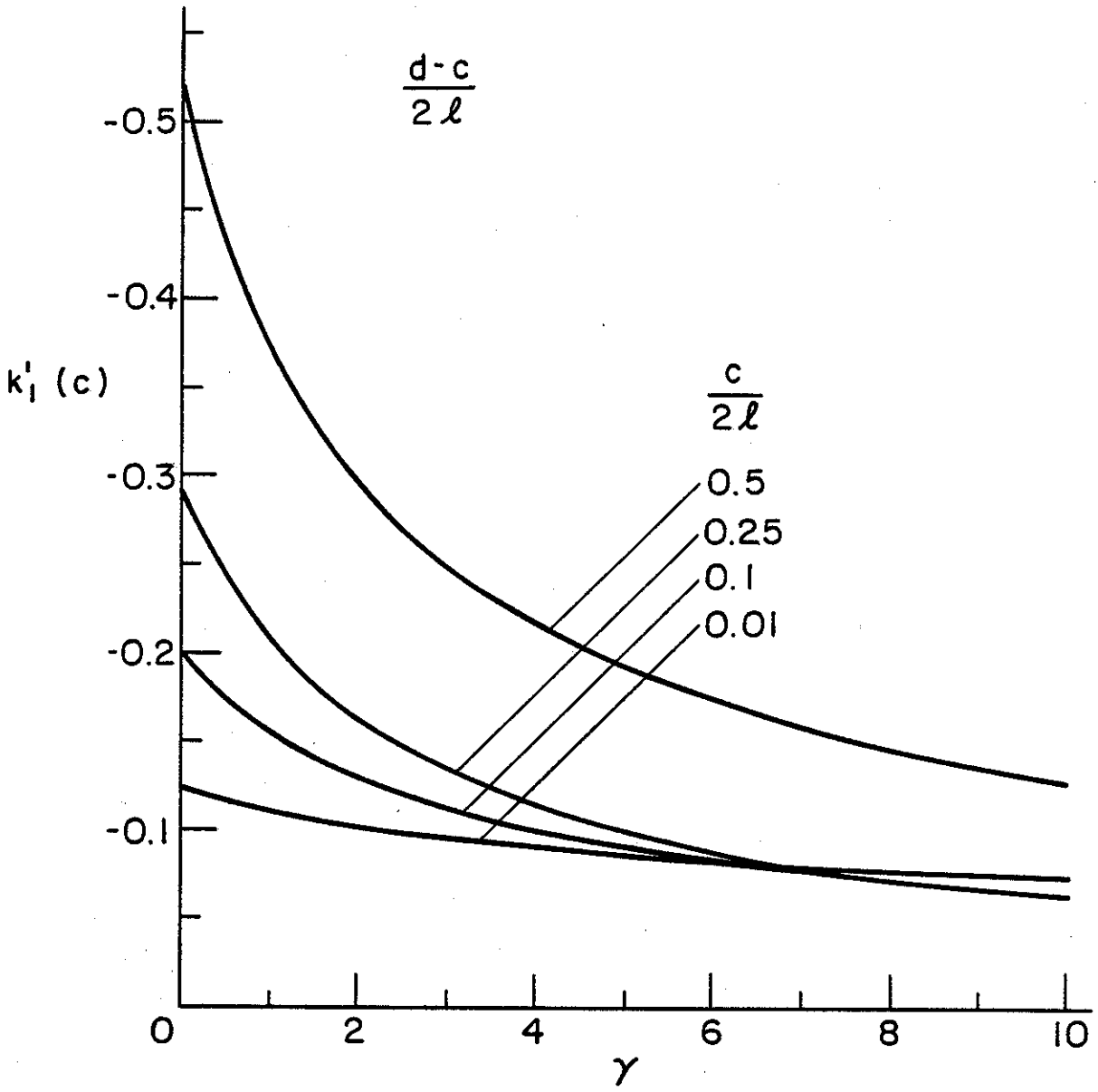

Figure 23. Stress intensity factor at the inclusion end y = c; $\sigma_{yy}^{\infty} \neq 0$, $\sigma_{xx}^{\infty} = \sigma_{xy}^{\infty} = 0$, $\nu = 0.3$, $\theta = \pi/2$, d-c = 2ℓ, b = ℓ = -a.

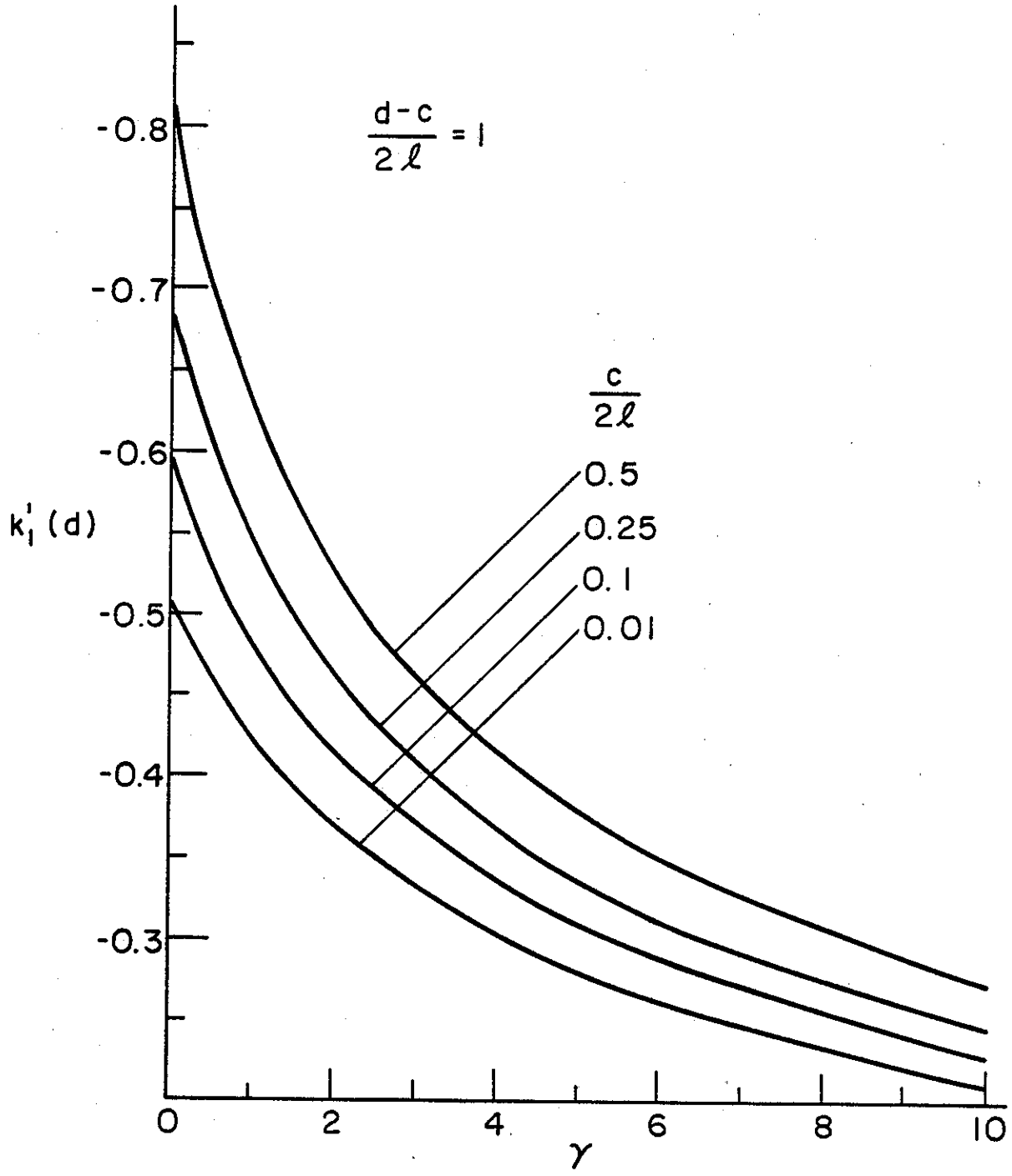

Figure 24. Stress intensity factor at the inclusion end y=d; $\sigma^{\infty}_{yy} \neq 0$, $\sigma^{\infty}_{xx} = \sigma^{\infty}_{xy} = 0$, $\nu = 0.3$, $\theta = \pi/2$, d-c = 2ℓ, b = ℓ = -a.

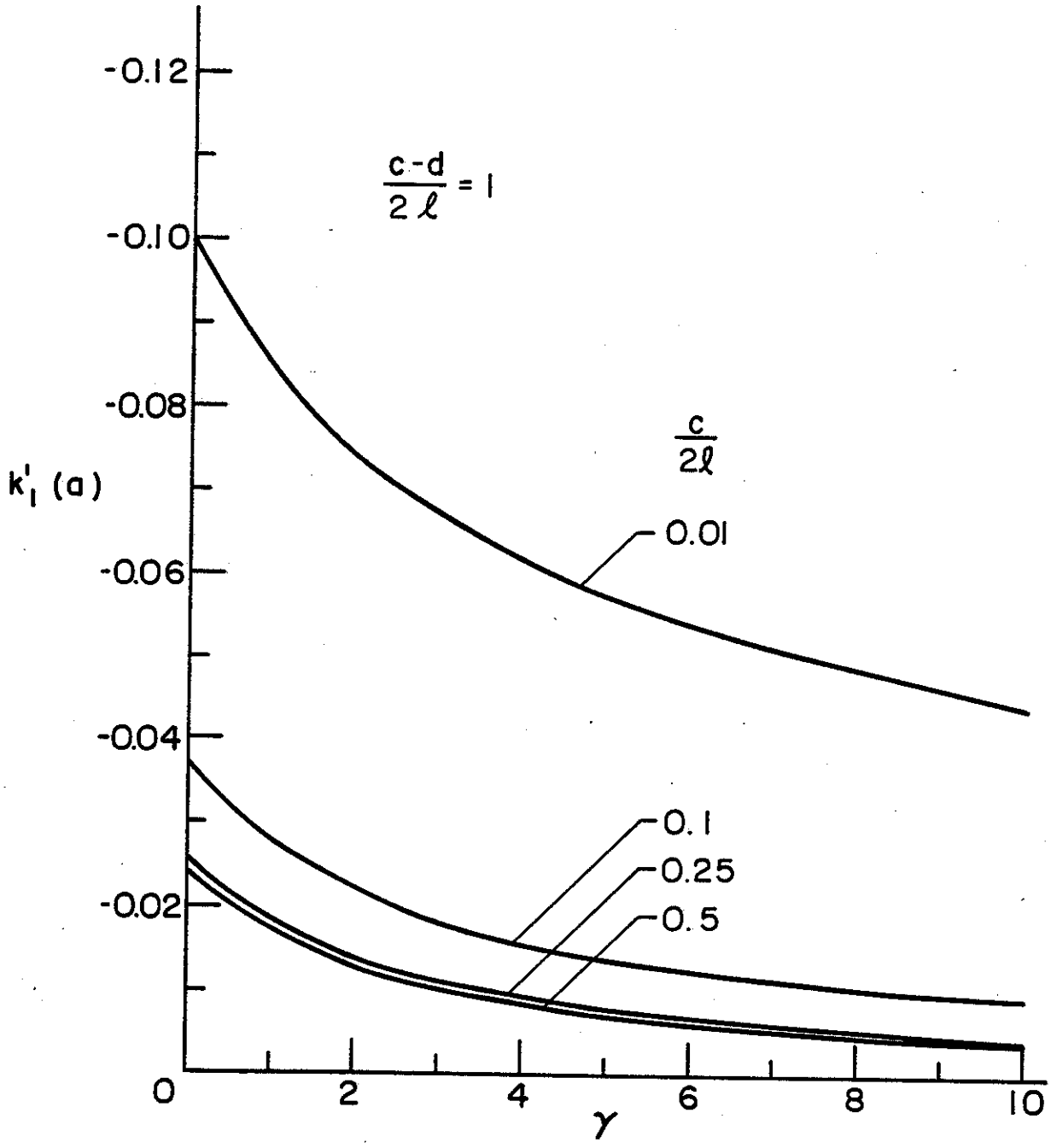

Figure 25. Mode I stress intensity factor at the crack tip $x = a = -\ell$; $\sigma_{xx}^{\infty} \neq 0$, $\sigma_{yy}^{\infty} = \sigma_{xy}^{\infty} = 0$, $\nu = 0.3$, $\theta = \pi/2$, $b = \ell$, $d-c = 2\ell$

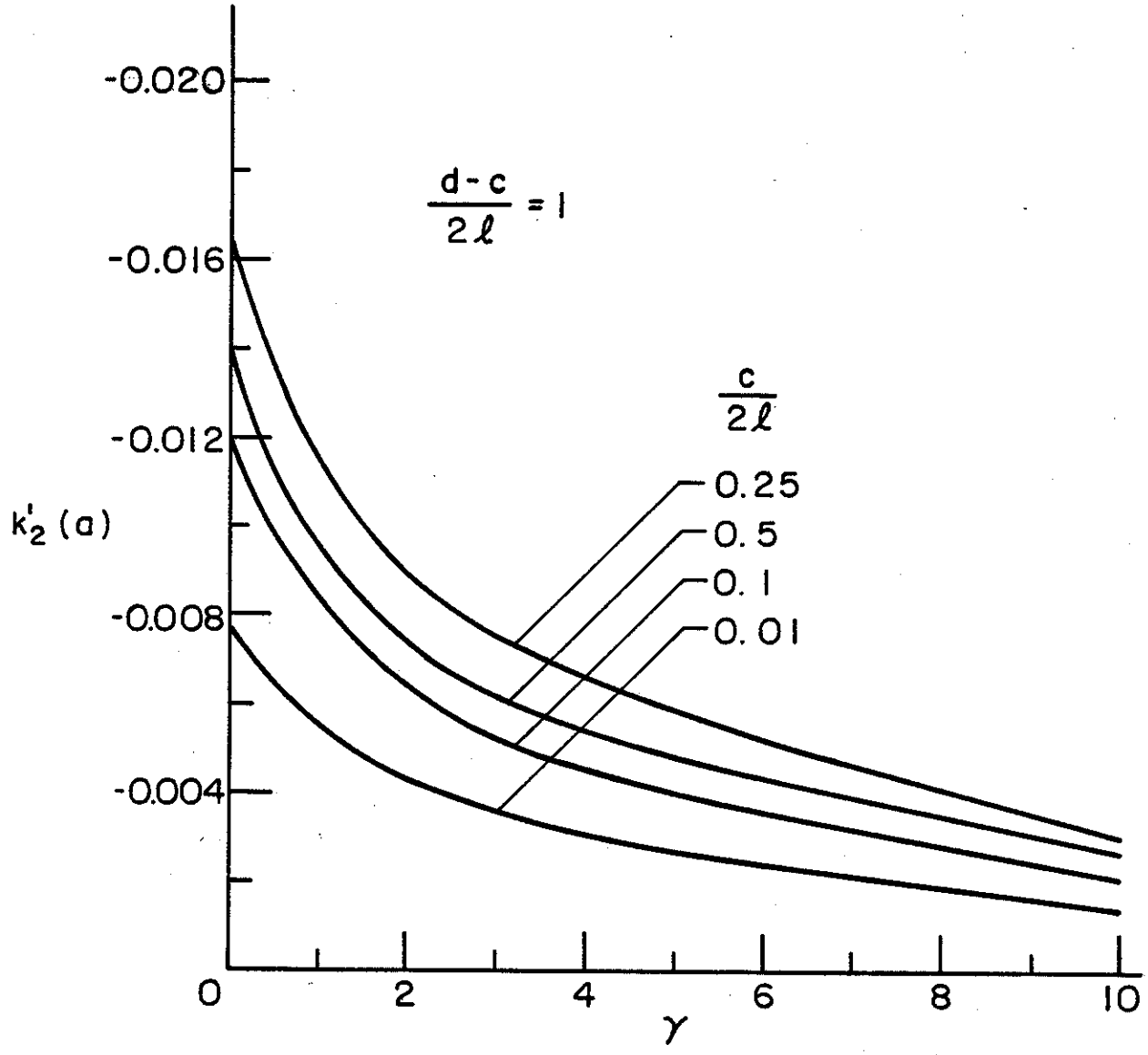

Figure 26. Mode II stress intensity factor at the crack tip x = a = $-\ell$; $\sigma^{\infty}_{xx} \neq 0$, $\sigma^{\infty}_{yy} = \sigma^{\infty}_{xy} = 0$, $\nu = 0.3$, $\theta = \pi/2$, d-c = 2ℓ, b = ℓ.

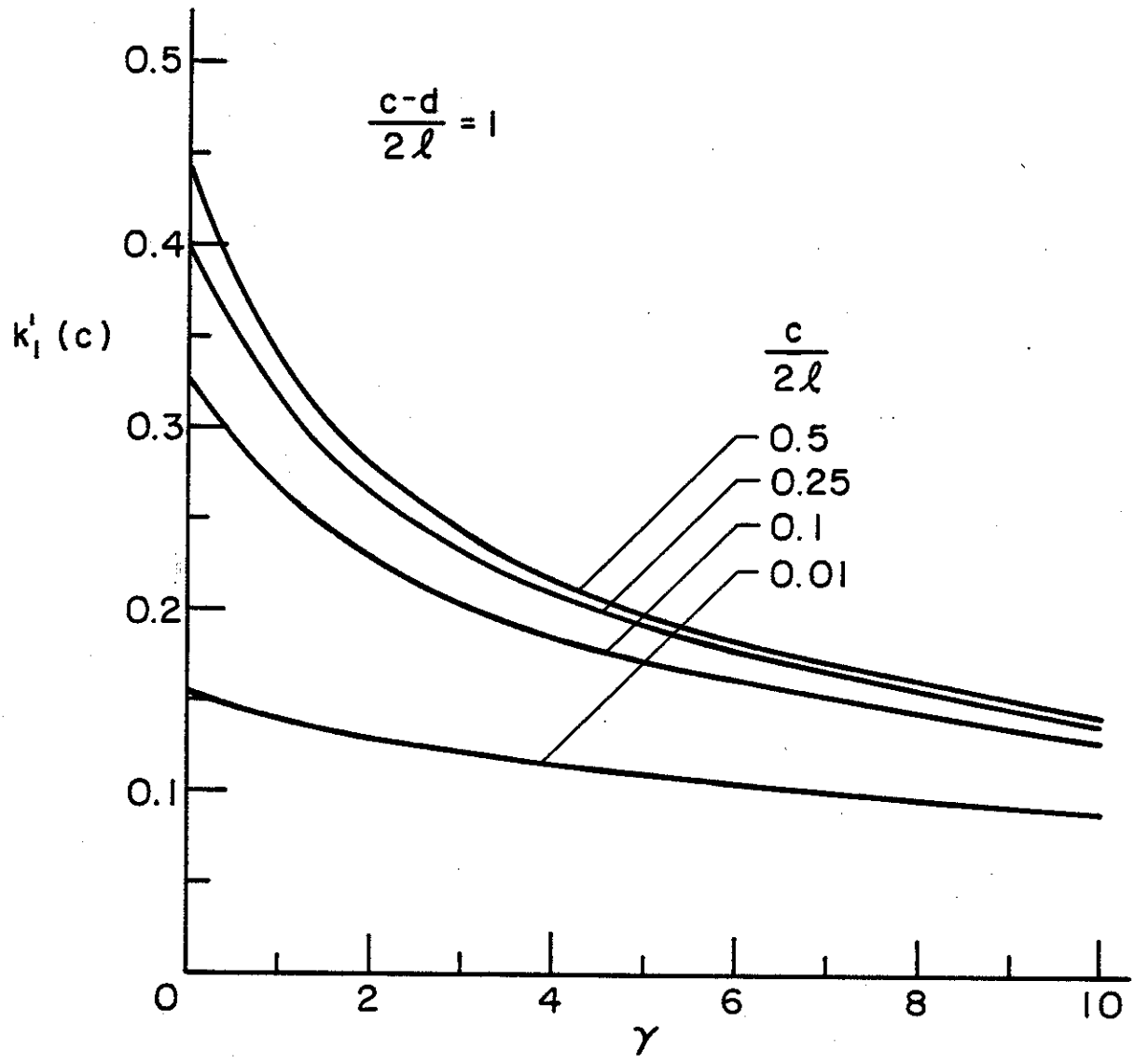

Figure 27. Stress intensity factor at the inclusion end y = c; $\sigma_{xx}^{\infty} \neq 0$, $\sigma_{yy}^{\infty} = \sigma_{xy}^{\infty} = 0$, $\nu = 0.3$, $\theta = \pi/2$, d-c = 2ℓ, b = ℓ = -a.

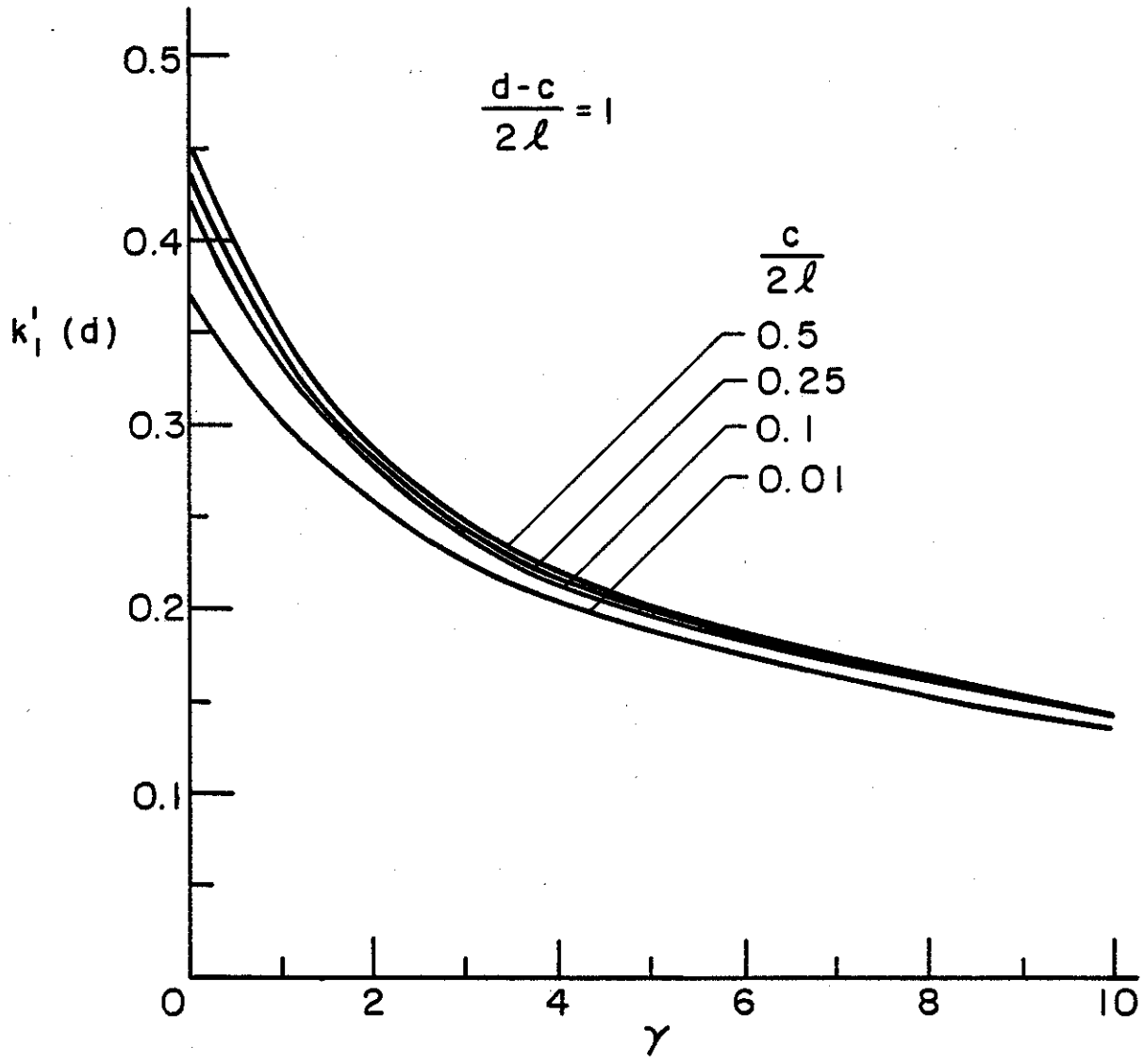

Figure 28. Stress intensity factor at the inclusion end y = d; $\sigma_{xx}^{\infty} \neq 0$, $\sigma_{yy}^{\infty} = \sigma_{xy}^{\infty} = 0$, $\nu = 0.3$, $\theta = \pi/2$, d-c = 2ℓ, b = ℓ = -a.

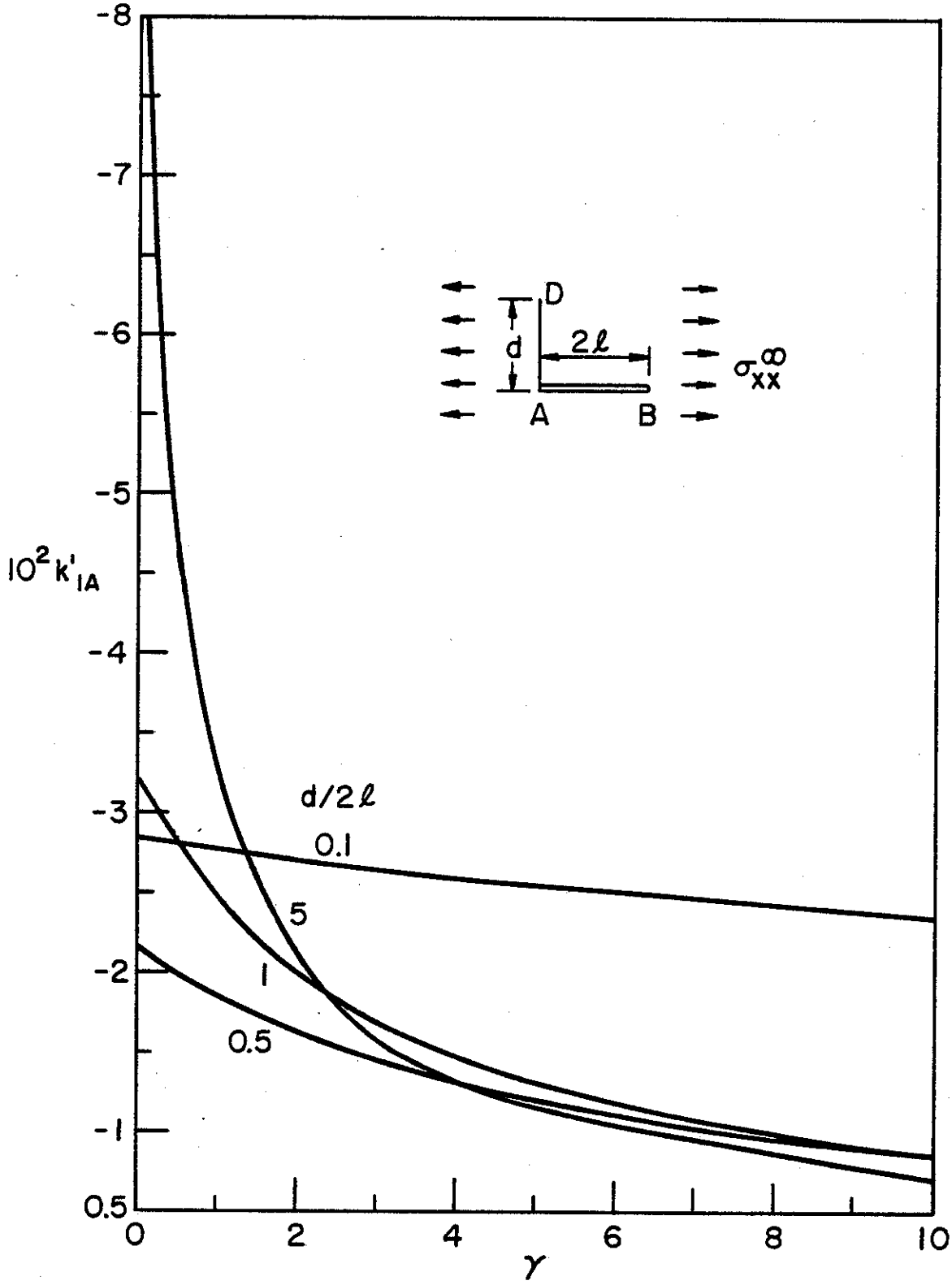

Figure 29. Normalized stress intensity factor for the inclusion-crack intersection problem for which $\theta = \pi/2$, $a = 0$, $b = 2\ell$, $c = 0$, $d/2\ell$ and γ variables. k'_{1A} for $\sigma_{xx}^{\infty} \neq 0$, $\sigma_{xy}^{\infty} = 0$, $\sigma_{yy}^{\infty} = 0$.

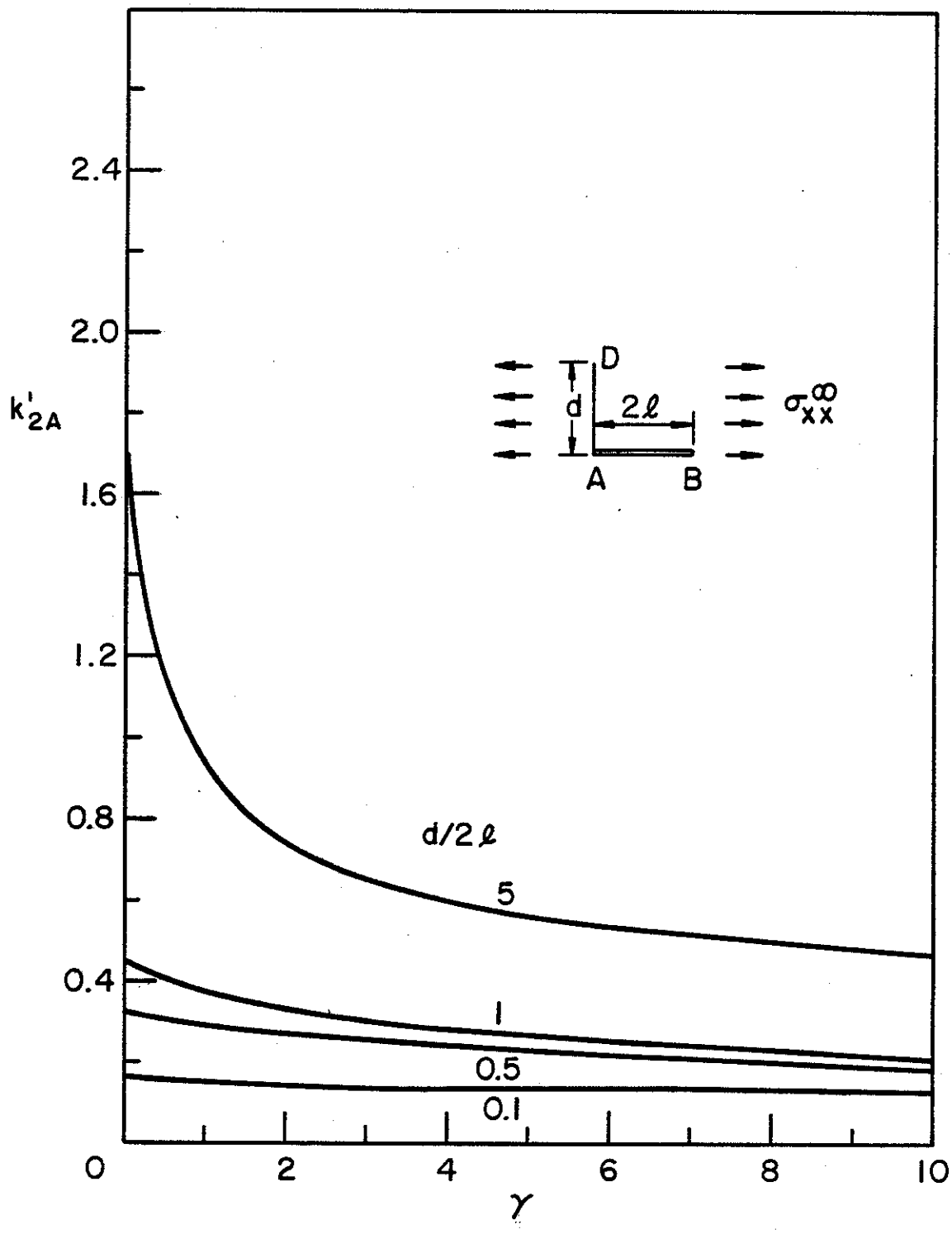

Figure 30. Normalized stress intensity factor for the inclusion-crack intersection problem for which $\theta = \pi/2$, $a = 0$, $b = 2\ell$, $c = 0$, $d/2\ell$ and γ variables. k'_{2A}, $\sigma^{\infty}_{xx} = 0$, $\sigma^{\infty}_{xy} = \sigma^{\infty}_{yy} = 0$.

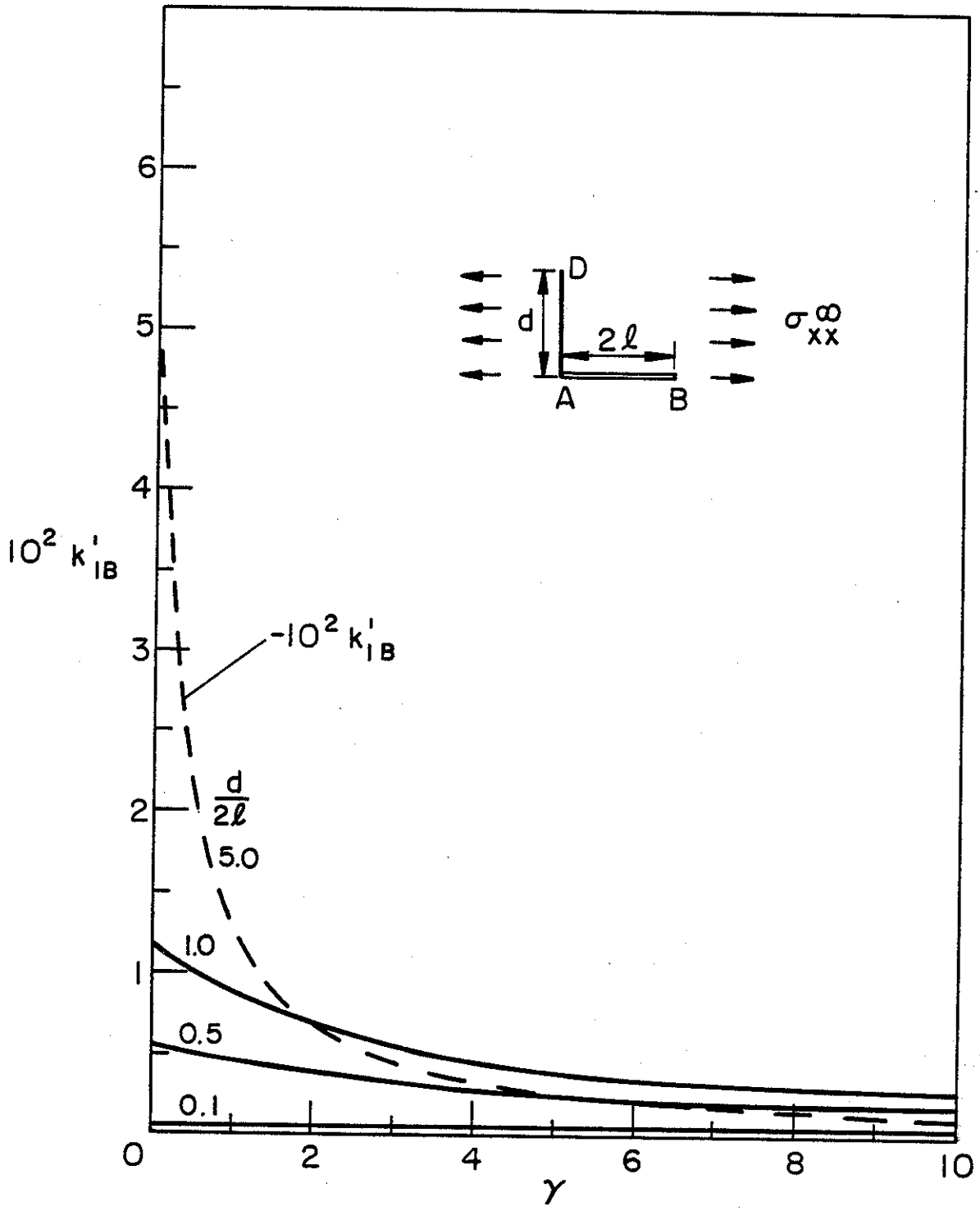

Figure 31. Normalized stress intensity factor for the inclusion-crack intersection problem for which $\theta = \pi/2$, $a = 0$, $b = 2\ell$, $c = 0$, $d/2\ell$ and γ variables. k'_{IB}, $\sigma^{\infty}_{xx} \neq 0$.

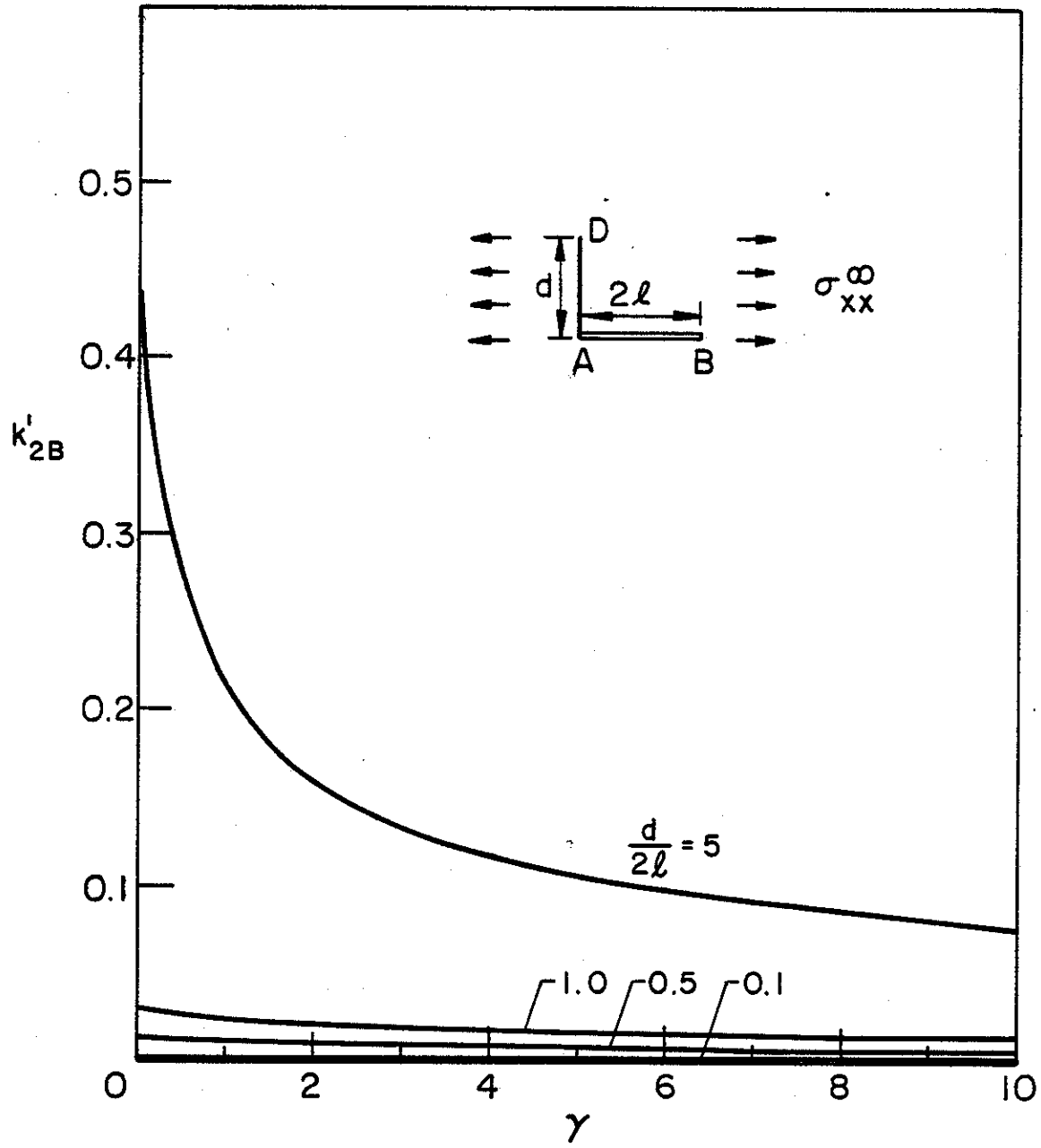

Figure 32. Normalized stress intensity factor for the inclusion-crack intersection problem for which $\theta = \pi/2$, $a = 0$, $b = 2\ell$, $c = 0$, $d/2\ell$ and γ variables. k_{2B} , $\sigma^{\infty}_{xx} \neq 0$.

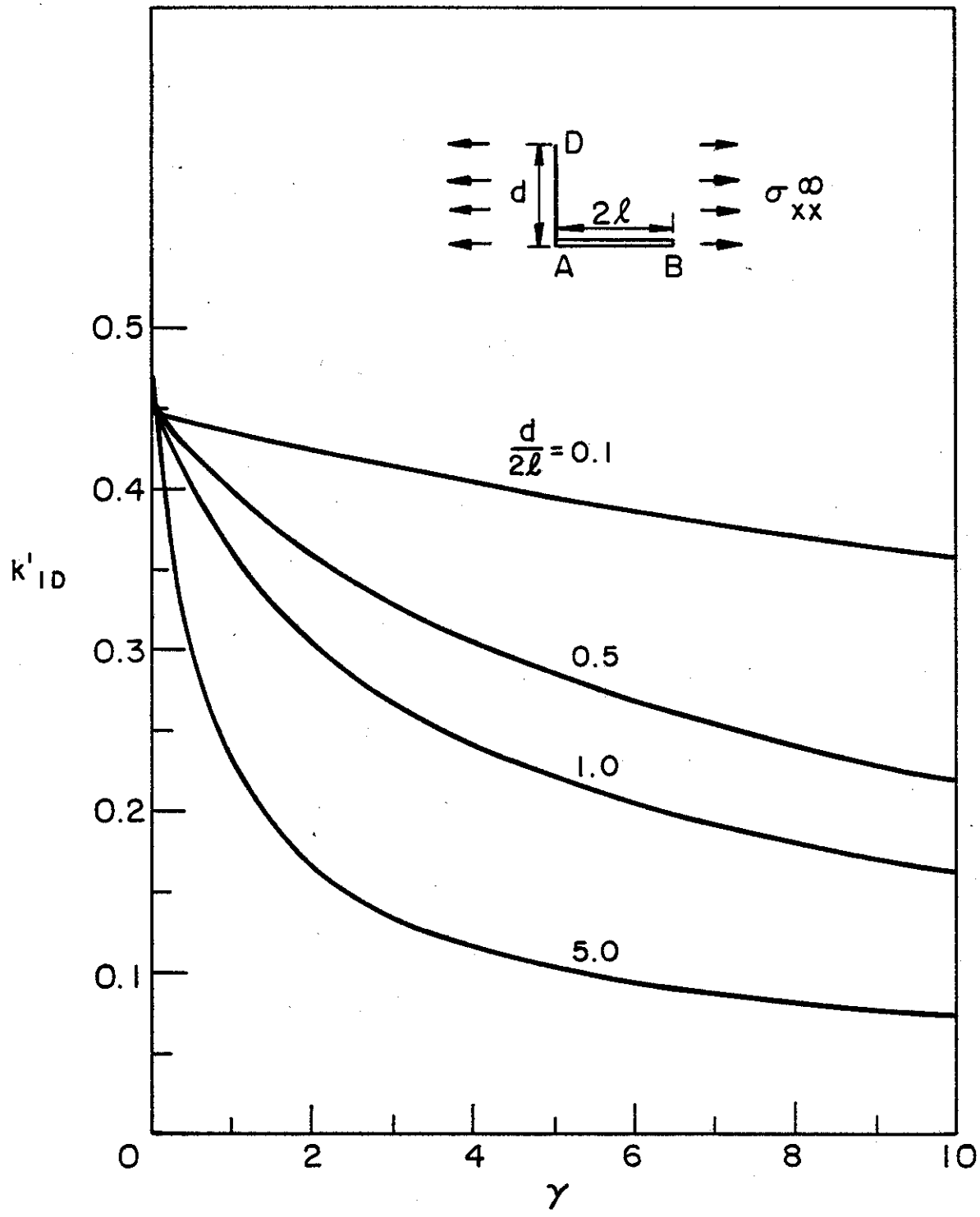

Figure 33. Normalized stress intensity factor for the inclusion-crack intersection problem for which $\theta = \pi/2$, a = 0, b = 2ℓ, c = 0, d/2ℓ and γ variables. k_{1D} , $\sigma^{\infty}_{xx} = 0$.

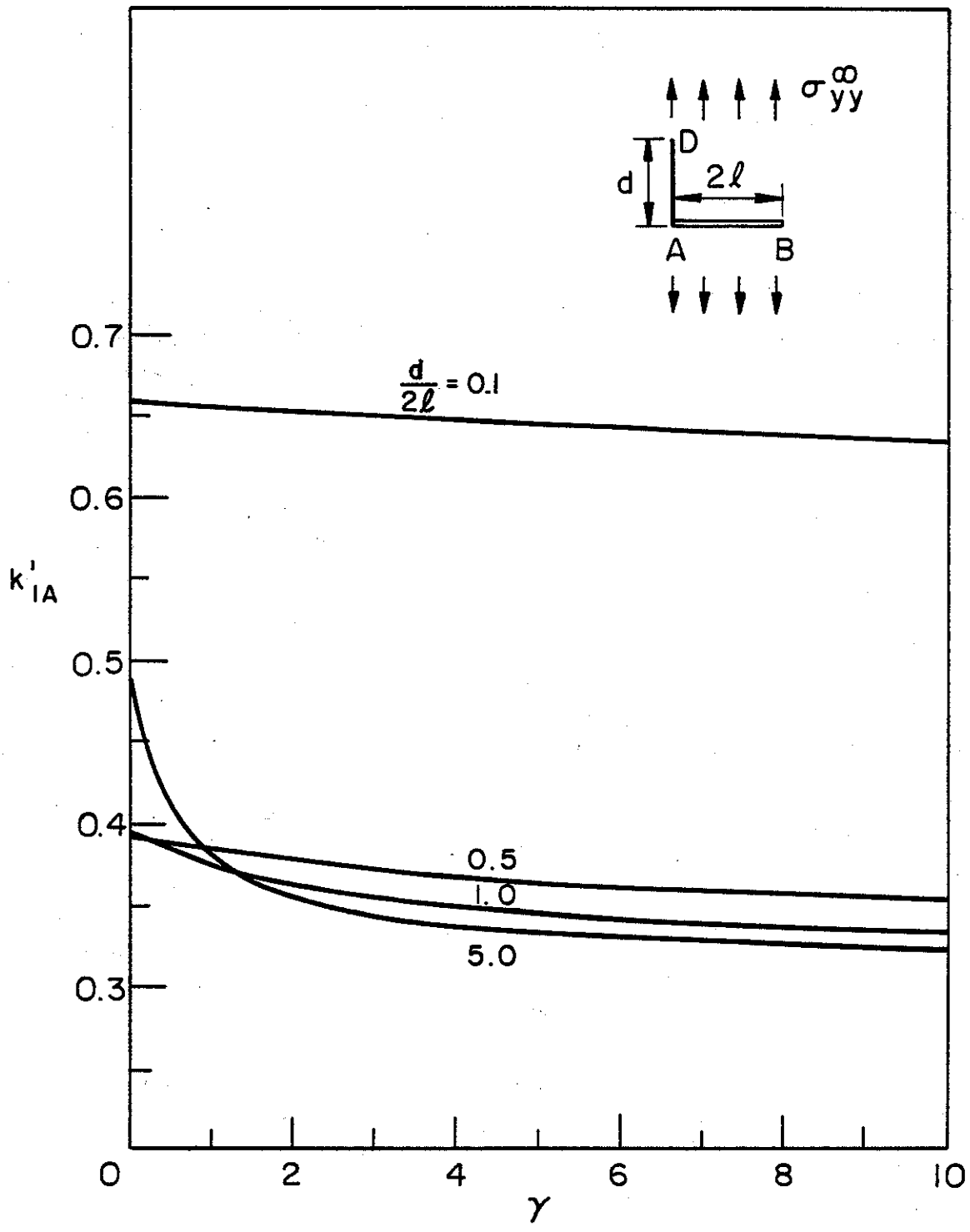

Figure 34. Normalized stress intensity factor for the inclusion-crack intersection problem for which $\theta = \pi/2$, a = 0, b = 2ℓ, c = 0, d/2ℓ and γ variables. k_{IA} , $\sigma^{\infty}_{yy} \neq 0$.

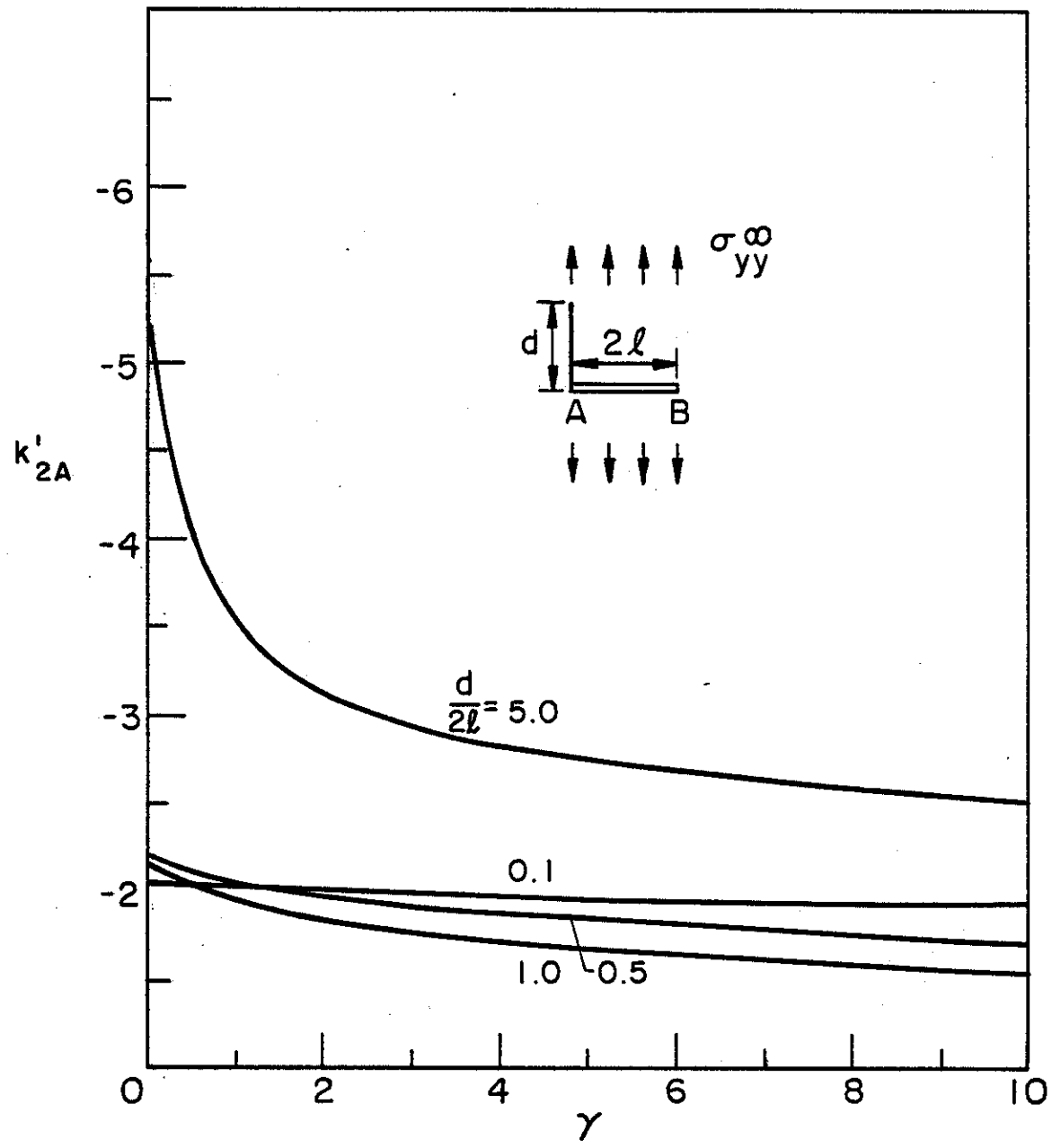

Figure 35. Normalized stress intensity factor for the inclusion-crack intersection problem for which $\theta = \pi/2$, a = 0, b = 2ℓ, c = 0, d/2ℓ and γ variables. k_{2A} , $\sigma^{\infty}_{yy} \neq 0$.

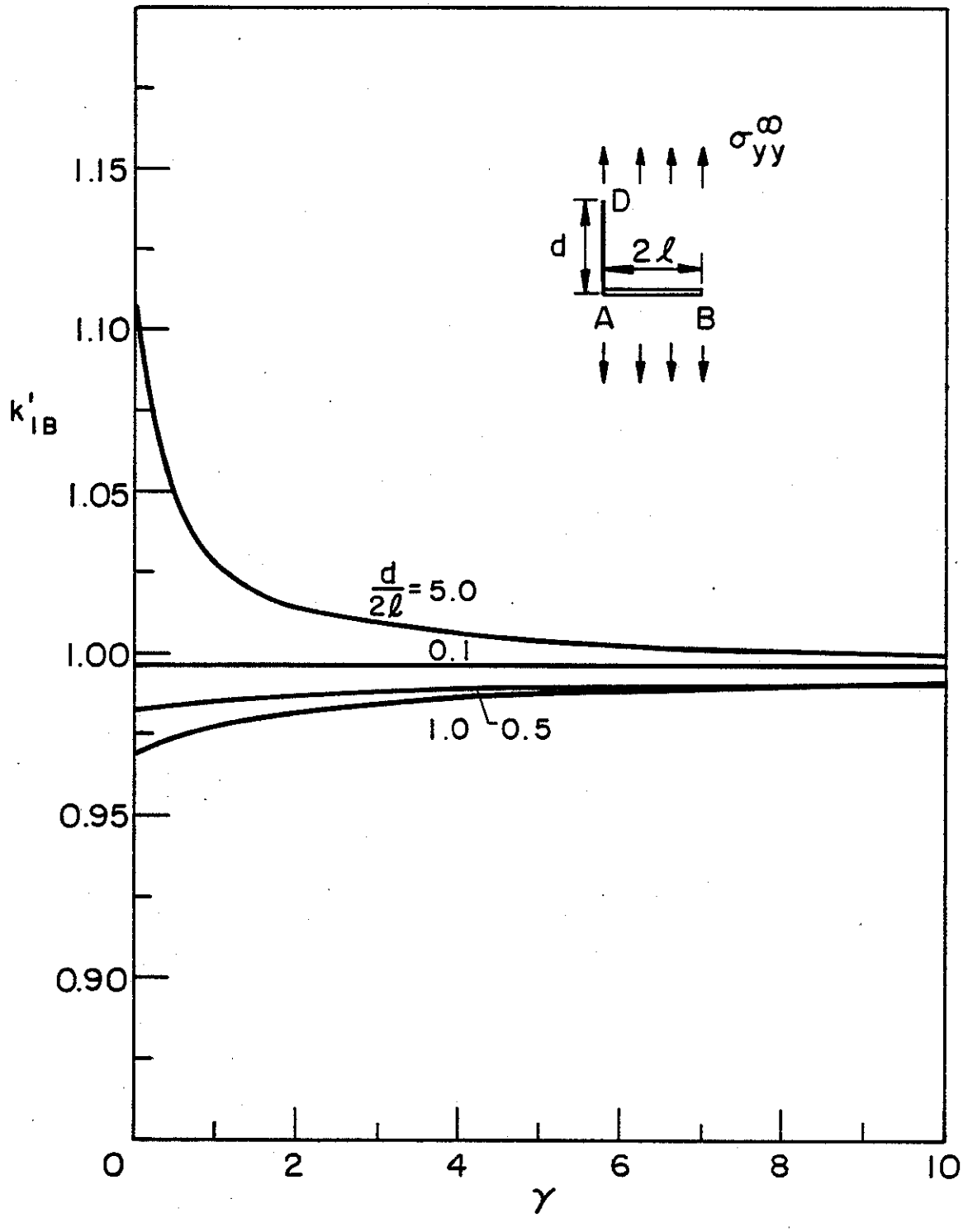

Figure 36. Normalized stress intensity factor for the inclusion-crack intersection problem for which $\theta = \pi/2$, a = 0, b = 2ℓ, c = 0, $d/2\ell$ and γ variables. k_{IB} , $\sigma^{\infty}_{yy} \neq 0$.

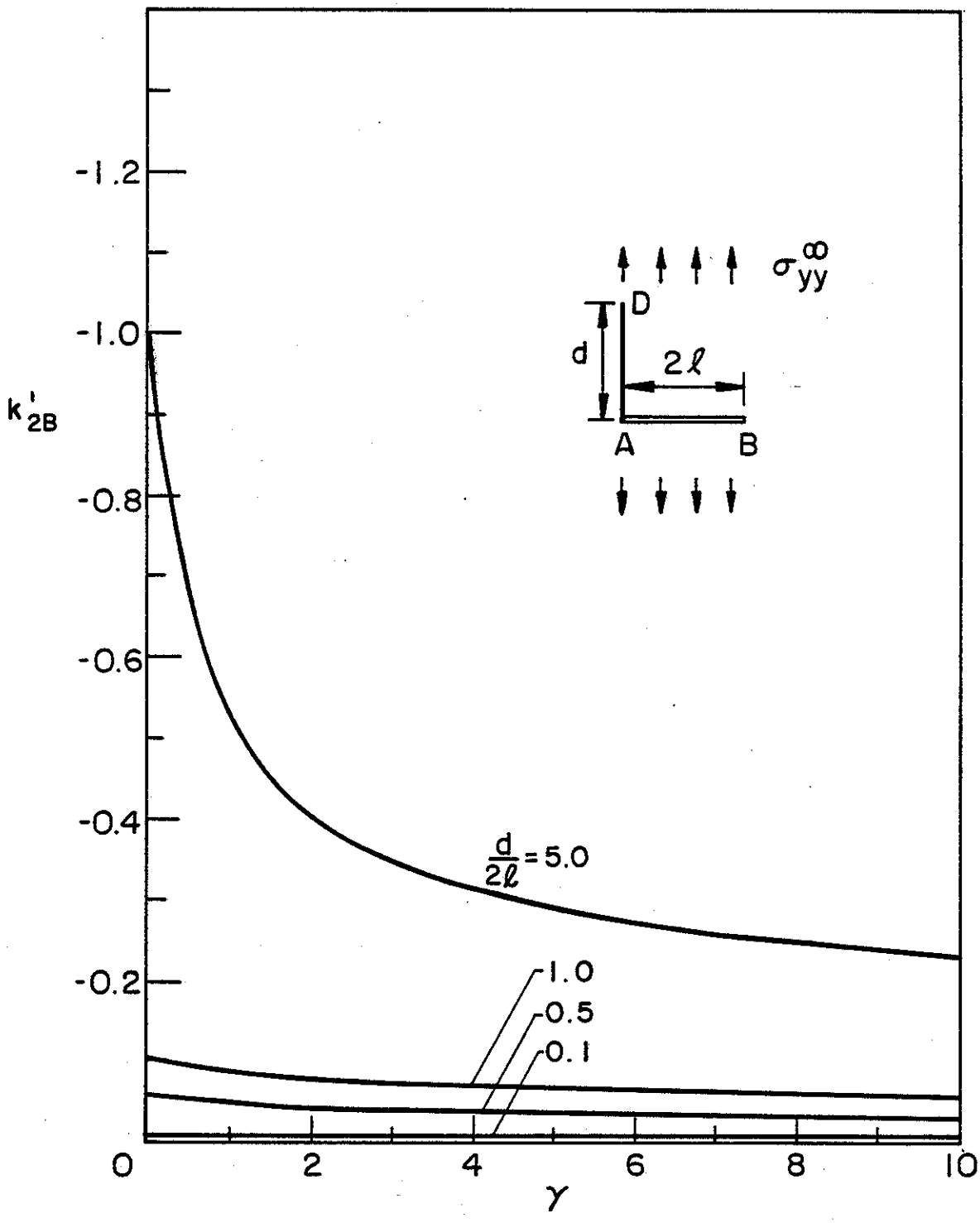

Figure 37. Normalized stress intensity factor for the inclusion-crack intersection problem for which $\theta = \pi/2$, $a = 0$, $b = 2\ell$, $c = 0$, $d/2\ell$ and γ variables. k'_{2B}, $\sigma^{\infty}_{yy} \neq 0$.

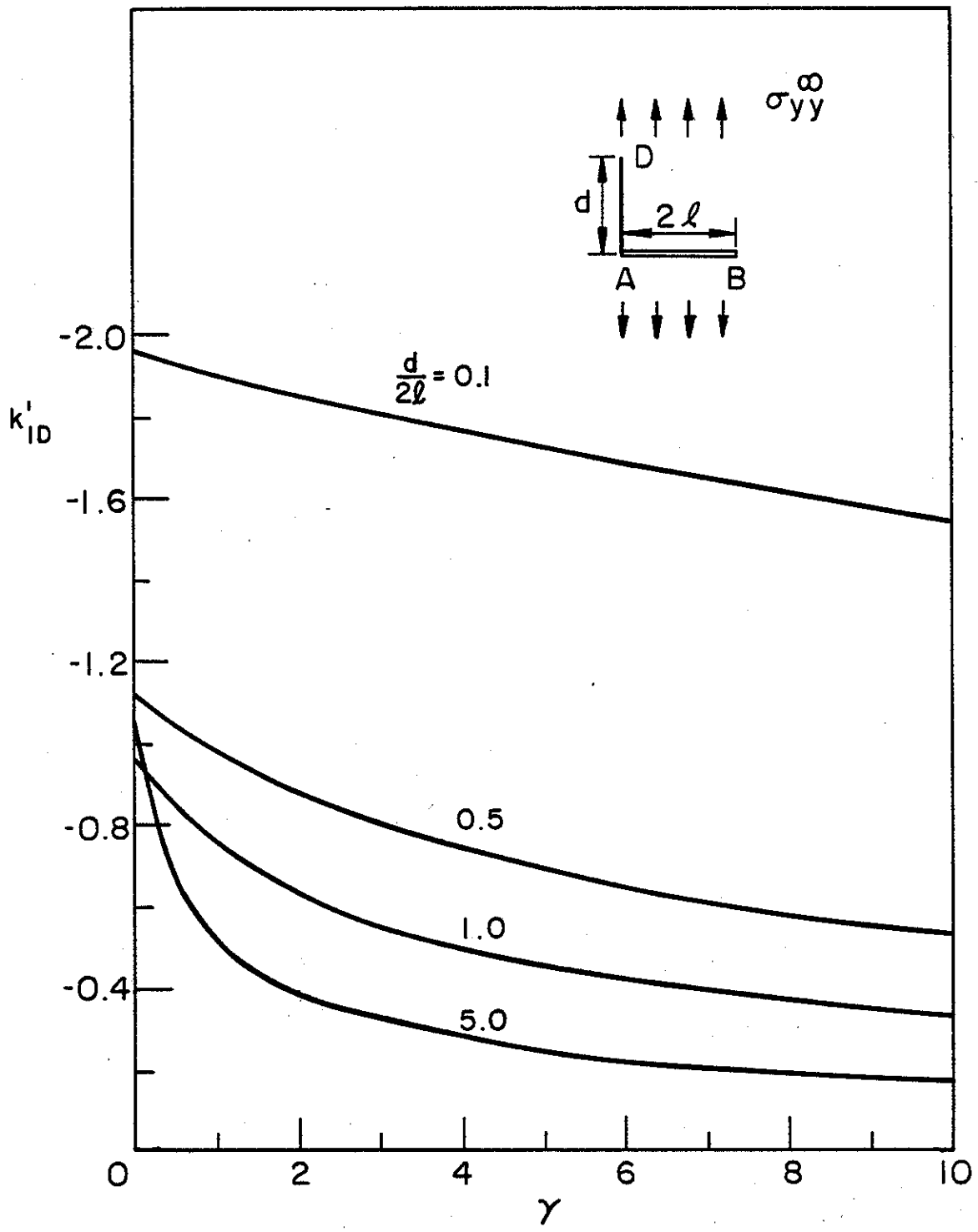

Figure 38. Normalized stress intensity factor for the inclusion-crack intersection problem for which $\theta = \pi/2$, $a = 0$, $b = 2\ell$, $c = 0$, $d/2\ell$ and γ variables. k_{1D}, $\sigma_{yy}^{\infty} \neq 0$.

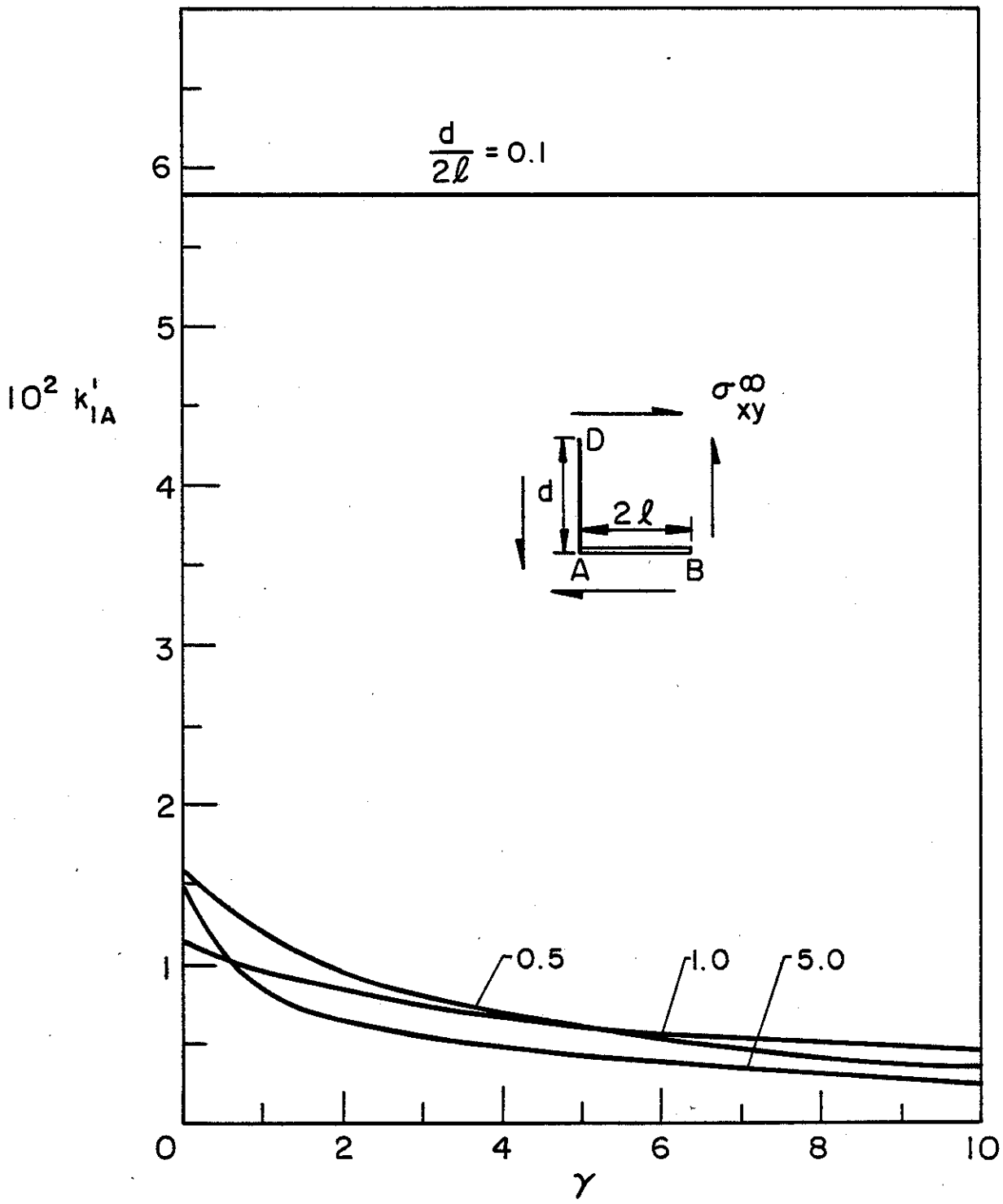

Figure 39. Normalized stress intensity factor for the inclusion-crack intersection problem for which $\theta = \pi/2$, a = 0, b = 2ℓ, c = 0, $d/2\ell$ and γ variables. k_{1A} , $\sigma^{\infty}_{xy} \neq 0$.

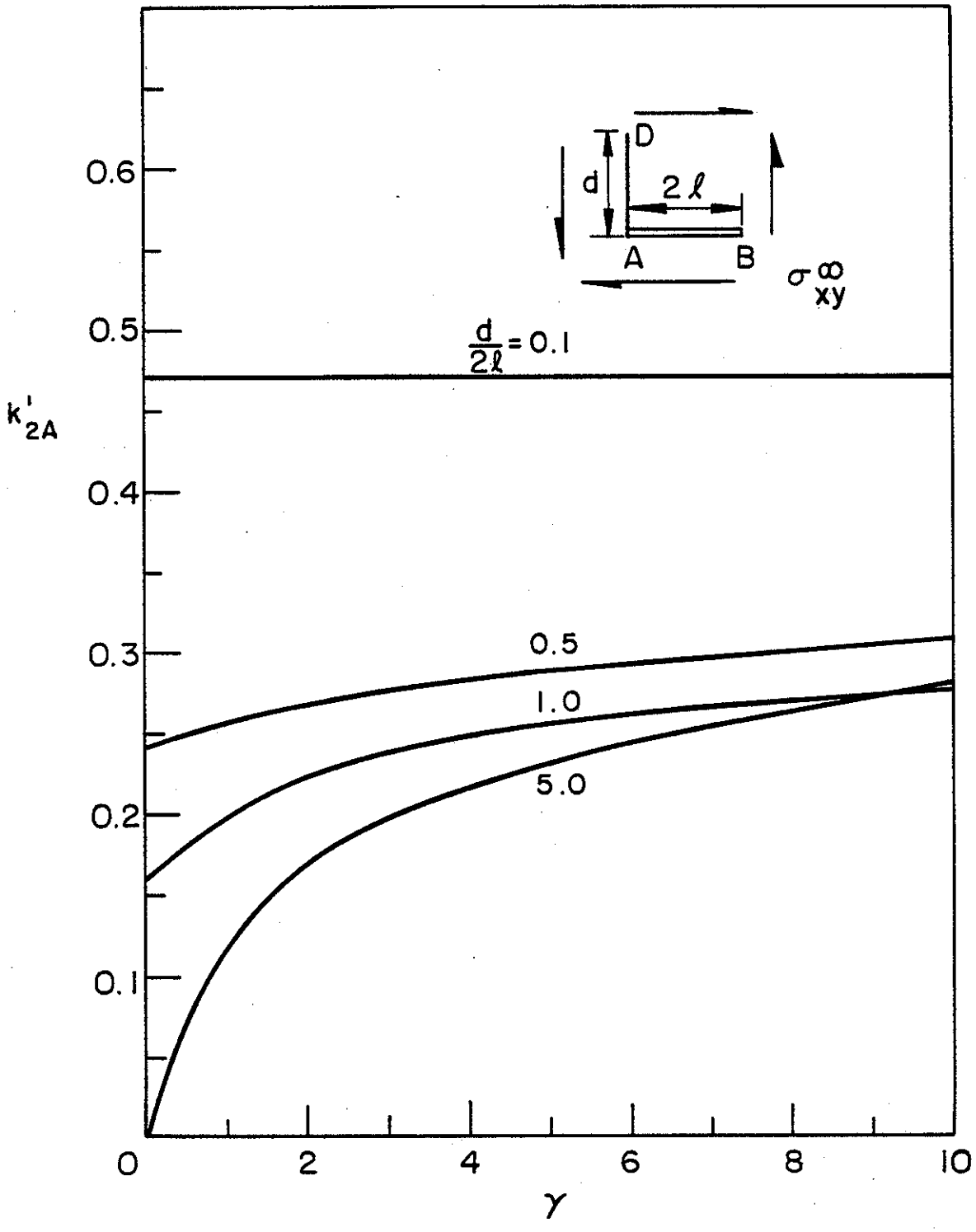

Figure 40. Normalized stress intensity factor for the inclusion-crack intersection problem for which $\theta = \pi/2$, $a = 0$, $b = 2\ell$, $c = 0$, $d/2\ell$ and γ variables. k_{2A}, $\sigma^{\infty}_{xy} \neq 0$.

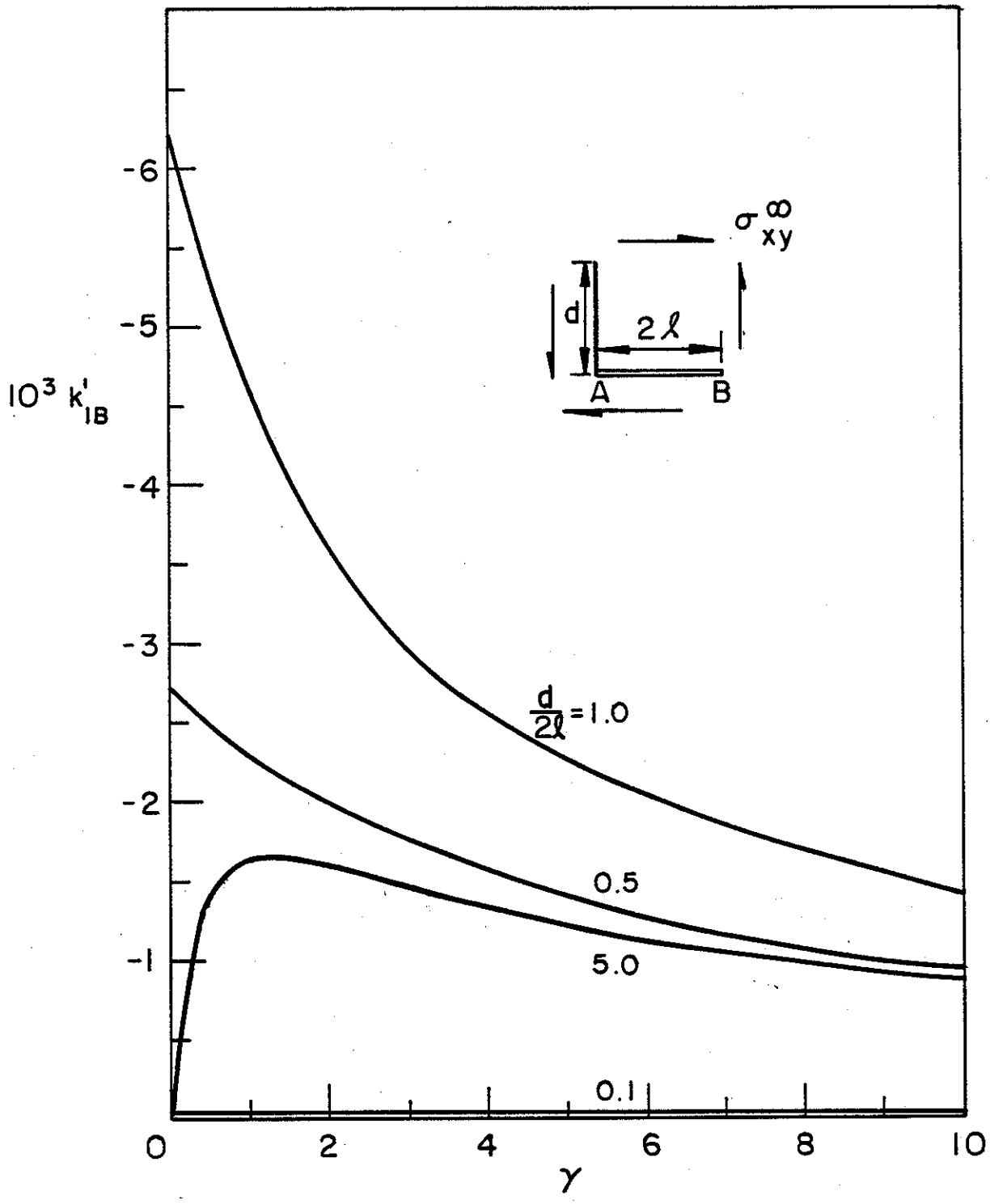

Figure 41. Normalized stress intensity factor for the inclusion-crack intersection problem for which $\theta = \pi/2$, a = 0, b = 2ℓ, c = 0, $d/2\ell$ and γ variables. k'_{IB} , $\sigma^{\infty}_{xy} \neq 0$.

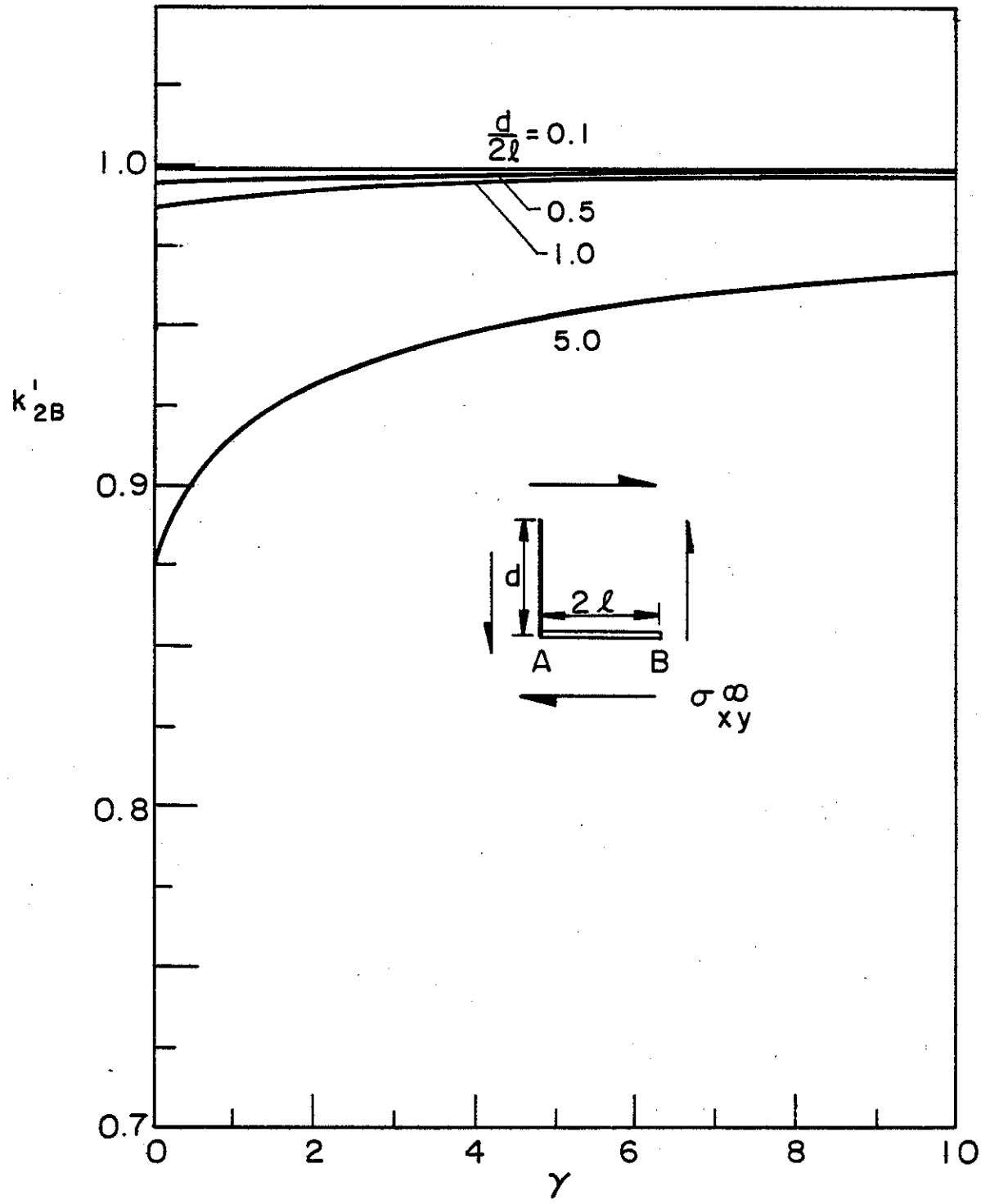

Figure 42. Normalized stress intensity factor for the inclusion-crack intersection problem for which $\theta = \pi/2$, a = 0, b = 2ℓ, c = 0, $d/2\ell$ and γ variables. k'_{2B}, $\sigma^{\infty}_{xy} \neq 0$.

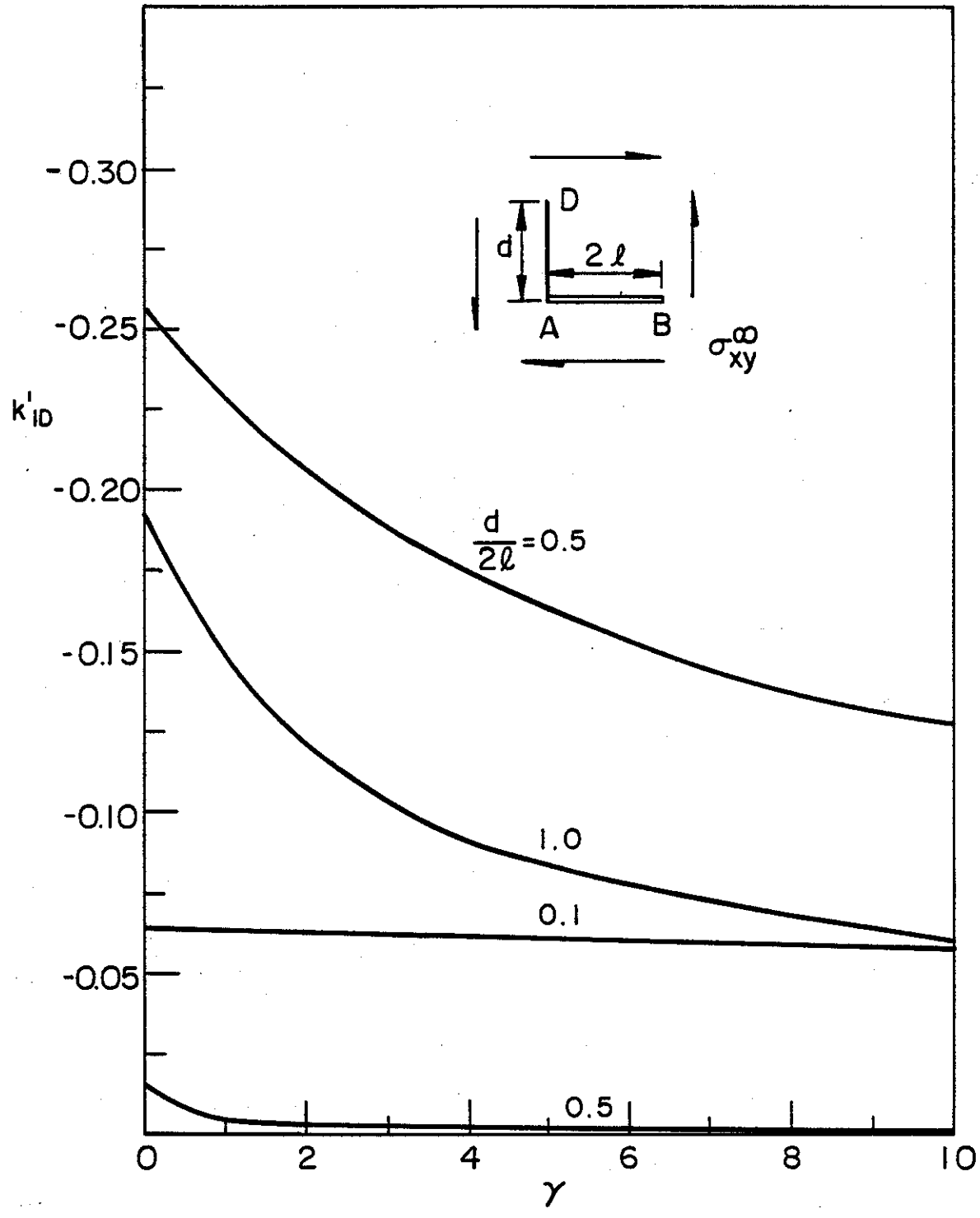

Figure 43. Normalized stress intensity factor for the inclusion-crack intersection problem for which $\theta = \pi/2$, $a = 0$, $b = 2\ell$, $c = 0$, $d/2\ell$ and γ variables. k'_{1D}, $\sigma^{\infty}_{xy} \neq 0$.

APPENDIX B

A PLATE WITH AN INTERNAL FLAW UNDER EXTENSION OR BENDING

1. Introduction

Some of the common flaws in pipe welds are planar internal flaws. In studying the question of flaw evaluation in pipes containing multiple flaws, an important problem is therefore the problem of interaction between the internal planar flaws and between flaws and the free surfaces. The general three-dimensional elasticity problem is, at the present time, analytically intractable. However, the previous studies show that the application of the "line spring" model to surface cracks in plates and shells seems to give results which agree with very limited existing finite element results reasonably well [1,2].

The objective of this study is to extend the application of the line spring model to internal cracks and, by comparing the results with the existing finite element solutions, to establish its degree of accuracy. The broader aim is, of course, to use the technique in the interaction problems of multiple internal cracks the solution of which is needed and is not available. After solving the single crack problem and showing that the stress intensity factors compare quite well with the existing solutions, extensive results are obtained for an internal crack with an elliptic or a rectangular boundary in a plate under extension or bending.

2. On the Formulation of the Problem

The formulation of the general problem follows very closely the treatment given in [1]. In the special symmetric crack geometry and symmetric loading shown in Fig. 1 the tension and bending problems are uncoupled. Thus, the integral equations given in [1] would also be uncoupled and the formulation and the method of solution would remain

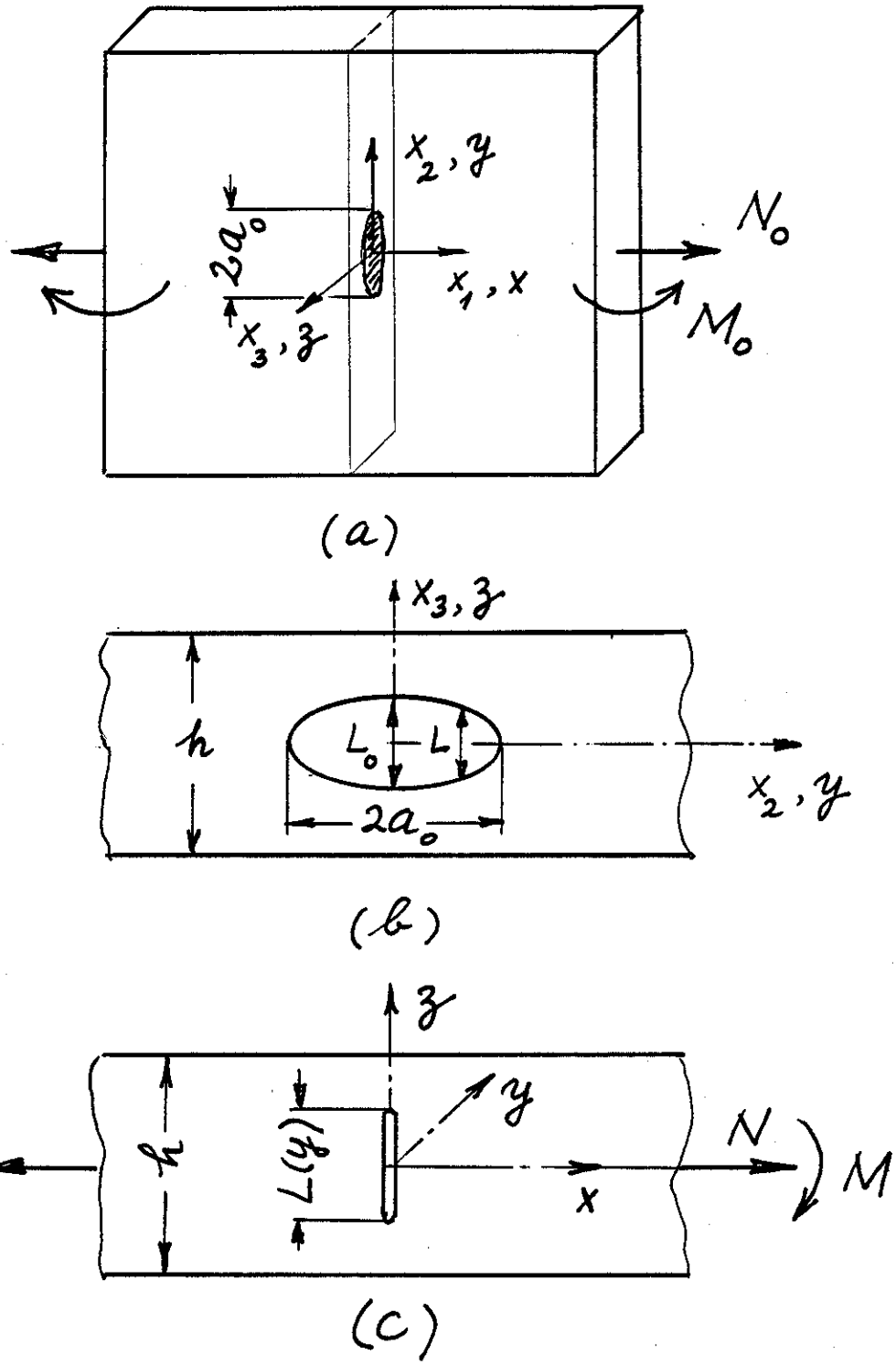

Fig. 1 Geometry and notation for a plate containing an internal planar crack.

the same. However, in order to solve the problem new stress intensity shape functions g_t and g_b for the new crack geometry under consideration are needed. In terms of these functions the Mode I stress intensity factor K along the crack front is given by

$$K(y) = \sqrt{h}\,[g_t\sigma(y) + g_b m(y)] \tag{1}$$

where g_t and g_b are functions of L/h and σ and m are defined by

$$\sigma(y) = \frac{N(y)}{h} \quad , \quad m(y) = \frac{6M(y)}{h^2} \quad . \tag{2}$$

In (1) and (2) y is the coordinate along the crack normalized with respect to the half crack length a_o, i.e., $y = x_2/a_o$ (Fig. 1 a,b), and N(y) and M(y) are membrane and bending resultants along the net ligament (Fig. 1c).

The unknown functions $\sigma(y)$ and m(y) are determined after solving the integral equations [1], whereas the shape functions g_t and g_b are obtained from the corresponding plane strain problem (Fig. 1c). The stress intensity factors K_N and K_M obtained from the solution of the plane strain problem described in Fig. 1c under membrane and bending resultants N and M are given by Table 1 [3].

Table 1. Stress intensity factors for centrally cracked plate subjected to tension (N) or bending (M) under plane strain conditions. (σ=N/h, m=6M/h^2)

L/h	$\frac{K_N}{\sigma\sqrt{\pi L/2}}$	$\frac{K_M}{m\sqrt{\pi L/2}}$
0.05		0.1500
0.1	1.0060	0.3000
0.2	1.0246	0.6004
0.3	1.0577	0.9031
0.4	1.1094	1.2135
0.5	1.1867	1.5435
0.6	1.3033	1.9179
0.7	1.4884	2.3918
0.8	1.8169	3.1113
0.9	2.585	4.6653
0.95	4.252	6.8526

In order to use in the analysis the results given in Table 1 must be represented by analytic expressions. Thus, from (1) observing that

$$K = K_N + K_M \ ,$$

$$K_N = \sigma\sqrt{h}\ g_t \ , \quad K_M = m\sqrt{h}\ g_b \tag{3}$$

and by expressing

$$g_t(L/h) = \sqrt{\pi L/h} \sum_{j=1}^{n} b_j (L/h)^{2(j-1)} \ , \tag{4}$$

$$g_b(L/h) = \sqrt{\pi L/h} \sum_{j=1}^{n} c_j (L/h)^{j-1} \ . \tag{5}$$

The coefficients b_j and c_j may be obtained by curve-fitting (see Table 2).

3. The Results for a Single Crack

In the analysis used for the present study the contour of the planar crack described by $L = L(x_2)$ or $L = L(y)$ can be any function. If,

Table 2. The coefficients b_j and c_j for the shape functions g_t and g_b (Eqs. 4 and 5).

j	b_j	c_j
1	0.7071	0.1013
2	0.4325	-2.7775
3	-0.1091	90.3734
4	7.3711	-862.4307
5	-57.7894	4843.4692
6	271.1551	-17069.1142
7	-744.4204	38813.4897
8	1183.9529	-56865.3055
9	-1001.4920	51832.6941
10	347.9786	-26731.2995
11		5959.4888

however, some subcritical crack growth takes place in the medium, the contour defining the crack is usually a convex smooth function. Here we will give examples for two contours, namely an ellipse and a rectangle, which roughly speaking may be considered as the two limiting cases for the shape such an internal crack may assume. The ellipse is defined by

$$(x_2/a_o)^2 + x_3^2/(L_o/2)^2 = 1 \tag{6}$$

or

$$x_2 = a_o \cos\theta \quad , \quad x_3 = (L_o/2) \sin\theta \tag{7}$$

which, by observing that $x_2/a_o = y$ and $L(y) = 2x_3$ (Fig. 1b), gives the function L(y) as follows

$$L(y) = L_o\sqrt{1-y^2} \quad , \quad (-1<y<1). \tag{8}$$

For a rectangular contour it is simply assumed that $L(y) = L_o$, $(-1<y<1)$. The stress intensity factors for a single crack calculated from (3) after solving the integral equations and determining the functions $\sigma(y)$ and $m(y)$ are given in Tables 3-7 and Figures 2-9.

Table 3 shows the comparison between the stress intensity factor at the midsection of a long internal elliptic crack (i.e., for y=0, $L=L_o$, $a_o<\infty$) and that obtained from the corresponding plane strain solution (i.e., Table 1 or equations (3) and (4) with $\sigma=\sigma_o$, $L=L_o$, $a_o=\infty$) in a plate under uniform tension σ_o perpendicular to the crack surface(*). Note that, as expected, the stress intensity factors $K(L_o)$ for the

(*) K_∞ shown in Table 3 is calculated from Eqs. (3) and (4) by using the coefficients b_j given in Table 2. Comparison of K_∞ of Table 3 and K_N of Table 1 gives some idea about the accuracy of the curve fitting, Eq. (4).

Table 3. Comparison of the stress intensity factor $K(L_o)$ at the center of an internal elliptic crack of length $2a_o$ with the corresponding plane strain value K_∞ (for which $a_o=\infty$) in a plate under uniform membrane stress $\sigma_o=N_o/h$.

L_o/h	$\frac{K_\infty}{\sigma_o\sqrt{\pi L_o/2}}$	$\frac{K(L_o)}{\sigma_o\sqrt{\pi L_o/2}}$			$100\,\frac{K(L_o)-K_\infty}{K_\infty}$		
	$(a_o/L_o=\infty)$	$a_o/L_o=10$	$a_o/L_o=20$	$a_o/L_o=100$	$\frac{a_o}{L_o}=10$	$\frac{a_o}{L_o}=20$	$\frac{a_o}{L_o}=100$
0.1	1.005997	0.999043	0.995528	0.997353	-0.7	-1.0	-0.9
0.2	1.024588	1.013152	1.011516	1.015310	-1.1	-1.3	-0.9
0.3	1.057743	1.041450	1.041460	1.047558	-1.5	-1.5	-1.0
0.4	1.109368	1.091117	1.089049	1.098079	-1.6	-1.8	-1.0
0.5	1.186659	1.144763	1.160564	1.173659	-3.5	-2.2	-1.1
0.6	1.303310	1.245248	1.268245	1.287556	-4.5	-2.7	-1.2
0.7	1.488234	1.483155	1.437816	1.467902	-0.3	-3.4	-1.4
0.8	1.815976	1.747479	1.733496	1.786292	-3.8	-4.5	-1.6
0.9	2.579413	2.271758	2.400426	2.522210	-11.9	-6.9	-2.2

Table 4. Comparison of the stress intensity factors K(y) calculated in this study at y=0 and y=1/2 ($y=x_2/a_0$) for an internal planar elliptic crack in a plate under uniform tension σ_0 with the corresponding values $\bar{K}(y)$ given in Ref. 4; $K_0 = \sigma_0\sqrt{\pi L_0/2}$.

L_0/h	a_0/L_0	y	$K(y)/K_0$	$\bar{K}(y)/K_0$	$\frac{\bar{K}-K}{\bar{K}}$ 100
0.1	0.5	0	0.916	0.637	43.7
		1/2	0.868	0.637	36.2
	1.0	0	0.955	0.827	15.5
		1/2	0.896	0.785	14.2
	2.0	0	0.976	0.935	4.3
		1/2	0.911	0.875	4.1
	3.0	0	0.983	0.967	1.7
		1/2	0.916	0.902	1.6
	4.0	0	0.987	0.980	0.6
		1/2	0.919	0.914	0.5
	10.0	0	0.993	0.999	-0.6
		1/2	0.923	0.930	-0.7
0.2	0.5	0	0.862	0.638	35.1
		1/2	0.827	0.638	29.6
	1.0	0	0.931	0.830	12.2
		1/2	0.880	0.788	11.6
	2.0	0	0.971	0.942	3.1
		1/2	0.908	0.881	3.1
	3.0	0	0.986	0.976	1.0
		1/2	0.918	0.910	0.9

Table 4 - cont.

L_o/h	a_o/L_o	y	$K(y)/K_o$	$\bar{K}(y)/K_o$	$\frac{\bar{K}-K}{\bar{K}}$ 100
0.2	4.0	0	0.993	0.991	0.2
		1/2	0.923	0.923	0.0
	10.0	0	1.007	1.013	-0.6
		1/2	0.933	0.942	-1.0
0.3	0.5	0	0.824	0.641	28.6
		1/2	0.796	0.640	24.4
	1.0	0	0.920	0.837	9.9
		1/2	0.871	0.794	9.8
	2.0	0	0.979	0.957	2.3
		1/2	0.914	0.893	2.3
	3.0	0	1.001	0.996	0.5
		1/2	0.930	0.927	0.3
	4.0	0	1.012	1.014	-0.2
		1/2	0.937	0.942	-0.5
	10.0	0	1.034	1.041	-0.7
		1/2	0.952	0.966	-1.5
0.4	0.5	0	0.798	0.645	23.6
		1/2	0.775	0.644	20.3
	1.0	0	0.920	0.851	8.1
		1/2	0.871	0.804	8.3
	2.0	0	1.000	0.984	1.6
		1/2	0.929	0.915	1.6
	3.0	0	1.030	1.031	-0.1
		1/2	0.950	0.955	-0.4

Table 4 - cont.

L_o/h	a_o/L_o	y	$K(y)/K_o$	$\bar{K}(y)/K_o$	$\frac{\bar{K}-K}{\bar{K}}$ 100
0.4	4.0	0	1.047	1.054	-0.7
		1/2	0.961	0.974	-1.3
	10.0	0	1.078	1.091	-1.2
		1/2	0.982	1.005	-2.3
0.5	0.5	0	0.783	0.654	19.8
		1/2	0.761	0.650	17.2
	1.0	0	0.932	0.874	6.7
		1/2	0.880	0.821	7.3
	2.0	0	1.036	1.030	0.6
		1/2	0.956	0.949	0.7
	3.0	0	1.078	1.090	-1.1
		1/2	0.984	0.998	-1.4
	4.0	0	1.101	1.121	-1.8
		1/2	0.998	1.023	-2.4
	10.0	0	1.145	1.172	-2.4
		1/2	1.025	1.063	-3.5
0.6	0.5	0	0.779	0.667	16.9
		1/2	0.756	0.658	14.9
	1.0	0	0.960	0.911	5.4
		1/2	0.901	0.846	6.4
	2.0	0	1.095	1.103	-0.8
		1/2	0.997	0.999	-0.2
	3.0	0	1.151	1.183	-2.7
		1/2	1.033	1.061	-2.6
	4.0	0	1.183	1.225	-3.5
		1/2	1.052	1.092	-3.6
	10.0	0	1.245	1.298	-4.0
		1/2	1.088	1.143	-4.7

Table 4 - cont.

L_o/h	a_o/L_o	y	$K(y)/K_o$	$\bar{K}(y)/K_o$	$\frac{\bar{K}-K}{\bar{K}}$ 100
0.7	0.5	0	0.788	0.687	14.7
		1/2	0.760	0.671	13.3
	1.0	0	1.009	0.968	4.3
		1/2	0.935	0.882	6.0
	2.0	0	1.187	1.213	-2.2
		1/2	1.058	1.067	-0.8
	3.0	0	1.266	1.322	-4.2
		1/2	1.106	1.144	-3.3
	4.0	0	1.310	1.381	-5.1
		1/2	1.132	1.183	-4.4
	10.0	0	1.403	1.483	-5.4
		1/2	1.179	1.242	-5.1
0.8	0.5	0	0.818	0.717	14.1
		1/2	0.777	0.686	12.9
	1.0	0	1.096	1.051	4.3
		1/2	0.991	0.930	6.6
	2.0	0	1.341	1.372	-2.3
		1/2	1.152	1.152	0.0
	3.0	0	1.457	1.521	-4.3
		1/2	1.218	1.245	-2.2
	4.0	0	1.525	1.603	-4.9
		1/2	1.253	1.290	-2.9
	10.0	0	1.674	1.747	-4.2
		1/2	1.318	1.349	-2.3

Table 4 - cont.

L_o/h	a_o/L_o	y	$K(y)/K_o$	$\bar{K}(y)/K_o$	$\frac{\bar{K}-K}{\bar{K}}$ 100
0.9	0.5	0	0.905	0.759	19.3
		1/2	0.813	0.709	14.7
	1.0	0	1.284	1.167	10.0
		1/2	1.086	0.987	10.1
	2.0	0	1.661	1.594	4.2
		1/2	1.310	1.246	5.1
	3.0	0	1.858	1.799	3.3
		1/2	1.405	1.347	4.2
	4.0	0	1.981	1.912	3.6
		1/2	1.456	1.392	4.6

elliptic crack are consistently smaller than the plane strain values K_∞; $K(L_o) \to K_\infty$ as $a_o/L_o \to \infty$, and despite the approximate nature of the line spring method used to calculate $K(L_o)$ the relative error is surprisingly small.

Extensive results and formulas developed from the numerical solution obtained from a finite element method for an internal elliptic crack in a plate under tension are given in [4]. Figures 2-9 and Table 4 show the comparison of the stress intensity factors obtained from this study with those generated from the formulas given in [4]. Again K_∞ is the corresponding plane strain value given by Table 1 or Eq. (4) and the normalizing stress intensity factor is $K_o = \sigma_o\sqrt{\pi L_o/2}$. The table gives the stress intensity factors calculated at $y = 0$ (the mid-section of the ellipse) and $y = 1/2$ (or $x_2 = a_o/2$). The table and the figures show that with the exception of relatively small values of a_o/L_o at small L_o/h ratios (for which physically the line-spring is really not a suitable model) the agreement is generally good.

Another comparison with the previous finite element results [5] is shown in Table 5. It should be noted in the results given in Table 5

Table 5. Comparison of the stress intensity factors $K(L_o)$ calculated in this study at the midsection of an internal planar elliptic crack in a plate under uniform tension σ_o with the corresponding results $\bar{K}$ given in [5]; $K_o=\sigma_o\sqrt{\pi L_o/2}$, $y=x_2/a_o=\cos\theta$ (Eqs. 6-8), $L_o/h=0.75$, $a_o/L_o=1.25$.

θ	y	$\bar{K}/K_o$	$K(L_o)/K_o$	$100\,\frac{K-\bar{K}}{\bar{K}}$
90°	0	0.985	1.120	13.7
80°	0.174	0.971	1.103	13.6
70°	0.342	0.944	1.052	11.4
60°	0.500	0.898	0.973	8.4
45°	0.707	0.810	0.832	2.7
40°	0.766	0.770	0.742	-3.6

Table 6. Stress intensity factors in a plate containing a rectangular planar crack and subjected to uniform tension σ_o.

$\frac{L_o}{h}$	y	a_o/L_o					
		0.5	1.0	2.0	3.0	4.0	10.0
0.1	0	0.975	1.015	1.053	1.078	1.098	1.172
	0.6	0.946	1.001	1.046	1.073	1.095	1.170
0.2	0	0.931	0.991	1.033	1.055	1.071	1.134
	0.6	0.879	0.962	1.018	1.045	1.064	1.131
0.3	0	0.901	0.988	1.040	1.064	1.080	1.137
	0.6	0.831	0.943	1.017	1.048	1.069	1.133
0.4	0	0.883	0.998	1.067	1.096	1.113	1.169
	0.6	0.798	0.938	1.033	1.073	1.096	1.162
0.5	0	0.875	1.024	1.115	1.151	1.172	1.231
	0.6	0.777	0.947	1.068	1.118	1.147	1.221
0.6	0	0.879	1.068	1.192	1.239	1.266	1.333
	0.6	0.768	0.973	1.128	1.193	1.230	1.318
0.7	0	0.899	1.142	1.313	1.378	1.416	1.500
	0.6	0.774	1.023	1.225	1.313	1.364	1.478
0.8	0	0.946	1.269	1.520	1.623	1.680	1.800
	0.6	0.803	1.116	1.393	1.522	1.597	1.764
0.9	0	1.068	1.542	1.969	2.162	2.271	2.496
	0.6	0.892	1.326	1.760	1.981	2.115	2.420

Table 7. Normalized stress intensity factors $K(y)/K_o$ in a plate containing a symmetrically located elliptic or rectangular planar crack and subjected to pure bending M_o; $y=x_2/a_o$, $K_o = (6M_o/h^2)\sqrt{\pi L_o/2}$.

		ELLIPTIC CRACK				RECTANGULAR CRACK			
$\frac{L_o}{h}$	y	a_o/L_o				a_o/L_o			
		0.5	1.0	2.0	4.0	0.5	1.0	2.0	4.0
0.1	0.0	0.296	0.297	0.297	0.297	0.353	0.369	0.382	0.390
	0.2	0.288	0.288	0.289	0.289	0.353	0.369	0.382	0.390
	0.4	0.261	0.261	0.261	0.262	0.353	0.369	0.382	0.390
	0.6	0.214	0.214	0.214	0.214	0.353	0.369	0.382	0.390
	0.8	0.135	0.135	0.135	0.135	0.352	0.369	0.382	0.390
	0.9	0.090	0.090	0.090	0.090	0.351	0.368	0.381	0.390
0.3	0.0	0.788	0.834	0.859	0.873	0.860	0.896	0.929	0.969
	0.2	0.775	0.816	0.838	0.850	0.858	0.895	0.928	0.969
	0.4	0.728	0.756	0.770	0.778	0.850	0.891	0.927	0.968
	0.6	0.635	0.643	0.646	0.649	0.832	0.882	0.923	0.966
	0.8	0.432	0.427	0.419	0.417	0.773	0.849	0.907	0.958
	0.9	0.290	0.280	0.275	0.273	0.685	0.790	0.873	0.942
0.5	0.0	0.948	1.122	1.248	1.341	1.107	1.264	1.373	1.467
	0.2	0.948	1.113	1.231	1.317	1.098	1.258	1.370	1.464
	0.4	0.941	1.079	1.171	1.234	1.064	1.236	1.357	1.454
	0.6	0.912	0.994	1.040	1.069	0.993	1.186	1.327	1.433
	0.8	0.746	0.736	0.723	0.715	0.827	1.044	1.232	1.374
	0.9	0.556	0.511	0.485	0.472	0.657	0.871	1.087	1.275
0.7	0.0	0.846	1.119	1.382	1.643	1.001	1.313	1.613	1.904
	0.2	0.856	1.125	1.381	1.629	0.987	1.301	1.602	1.893
	0.4	0.884	1.139	1.369	1.574	0.944	1.261	1.567	1.857
	0.6	0.934	1.147	1.318	1.446	0.856	1.174	1.491	1.782
	0.8	0.929	1.010	1.046	1.056	0.675	0.971	1.300	1.611
	0.9	0.836	0.802	0.761	0.728	0.514	0.765	1.074	1.400
0.9	0.0	0.712	1.031	1.436	1.952	0.825	1.224	1.758	2.457
	0.2	0.713	1.029	1.422	1.915	0.813	1.210	1.739	2.431
	0.4	0.739	1.051	1.421	1.852	0.772	1.162	1.679	2.345
	0.6	0.814	1.118	1.447	1.772	0.692	1.065	1.559	2.180
	0.8	0.926	1.149	1.329	1.443	0.534	0.854	1.300	1.853
	0.9	0.979	1.061	1.086	1.070	0.400	0.656	1.036	1.632

$a_o/L_o = 1.25$ is relatively small for the line spring model to be effective. Despite that the relative error does not seem to be very high. The angle θ shown in the table is the parameter defining the point on the ellipse (see (7)).

Table 6 shows the stress intensity factors in a plate containing a rectangular planar crack and subjected to uniform tension σ_o. Referring to Fig. 1b, in this case the crack is defined by

$$-\frac{L_o}{2} < x_3 < \frac{L_o}{2} \quad , \quad -a_o < x_2 < a_o$$

One may note that, as expected, the stress intensity factors for the rectangular crack are generally somewhat greater than the corresponding values for an elliptic crack.

The results for a plate containing a symmetrically located (Fig. 1b) elliptic or rectangular planar crack and subjected to pure bending (Fig. 1a) are given in Table 7. It should again be noted that for larger values of y and smaller values of a_o/L_o the line-spring model which is used to calculate these results is not a suitable model. Table 7 shows the stress intensity factor along the border of the crack on the tension side of the plate. On the compression side the stress intensity factors have the same values with a negative sign. Under pure bending since the crack faces on the compression side of the plate would close, the results given in the table cannot be used separately. The results are, of course, useful and valid if the plate is subjected to tension, as well as bending in such a way that the superimposed stress intensity factor is positive everywhere.

4. References

1. F. Delale and F. Erdogan, "Line Spring Model for Surface Cracks in a Reissner Plate", Int. J. Engng. Science, Vol. 19, pp. 1331-1340, 1981.

2. F. Delale and F. Erdogan, "Application of the Line Spring Model to a Cylindrical Shell Containing a Circumferential or an Axial Part-Through Crack", J. Appl. Mech., Vol. 49, Trans. ASME, pp. 97-102, 1982.

3. A.C. Kaya and F. Erdogan, "Stress Intensity Factors and COD in an Orthotropic Strip", Int. J. of Fracture, Vol. 16, pp. 171-190, 1980.

4. J.C. Newman, Jr. and I.S. Raju, "Stress Intensity Factor Equations for Cracks in Three-Dimensional Finite Bodies", ASTM STP-791, pp. 238-265, 1983.

5. T. Nishioka and S.N. Atluri, "Analytical Solution for Embedded Elliptical Cracks, and Finite Element Alternating Method for Elliptical Surface Cracks, Subjected to Arbitrary Loadings", Engineering Fracture Mechanics, Vol. 17, pp. 247-268, 1983.

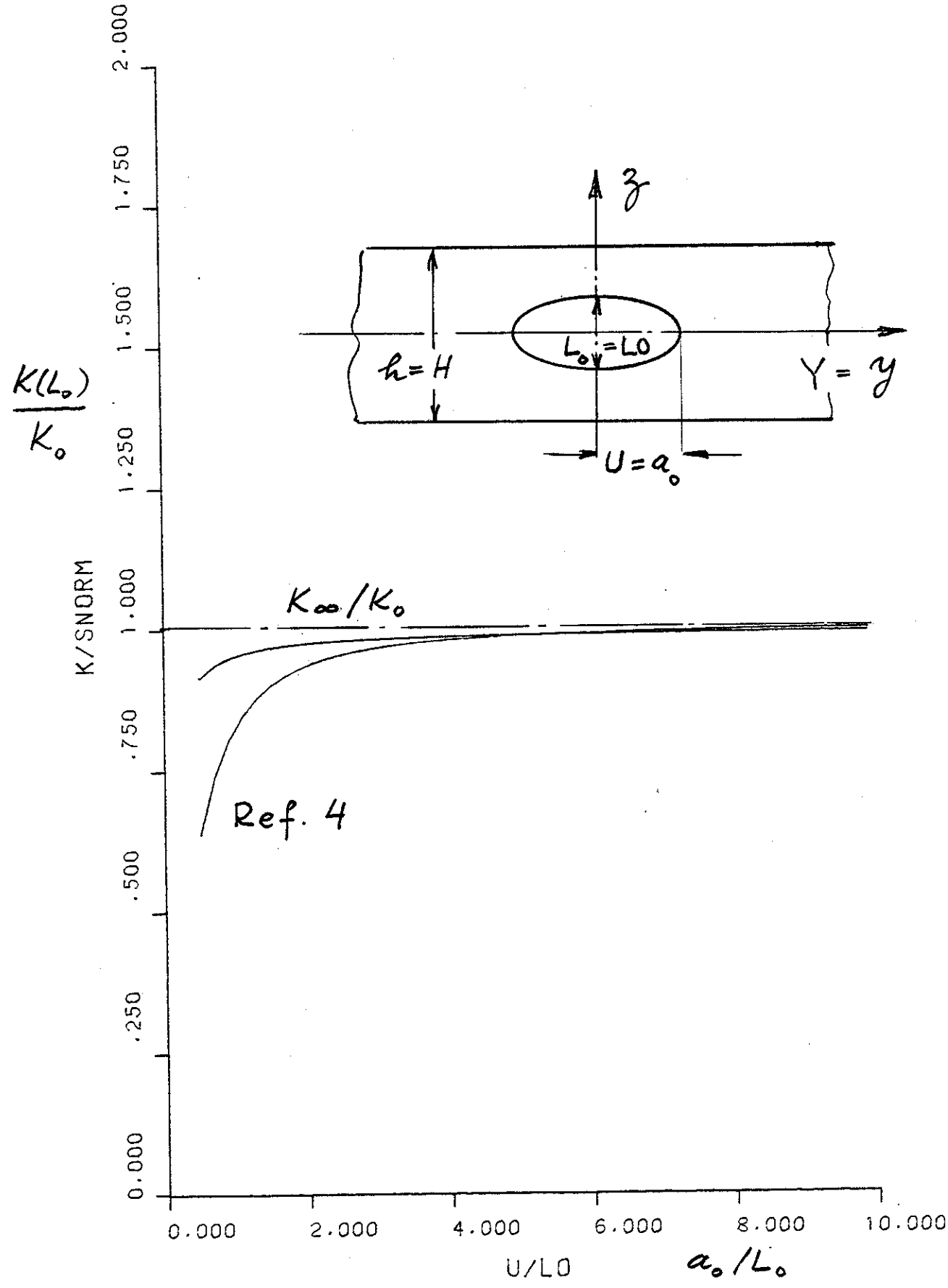

Fig. 2 Stress intensity factor at the midsection of a planar elliptic crack in a plate subjected to uniform tension $\sigma^{\infty}_{xx} = \sigma_0$ for $L_0/h = 0.1$; $K_0 = \sigma_0\sqrt{\pi L_0/2}$, K_∞ the plane strain value (for which $a_0 = \infty$).

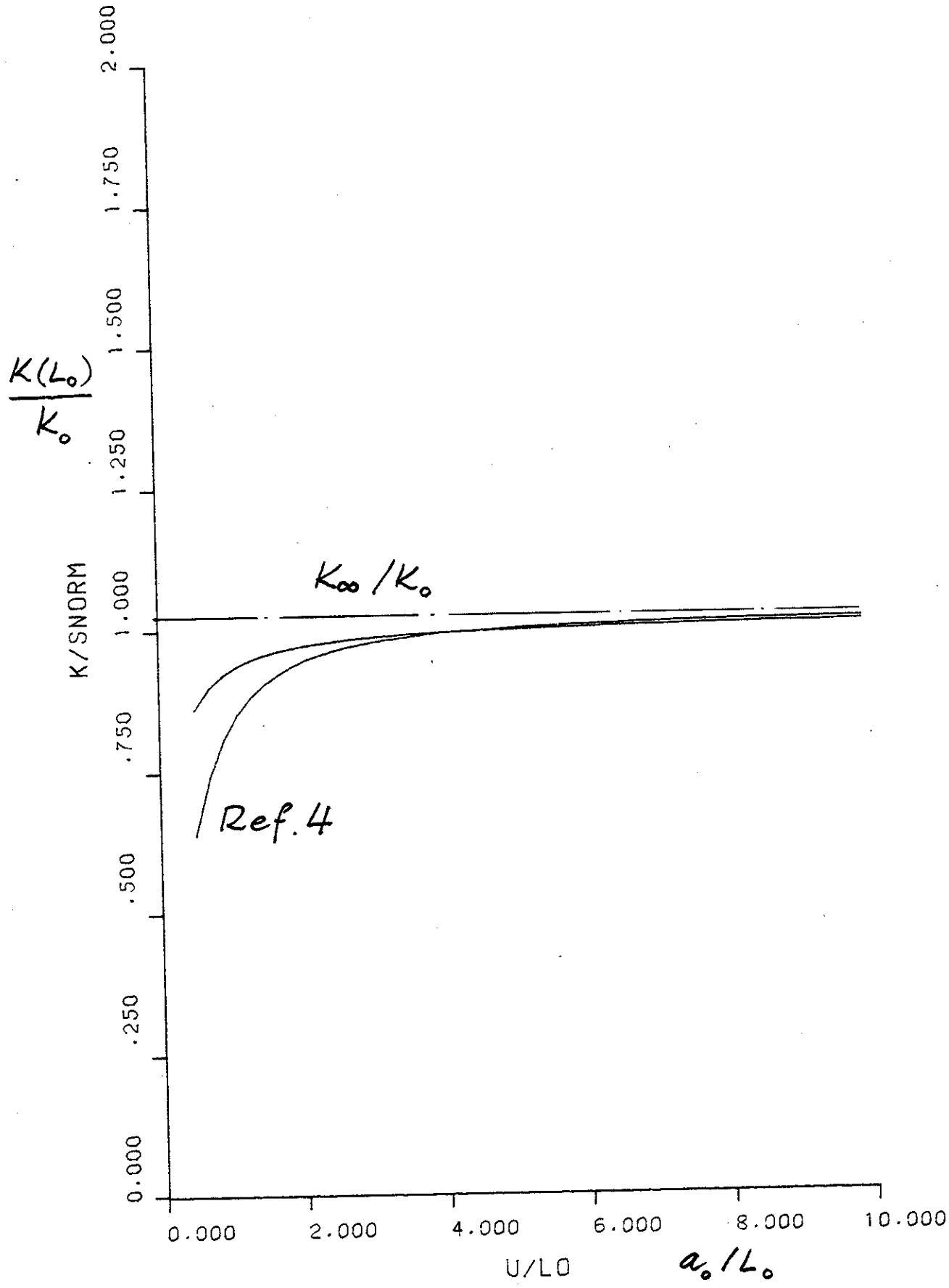

Fig. 3 Stress intensity factor at the midsection of a planar elliptic crack in a plate subjected to uniform tension $\sigma^{\infty}_{xx} = \sigma_0$ for $L_0/h = 0.2$; $K_0 = \sigma_0\sqrt{\pi L_0/2}$, K_∞ the plane strain value (for which $a_0 = \infty$).

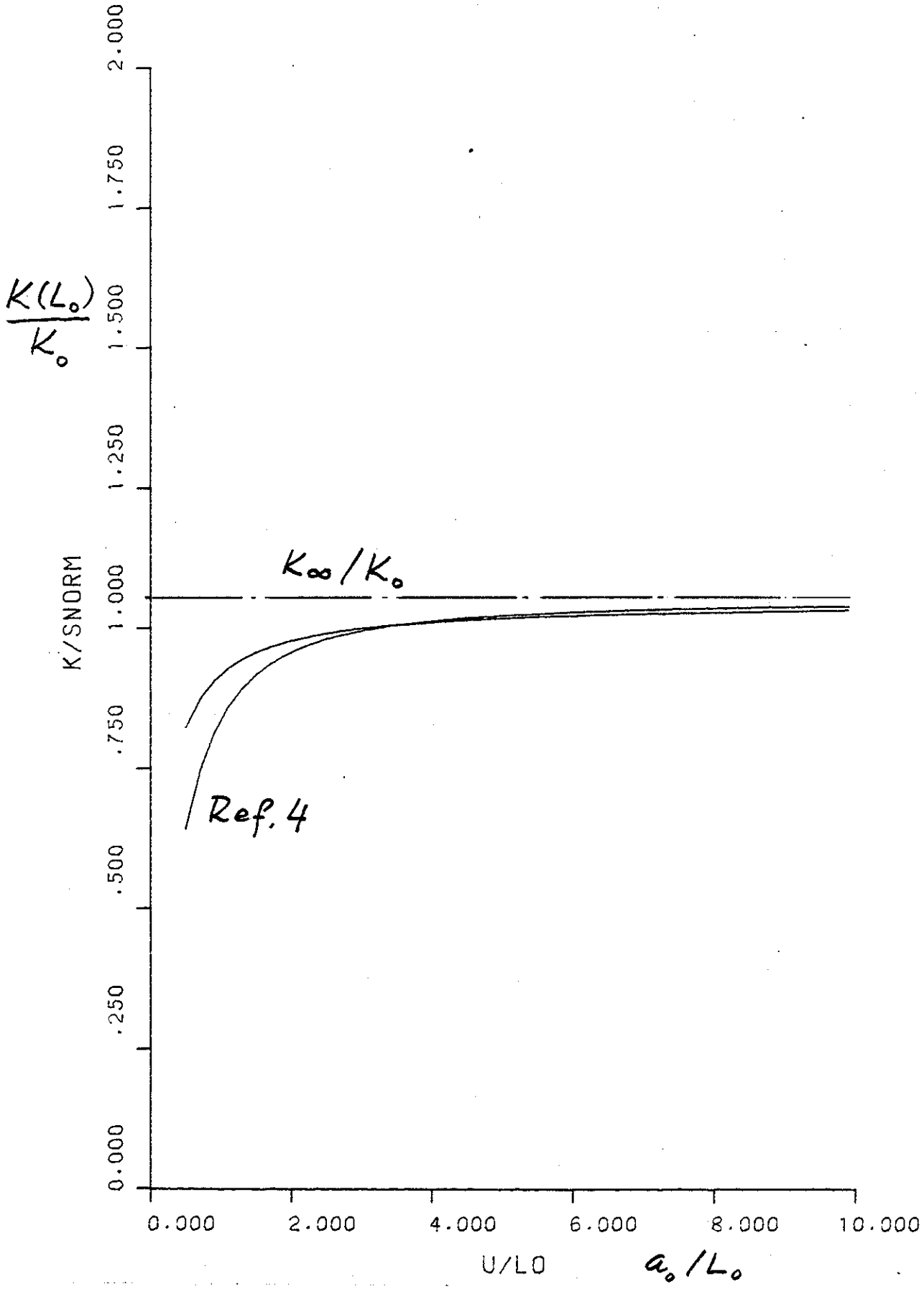

Fig. 4 Stress intensity factor at the midsection of a planar elliptic crack in a plate subjected to uniform tension $\sigma^{\infty}_{xx} = \sigma_0$ for $L_0/h = 0.3$; $K_0 = \sigma_0\sqrt{\pi L_0/2}$, K_∞ the plane strain value (for which $a_0 = \infty$).

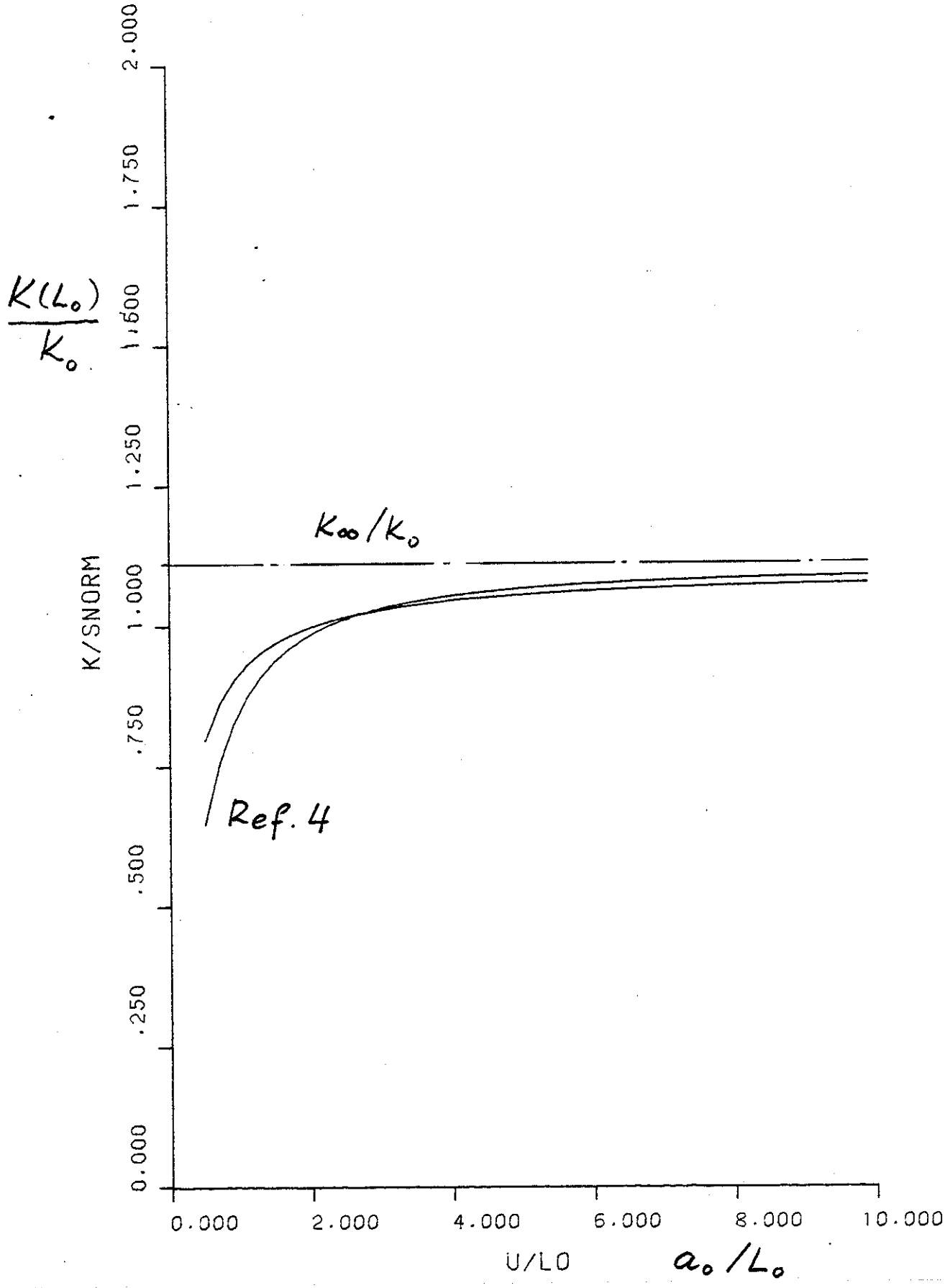

Fig. 5 Stress intensity factor at the midsection of a planar elliptic crack in a plate subjected to uniform tension $\sigma^{\infty}_{xx} = \sigma_0$ for $L_0/h = 0.4$; $K_0 = \sigma_0\sqrt{\pi L_0/2}$, K_∞ the plane strain value (for which $a_0 = \infty$).

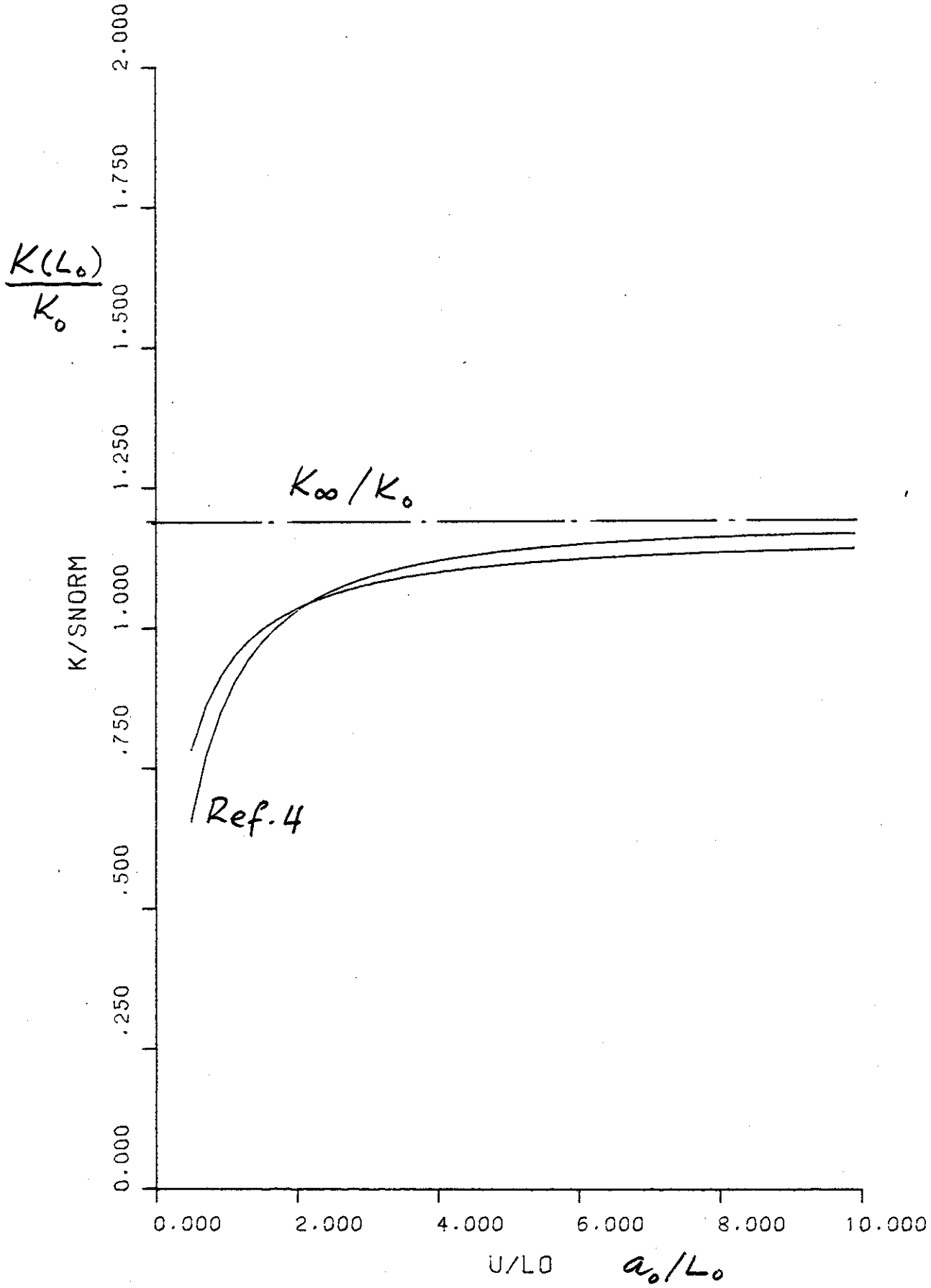

Fig. 6 Stress intensity factor at the midsection of a planar elliptic crack in a plate subjected to uniform tension $\sigma^{\infty}_{xx} = \sigma_0$ for $L_0/h = 0.5$; $K_0 = \sigma_0\sqrt{\pi L_0/2}$, K_∞ the plane strain value (for which $a_0 = \infty$).

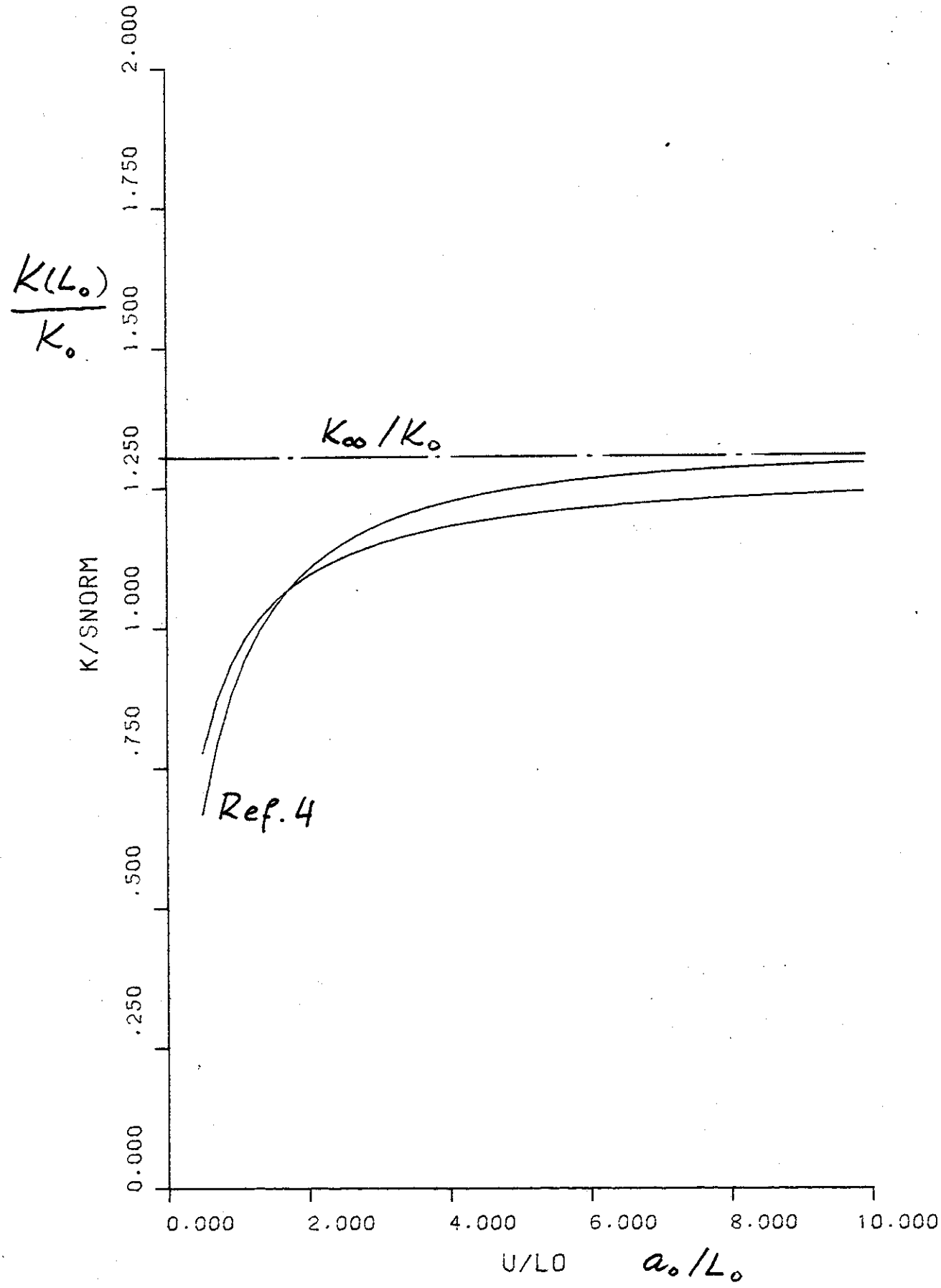

Fig. 7 Stress intensity factor at the midsection of a planar elliptic crack in a plate subjected to uniform tension $\sigma^{\infty}_{xx} = \sigma_0$ for $L_0/h = 0.6$; $K_0 = \sigma_0\sqrt{\pi L_0/2}$, K_∞ the plane strain value (for which $a_0 = \infty$).

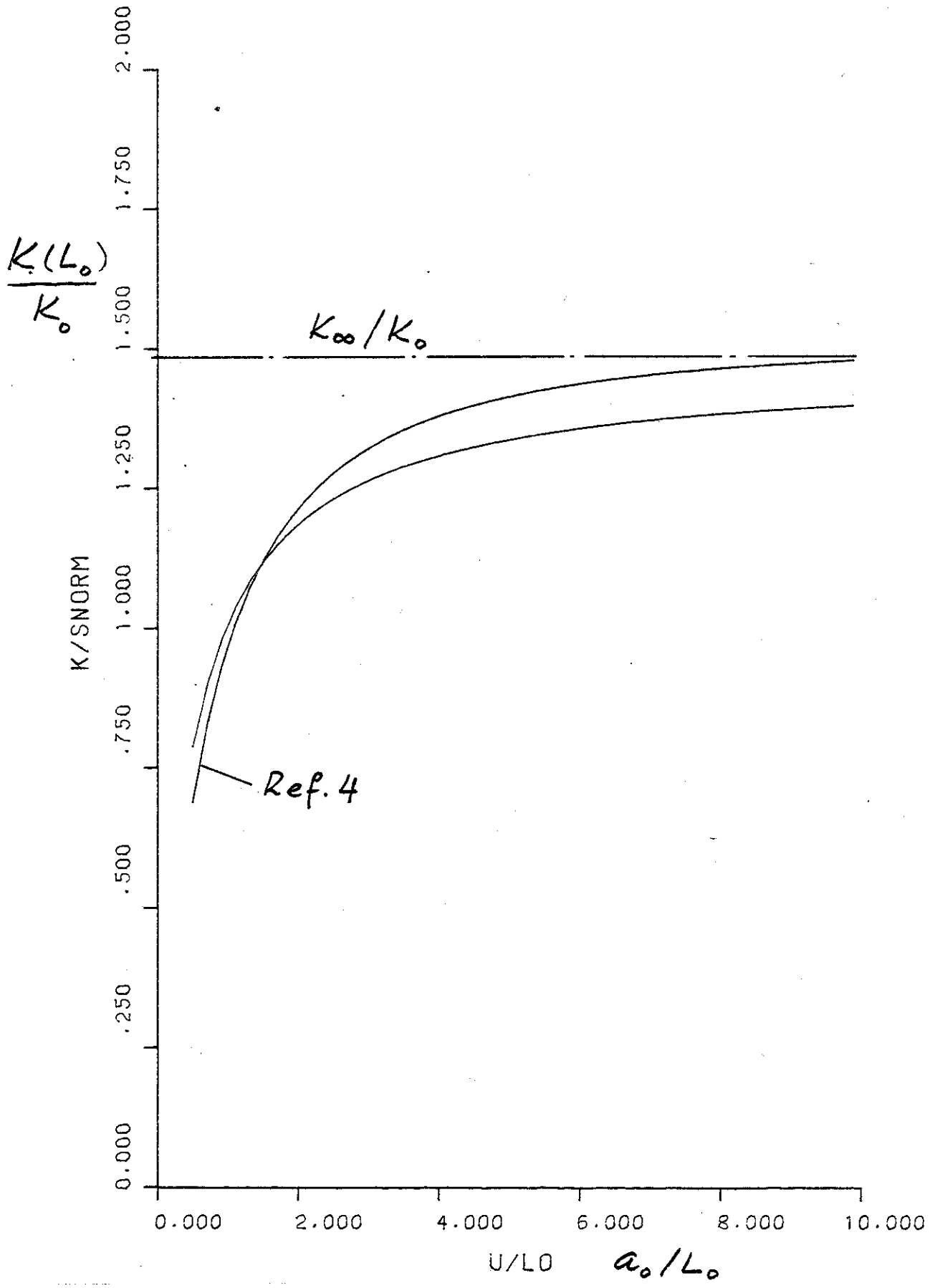

Fig. 8 Stress intensity factor at the midsection of a planar elliptic crack in a plate subjected to uniform tension $\sigma^{\infty}_{xx} = \sigma_0$ for $L_0/h = 0.7$; $K_0 = \sigma_0\sqrt{\pi L_0/2}$, K_∞ the plane strain value (for which $a_0 = \infty$).

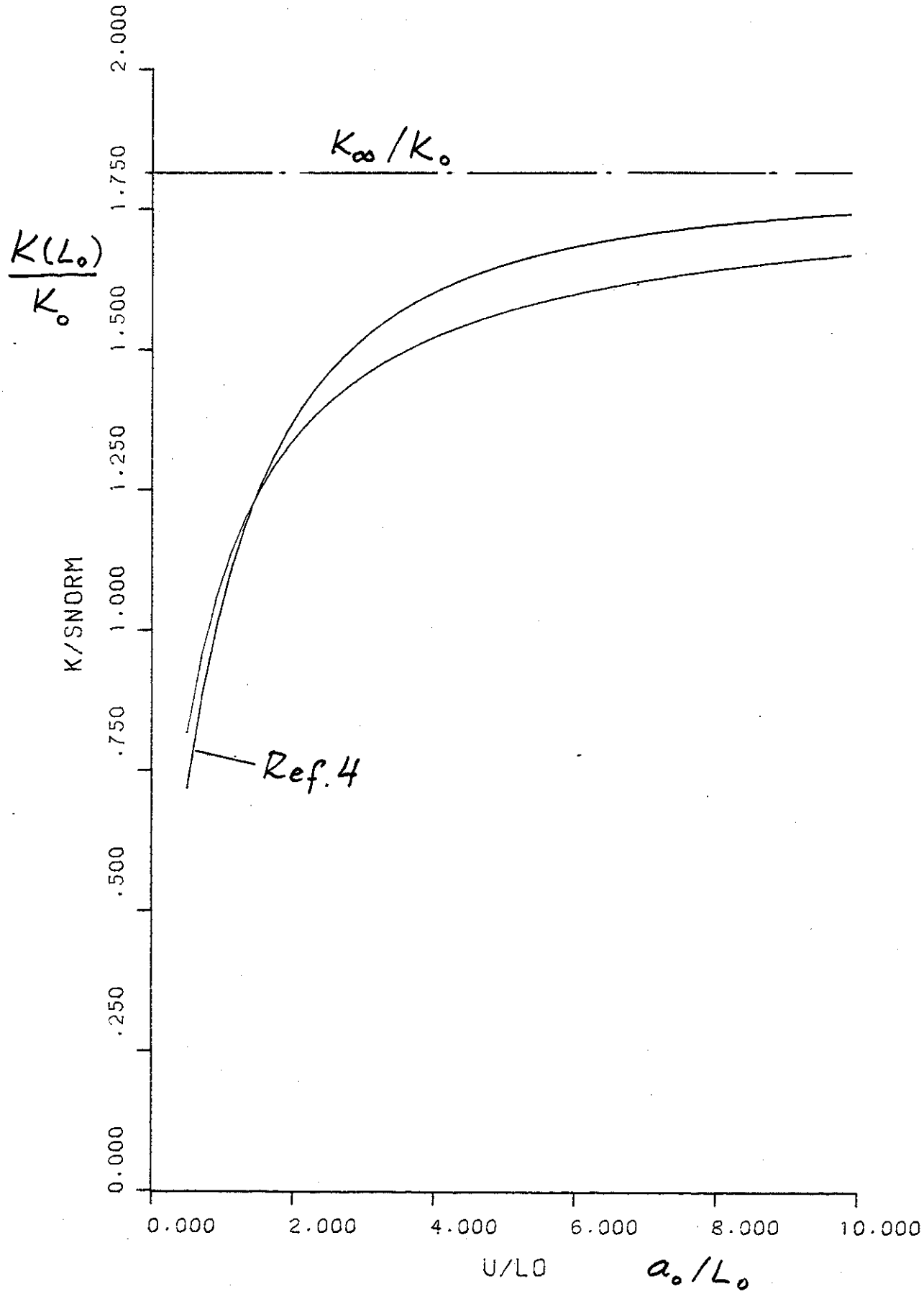

Fig. 9 Stress intensity factor at the midsection of a planar elliptic crack in a plate subjected to uniform tension $\sigma^{\infty}_{xx} = \sigma_0$ for $L_0/h = 0.8$; $K_0 = \sigma_0\sqrt{\pi L_0/2}$, K_∞ the plane strain value (for which $a_0 = \infty$).